UNIVERSITÀ
DEGLI STUDI
DI PADOVA

TESI DI DOTTORATO

Sede Amministrativa: Università degli Studi di Padova

Dipartimento di
INGEGNERIA INDUSTRIALE

CORSO DI DOTTORATO DI RICERCA IN: Ingegneria Industriale
CURRICOLO: Ingegneria Chimica ed Ambientale
CICLO XXXIV

Development of transient experimental techniques to investigate heterogenous catalytic reactions

Coordinatore: Ch.mo Prof. Giulio Rosati
Supervisore: Ch.mo Prof. Paolo Canu

Dottoranda: BENEDETTA OLIANI

Abstract

The research activities reported in this PhD thesis focus on one class of time-depending input variables: temperature and reactant concentration. Specifically, reactivity parameters (reagents conversion and products formation) were recorded as a function of temperature in temperature-programmed experiments with variable feed conditions (reducing or oxidizing atmospheres) and spent materials were characterized with surface analyses (SEM, EDS) to correlate their activity to chemical (mass and heat transfer) and physical (aggregation, segregation) phenomena. Also, the common feature between the catalytic materials investigated is the oxygen-storage capacity, i.e. their ability to store and release oxygen in oxygen-lean conditions, that represents a critical feature for more flexible operations, highly-selective oxidations and safer working conditions.

Two model materials were selected as oxygen-donors for two distinct applications: CuO was chosen to correlate the effect of different reaction parameters to its morphological features, long-time stability during redox cycles (H_2-O_2) and formation of peculiar superficial nanostructures while $LaFeO_3$ (perovskite) was identified as a possible candidate for the oxidative function, in automotive converter by taking advantage of oxygen diffusion in the lattice to transform CO into CO_2.

The last class of materials (CuY zeolites) was studied in CH_4 activation to assess their potential application to an industrial-relevant reaction (methane-to-methanol, MTM) in which the oxygen provided by the zeolites selectively reduces the extent of over-oxidation products in favour of the partial oxidation to methanol.

Index

Chapter 1

Research context

The central idea of the research activities reported in the PhD thesis is that catalysts are dynamic materials: the structure changes together with the local reaction conditions and it is strictly connected to the reactivity. This feature is crucial in the current energy transition from a fossil-based to low-carbon emission society: novel strategies and technologies are developed on renewable energies in combination with (electro-)chemical conversion solutions [1,2]. One of the biggest challenges to face in this changeover is the time-dependent availability of raw materials (e.g. biomass) and energy (solar and wind power). The use of alternative, renewable and fluctuating sources has a strong impact on their subsequent utilization and transformation into chemicals and fuels through catalytic processes [3]. Thus, chemical plants already designed and working at steady-state conditions (feed, temperature, pressure) should face a new operation mode characterized by frequent shut-offs and start-ups depending on the energy and feedstock availability. Buffering systems and adaptation of the catalyst properties to oscillating conditions are required to reduce the production fluctuations to preserve the same efficiency and affordability in a high-demanding market.

The perspective of more sustainable catalytic processes focused the academic and industrial research towards the design and implementation of new materials able to maintain high performance and productivity even with different reaction pathways and conditions. The boundary conditions for these new systems differentiate with current and former chemical processes, typically performed at steady-state with a narrow operation window identified with standard activity experiments and process simulations. Thus, the vision of the catalyst as static material with a chemical and physical structure unaltered by the reaction, kept at the same experimental conditions unless some deactivation processes start, could not be the modern view for catalysts and catalytic processes, in which a high flexibility is required. Additionally, transient conditions are not only related to few elitist and selected processes, as some applications are intrinsically dynamic and thus the real performance strongly depends on the oscillating input variable environment, either to restore the catalytic activity or as result of engine working principle. In fluid-catalytic cracking (FCC) the catalyst is regularly regenerated to burn off coke deposition [4] as well as Chemical-Looping Combustion (CLC) in which the material provides the oxygen for fuel combustion and it is subsequently restored in an oxidation reactor [5]. In automotive applications the operation conditions are intrinsically dynamic as the catalytic converter is subjected to different reaction atmosphere caused by start-ups, accelerations, engine temperature and variable air-to-fuel ratio [6]. Also, the variation of reactive atmosphere could improve the catalyst life-time and reaction rate, e.g. improving the redispersion of metal particles on the surface thanks to the reducing conditions (Pd on $LaFeO_3$ [7]) or increasing the production of NH_3 by periodically switching between H_2 and N_2 atmosphere [8].

Time-dependent conditions (concentration, temperature, pressure, electric potential) influence transport processes for both macroscopic (reactor) and microscopic (particle) scale, causing changes and rearrangements at atomic level [9–11] . These modifications reflect on the particle itself, on the mutual interactions between particles and the gas phase: changes at microscopic level induce transformation of the chemical and physical properties with structural changes such as sintering and redispersion, dissolution/leaching, surface alloying and segregation, morphological restructuring, phase change and the formation of other species (metal complexes, carbides, composites, etc.) [11]. Therefore, the knowledge of a catalytic system should not be determined just by the optimum reaction conditions but also the connection between reactivity parameters (conversion, yield, selectivity) and relevant microscopic processes between catalyst bulk and surface. The complete understanding of these phenomena gives important details for catalyst and reactor design, improvement of the overall performance, prediction of deactivation behaviours and life-time/stability and actions to increase catalyst and process efficiency.

Under these perspectives, this PhD thesis was focused on correlating the reactivity of different materials and applications to chemical (mass and heat transfer) and physical (aggregation, segregation) phenomena with temperature-programmed experiments under variable feed conditions. In **Chapter 2**, the influence of several experimental conditions (sample mass, reagent concentration, particle size, total volumetric flowrate, heating rate) applied to temperature-programmed reduction (TPR) and oxidation (TPO) was thoroughly investigated on a model system (bulk CuO reduction with H_2 and Cu reoxidation with O_2) to correlate the reduction (or oxidation) profiles to macroscopic performance (degree of reduction/oxidation) and chemical/physical phenomena (reaction mechanism, mass- and heat-transfer limitations). In **Chapter 3**, the identification of the process (reduction, oxidation, thermal/non-reactive cycle) responsible for the loss in reactivity caused by agglomeration in CuO/Cu system was analyzed. In **Chapter 4**, long-term reactivity in CuO/Cu system was also investigated with 11 sequential TPR-TPO experiments and a progressive loss in activity was visible from the degree of reduction/oxidation. In **Chapter 5**, axial temperature measurements were performed on CuO/Cu system to identify the role of temperature distribution during the agglomeration process. In **Chapter 6**, the formation of nanostructures to act as oxygen-donors on Cu/CuO surfaces (Cu foil and Cu/CuO powder) was investigated. In **Chapter 7**, transient experimental techniques were applied to analyze the oxygen mobility in $LaFeO_3$ for CO oxidation. In **Chapter 8**, Cu-exchanged Y zeolites were tested in CH_4 activation to preliminary assess the activity of CuY zeolites towards methane-to-methanol reaction, and finally **Chapter 9** collects general conclusions.

Most of the experimental and computing activities were performed the premises of K-INN Lab research group at the Department of Industrial Engineering (Università degli Studi di Padova). The results reported in Chapter 8 were collected at the Atomic-Scale Analysis Department at Haldor Topsøe (Kongens Lyngby, Denmark) during a visiting fellowship.

References

[1] J.M. Thomas, Heterogeneous catalysis and the challenges of powering the planet, securing chemicals for civilised life, and clean efficient utilization of renewable feedstocks, ChemSusChem. 7 (2014) 1801–1832. https://doi.org/10.1002/cssc.201301202.

[2] F. Schüth, Chemical compounds for energy storage, Chemie-Ingenieur-Technik. 83 (2011) 1984–1993. https://doi.org/10.1002/cite.201100147.

[3] R. Schlögl, Sustainable Energy Systems: The Strategic Role of Chemical Energy Conversion, Topics in Catalysis. 59 (2016) 772–786. https://doi.org/10.1007/s11244-016-0551-9.

[4] E.T.C. Vogt, B.M. Weckhuysen, Fluid catalytic cracking: recent developments on the grand old lady of zeolite catalysis, Chemical Society Reviews. 44 (2015) 7342–7370. https://doi.org/10.1039/c5cs00376h.

[5] J. Adanez, A. Abad, F. Garcia-Labiano, P. Gayan, L.F. de Diego, Progress in chemical-looping combustion and reforming technologies, Progress in Energy and Combustion Science. 38 (2012) 215–282. https://doi.org/10.1016/j.pecs.2011.09.001.

[6] P.L. Silveston, Automotive exhaust catalysis under periodic operation, Catalysis Today. 25 (1995) 175–195.

[7] H. Tanaka, M. Uenishi, M. Taniguchi, I. Tan, K. Narita, M. Kimura, K. Kaneko, Y. Nishihata, J. Mizuki, The intelligent catalyst having the self-regenerative function of Pd, Rh and Pt for automotive emissions control, Catalysis Today. 117 (2006) 321–328. https://doi.org/10.1016/j.cattod.2006.05.029.

[8] G. Rambeau, H. Amariglio, Improvement of the catalytic performance of a ruthenium powder in ammonia synthesis by the use of a cyclic procedure, Applied Catalysis. 1 (1981) 291–302.

[9] B.M. Weckhuysen, Chemical imaging of spatial heterogeneities in catalytic solids at different length and time scales, Angewandte Chemie - International Edition. 48 (2009) 4910–4943. https://doi.org/10.1002/anie.200900339.

[10] J.D. Grunwaldt, J.B. Wagner, R.E. Dunin-Borkowski, Imaging Catalysts at Work: A Hierarchical Approach from the Macro- to the Meso- and Nano-scale, ChemCatChem. 5 (2013) 62–80. https://doi.org/10.1002/cctc.201200356.

[11] M.A. Newton, Dynamic adsorbate/reaction induced structural change of supported metal nanoparticles: Heterogeneous catalysis and beyond, Chemical Society Reviews. 37 (2008) 2644–2657. https://doi.org/10.1039/b707746g.

Chapter 2

Parametric sensitivity in temperature-programmed experiments on CuO reduction and reoxidation

Abstract

The influence of several experimental conditions (sample mass, reagent concentration, particle size, total volumetric flowrate, heating rate) applied to temperature-programmed reduction (TPR) and oxidation (TPO) was thoroughly investigated on a model system bulk CuO reduction with H_2 and Cu reoxidation with O_2) to correlate the reduction (or oxidation) concentration profiles to macroscopic performance (degree of reduction/oxidation) and chemical/physical phenomena (reaction mechanism, mass- and heat-transfer limitations). The profiles were significantly affected by the experimental parameters and their combinations, identifying a primary role for the sample mass, reactant inlet concentration and heating rate, while a negligible contribution was given by the particle size for both CuO reduction and Cu reoxidation. Agglomeration phenomena were observed during the reduction and severe morphological changes were observed in the final sample form, implying that the selection of the experimental variables for TPR/TPO protocols could not be solely performed through a characteristic number retrieved from the combination of parameters in which mass-transfer limitations have been disregarded.

Introduction

Metal oxides and the reduction to the corresponding metals have emerged as prominent active compounds in heterogenous catalysed reactions, covering a large variety of industrial and environmental processes.

The identification of the oxidation state at which are active and the analysis of their specific properties along with their effects on the reaction performance is essential to rationally design optimized catalysts capable of increasing the overall process efficiency in medium- and long-term operation. In connection with this purpose, several characterization techniques are applied to evaluate morphological, surface and bulk features of solid catalyst [1,2]. In a heterogeneous reactive system, the interaction between gas species and active sites on the solid surface is the key to characterize and investigate the reactivity towards specific reaction categories, such as reductions and oxidations. Temperature-programmed experiments belongs to the thermo-analytical techniques that provide quantitative information on the redox properties of metal oxides and metals as a function of temperature [3–5]. Specifically, the reduction behaviour of metals either in the bulk or dispersed on support materials forms is examined through Temperature-Programmed Reduction (TPR) experiments, in which a reducing gas (H_2, CO) flows on the metals oxide sample while temperature is increased at constant rate and the reductant consumption is continuously recorded with a high-frequency detector (thermal conductivity detector or mass-spectrometer). Similarly, Temperature-Programmed Oxidation (TPO) are carried out using an oxidizing atmosphere (O_2, air) and the reduced sample is reoxidizes to determine the facility to restore the metal oxide form. These temperature-programmed analyses elucidate primary phenomena such as metal-support interaction, pre-treatment impact, role of promoters and influence of more metal oxides on the reducibility of a specific phase. Also, calculation of kinetic parameters and reaction rate are performed, indicating the ease of oxygen removal and thus the strength of metal-oxygen bond [3].

The information obtained through these analyses are numerous, but the results can significantly vary depending on the physical and chemical characteristics of the system along with the experimental parameters selected, affecting multiple aspects of reduction profiles [6–10]. Specifically, the incorrect combination of experimental variables (sample mass, particle size, total volumetric flowrate, initial reducing gas concentration, heating rate) could lead to severe misinterpretations, decreasing the reliability of the results obtained through TPR experiments. Deviations from standard values are indeed affecting the activation energies calculation, e.g. ranging from 18 to 246 kJ/mol in NiO reduction [11], the shape and characteristic temperatures (activation and peak) of the reduction trends.

Parametric sensitivity studies were already carried out in the past, on a model material (CuO, reduced with H_2) to identify a general rule to properly choose a reliable set of operating variables. Characteristic numbers (called K in [6] and P in [9]) have been defined together with their optimal range of application, by analysing the influence of different experimental parameters. Reduction profile shape and maximum reduction temperature are both affected by peculiar features of the reactive system (chemical and physical properties, such as mass-transfer limitations and particle agglomeration) and distinctive factors of the experimental technique (fluidynamic and heat distribution). The parameter K is defined as K(s) = $n_{oxide}/(\dot{V}_{tot} \cdot C_{red})$ [6] in which n_{oxide} is the amount of reducible species [mol], $\dot{V}_{tot}$ is the total volumetric flowrate [Ncm^3/min] and y_{red} is the fraction of the reducing gas [-]. It compares the amount of material with the flow rate of reducing gas. It was developed as a combination of operating variables and the limits of applicability were built based on the instrument sensitivity (for $K <$ 55 s the sensitivity is too low to detect any change in the reduction profile) and reaction kinetics. K is derived assuming a differential reactor (if $K >$ 140 s the reductant consumption is too fast and the assumption of linear concentration profile is not preserved) and a specific heating rate range (β = 6 to 18 °C/min). The parameter P is defined as $P(\mathrm{K}) = \beta \cdot n_{oxide}/(\dot{V}_{tot} \cdot y_{red})$ in [9]; it is the evolution of K, accounting for the heating rate. The suggested range of application is $P < 20$ K as higher values deform the reduction peak, by flattening the curve. This effect was still assigned to the large consumption of reducing gas, violating the assumption of the reaction driving force residing in a mean reducing gas concentration, i.e. low conversion (> 10%). However, the reduction profiles exhibited perturbations (multiple peaks for one-step reduction mechanism and/or flat profiles at the maximum reduction peak) even when K and P numbers were selected in their optimal range of applicability [10]. This result is clearly an indication of the crucial role of mass-transfer limitations on a heterogeneous, gas-solid reaction, as the apparent reaction rate becomes affected by the gas transfer rate to the solid and within its porosity, up to the active sites; these processes are neglected in the development of both characteristic parameters, K and P. Both internal and external mass transfer may have a relevant impact in the reaction progress, particularly at higher temperature, and it is affected by the initial morphology and the final bulk/surface configuration of the oxide [12]. Specifically, the reduction of a metal oxide to its corresponding metal is described with two models (interface and nucleation model) in which the formation of the metal occurs on the surface of the oxide as a uniform layer or a series metal nucleus with reduced porosity and thus the reaction boundary is shifted towards the particle bulk, modifying the overall morphology and porosity, i.e. enhancing diffusion limitations caused by physical features and affecting the reactivity [13]. Increasing the complexity of the reactive system (supported multi-metal oxides with micro- and meso-porosity), more errors in interpreting the reduction profiles could arise and thus the indications of K and P parameters are misleading. unreliable information could be obtained from the analysed reactive system.

In this work, bulk CuO reduction with H_2 and its re-oxidation with O_2 was selected as model system, to correlate the reduction (or oxidation) profiles to macroscopic performance (degree of reduction/oxidation) and chemical/physical phenomena (reaction mechanism, mass- and heat-transfer limitations), by means of temperature-programmed experiments (TPR, TPO). Specifically, a sensitivity analysis was performed for each experimental condition (sample mass, reactant concentration, particle size, total volumetric flowrate and heating rate) to retrieve specific key descriptors of the reduction and oxidation processes, such as reduction and oxidation degree, activation and peak temperature. The influence of the listed parameters is already reported in literature as well as characteristic numbers to properly select the set of experimental parameters to perform TPR and TPO reaction. Based on the results obtained in this study, more details and recommendations will be added for the use of these numbers including a preliminary analysis on agglomeration phenomena.

Materials and methods

The effect of different experimental parameters on CuO (Alfa Aesar, 99.995%) reduction with H_2 and its reoxidation was carried using pure gases (H_2, O_2, Ar) connected to mass-flowmeters (Brooks and Bronkhorst High-Tech) through which the desired inlet composition was achieved. Before entering the reactor, the gas feed went through an automatic four-way valve (VICI Valco, Figure 1) to optimize the reaction protocol, ensure the total separation between the reducing and oxidizing atmosphere in CuO cyclic experiments. The valve switch between the two positions and mass-flowmeters operation were controlled though purpose-built MATLAB executable programs. The reactive section could be approximated to a plug-flow reactor, in which the sample bed (~ 2 – 5 mm) was inserted into a quartz tube (ID 6 mm) and kept in position by two quartz wool layers. It was then introduced into an electrically heated furnace (Watlow) and two thermocouples (type K) were present in the system to control and monitor the temperature in two different positions (the controlling thermocouple is downstream under the second quartz wool layer and the monitoring thermocouple is upstream, close to the upper surface of the bed) and the temperature-protocols were set on the thermoregulator (Omron) with CX-Thermo software and a purpose-built MATLAB executable program. The temperature used to plot the H_2 or O_2 consumption profiles was the one measured upstream with the monitoring thermocouple, as it better approximate the real bed temperature and it is more sensitive to thermal effects caused by the heat of reaction as it is closer to the bed surface. The monitoring temperature reported in the plots was also corrected for the delay between the thermocouple and the gas-analysis measurements with the following correlation: $T = T_{meas} + \beta(\frac{V_t}{\dot{V}_{tot}})$ in which: T= temperature value corrected from the delay and used in the plots [°C], T_{meas} =

temperature measured by the thermocouple [°C], β = heating rate [°C/min], V_t = tubing volume [cm^3] and $\dot{V}_{tot}$= total volumetric flowrate [Ncm^3/min]. A pressure transmitter (MPX coupled with a PicoLog data logger) with a range of 0-500 mbar was also added before the reactor inlet to continuously measure the pressure drop along the reactor, as an indication of macro-agglomeration phenomena during the reaction. Before the analysis section, a silica-gel or zeolite traps (volume < 1 cm^3) were added to remove the water produced during the reducing cycles. The measurement of H_2 and O_2 consumption was performed with a thermal conductivity detector (TCD) and O_2 chemical sensor (Alphasense O2-C2) respectively. The TCD (from Agilent 6890 HP) was optimized to have a high analysis frequency (1 Hz) as the reactor outlet was directly conveyed into the detector without any previous separation with packed columns. Using this strategy, a fast and sensitive identification of transient effects during the reaction was possible and the same measurement frequency was obtained in the oxidation stage with an oxygen sensor. The same experimental protocol was kept for all the tests; it was 1) an inert pre-treatment to desorb water and/or contaminants at 200°C for 30 min with Ar, 2) isothermal oxidative pre-treatment at 250°C achieved at 5°C/min, 5%O_2/Ar with 50 Ncm^3/min), 3) H_2 reduction followed by 4) O_2 oxidation with ramping temperature at fixed heating rate. The selection of an inert bed dilutant was based on its thermal conductivity to investigate the thermal effects associated to both reactions and thus silicon carbide (SiC) was chosen. Details of the test conditions, experimental parameter values and thermal properties [7,18,19] are reported in Table 2.

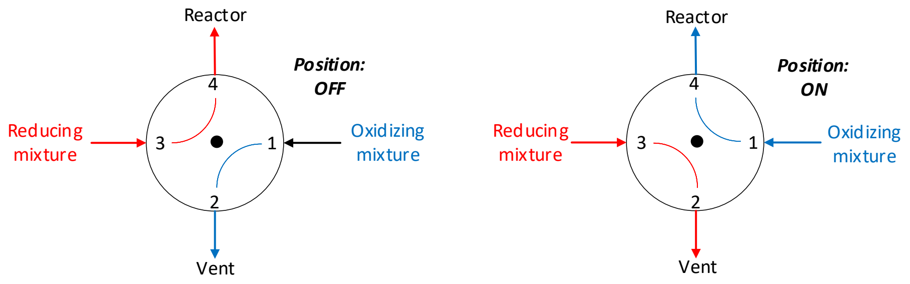

Figure 1: *Scheme of the automatic four-way valve.*

Table 1: *List of experimental parameters, values and combinations utilized in parametric sensitivity analyses for reduction and oxidation reaction.*

Parameter	Symbol	UoM	Values	SiC dilution
Sample mass	m_s	mg	10, 50	No
Particle size width	d_p	μm	<45, 100-150, 200-250	No
Total volumetric flowrate	$\dot{V}_{tot}$	Ncm^3/min	25, 50, 100	No
H_2 or O_2 volumetric percentage	y_{H_2} y_{O_2}	%	1, 5, 10	No
Heating rate	β	°C/min	1, 2.5, 5, 10	No
H_2 or O_2 volumetric percentage	y_{H_2} y_{O_2}	%	1, 5, 10	Yes
Heating rate	β	°C/min	2.5, 5, 10	Yes

Table 2: *Thermal properties of CuO, Cu_2O, Cu and SiC (cp=specific heat capacity, λ=thermal conductivity, T_m=melting temperature).*

Material	cp [J/Kg/K]	λ [W/m/K]	T_m [°C]
CuO	705	6	1326
Cu_2O	489	4.5	1235
Cu	460	350	1085
SiC	675	490	2730

Results and Discussion

Parametric sensitivity - Reduction

The influence of the experimental conditions (single and combined) on CuO reduction and oxidation performance was evaluated by varying the process parameters reported in Figure 1. The relationship between the CuO reactivity and mass and heat transfer phenomena in temperature-transient conditions will be discussed for each variable, through the profile of instantaneous H_2 consumption, as function of temperature. Also, a number of key parameters will be discussed in distinct table; these include the activation temperature T_{act} (temperature at which the H_2 molar flowrate consumed starts to increase), the maximum reduction temperature T_{peak} (temperature of the peak), the shoulder temperature (if present) T_s (temperature at which the H_2 molar flowrate consumed has a slope variation), the range of the reduction peak T_{range}

(temperature range from the activation to the end of the H_2 consumption), the total H_2 moles consumed is equal to the oxygen from CuO consumed $n_{H2,CuO}^{cons} = n_{O,CuO}^{cons}$ and it was calculated through the peak integration. The percentage of O from CuO consumed with respect to the initial amount ($n_{O,CuO}^{initial}$) and assuming the complete reduction to Cu $\%_{O,CuO}^{cons} = \left(\frac{n_{O,CuO}^{initial}}{n_{O,CuO}^{cons}}\right) \cdot 100$.

The distinct nature of these parameters enables a more detailed point of view on the CuO physical and chemical effects during reduction: temperatures and peak shape will give information on the punctual/specific response and the overall efficiency or reducibility degree will be provided by the total H_2 moles and lattice O consumed.

Based on the values used in standard TPR analyses on commercial instruments [20], the reference case was chosen using 50 mg CuO sample with an average particle size < 45 μm reduced with 50 Ncm^3/min of total flowrate, with 5% H_2/He and heated up at a rate of 2.5°C/min The results related to this experiment will be always shown in the plots with an orange curve. A high-thermal conductivity (λ) material (SiC) was mixed with CuO with 1:1 weight ratio to test the influence of increased heat propagation on H_2 reduction activity and correlate the temperature distribution along the bed to H_2 consumption profiles. Furthermore, the addition of a solid diluent prevents or reduce the extent of any particle agglomeration phenomena leading to diffusion limitations and thus to lower reactivity. Primary bed diluent properties are reported in Table 2, observing that the particle size range is consistent with the CuO granulometry to avoid an impact on bed porosity that may modify the gas distribution in the bed, affecting the resulting reaction profile. The addition of SiC was implemented in two sets of parameters, i.e. H_2 and O_2 concentration and heating rate variation. Plots will report the H_2 molar flowrate consumed ($n_{H_2}^{dot,cons}$) as a function of the monitoring temperature; the reduction peak is associated to a higher H_2 consumption.

Sample mass (m_s)

The influence of an increased CuO sample mass (compared to the reference case) on the reduction profile is shown in Figure 2, while key temperatures and quantification results are reported in Table 3.

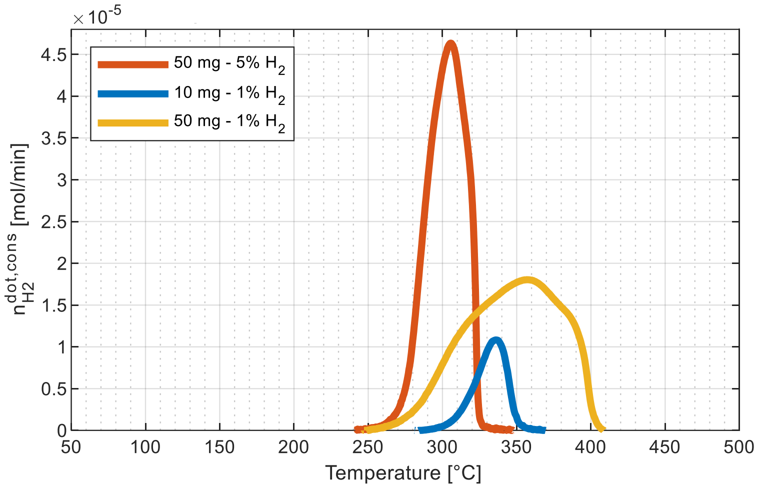

***Figure 2**: Reduction profiles for CuO at different H_2 inlet concentration (d_p< 45 µm, $\dot{V}_{tot}$=50 Ncm^3/min, y_{H_2}= 1% or 5%, β = 2.5°C/min).*

***Table 3:** Relevant calculated parameters for the sample mass variation experiments.*

m_s [mg]	y_{H2} [%]	K [s]	T_{act} [°C]	T_{peak} [°C]	T_s [°C]	Peak width [°C]	$\%^{cons}_{O,CuO}$ [%]
10	1	359	291	337	-	52	90.6
50	1	1832	251	358	315, 385	163	96.7
50	5	366	248	305	320	79	92.8

From Figure 2 it is immediately apparent that both the sample amount and the concentration of reducing gas can affect the position of the peak, and also its shape. That questions the use of tabulated reduction temperatures to identify specific oxidation states. Apparently, either a small sample or a larger H_2 concentration (i.e. a small *K* value) are required to shape a fairly symmetric, sufficiently sharp peak. Unfortunately, they differ by approx. 30°C.

Less obvious features of the reported profiles, suggest finer details. Comparing the reduction profiles of high (50 mg) and low (10 mg) CuO mass before the reduction peak, a similarity between the slopes is apparent. The parallel increase in H_2 consumption as the temperature increases suggesting that the O lattice consumption for 50 mg (corresponding to $6.35 \cdot 10^{-4}$ mol CuO moles) is confined to the superficial layer of the entire CuO bed. The mass for this limited layer can be approximated to 10 mg ($1.24 \cdot 10^{-4}$ mol), demonstrated by the consumption slopes and the physical appearance in the reactor tube: the low sample mass loaded in a 6 mm internal diameter tube barely covers the supporting quartz wool bed, forming a CuO monolayer of particles, completely exposed to the gas. Also for 10 mg, the total amount of reducible oxide is

5 times lower than the 50 mg sample; given that the CuO particle are sieved in the same size range, the 50mg case provides 5 times the surface of the 10mg one. Since the H_2 consumption is proportional to the particle surface, we expect a 1/5 ratio for each temperature scanned. At the same time, the increase of CuO mass implies a thicker bed, where external mass-transfer limitations may play a role; accordingly, the maximum H_2 consumption requires higher temperature to counteract diffusion limitations. The causes of H_2 external mass transfer limitations could lie on three different and interacting reasons: low H_2 initial concentration (1%) thus lower the driving force, bed agglomeration during reduction and the reduction mechanism itself. The consumption of O_{CuO} with H_2 is not a uniform process at the interface between Cu and CuO aggregates and when CuO conversion is > 50%, the Cu formed covers the non-converted CuO increasing diffusion resistances [21]. Differently, internal mass-transfer limitations could be neglected as the degree of reduction ($\%_{O,CuO}^{cons}$) shows that the CuO conversion to Cu is almost complete in all the cases, given the low particle size of CuO particles (< 45 μm).

Additionally, macroscopic bed agglomeration was observed (see Figure 10 and Figure 11) always present when reducing with H_2 and this effect is also suggested by the broader peaks (52°C for 10 mg sample and 263°C for 50 mg); agglomeration will be extensively explained in section "*Pressure drop and thermal effects"* later in Chapter 3. The maximum reduction temperature shift between the 50 mg and 10 mg case is around 20°C and it is another evidence of the increased mass-transfer limitations as the reaction is progressing. The shift of the activation temperature by 50°C is a counterintuitive result, as the chemistry of the process is the same for both cases. However, a possible explanation for this phenomenon could be found in the exothermicity nature of the reaction: as the superficial CuO layers are reduced, a local temperature increment, at the particle surface is produced but not detected by the monitoring thermocouple placed at the proximity of the bed, particularly when the heat generated is lower, as in the case of 10 mg (it is an extensive propriety). This hypothesis is also proven by the results of the combined experiments in Figure 2, in which both the initial CuO mass and H_2 concentration were varied. The 50 mg sample treated with 1% and 5% H_2 activate at the same temperature, i.e. 40-43°C lower than the 10 mg sample, meaning that the heat of reaction produced with the small sample is not enough to heat the surrounding particles, and reach the required activation energy in the whole volume; thus a shift in T_{act} is observed.

A peculiar feature in the 50 mg reduction curves for H_2 initial concentrations, is the appearance of shoulders, at T_S (Table 3). This variation in the profiles could be assigned to a physical and/or chemical phenomena: release of embedded hydrogen and activation of different reaction mechanism, involving other copper oxides (Cu_2O, Cu_3O_4). The former occurrence is typical for face-cubic crystal structure, such as Cu, with structural defects (dislocations and micro-voids) acting as hydrogen trap sites [21,22], thus a small amount of the initial H_2 fed could be consumed by this physical process, rather than the reduction itself. The presence of different reduction pathways was observed with specific combinations of reaction conditions and oxide structures [21]. Specifically, CuO converts directly into Cu (Reaction 2) without undergoing into intermediates/suboxides formation under standard H_2 initial concentration (5%) as the system attains metastable states reacting with H_2 rather than generating Cu_2O (Reaction 1) because of higher activation energy for CuO reduction to Cu_2O (114.6 kJ/mol) compared to Cu formation (60.7 kJ/mol) [21,23]. The conversion to Cu_2O is visible by decreasing the H_2 flow (decreasing H_2 initial concentration and/or increasing the contact time between gas and solid phase) or at high heating rates (>20°C/min). The formation of other copper oxides (e.g. Cu_3O_4) is discarded as a considerable distortion of cell parameters would be required.

$$2CuO + H_2 \rightarrow Cu_2O + H_2O \qquad \text{Reaction 1}$$

$$CuO + H_2 \rightarrow Cu + H_2O \qquad \text{Reaction 2}$$

The hypotheses of trapped H_2 and formation of other oxides can explain the slight decrease in H_2 consumption at higher temperatures (385°C), low H_2 concentration (1%) and higher CuO initial mass.

Particle size (d_p)

The particle size influence on reduction profiles is reported in Figure 3 and Table 4. Three ranges were investigated (dp_{low}=< 45 µm, dp_{med}=100-150 µm and dp_{high}=200-250 µm) to have a wide representation of usual powder size ranges.

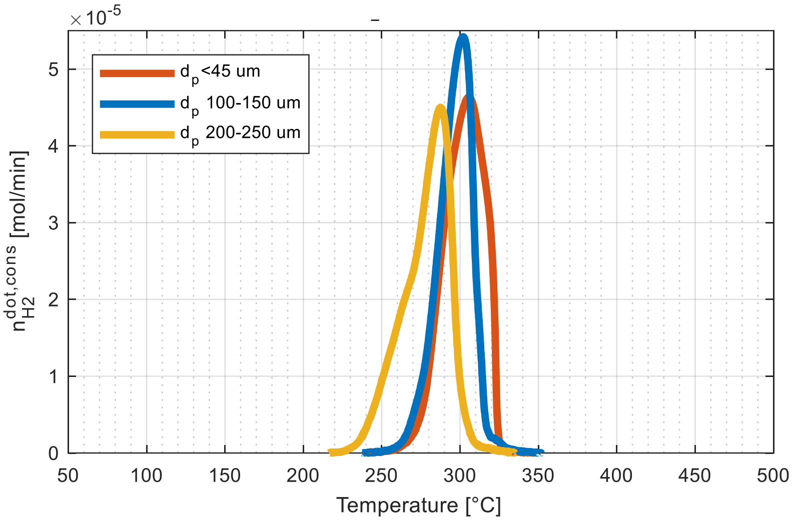

***Figure 3**: Reduction profiles for CuO at different particle size ($\dot{V}_{tot}$=50 Ncm³/min, y_{H_2}= 5%, β = 2.5°C/min).*

***Table 4:** Relevant calculated parameters for the particle size variation experiments.*

d_p [µm]	K [s]	T_{act} [°C]	T_s [°C]	T_{peak} [°C]	Peak width [°C]	$\%^{cons}_{O,CuO}$ [%]
<45	366	241	318	305	79	92.8
100-150	371	240	274	302	85	86.1
200-250	375	229	270	288	96	88.4

Surprisingly, larger particles are reduced first, but to a lower extent, as expected. Larger particles (dp_{high}) increase the local CuO reduction rate by decreasing the activation and peak temperature, while increasing the peak width by 11°C and 17°C compared to dp_{med} and dp_{low} respectively. This effect is associated with a lower surface area [10] and it is consistent with the results obtained, as the surface area decreases by increasing the particle size with the same porosity, assuming low porosity [24]. Also, the temperature shift at higher temperature for smaller particles suggests a H_2 diffusion limitation through the bed and inside the particle as an effect of the higher packing caused. The presence of shoulders at high temperatures indicates morphological restructuration (agglomeration and/or formation of surface defects) supporting different reduction mechanisms as reported in *Sample mass (m_s)*. To prevent interparticle mass transfer limitations, a particle size distribution as narrow as possible is recommended.

Total volumetric flowrate ($\dot{V}_{tot}$)

The changes in CuO reactivity were correlated to the fluidynamic of the system by varying the total volumetric flowrate from the reference (50 Ncm^3/min) to half (25 Ncm^3/min) and double value (100 Ncm^3/min). The results are reported in Figure 4 and Table 5.

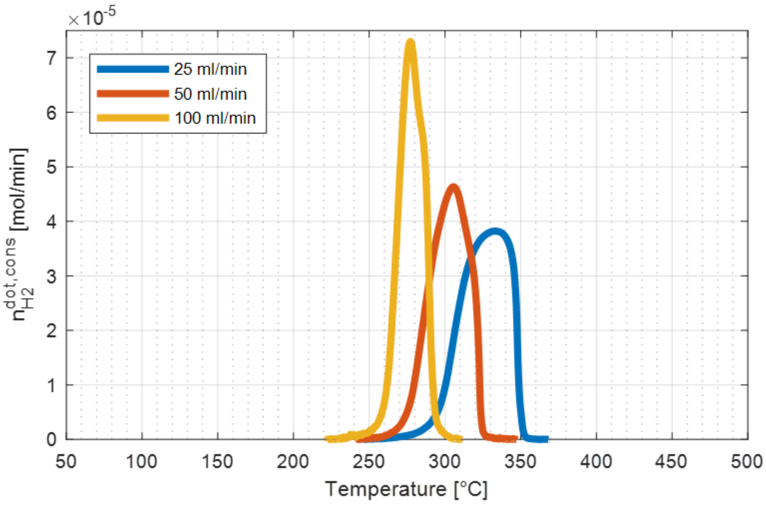

***Figure 4**: Reduction profiles for CuO at different total volumetric flowrates (m_s = 50 mg, d_p < 45 µm y_{H_2} = 5%, β = 2.5°C/min).*

***Table 5:** Relevant calculated parameters for the total volumetric flowrate variation experiments.*

$\dot{V}_{tot}$ [Ncm^3/min]	K [s]	T$_{act}$ [°C]	T$_s$ [°C]	T$_{peak}$ [°C]	Peak width [°C]	$\%^{cons}_{O,CuO}$ [%]
25	714	247	-	334	93	99.1
50	366	248	318	305	79	92.8
100	180	230	290	277	63	95.2

Applying a lower volumetric flowrate decreases the overall reduction performance (T_{peak}) as a combination of different phenomena such as internal and external mass-transfer limitations. At the beginning of the reaction, the intra-particle H_2 diffusion is inhibited by the reduced H_2 concentration gradient between the gas phase and CuO, i.e. the diffusion driving force is decreased, shifting the activation temperature towards higher values and slowing down the global reaction rate. As the reduction progresses, more surface defects and Cu nuclei are formed [21] starting to cover the non-converted CuO, making H_2 diffusion is even more limited by the lower Cu porosity and the overall effect is the reduction profile shifted at higher temperatures. In the case of lower volumetric flowrate, the inlet gas mixture has a reduced fluid velocity suggesting a possible external mass-transfer limitation as the mass-transfer coefficient $h_{m,H2}$ depends upon the properties of the gas and solid phase with the reported in Equation 1.

$$h_{m,H2} \propto \left(\frac{v_{rel}}{d_p}\right)^{1/2} D_{H2,mix}^{2/3} \nu_{mix}^{-1/6} \qquad \text{Equation 1}$$

where v_{rel} is the relative velocity of the fluid with respect to the particles, d_p is the particle diameter, $D_{H2,mix}$ is the H_2 diffusion coefficient in the binary mixture fed, and ν_{mix} its kinematic viscosity. As an effect of internal and external mass-transfer limitations, the temperature window for the complete CuO reduction is shifted at higher temperatures: the T_{act} difference between the lowest and highest flowrate is 7% and this value increases to 17% when comparing T_{peak}. The broadening of the peak is another evidence of the inferior reduction performance (i.e. reaction rate) when the H_2 molar amount fed to the system is decreased. These results demonstrates that mass-transfer limitations are mainly external, as the H_2 flux is controlled by the mass-transfer coefficient $h_{m,H2}$ but also from the concentration gradient between the gas phase and the surface. At the same H_2 concentration but at lower flowrate, the creation of H_2 low-concentration areas around the particle and their slow replenishment decreases the external mass-transfer. Increasing the flowrate, the average H_2 concentration around the surface is increasing as well as the mass-transfer driving force.

Initial hydrogen concentration (y_{H2})

The inlet H_2 concentration influence on CuO reduction was evaluated by selecting a H_2 concentration below (1%) and above (10%) the reference value (5%). Additionally, the effect of bed dilution with an inert material (SiC) was investigated in the whole H_2 concentration range. The profiles and quantification data with and without SiC dilution are reported in Figure 5 and Table 6.

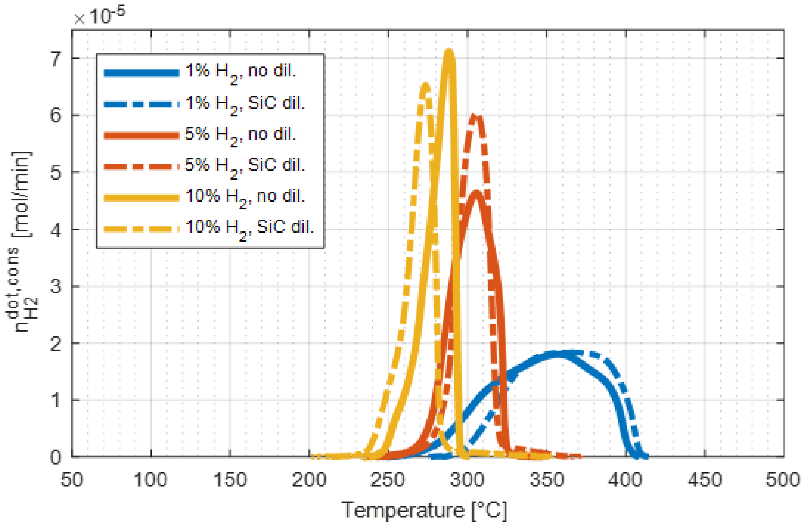

***Figure 5**: Reduction profiles for CuO at different a) H_2 inlet concentration with and without SiC dilution In both cases, m_s (only CuO) = 50 mg, d_p< 45 μm, $\dot{V}_{tot}$=50 Ncm^3/min, β = 2.5°C/min.*

***Table 6:** Relevant calculated parameters for the H_2 inlet concentration variation experiments.*

y_{H2}^{in} [%]	K [s]	T_{act} [°C]	T_s [°C]	T_{peak} [°C]	Peak width [°C]	SiC dilution	$\%_{O,CuO}^{cons}$ [%]
1	1831	251	315, 385	358	163	-	96.7
5	366	248	318	305	79	-	92.8
10	184	240	270	288	67	-	85.3
1	1908	270	-	369	131	Yes	89.3
5	368	245	320	306	76	Yes	91.1
10	184	230	260	273	63	Yes	94.5

Regardless the bed dilution, increasing the initial H_2 concentration enhances the reduction activity by markedly decreasing the overall reduction profiles in terms of T_{act}, T_{peak} and T_{range}. The maximum difference among relevant temperatures is even more evident for the diluted bed, as the high SiC thermal conductivity allows a uniform temperature distribution and thus a more homogeneous reaction progress throughout the bed. Indeed, 4.3%, 19.5% and 58.9% are the percentage variation between T_{act}, T_{peak} and T_{range} at the lowest (1%) and highest (10%) of the non-diluted samples while 14.8%, 26.0% and 51.9% are related to the difference between highest and lowest heating rate in the SiC diluted samples. Increasing the initial H_2 concentration improves the reagent mass-transfer rate from the gas phase to the surface, its concentration at the surface and thus the surface kinetics. At a microscopic scale two counteractive events occur, that involve the CuO reduction mechanism with H_2. According to the *nucleation model*, the CuO particles do not undergo a sequential and uniform reduction, but small Cu aggregates/clusters initially evolve on the CuO surface and the Cu nuclei overlap when Cu >50% shifting the reaction interface inwards [13,21]. Specifically, the key feature in the reduction mechanism is the removal of O lattice through the H_2 adsorption on the surface, the subsequent dissociation into H atoms and the reaction with surface oxygen generating a superficial vacancy [21] by the release of steam. However, if the H_2 available is significantly high, the H-atom diffusion in the unreacted bulk activates and hydroxy species are formed as intermediates that desorb as H_2O, simultaneously generating O vacancies [13]. The mechanism also involves an initial induction period in which surface defects, i.e. active sites for H_2 adsorption and dissociation, are formed and both higher temperature and high H_2 concentration increase the presence of defects and thus reduce the induction period [23]. The H atom embedding is negligible during this reaction step and thus the reduction profile appears flat at the beginning of the reaction, while it becomes crucial when increasing the reduction rate. The effect of higher H_2 concentration is visible for the induction period temperature, underlining an increased active sites formation extent. As the same heating protocol was applied for the experiments reported in Figure 5.a, the different duration and temperature range of the induction period could be ascribed to the different H_2 composition: 240°C, 260°C and 270°C are the temperatures from which the reaction rate becomes faster due to the migration of atomic H into CuO bulk and simultaneously H_2O formation by O removal from the lattice [8,21,23,25].

The SiC addition is not significatively affecting the induction period at high H_2 initial concentration (5, 10%) as its final temperature value is decreased by 10°C, but a strong delay in activation temperature and overall reduction profile is visible for the low H_2 concentration sample (1%). The reason for a 20°C delays in the induction temperature could be assigned to a decreased surface exposed to the reducing atmosphere as the SiC is partly covering the CuO surface, thus inhibiting the formation of H_2 dissociation sites until higher temperatures are reached. The bed dilution with an inert and high conductive material enhances both the thermal properties and structural features by delaying the agglomeration process, discussed in detail in the section.

Heating rate (β)

The application of different heating policies and their effect on CuO reduction profiles was investigated by varying the heating rate from 1°C/min to 10°C/min (Figure 6, Table 7). H_2 consumption was studied through the thermal characteristics of the reactive CuO/Cu reactive system and thus the bed dilutant with high thermal conductivity was added to compare the results with the non-diluted cases (Figure 6, Table 7).

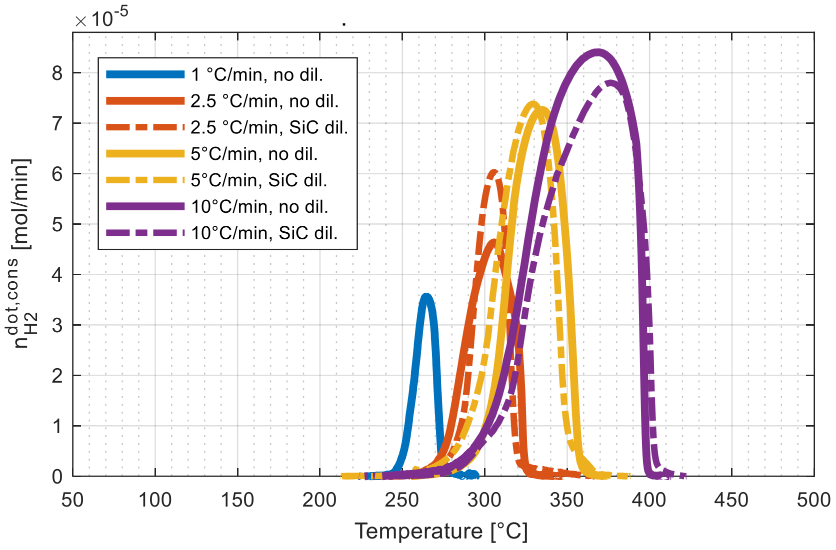

Figure 6: *Reduction profiles for CuO at different heating rate with and without SiC dilution (m_s = 50 mg, d_p< 45 µm, $\dot{V}_{tot}$=50 Ncm³/min, y_{H_2}= 5%)*

Table 7: *Relevant calculated parameters for the heating rate variation experiments.*

β [°C/min]	K [s]	P [K]	T_{act} [°C]	T_{peak} [°C]	Peak width [°C]	SiC dilution	$\%^{cons}_{O,CuO}$ [%]
1	367	6.1	230	264	58	-	87.1
2.5	366	15.2	241	305	79	-	92.8
5	367	30.6	240	334	126	-	88.8
10	363	60.5	256	368	144	-	91.2
2.5	368	15.3	240	306	76	Yes	91.1
5	367	30.6	239	330	122	Yes	95.0
10	358	59.7	244	377	165	Yes	85.8

Increasing the heating rate shifts the reduction profiles to higher temperatures, in terms of maximum reduction rate and activation temperature; in addition, peaks become broader. All these effects are independent from the bed dilution. Lower heating rates, such as 1°C/min, allow a thermal and chemical steady-state to be better approached; a high temperature scanning velocity (e.g. 10°C/min) do not allow a uniform temperature distribution to stabilize in the reactive bed. In other words, the characteristic time scale of heat transfer across the bed can become larger that the heating duration, so that differences in reduction profiles appear [26]. The non-uniform heat propagation for higher heating rates affects the distribution of initial surface defects and the surface composition and thus influences the overall reactivity [27,28] and shifts the reduction peaks to higher temperatures (from 264°C at 1°C/min to 368°C at 10°C/min) and increase the peak width (from 58°C at 1°C/min to 144°C at 10°C/min). The reduction benefits of the SiC addition to the CuO sample, up to a maximum heating rate of 5°C/min, as the high conductivity supports a more uniform reaction interface between H_2 and CuO, thus the maximum reduction temperature is shifted to lower values, sustained also by smaller agglomeration phenomena. At higher heating rates (β>5°C/min) the addition of a bed dilutant appears detrimental, as the overall performance decrease but a satisfactory degree of reduction is achieved with intermediate heating rates (2.5°C/min) with and without bed dilution. Thus, the heating rate could be increased up to 5°C/min and coupled with bed dilution to reach higher reduction efficiency and a narrow reduction peak.

CuO reduction with H_2 at constant characteristic number K and P

The selection of suitable experimental parameters is crucial to obtain reliable data on reduction processes, as their inappropriate combination could mislead the understanding of the reaction mechanism and the correct utilization in other applications, such as in characterization studies and catalytic performance investigations. Great efforts were made to identify a general parameter to easily select the combination of variables (initial H_2 concentration, total flowrate, sample mass, heating rate) within a fixed range to guarantee an accurate view of the chemistry and kinetic parameters involved in the process. *K* [6] and *P* [9] were retrieved through the comparison of simulated and experimental reduction profiles and simple relations such as the one for *K* and *P* are still widely used in temperature-programmed experiments to select the operating variables. The limiting values for *K* (15s – 140s) [6] were calculated from empirical criteria based on instrument sensitivity, differential reactor assumption and limited heating rate values (6 – 18°C/min). Also, the kinetic modelling neglect the occurrence of mass-transfer (inter- and intra-particle diffusion) limitations and heat balance, considering differences in local temperature caused by adsorption/desorption enthalpies and reaction exothermicity (-85.7

kJ/mol K). However, reduction processes with multiple peaks were not fully explained by the *K* number [7,27,29] and thus *P* characteristic number [9] was introduced to investigate the reduction processes following a first-order kinetic with respect to H_2 and simultaneously overcome *K* constraints, directly correlating the dependence on the heating rate. According to a similar kinetic analysis performed in the previous study, the appropriate range of applicability is $P < 20$ K to avoid curve distortion and loss of resolution in multistep reductions. The cause of such differences was mainly ascribed to the reduction process itself through the sample mass and the transient nature of the study, while mass- and heat-transfer limitations is believed to have a minor role in changing the reduction profile shape [30]. The validation of *P* design criteria was performed through the comparison of the activation energies calculated at different *P* values, obtaining low relative error for constant *P* lower than 20 K [9]. The validity of the assumptions and reliability of *P* characteristic number as a tool to select the experimental parameters in temperature-programmed reductions was investigated by choosing a *P* value in the optimal range (15.3 K) and generating different combinations of sample mass, total volumetric flowrate, H_2 initial concentration and oxidative pre-treatment at fixed heating rate (2.5°C/min) to obtain the desired *P* value (Table 8). The corresponding *K* value is 367.5 s. Reduction profiles for 5 sets of experiments are reported in Figure 7.

Table 8: *Experimental parameters used in constant K = 367.5 s and P =15.3 K experiments; fixed heating rate (2.5°C/min).*

Set	**m_s [mg]**	**$\dot{V}_{tot}$ [Ncm3/min]**	**y_R [%]**	**Bed dilution**	**Ox. Pre-treatment**	**$\%_{O,CuO}^{cons}$ [%]**
1	51	50	5	-	✓	96.0
2	203	100	10	-	✓	87.2
3	203	100	10	-	-	81.9
4	9.9	50	1	-	✓	90.6
5	201	100	10	✓	✓	89.9

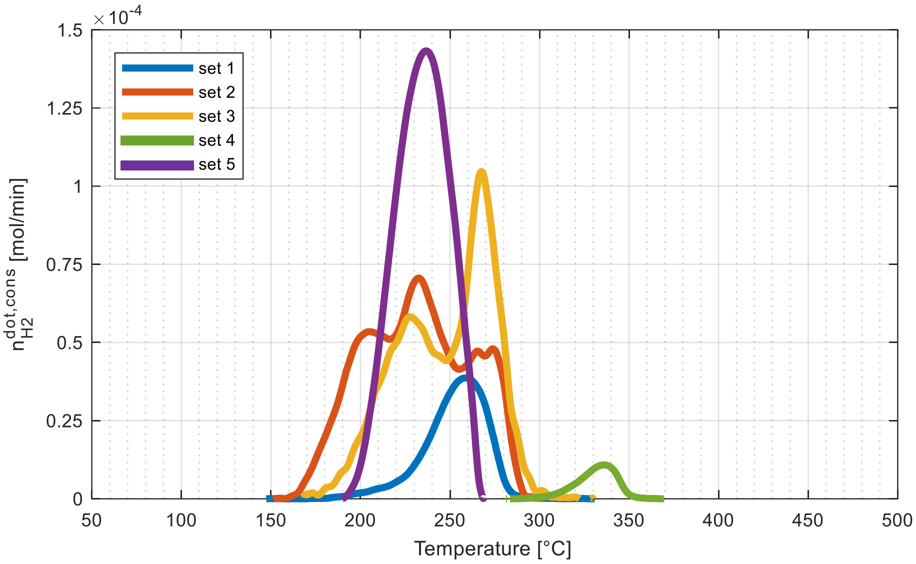

***Figure** 7: Reduction profiles for CuO at constant K= 367.5 s and P=15.3 K.*

CuO reduction with H_2 is a one-step reaction ($Cu^{2+} \rightarrow Cu^0$) in standard conditions of H_2 supply (no H_2 starvation) and/or heating rate (< 20°C/min) [21] and Cu_2O could be formed as an intermediate product if the reaction conditions are varied from the standard ones. The series of experiments at constant *P* were performed in standard conditions to achieve a constant *P* value in the optimal range. The expected CuO reduction profile is formed by one single reaction peak characteristic for the CuO conversion to Cu and the appearance of secondary peaks is associated to physical/chemical phenomena. Low sample masses (set 1 and 4) and high sample masses diluted with SiC (set 5) yield to a single H_2 consumption peak, while the use of higher masses, without any solid dilutant generates multiple reduction peaks [7,27,29]. Even if this output could be correlated to different Cu oxidation states, data show that this inhomogeneous reduction is caused by interacting effects of temperature and H_2 gradients and consequent with physical agglomeration of the bed, as it will be shown in section *Pressure drop and thermal effects*; higher amount of reducible species enhances H_2 diffusion and heat transfer limitations, and thus generating an uneven temperature distribution caused by the reaction exothermicity, if the heat of reaction is not uniformed with a highly conductive material. Other explicative phenomena of multiple reduction peaks are also emphasized at higher CuO masses, such as embedded H_2 in CuO lattice as discussed in section *Sample mass (*m_S*).*

Furthermore, decreasing the H_2 initial concentration along with the sample mass shifts the reduction profiles to higher temperatures as H_2 convective transport from the bulk of the gas to the surface is the limiting step caused by a lower concentration gradient. Mass- and heat-transfer phenomena neglected for *K* and *P* characteristic numbers have a large contribution in the development of reduction profiles for specific combination of parameters. Summarizing, results suggest using higher sample masses (≥ 50 mg), a larger H_2 concentration (≥10%), a total volumetric flowrate (≥50 Ncm^3/min) and a solid dilutant for the oxide bed are required to produce one single peak and thus obtain more reliable results of the chemical process under investigation. Being *K* characteristic number equal, this result demonstrates that increasing the values of the experimental parameters included its definition (amount of reducible species, H_2 concentration and total volumetric flowrate) and the addition of a bed dilutant has an advantageous effect on the reduction profiles.

Summary of parametric sensitivity on CuO reduction

The reduction degree (the ratio between the total H_2 consumed during the reduction and the initial amount of reducible oxide, $\%_{O,CuO}^{cons}$), was found poorly sensitive to detailed reaction features (reduction mechanism and physical or chemical phenomena), compared to the analysis of H_2 consumption profiles in relation to temperature; the reduction degree provides a general overview of the reaction performance. The parameter was calculated for each condition and reported in the corresponding tables (from Table 3 to Table 8) from which some conclusions and practical indications could be extracted. The most critical experimental parameter is the sample mass as it influences the H_2 and temperature distribution during the reduction, thus the choice of the other parameters (H_2 initial concentration, particle size, total volumetric flowrate and heating rate) is strongly connected to its value. An approximate distinction could be pointed out between low (< 50 mg, in our reactor, having 6mm ID) and high (≥ 50 mg) sample masses, from which it is clear that increasing the initial H_2 concentration is detrimental in the first case as a faster agglomeration of the entire bed occurs (as it will be reported in section *Pressure drop and thermal effects*) and inner unreacted CuO particles are not efficiently converted into Cu. Decreasing the H_2 concentration reduces H_2 mass transfer rate, affecting the reduction kinetic, increasing the time required to complete the reaction (i.e. convert > 95% CuO) and shifting the peak temperature to higher values. To avoid this confusing effect, higher H_2 initial concentration could be used, but it must be coupled with the addition of a highly conductive inert material, such as silicon carbide. The selection of the total volumetric flowrate mainly depends on the influence of internal and external mass-transfer limitations, along with the delay between the reactive area and the measurement system. In the case of higher sample masses,

H_2 concentration should be increased to overcome diffusion limitations generated by the low concentration gradient between the gas and solid phase along with a higher penetration depth. The influence of the particle size interval is not crucial in terms of total reduction efficiency as the oxygen consumed from the CuO lattice is comparable for three different intervals as reported in *Particle size (dp)*, however a narrow diameter (or equivalent diameter) interval should be as narrow as possible to reduce additional pressure drop caused by variations in the bed porosity during the H_2 reduction. Finally, the heating rate value should be set up with a value < 5°C/min to avoid non-uniform temperature distribution caused by the reactor heating and increase temperature gradients inside the bed and it can be achieved by decreasing the heating rate.

Parametric sensitivity - Oxidation

The impact of the experimental variables listed in the *Materials and Methods* was evaluated also for the oxidation reaction (Table 1). Specifically, the same conditions used in the reduction experiments were reproduced also in the following oxidation stage; when the reductions were carried out at 1, 5, or 10% H_2 concentration, then re-oxidations adopted the same 1, 5, or 10% O_2 inlet concentration, respectively. The same key parameters T_{act}, $T_{peak,1}$ and $\%_{O,CuO}^{reg}$ (percentage of oxygen regained after the reoxidation, calculated on the Cu obtained after the reduction) are used to discuss the results, with an additional indication for the final temperature at which the oxygen is consumed (T_{fin}), assuming the total Cu oxidation to CuO [31]. This additional parameter was added in the Cu reoxidation analyses as the oxygen consumption continues also in the isothermal and cooling stage and T_{fin} represents the temperature during the cooling ramp at which the oxygen consumption reaches the zero. The reference case is still reported as the orange curve, obtained with 50 mg of initial CuO pre-reduction. The amount of Cu after the reduction will be less than the initial CuO mass as the oxygen was consumed, but the same value was reported for an easier comparison between reduction and reoxidation cycle. Other characteristics (particle size < 45μm before reduction, 50 Ncm^3/min of total volumetric flowrate, 5% O_2 inlet concentration, and 2.5 °C/min as heating rate) were kept constant. Data have been obtained by constant heating and cooling, up to 500°C and cooling to T_{fin} is also reported.

Sample mass

Total volumetric flowrate

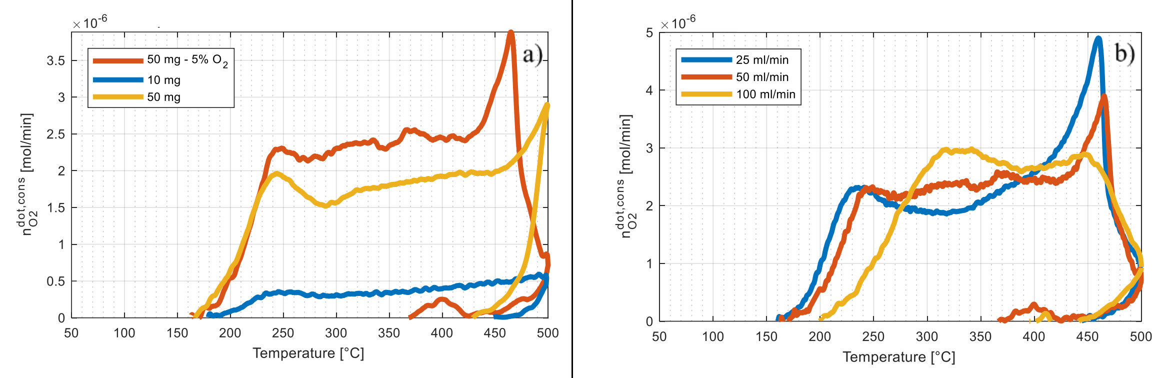

m_s [mg]	y_{O2} [%]	T_{act} [°C]	$T_{peak,1}$ [°C]	$T_{peak,2}$ [°C]	T_{fin} [°C]	$\%^{reg}_{O,CuO}$ [%]
10	1	169	244	500	452	84.4
50	1	167	244	500	430	75.6
50	5	163	244	465	371	86.1

$\dot{V}_{tot}$ [Ncm^3/min]	T_{act} [°C]	$T_{peak,1}$ [°C]	$T_{peak,2}$ [°C]	T_{fin} [°C]	$\%^{reg}_{O,CuO}$ [%]
25	161	235	461	404	92.5
50	163	244	465	371	86.1
100	201	327	448	448	81.8

O_2 concentration

Heating rate

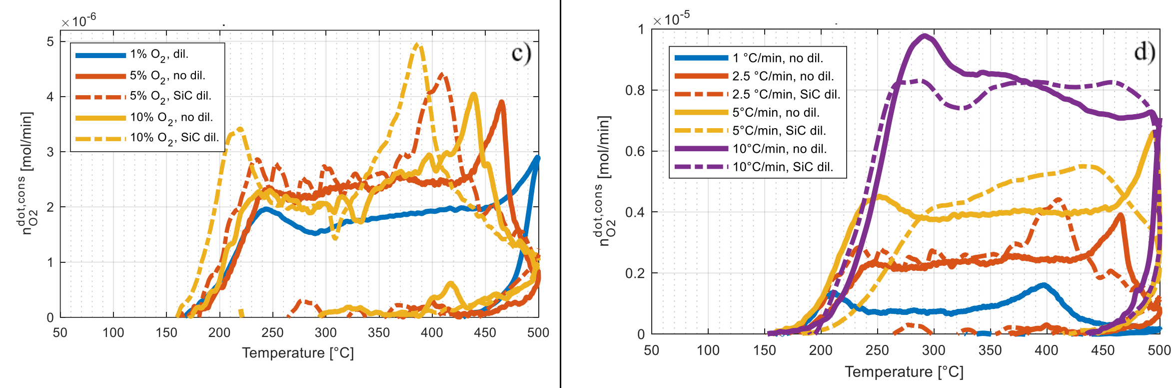

y^{in}_{O2} [%]	T_{act} [°C]	$T_{peak,1}$ [°C]	$T_{peak,2}$ [°C]	T_{fin} [°C]	SiC dilution	$\%^{reg}_{O,CuO}$ [%]
1	167	235	500	431	-	75.6
5	168	244	465	371	-	86.1
10	175	245	439	303	-	86.9
5	180	236	411	264	Yes	98.1
10	155	215	388	369	Yes	99.5

β [°C/min]	T_{act} [°C]	$T_{peak,1}$ [°C]	$T_{peak,2}$ [°C]	T_{fin} [°C]	$\%^{reg}_{O,CuO}$ [%]
1	161	211	399	443	77.9
2.5	168	244	465	371	86.1
5	152	251	496	449	83.6
10	156	292	494	439	83.8
2.5	180	236	411	264	98.1
5	187	300	435	415	76.4
10	196	276	458	437	78.6

Figure 8 *and* ***Table 9****: Reoxidation profiles and relevant calculated parameters for CuO at different a) initial sample mass, b) total volumetric flowrate c) O_2 inlet concentration (with and without SiC dilution) d) heating rate (with and without SiC dilution). Always* m_s *= 50 mg,* d_p *< 45 µm,* $\dot{V}_{tot}$ *=50 Ncm*^{3}*/min,* y_{O_2} *= 5%,* β *= 2.5°C/min where not differently specified in the legend.*

Oxidation profiles will be presented as the consumed O_2 molar flowrate ($\dot{n}_{O_2}^{cons}$, which is the difference between the inlet and the outlet molar flow rate) as a function of the monitoring temperature, in Figure 8.a to Figure 8.d. As a general comment, we can observe that oxidation apparently occurs over a wide range of temperature, without sharp peaks as in the reduction phase. That is likely an artifact, due to the slow rection progress compared to the relatively fast heating rate, as clarified below. Almost always two peaks of activity are reported, suggesting a 2-steps mechanism, following the reactions (Reaction 3 and Reaction 4)

$$2Cu + 1/2O_2 \rightarrow Cu_2O \qquad \text{Reaction 3}$$

$$Cu_2O + 1/2O_2 \rightarrow 2CuO \qquad \text{Reaction 4}$$

Differently from the reduction process, Cu oxidation shows a sequential reaction pathway in which Cu_2O is the intermediate oxide obtained before the total oxidation to CuO. The explanation of such difference could be found in the modification of the lattice cell geometry, i.e. an expansion of the Cu lattice to incorporate O atoms and form Cu_2O while an expansion and modification of cell geometry is necessary for the direct CuO formation from Cu [21,23,32] and the lower activation energy for the second reaction [21,23,33]. Furthermore, the copper phase reoxidizes completely at 400°C [34].

Further, the heating and cooling policy results in part of the oxidation taking place during cooling. The very slow oxidation suggests a strong internal diffusion resistance, and ultimately lead to an incomplete oxidation of the solid. This prolongation of reaction time is attributed to the reduced surface area and porosity that prevent O_2 diffusion and the occurrence of simultaneous oxidation of different Cu phases (dispersed, segregated and H_2 trapped in the lattice) [45] is limited.

Figure 8.a shows that oxidizing higher sample masses with low O_2 inlet concentration (1%) reduces the overall oxidation degree (-8.8%) with respect to the same sample oxidized at the reference conditions (5% O_2). This result supports the speculation formulated in the CuO reduction study, that agglomeration takes place in the reduction, modifying the bed morphology and increasing the O_2 diffusive resistances. As a matter of fact, higher oxidation degrees (+10.5%) are obtained with more concentrated O_2 mixtures (5%) at the same CuO initial mass (50 mg, before reduction). The variation of the sample mass does not influence the first oxidation peak temperature (167°C ± 4°C) and the same behavior is recurrent also for the different total volumetric flowrate (Figure 8.b) at 25 Ncm^3/min and 50 Ncm^3/min. The

observation that oxidation begins always the same temperature confirm that the further progress is controlled by internal diffusion, while the surface oxidation always begins easily. A deviation on the onset of oxidation was observed at a higher total volumetric flowrate (100 Ncm^3/min). In this condition, the reaction apparently starts at higher temperatures (+ 90°C) and the peak resolution is not pronounced, decreasing the oxygen consumption between the two oxidation peaks; such a higher flow rate is likely to affect the temperature distribution in the bed, resulting in a local temperature a few tens of degree less that the measure one (used in the plots). Differently from the reduction stage, smaller volumetric flowrates increase the oxidation efficiency; likely, the different initial morphology (powder for reduction and agglomerated bed for oxidation) influences the consumption of the corresponding reactive gas by means of less effective mass- and heat-transfer rates. The structural bed conformation also impacts the activation temperature at various O_2 inlet concentration, without bed dilution (Figure 8.c) resulting in similar values for all the cases (171°C± 4°C for 1%, 5%, 10%), disregarding the reactant concentration. Moreover, the first oxidation peak temperatures are similar for all the non-diluted cases (240°C± 5°C). A larger reactant concentration does not affect the rate of the first oxidation step (first peak), the second oxidation peak that appears at lower temperature at increasing O_2 concentration. Once again, this could be an artifact, of a slow reaction (particularly the second step) compared to the heating rate; increasing the reaction rate of the second oxidation step (by larger O_2 concentration), this step is observed earlier, and reported at a lower temperature. Consistently, the oxidation degrees achieved a higher O_2 concentration markedly improve, by 11%. The addition of bed dilution further enhances the oxidation performance in terms of peak temperatures ($T_{peak,1}$ is 30°C lower with 10% O_2, and $T_{peak,2}$ is 54°C lower with 5% O_2 and 51°C with 10% O_2) and oxidation degrees, approximating total oxidation, with a dramatic increase (+12% on average) compared to the absence of a dilutant. As reported for the reduction process, the addition of a bed dilutant both delays bed agglomeration phenomena and promotes a more uniform oxidation by flatten temperature gradients. The analysis of the oxidation profiles obtained at different heating rates (Figure 8.d) suggests that lower values ($\beta \leq 5$°C/min) produce two distinct and resolved peaks and their position ($T_{peak,2}$) shifts towards lower values (around -100°C from 5°C/min to 1°C/min). A higher heating rate (10°C/min) prevents the formation of a fully resolved second oxidation peak in the temperature range analyzed and the cause could be attributed to a slow reaction, that lags behind the temperature constantly increasing, producing the artifact of a O_2 uptake to be reported at a higher temperature than effectively required. Also, a non-uniform heat and temperature distribution as reported can explain the shift of peaks at a lower temperature with smaller heating rates, as discussed in the section *Heating rate (β)*. The presence of a bed dilutant strongly deforms the shape of the oxidation profiles in which the distinction between $T_{peak,1}$ and $T_{peak,2}$ is confused for $\beta \geq 5$°C/min, implying that the Cu oxidation to Cu_2O (Reaction 3) and its further conversion into CuO (Reaction 4) are overlapping to some extents.

Pressure drop and thermal effects

The evidence collected in TPR and TPO tests at different conditions, suggest that dramatic modifications of the bed and particle texture takes place, tentatively mentioned above as 'agglomeration'. Here we investigate possible changes in morphology by pressure drop measurements. They are expected to follow, directly and reversibly, the temperature, because of its role on density, mainly. So, pressure drop must increase and decrease with rising and falling temperature, in a morphologically stable bed of solid particles.

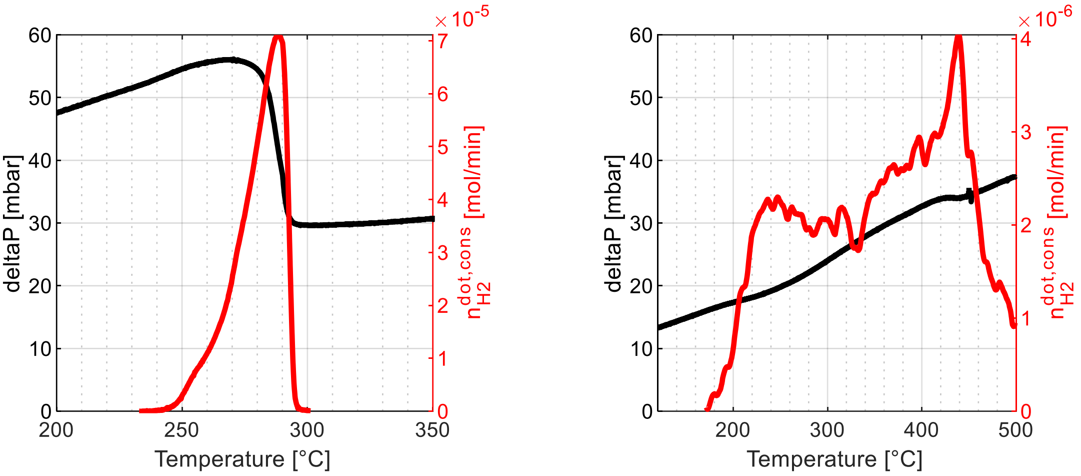

a) b)

Figure 9*: a) Reduction and pressure drop profiles, y_{H_2} = 10%, b) Reoxidation and pressure drop profiles y_{O_2} = 10%. Common conditions: (m_s = 50 mg, d_p < 45 µm, $\dot{V}_{tot}$=50 Ncm^3/min, β = 2.5°C/min).*

Overlapping H_2/O_2 consumption curves to pressure drop measurements, Figure 9 we find quite unexpected results. Figure 9.a shows the pressure drop curve increasing due to the increasing temperature, as expected; suddenly, the hydraulic resistance of the bed falls approaching 270°C, where the reduction has a vigorous acceleration. That suggests the agglomeration of the bed, leaving free channels for the gas to flow through, likely at the inner reactor wall. Such an onset temperature of CuO agglomeration is largely lower than the Tammann temperature for CuO/Cu redox pairs (526 °C, reported as the activation temperature for bulk material sintering and empirically calculated with $0.5T_m$) [35] as extra heat is provided by the exothermic reaction occurring on the surface [48] . Negligible pressure drop variations are observed during the oxidation (Figure 9.b), just the linear dependence on temperature expected. However, the hydraulic resistance is much lower than in the early steps of reduction, even though the total flow rate and its prevailing component (Ar) is the same. That implies that 1) the bed in TPOs is the agglomerated one left by reduction, and 2) the structural conformation generated by the reduction step is stable and no further modifications occur. Two small pressure drop fluctuations are discernible at the same position of the oxidation peaks (240°C, 420°C) but the temperature effect is larger and misleading.

Such hypothesis about bed agglomeration and shrinkage have been confirmed by the observation of the sample after a TPR+TPO sequence, Figure 10. The final bed morphology was dissimilar to the initial configuration, and peripherical by-passes clearly formed. Figure 10.a.

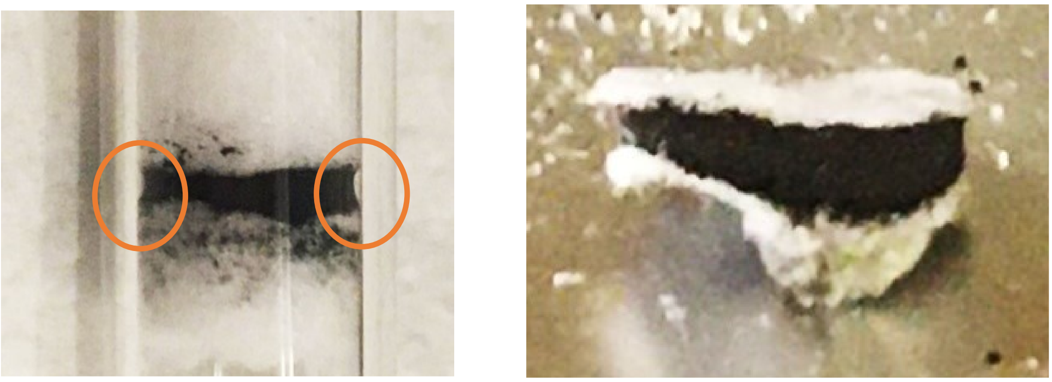

a) b)

Figure 10*: Spent CuO sample after one reduction and oxidation cycles with focus on a) the lateral bed shrinkage and b) the agglomerated, self-sustaining structure.*

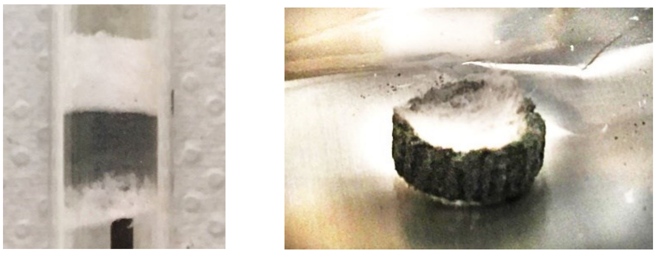

a) b)

Figure 11*:* (a*) Fresh 50 mg CuO sample diluted with SiC (1:1 w/w) before pre-treatment,* (b) *Spent CuO sample after one reduction and oxidation cycles.*

Agglomeration phenomena identified by a decrease in pressure drop measurements cause an opposing effect: clustering via agglomeration or sintering causes an irreversible merging of particles with reduced porosity and the accessibility to active sites decreases the overall sample performance [37]. Therefore, the initial configuration of the material (powder) undergoes to microstructural modifications caused by CuO reduction to Cu and a final bulky form of a solid non-porous pellet is obtained, Figure 10.b, that should increase the pressure drop along the bed. However, a shrinking deformation in the horizontal direction is generated and preferential pathways are created both in the sample volume and between the sample and reactor walls, Figure 10.a, while axial deformations (vertical direction) are negligible or absent. The sintering mechanism of unsupported CuO particles involves the formation of a neck between two particles assisted by the surface atoms migration and grain boundary diffusion activated at temperatures lower than the melting temperature [15,35], e.g. typical operating temperatures for CuO reduction.

Detectable axial temperature gradients are measured during reduction and oxidation, with and without SiC dilution, proving that the exothermicity of the reaction, i.e. thermal effects, have a substantial role in the reaction progress. Axial temperature gradients were measured by subtracting the temperature measured by the controlling and monitoring thermocouple respectively, and reported in Figure 12, at 5% reactant (H_2 or O_2), and Figure 13, at 10% reactant concentration.

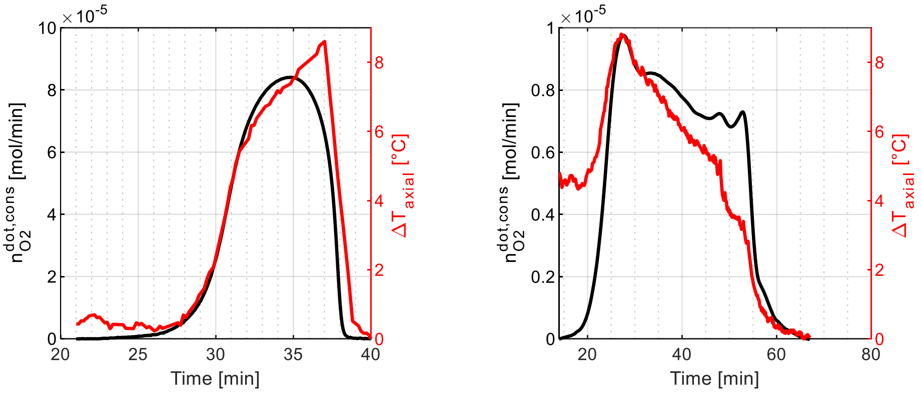

a) b)

***Figure 12**: a) Reduction and temperature gradient profiles, y_{H_2} = 5%, b) Reoxidation and temperature gradient profiles y_{O_2} = 5%. Common conditions: m_s = 50 mg, d_p < 45 μm, $\dot{V}_{tot}$=50 Ncm^3/min, β = 2.5°C/min, No SiC.*

The temperature profile follows the H_2/O_2 consumption curve for both samples, with and without SiC dilution. However, a lower peak is observable in Figure 12.a (no dilution) as the maximum temperature difference is 50% higher compared to Figure 13.a (SiC dilution) during the reduction. This difference is also present for the oxidation curves (Figure 12.b and Figure 13.b) with a milder degree (+25%), implying that even at harsher experimental conditions (m_s

= 200 mg, $\dot{V}_{tot}$=100 Ncm^3/min, y_{H_2}= 10%) for the SiC-diluted sample the addition of an highly conductive material is able of uniformly distribute the heat of reaction and thus decreasing local or axial temperature gradients compared to the non-diluted case (m_s = 50 mg, $\dot{V}_{tot}$=50 Ncm^3/min, y_{H_2}= 5%).

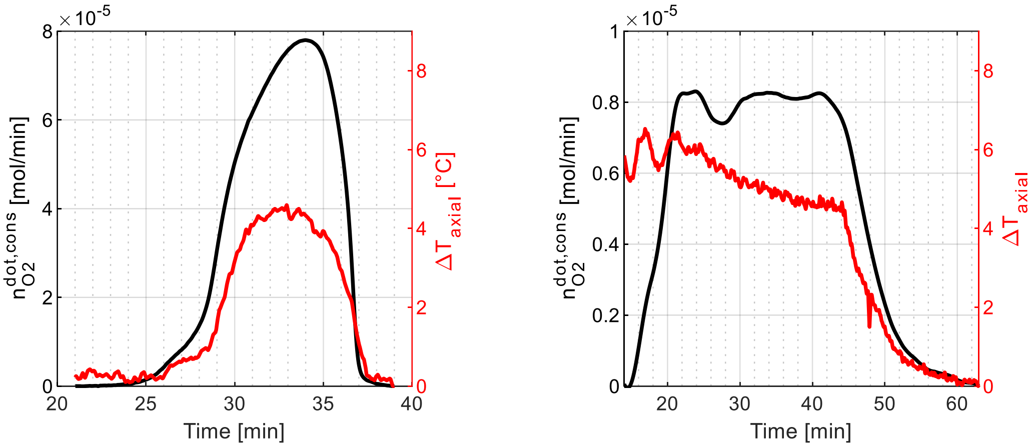

a) b)

***Figure 13**: a) Reduction and temperature gradient profiles, y_{H_2}= 10%. b) Reoxidation and temperature gradient profiles, y_{O_2}= 10%, SiC dilution (SiC : CuO=1:1 w/w). Common conditions: m_s = 200 mg, d_p < 45 μm, $\dot{V}_{tot}$=100 Ncm^3/min, β = 2.5°C/min).*

Given that the reported temperature is just the average gas temperature before and after the bed, we may expect that the temperature at the surface could be much higher than the one measured, likely to play a role in the agglomeration process.

Conclusions

The application of temperature-programmed experiments (reduction and oxidation) to a model reactive system (unsupported CuO reduction with H_2 and reoxidation with O_2) was thoroughly investigated under different aspects. The influence of experimental conditions (sample mass, particle size, gas reactant concentration, total volumetric flowrate, heating rate) was studied to correlate the reduction (or oxidation) profiles to macroscopic performance (degree of reduction/oxidation) and chemical/physical phenomena (reaction mechanism, mass- and heat-transfer limitations). The profiles (peak shape and key temperatures, such as T_{act} and T_{peak}) were significantly affected by the experimental conditions and their combinations, identifying a primary role for the sample mass, gas reactant flow rate (i.e. higher concentration or total flow rate) and heating rate, while a negligible contribution was given by the particle size, for both CuO reduction and Cu oxidation. The common explanation key is the limitation due to external mass transfer, in a heterogenous reaction without significant internal mass transfer limitations.

The rate of reactions appears always high enough to determine a controlling role in the H_2 (or O_2) supply to the surface. Accordingly, a higher H_2 flow rate accelerates the TPR, producing sharper peaks at lower temperature.

Heat effects play a relevant, underestimated effect. The addition of an inert, highly heat-conductive bed dilutant (SiC) promoted the CuO reduction to Cu at higher H_2 concentration, i.e. both favoring the kinetics, levelling out temperature gradients in the sample, reducing the diffusive limitations as soon as Cu nuclei are formed on the surface of the unreacted CuO and delaying agglomeration phenomena.

The final morphological configuration was severely affected by the sequential reduction and oxidation processes, implying that the selection of the experimental variables for TPR/TPO protocols could not be solely performed through a characteristic number (disregarding mass-transfer limitations). Specifically, it was demonstrated that the selection of different set of variables to fit P characteristic number in its optimal range produces divergent results in terms of peak shape, characteristic temperatures and reduction degree and thus it should not be used as benchmark.

Nomenclature

c_p = Specific heat capacity
C_{red} = Reducing gas concentration
$D_{H2,mix}$ = Diffusion coefficient in the binary mixture
d_p = Particle diameter
dp_{low} = Lower particle size range (< 45 μm)
dp_{med} = Intermediate particle size range (100 - 150 μm)
dp_{high} = Higher particle size range (200 - 250 μm)
h_{m,H_2} = External mass transfer coefficient
m_s = Sample mass
$n_{H2,CuO}^{cons}$ = H_2 mol consumed
$n_{H2}^{dot,cons}$ = H_2 molar flowrate consumed
n_{oxide} = Mol of reducible species
$n_{O,CuO}^{initial}$ = Initial O mol in CuO
n_{O2}^{cons} = O_2 mol consumed from gas phase
$n_{O,CuO}^{cons}$ = Total sample oxygen consumed
$n_{O,CuO}^{reg}$ = Total oxygen regained by the sample
O_{CuO} = Oxygen in CuO lattice
K = Monti-Baiker characteristic number [6]
P = Malet-Caballero characteristic number [9]
T = Temperature
T_{act} = Activation temperature
T_{fin} = Final temperature
T_m = Melting temperature
T_{meas} = Measured temperature (monitoring)
T_{peak} = Temperature of the peak
$T_{peak,1}$ = Temperature of the first peak
$T_{peak,2}$ = Temperature of the second peak
T_{range} = Temperature range of the reduction peak
T_s = Temperature of the shoulder
v_{mix} = Kinematic viscosity
V_t = Tubing volume
$\dot{V}_{tot}$ = Total volumetric flowrate
y_R or y_{red} = Volumetric percentage
y_{H_2} = H_2 molar fraction
y_{O_2} = O_2 molar fraction
$\%_{O,CuO}^{cons}$ = Degree of reduction

$\%_{O,CuO}^{reg}$ = Degree of oxidation

Greek letters:

β = Heating rate
λ = Thermal conductivity

Acronyms:
TCD = Thermal conductivity detector
TPO = Temperature programmed oxidation
TPR = Temperature programmed reduction

References

[1] B. Imelik, J.C. Védrine, Catalyst characterization: physical techniques for solid materials, New York: Plenum Press, 1994.

[2] R. Richards, Z. Ma, F. Zaera, Surface and Nanomolecular Catalysis, Ryan Richards, Taylor an Francis (CRC Press), 2006.

[3] A. Jones, B.D. McNicol, Temperature-programmed reduction for solid materials characterization, M. Dekker, 1986.

[4] J.A. Schwarz, Temperature-Programmed Desorption and Reaction: Applications to Supported Catalysts, Catalysis Reviews. 25 (1983) 141–227. https://doi.org/10.1080/01614948308079666.

[5] C. Pirola, F. Galli, G.S. Patience, Experimental methods in chemical engineering: Temperature programmed reduction—TPR, Canadian Journal of Chemical Engineering. 96 (2018) 2317–2320. https://doi.org/10.1002/cjce.23317.

[6] D.A.M. Monti, A. Baiker, Temperature-Programmed Reduction. Parametric Sensitivity and Estimation of Kinetic Parameters, 1983.

[7] S.J. Gentry, N.W. Hurst, A. Jones, Temperature Programmed Reduction of Copper Ions in Zeolites, Journal of the Chemical Society, Faraday Transactions 1: Physical Chemistry in Condensed Phases. 75 (1978) 1688–1699.

[8] N.W. Hurst, S.J. Gentry, A. Jones, Temperature Programmed Reduction, Catalysis Reviews. 24 (1982) 233–309. https://doi.org/10.1080/03602458208079654.

[9] P. Malet, A. Caballero, The Selection of Experimental Conditions in Temperature-programmed Reduction Experiments, J. Chem. SOC., Faraday Trans. I. 84 (1988) 2369–2375.

[10] G. Fierro, M. lo Jacono, M. Inversi, P. Porta, R. Lavecchia, F. Cioci, A study of Anomalous Temperature-Porgrammed Reduction Profiles of Cu2O, CuO, and CuO-ZnO Catalysts, Journal of Catalysis. 148 (1994) 709–721.

[11] A. Pineau, N. Kanari, I. Gaballah, Kinetics of reduction of iron oxides by H2. Part I: Low temperature reduction of hematite, Thermochimica Acta. 447 (2006) 89–100. https://doi.org/10.1016/j.tca.2005.10.004.

[12] N. Wakao, J.M. Smith, Diffusion in catalyst pellets, Chemical Engineering Science. 17 (1962) 825–834.

[13] L. Zou, J. Li, D. Zakharov, E.A. Stach, G. Zhou, In situ atomic-scale imaging of the metal/oxide interfacial transformation, Nature Communications. 8 (2017). https://doi.org/10.1038/s41467-017-00371-4.

[14] J. Adanez, A. Abad, F. Garcia-Labiano, P. Gayan, L.F. de Diego, Progress in chemical-looping combustion and reforming technologies, Progress in Energy and Combustion Science. 38 (2012) 215–282. https://doi.org/10.1016/j.pecs.2011.09.001.

[15] H. Zhao, J. Gui, J. Cao, C. Zheng, Molecular Dynamics Simulation of the Microscopic Sintering Process of CuO Nanograins Inside an Oxygen Carrier Particle, Journal of Physical Chemistry C. 122 (2018) 25595–25605. https://doi.org/10.1021/acs.jpcc.8b04253.

[16] P. Gayán, C.R. Forero, A. Abad, L.F. de Diego, F. García-Labiano, J. Adánez, Effect of support on the behavior of Cu-based oxygen carriers during long-term CLC operation at temperatures above 1073 K, Energy and Fuels. 25 (2011) 1316–1326. https://doi.org/10.1021/ef101583w.

[17] L.F. de Diego, P. Gayán, F. García-Labiano, J. Celaya, A. Abad, J. Adánez, Impregnated CuO/Al2O3 oxygen carriers for chemical-looping combustion: Avoiding fluidized bed agglomeration, Energy and Fuels. 19 (2005) 1850–1856. https://doi.org/10.1021/ef050052f.

[18] F. Biccari, Intrinsic and Extrinsic Defect Characterization of Copper(I) Oxide Semiconductor", 2008.

[19] D.W. Green, R.H. Perry, Perry's Chemical Engineers' Handbook, 8th Edition, McGraw-Hill, 2008.

[20] A. Pintar, J. Batista, S. Hočevar, TPR, TPO and TPD Examination of Cu 0.15 Ce 0.85 O 2-y Mixed Oxide Catalyst Prepared by Co-precipitation Synthesis, n.d.

[21] J.Y. Kim, J.A. Rodriguez, J.C. Hanson, A.I. Frenkel, P.L. Lee, Reduction of CuO and Cu2O with H2: H embedding and kinetic effects in the formation of suboxides, Journal of the American Chemical Society. 125 (2003) 10684–10692. https://doi.org/10.1021/ja0301673.

[22] J.-Y. Lee, S.M. Lee, Hydrogen trapping phenomena in metals with B.C.C. and F.C.C. crystal structures by the desorption thermal analysis technique, Surface and Coatings Technology. 28 (1986) 301–314.

[23] J.A. Rodriguez, J.C. Hanson, A.I. Frenkel, J.Y. Kim, M. Pérez, Experimental and theoretical studies on the reaction of H2 with NiO: Role of O vacancies and mechanism for oxide reduction, Journal of the American Chemical Society. 124 (2002) 346–354. https://doi.org/10.1021/ja0121080.

[24] G. (Gerhard) Ertl, Handbook of heterogeneous catalysis, Wiley-VCH, 2008.

[25] J.G. Chen, D.A. Fisher, J.H. Hardenbergh, R.B. Hall, A fluorescence-yield near-edge spectroscopy (FYNES) investigation of the reaction kinetics of NiO/Ni(100) with hydrogen, Surface Science. 279 (1992) 13–22.

[26] A. Biasin, J. Fabro, N. Michelon, A. Glisenti, P. Canu, Investigation of thermal effects on heterogeneous exothermic reactions and their impact on kinetics studies, Chemical Engineering Journal. 377 (2019). https://doi.org/10.1016/j.cej.2018.10.116.

[27] H. Bosch, B.J. Kip, J.G. van Ommen, P.J. Gellings, Factors Influencing the Temperature-programmed Reduction Profiles of Vanadium Pentoxide, 1984.

[28] P. Arnoldy, J.C.M. de Jonge, J.A. Moulijn, Temperature-programmed reduction of MoO3 and MoO2, Journal of Physical Chemistry. 89 (1985) 4517–4526. https://doi.org/10.1021/j100267a021.

[29] O.J. Wimmers, P. Arnoldy, J.A. Moulijn, Determination of the Reduction Mechanism by Temperature-Programmed Reduction: Application to Small Fe203 Particles, 1986. https://pubs.acs.org/sharingguidelines.

[30] V. Stuchlý, Parametric sensitivity of complex temperature-programmed desorption, reaction and reduction, Journal of Thermal Analysis. 35 (1989) 837–847.

[31] F. García-Labiano, L.F. de Diego, J. Adánez, A. Abad, P. Gayán, Temperature variations in the oxygen carrier particles during their reduction and oxidation in a chemical-looping combustion system, Chemical Engineering Science. 60 (2005) 851–862. https://doi.org/10.1016/j.ces.2004.09.049.

[32] J.G. Chen, NEXAFS investigations of transition metal oxides, nitrides, carbides, sulfides and other interstitial compounds, Surface Science Reports. 30 (1997) 1–152.

[33] M. Fernández-García, XANES analysis of catalytic systems under reaction conditions, Catalysis Reviews - Science and Engineering. 44 (2002) 59–121. https://doi.org/10.1081/CR-120001459.

[34] A. Pintar, J. Batista, S. Hočevar, TPR, TPO, and TPD examinations of Cu0.15Ce0.85O 2-y mixed oxides prepared by co-precipitation, by the sol-gel peroxide route, and by citric acid-assisted synthesis, Journal of Colloid and Interface Science. 285 (2005) 218–231. https://doi.org/10.1016/j.jcis.2004.11.049.

[35] Q. Imtiaz, A. Armutlulu, F. Donat, M.A. Naeem, C.R. Müller, Preventing Agglomeration of CuO-Based Oxygen Carriers for Chemical Looping Applications, ACS Sustainable Chemistry and Engineering. 9 (2021) 5972–5980. https://doi.org/10.1021/acssuschemeng.1c00560.

[36] C. Moreno-Castilla, A. López-Peinado, J. Rivera_Utrilla, lnmaculada Fernández-Morales, F.J. López-Garzón, The striking behaviour of copper catalysing the gasification reaction of coal chars in dry air, Fuel. 66 (1987).

[37] M.D. Argyle, C.H. Bartholomew, Heterogeneous catalyst deactivation and regeneration: A review, Catalysts. 5 (2015) 145–269. https://doi.org/10.3390/catal5010145.

Chapter 3

Investigation on the origin and evolution of solids agglomeration during reduction by H_2

Abstract

Additional analyses were performed to identify the responsible process (reduction, oxidation, thermal/non-reactive cycle) for the loss in reactivity caused by agglomeration. Reduction was found to be the key step for the activity decrease, as pressure drop was drastically falling in correspondence of the reduction peak, while the contribution of other reaction/pre-treatments is negligible.

Introduction

In the current trend of reducing the utilization of Platinum Group Metals (PGMs) for their high cost and decreasing availability [1], metal oxides and their reduced form have been identified as prominent active compounds for heterogeneous catalyzed reactions. The identification of active metals and the critical analysis of their peculiar chemical properties as well as their activity is crucial to rationally design efficient catalytic materials and processes capable of enhancing the overall process efficiency in medium- and long-term operation.

Metal oxides are used both as active species [2] and oxygen carriers in chemical-looping processes [3] in which the materials are subjected to alternating reducing and oxidizing mixtures and the reactive performance should be preserved for multiple reaction cycles. Therefore, to develop new suitable materials for sequential redox loops, attention must be paid not only to the activity in one reaction cycle but also in long-term response in oscillating atmosphere. Specifically, Cu^{2+}/Cu^0 is an appropriate redox couple to be selected as principal component of oxygen donor thanks to its favorable properties (oxygen transport capacity, high reaction rates towards reduction and oxidation, lower cost and environmental issues [3]. However, CuO/Cu has a higher tendency to agglomerate and sinter at high temperatures [4] inevitably decreasing the reactivity, and thus strategies must be identified to avoid or reduce the agglomeration contribution. The identification of suitable supports (α and γ-Al_2O_3, $MgAl_2O_4$, $NiAl_2O_4$) on which specified CuO amount must be efficiently dispersed [5,6] and the synthesis method (mechanical mixing, wet-impregnation, co-precipitation) [7] should be optimized by thoroughly analyzing the correlation between activity and properties and using the information obtained in the process scale-up stage.

In this work, the CuO/Cu reactivity was studied under several conditions to correlate the loss in reactivity to bed agglomeration phenomena caused by different pre-treatments (thermal/non-reactive), reduction/oxidation itself and uneven temperature distribution in the reactive bed.

Materials and methods

The effect of different experimental parameters on CuO (Alfa Aesar, 99.995%) reduction with H_2 and its reoxidation was carried using pure gases (H_2, O_2, Ar) connected to mass-flowmeters (Brooks and Bronkhorst High-Tech) through which the desired inlet composition was achieved. Before entering the reactor, the gas feed went through an automatic four-way valve (VICI Valco) to optimize the reaction protocol, ensure the total separation between the reducing and oxidizing atmosphere in CuO experiments. The valve switch between the two positions and mass-flowmeters operation were controlled though purpose-built MATLAB executable programs. The reactive section could be approximated to a plug-flow reactor, in which the sample bed was inserted into a quartz tube (ID 6 mm) and kept in position by two quartz wool layers. It was then introduced into an electrically heated furnace (Watlow) and two thermocouples (type K) were present in the system to control and monitor the temperature in two different positions (the controlling thermocouple is downstream under the second quartz wool layer and the monitoring thermocouple is upstream, close to the upper surface of the bed) and the temperature-protocols were set on the thermoregulator (Omron) with CX-Thermo software and a purpose-built MATLAB executable program. The temperature used to plot the H_2 or O_2 consumption profiles was the one measured upstream with the monitoring thermocouple, as it better approximate the real bed temperature and it is more sensitive to thermal effects caused by the heat of reaction. The monitoring temperature reported in the plots was also corrected for the dead-volume between the thermocouple position and the gas-analysis detector with the following correlation: $T = T_{meas} + \beta(\frac{V_t}{\dot{V}_{tot}})$, in which T_{meas} = temperature measured by the thermocouple, β = heating rate, V_t = tubing volume and $\dot{V}_{tot}$= total volumetric flowrate. A pressure transmitter (MPX coupled with a PicoLog data logger) with a range of 0-500 mbar was also added before the reactor inlet to continuously measure the pressure drop along the reactor, as an indication of macro-agglomeration phenomena during the reaction.

Before the analysis section, a homemade silica-gel and zeolite traps (volume < 1 cm^3) were added to remove the water produced during the reducing cycles. The measurement of H_2 and O_2 consumption was performed with a thermal conductivity detector (TCD) and O_2 chemical sensor (Alphasense O2-C2) respectively. The TCD (from Agilent 6890 HP) was optimized to have a high analysis frequency (1 Hz) as the reactor outlet was directly conveyed into the detector without any previous separation with packed columns. Using this strategy, a fast and sensitive identification of transient effects during the reaction was possible and the same measurement frequency was obtained in the oxidation stage with an oxygen sensor. The same experimental protocol was kept for all the tests (inert pre-treatment to desorb water and/or contaminants at 200°C for 30 min with Ar, isothermal oxidative pre-treatment at 250°C achieved at 5°C/min, 5%O_2/Ar with 50 Ncm^3/min) H_2 reduction and O_2 oxidation with ramping temperature at fixed heating rate) and repeated in the case of long-term performance experiments. The selection of an inert bed dilutant was based on its thermal conductivity to investigate the thermal effects associated to both reactions and thus silicon carbide (SiC) was chosen. Surface morphology was examined with an Environmental Scanning Electron Microscope (ESEM) Fei-Quanta 200 (CEASC, University of Padova) equipped with Back-Scattered Electron Detector (BSE).

Results and Discussion

The parametric sensitivity experiments evidenced that the reactivity for the unsupported CuO reduction with H_2 and its sequent reoxidation with O_2 is strongly affected by the experimental parameters, which determine the kinetics, mass and heat transfer and macroscopic solids modifications (agglomeration). Here we deepen the effects of different and combined sample pre-treatments (inert or oxidative) with non-reactive thermal treatments and linked with H_2/O_2 consumption profiles with pressure drop and temperature gradient measurements. Also, sequential reduction and oxidation cycles were performed to correlate the loss in reactivity typical of unsupported metal oxide with variations in morphological features, with and without bed dilution.

Effect of non-reactive gas flow

The dramatic morphological modifications of the bed, mainly ascribed to TPR, may be supported by local overheating, due to the reaction. The contribution of temperature alone, and its cycling up and down from RT to 500°C, on the bed morphology and its variation was assessed with thermal cycles under an inert gas flow. This has been achieved by monitoring the pressure drop across the CuO bed, both during the thermal cycles and at ambient temperature to identify the step (just thermal cycle in inert gas, or the reduction, or the oxidation) mainly responsible for the bed agglomeration. The features of the initial CuO bed are reported in Table 1.

Table 1: *CuO sample features used to study the effect of non-reactive flows.*

Parameter	Symbol	Unit of measure	Values
Mass	m_s	[mg]	203
Particle size range	d_p	[µm]	<45
Bed height	H_{bed}	[mm]	6
Bed volume	V_{bed}	[cm^3]	0.284

The experimental protocol consists of a pre-treatment of the sample (thermal cycle under inert flow and a subsequent cycle with an oxidizing mixture), followed by a single TPR-TPO cycle, 3 heating and cooling cycles under inert flow and one additional TPR-TPO cycle. All cycles' parameters are listed in Table 2. The total duration of the experiment is 48 h.

Table 2*: Details of the experimental protocol to investigate the effect of non-reactive flows. (TPX-# = number of the sequential reduction or oxidation cycle, y_R = reagent (H_2 or O_2) concentration, β = heating rate, T_{fin} = final temperature after the heating ramp, t_s= time at T_{fin}).*
The total volumetric flowrate, $\dot{V}_{tot}$ is constant in all steps at 100 Ncm^3/min,

	Inert [-]	**Reagent [-]**	**y_R [%]**	**β [°C/min]**	**T_{fin} [°C]**	**t_s [min]**
Pre-treatment (inert)	Ar	-	-	5	200	30
Pre-treatment (oxidative)	Ar	O_2	10	5	250	60
TPR-1	Ar	H_2	10	2.5	500	0
TPO-1	Ar	O_2	10	2.5	500	0
Inert cycle	Ar	-	-	2.5	500	0
Inert cycle	N_2	-	-	2.5	500	0
Inert cycle	Ar	-	-	2.5	500	0
TPR-2	Ar	H_2	10	2.5	500	0
TPO-2	Ar	O_2	10	2.5	500	0

The macro- and microscopic (SEM) appearance of the fresh CuO bed is shown in Figure 1. It is worth noting that some of the grains stuck to the internal wall of the quartz tube and were caught by the upper quartz wool bed when it was assembled. A detail of the particle shape and size, provided by SEM, is also shown in Figure 1; the particles used in this test were predominantly flaky, almost flat, with sharp spikes at their edges, but grains of smaller size with rounded edges are also present. The high polydispersity of the sample suggests that the resulting bed packing must be much higher than spherical particles.

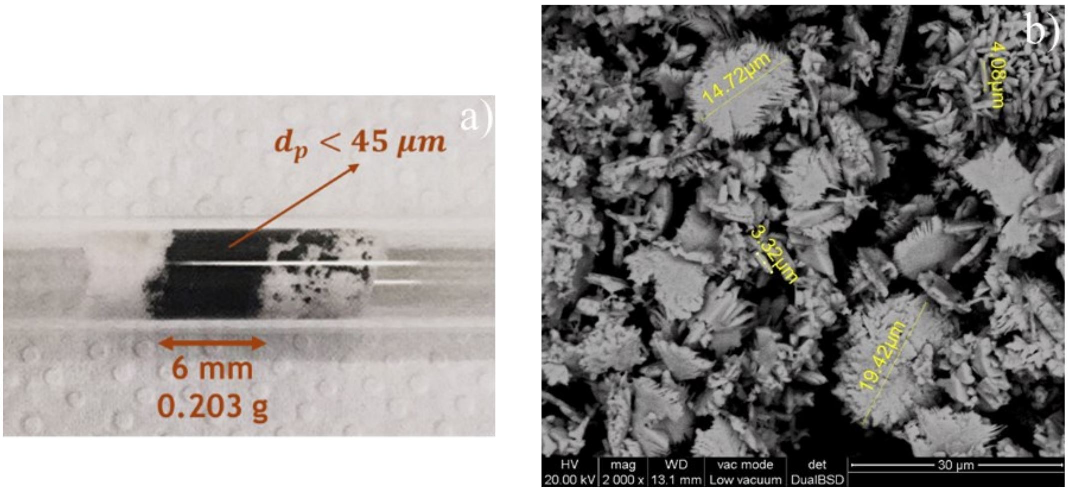

a) b)

Figure 1: *(a) Appearance of the fresh CuO bed in the reactor and (b) SEM analysis of the fresh CuO powder.*

The pressure drop variation with the gas flow was measured across the whole process line (reactor, up- and downstream tubing, and quartz wools) without any CuO, with an inert gas (Ar), by changing the total volumetric flowrate. This procedure was repeated when the reactive CuO bed was loaded inside the reactor. The measurements were fitted with a quadratic function $\Delta P(\dot{V}) = a\,\dot{V} + b\,\dot{V}^2$, for both cases, to determine the functions $\Delta P_{line}(\dot{V})$ and $\Delta P_{line+bed}(\dot{V})$. The pressure drop produced only by the reactive bed $\Delta P_{bed}(\dot{V})$ at room temperature was calculated by difference:

$$\Delta P_{bed}(\dot{V}) = \Delta P_{line+bed}(\dot{V}) - \Delta P_{line}(\dot{V}),\ T = 20°C \qquad \text{Equation 1}$$

The bed porosity was estimated comparing the fitting parameters *a, b* with the Ergun relation, Equation 2. The first term indicates the pressure drop variation in laminar regime, while the second term is related to the turbulent regime.

$$\frac{\Delta P_{bed}}{H_{bed}} = 150 \cdot \mu \cdot \frac{v}{d_p^2} \cdot \frac{(1-\varepsilon_{bed})^2}{\varepsilon_{bed}^3} + 1.75 \cdot \rho \cdot \frac{v^2}{d_p} \cdot \frac{1-\varepsilon_{bed}}{\varepsilon_{bed}^3} \qquad \text{Equation 2}$$

where H_{bed}= bed height, ε_{bed}= bed porosity, μ= gas dynamic viscosity, v = superficial gas velocity, d_p = equivalent particle diameter and ρ = gas density [8]. Bed features used in

Equation 2 are reported in Table 1, and pure Ar was used for the gas properties calculation [9]. The actual mixtures are different along the experiment (H_2/Ar for reduction and O_2/Ar for the oxidation), but the deviation is small as the gas mixture is very diluted. Particles were approximated as spherical and mono-dispersed with 45 μm as average diameter, implying an underestimation of bed porosity as the actual particle size and shape distribution, Figure 1, is quite distant from this premise. Even within the limits of this assumption, the calculated bed porosity is relatively small ($\varepsilon_{\mathrm{bed}} = 0.304$).

The pressure drop variation with temperature, $\Delta P_{bed}(T)$ was calculated performing a heating cycle with 100 Ncm^3/min of Ar and increasing the temperature up to 500°C at 2.5°C/min, both in the empty reactor and with the CuO bed, before any TPR or TPO. This allows to determine the bed pressure drop during the thermal cycles using Equation 3.

$$\Delta P_{bed}(T) = \Delta P_{line+bed}(T) - \Delta P_{line}(T), \ \dot{V}_{tot} = 100 \ Ncm^3/min \qquad \text{Equation 3}$$

After fitting the functions representing the line pressure drop $\Delta P_{line}(\dot{V})$ and $\Delta P_{line}(T)$, the inert and oxidant pre-treatments have been run in sequence using the parameters reported in Table 2. The pressure drop across the bed during these thermal cycles exhibited linear behavior, and no anomalies (i.e., pressure drop reductions) were detected. The procedure to calculate the bed's porosity with the function $\Delta P_{line}(\dot{V})$ and Equation 2 has been repeated after both pre-treatments, obtaining a value of $\varepsilon_{bed} = 0.304$ for both cases. It is then concluded that pre-treatments, either with inert or oxidative mixture, up to 250°C, did not affect the bed structure. The results of the following TPR, along with the pressure drop in the bed as the analysis was performed, are shown in Figure 2, whereas Table 3 reports the characteristic values derived by the plot, along with the quantification of the total hydrogen consumed during the reduction.

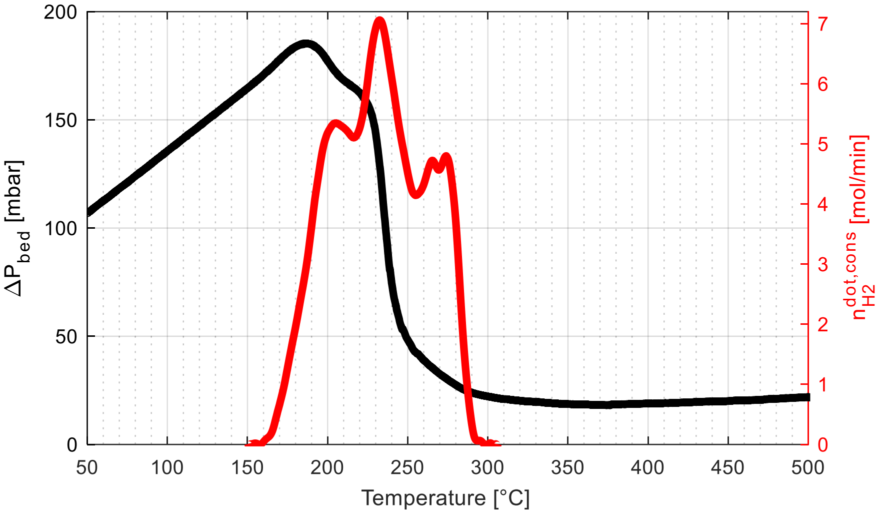

Figure 2: *Hydrogen consumption and pressure drop through the bed during TPR-1. Conditions as in Table 1.*

Table 3: *Relevant calculated parameters for TPR-1.*

TPR number [-]	T_{act} [°C]	$T_{peak,1}$ [°C]	**Secondary peak(s)**	T_s [°C]	**Peak range** [°C]	$\%^{cons}_{O,CuO}$ [%]
1	158	233	✓	204, 266, 276	142	87.2

As the data shows, with the selected parameters m_s, $\dot{V}_{tot}$ and y_R multiple peaks in the hydrogen consumption profile are observed. Moreover, the pronounced decrease of the bed pressure drop (already at T = 220°C) clearly indicates that the bed agglomerated during the reduction. Closely observing the $\Delta P_{bed}(T)$ profle, there are indications that the catalyst bed starts agglomerating soon after the reaction begins (T = 190°C), as a slight but noticeable decrease in pressure drop is detected. As the reaction proceeds the agglomeration continues, and when the pressure drop falls dramatically (T = 220°C), a by-pass for the gas is evidently created. The conditions for the application of Equation 2 following the merging of individual particles do no hold anymore, and the estimation of the porosity through the Ergun equation cannot be obtained. As discussed in the section *CuO reduction at constant characteristic number P*, the presence of multiple peaks could not be a chemical effect, connected with the reduction mechanism, but just the result of the agglomeration that has been identified at T = 220°C: this process would indeed enallage the effective 'particle' size, produce a layer through which the hydrogen needs to diffuse before reacting with the underlying oxide, adding a delay to the hydrogen consumption curve, which is indeed observed at T = 220°C. Further, gas by-pass manifest as drops in the H_2 consumption profile. One possible hypothesis for the onset of the secondary peak observed around T = 270°C could be a sudden physical re-arrangement of a small portion of the bed, where the gas passage was previously impossible. In this way some of the least reduced particles would become exposed to the gaseous reagent, increasing the rate of reaction. On the other hand, an inhomogeneous temperature distribution inside the sample, possibly caused by the local reaction exothermicity or by an uneven heat distribution in the system due toa poor heat transfer in an inhomogeneous bed, could also be the cause for the multiple peaks. In this case a higher rate of reaction would be experienced by the hotter zones, leading to an increase in the hydrogen consumption. In parallel, the colder zones would react later, resulting in delays in the peak and the creation of secondary peaks, as was observed in this case. The degree of reduction provided by the quantification (i.e., $\%_{O,CuO}^{cons}$ in Table 3), indicates that the bed has not reduced completely: because of that, some cuprous or CuO are expected to still be present in the reduced sample, apparently inaccessible to H_2 just because of the bed restructuring and agglomeration.

The results of the following TPO are shown in Figure 3 and Table 4. The pressure drop through the bed is quite low, which suggests an irreversible packing of the bed during the previous TPR, to which channeling is associated. Three peaks seem to be present in the oxygen consumption curve (i.e., a mechanism of reaction comprised of three steps is likely). As the shape of the profile indicates, the oxidation of the bed has also been carried out during the cooling process, and ended at T = 460°C. The degree of oxidation resulting from the quantifications suggests that the Cu effectively produced by the TPR-1 has been oxidized completely, as its value is comparable (+0.2%) to the previous TPR degree of reduction. The result confirms that oxidation cycles after a reduction cycle inevitably operate on a modified solid, that cannot be reversed to its original, particle bed arrangement.

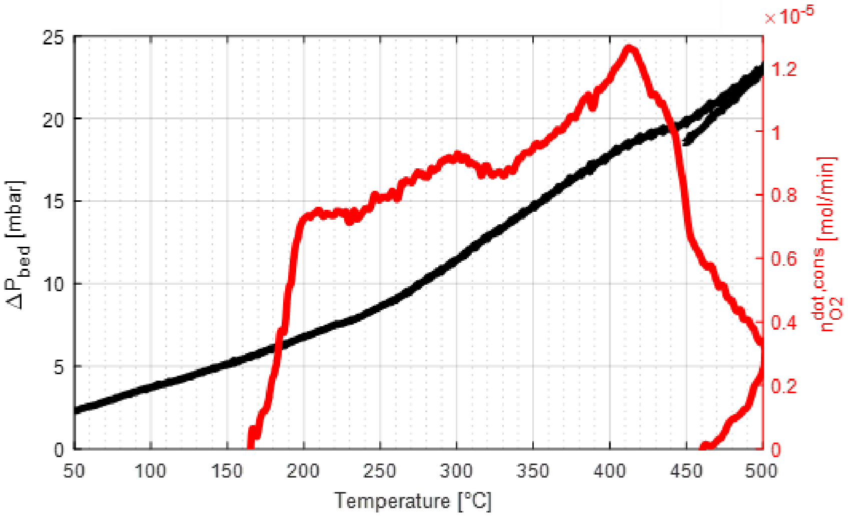

***Figure 3**: Oxygen consumption and pressure drop through the bed during TPO-1. Conditions as in Table 1.*

***Table 4:** Relevant calculated parameters for TPO-1.*

TPO number [-]	**T_{act} [°C]**	**$T_{peak,1}$ [°C]**	**$T_{peak,2}$ [°C]**	**$\%_{O,CuO}^{reg}$ [%]**
1	155	250	415	87.4

The following three thermal cycles have been carried out under inert flow. Figure 4 reports the raw pressure drop registered by the pressure transmitter rather than the $\Delta P_{bed}(T)$. They differ markedly depending on the inert gas used (argon and nitrogen), as expected. The viscosity of Ar is approx. 1.3 times the one of N_2, resulting in a higher pressure drop. Also, keeping the same volumetric flow rate in all tests, imply that the velocity for gases of different molecular weights is not the same. However, having measured similar pressure drops during the first and third cycles, both carried out using argon as an inert, suggests that these cycles do not further modify the macroscopic structure of the catalyst, even reaching 500°C for 3 times. Still, the bed structure was already modified by TPR-1 and results of Figure 3 suggest that thermal treatment cannot reverse the agglomeration caused by the reduction.

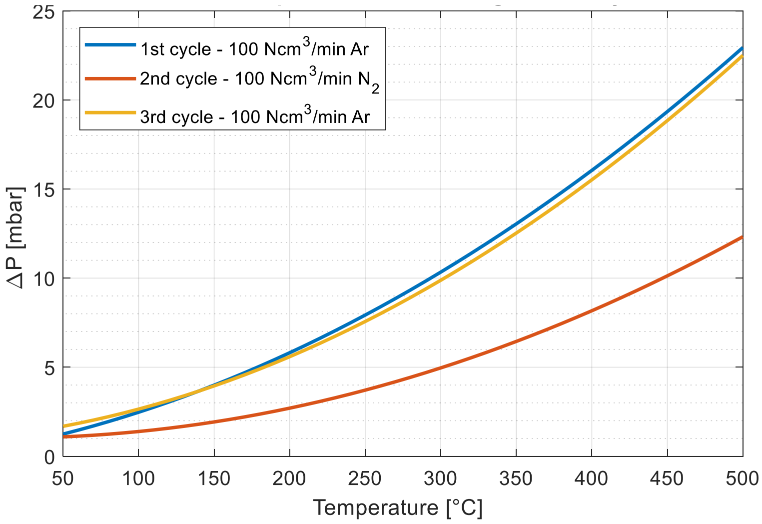

***Figure 4**: Pressure drop through the bed during three inert cycles. Conditions as in Table 1.*

After the thermal cycles under inert conditions, a second TPR has been performed, with results presented in Figure 5 and in Table 5. Differently to what observed during the first reduction cycle, only one peak is obtained in the second cycle, on an agglomerated bed. In this case the reaction starts at a lower temperature, possibly because some structural defects have appeared during the first cycle. Indeed, the formation of these more active sites lowers the induction time for reduction (i.e., the reaction starts at lower temperatures) [10].

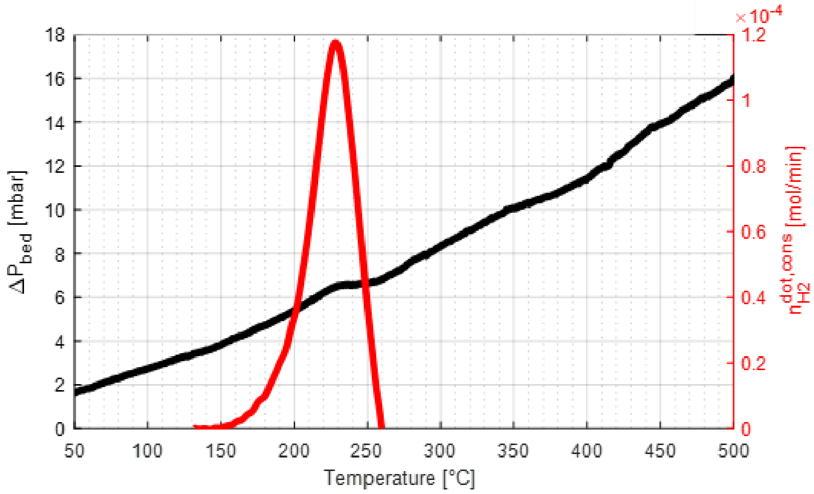

Figure 5: *Hydrogen consumption and pressure drop through the bed during TPR-2. Conditions as in Table 1.*

Table 5: *Relevant calculated parameters for TPR-2.*

TPR number [-]	**T_{act} [°C]**	**$T_{peak,1}$ [°C]**	**Secondary peak(s)**	**T_s [°C]**	**Peak range [°C]**	**$\%_{O,CuO}^{cons}$ [%]**
2	146	228	-	-	124	75.6

Conversely, the decrease of the surface area due to previous agglomeration of the sample lowers the reaction rate when T < 180°C, increasing diffusion limitations and thus producing a single peak. Moreover, since the secondary peak appearing at T = 270°C in TPR-1 does not show in this cycle, a further bed rearrangement likely did not happen. Two inflections in $\Delta P_{bed}(T)$ indicates the transition between laminar, intermediate and turbulent flow caused by preferential pathways close to the reactor walls and thus the ΔP_{bed} function is no more linearly dependent with the velocity. The calculated degree of reduction is further reduced, compared to the one in the first TPR (-11.6%): therefore, some copper oxides are expected to still be present in the sample, while other, produce by the TPO-1, could not be reduced, perhaps by further solids restructuring during TPR-2.

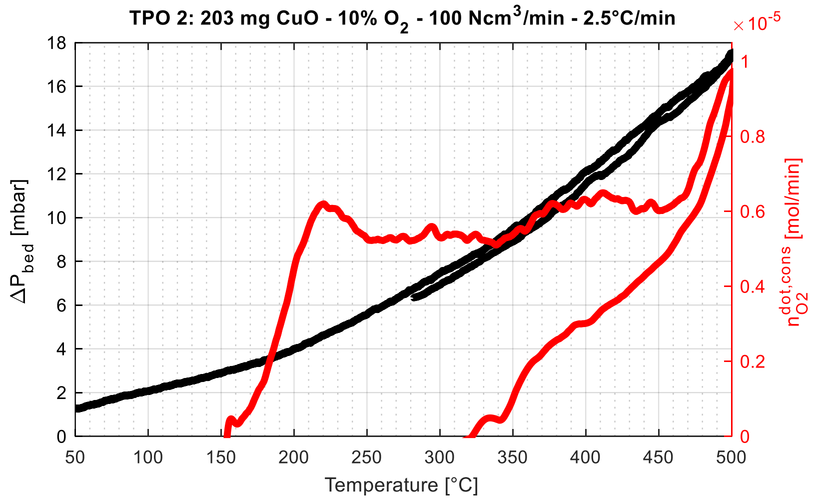

***Figure 6**: Oxygen consumption and pressure drop through the bed during TPO-2. Conditions as in Table 1.*

***Table 6:** Relevant calculated parameters for TPO-2.*

TPO number **[-]**	**T$_{act}$** **[°C]**	**T$_{peak,1}$** **[°C]**	**T$_{peak,2}$** **[°C]**	$\%^{reg}_{O,CuO}$ **[%]**
2	155	220	500	72.3

The results of the following TPO are shown in Figure 6 and in Table 6. During TPO-2 a rection mechanism consisting of two step occurs as well, in which the first peak appears at nearly the same temperature as TPR-1, while the second peak develops at a higher temperature, and the oxidation process is also carried out during cooling. Since this gap between peaks increases as more cycles are performed, and during every reduction the sample is subjected to further agglomeration, it is suggested that a correlation between these two phenomena could hold. The subject will be explored further in Chapter 4. The oxidation degree for TPO-2 is slightly lower than the degree of reduction for the previous TPR (-3.3%): as a result, some CuO or elemental Cu are expected to still be present in the sample.

As every thermal cycle completes, a scan of different argon flowrates through the reactor, at ambient temperature, have been carried out, and the corresponding pressure drops have been registered. $\Delta P_{bed}(\dot{V})$ has been calculated using Equation 1, the points have been fitted using a quadratic function, and the results are shown in Figure 7.

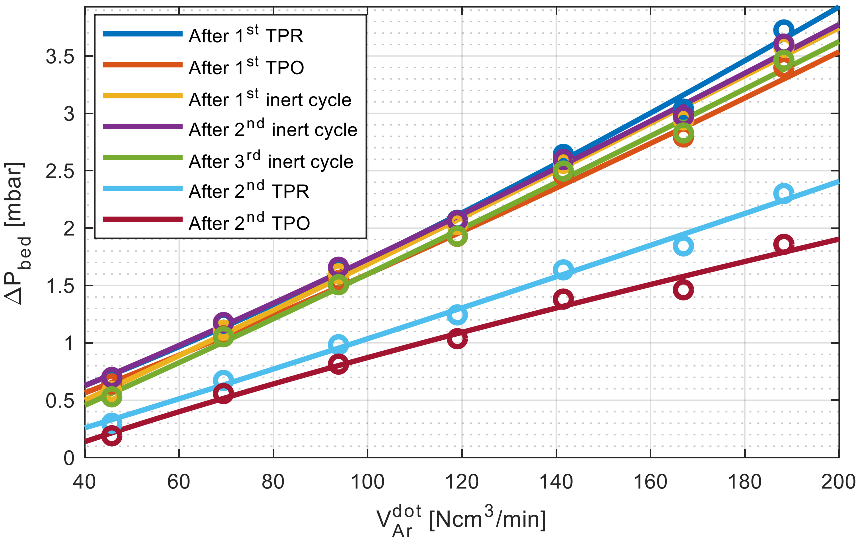

***Figure** 7: Pressure drops through the bed after each thermal cycle.*

Note that this plot does not report $\Delta P_{bed}(\dot{V})$ before TPR-1, since only a punctual value was available for the comparison (namely, $\Delta P_{bed}(100\ Ncm^3/\min Ar)$ = 93.3 mbar after the inert pre-treatment and $\Delta P_{bed}(100\ Ncm^3/\min Ar)$ = 92.8 mbar after the oxidant pre-treatment). Considering these values, it is seen that the higher pressure drop decrease between cycles is found immediately after TPR-1, for which at $\dot{V}_{Ar}$=100 Ncm^3/min the difference is of approximately 91 mbar (-99%!): this supports the previous conclusion that the main, dramatic agglomeration happened during TPR-1. Moreover, the plots show that a further agglomeration occurred during TPR-2, since the $\Delta P_{bed}(\dot{V})$ are even (slightly) lower than the ones registered after each inert cycle. That explains also the further loss of efficiency in TPR-2.

After all cycles described in Table 2 were concluded, the testing tube was extracted from the oven and observed, Figure 8. It appeared as a solid cylinder and showed a remarkable axial shrinkage of approx. 1 mm coupled with a comparable lateral shrinkage. According to the analysis above, this structure had been attained during TPR-1.

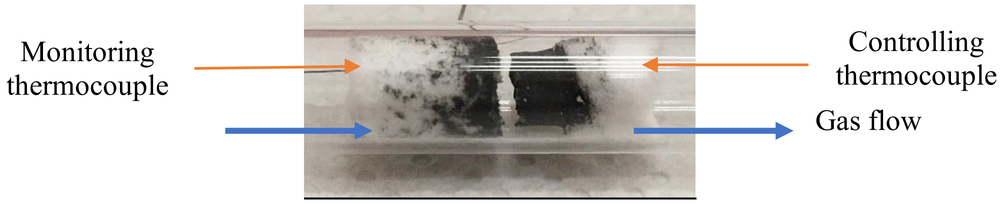

***Figure 8**: Sample appearance in the testing tube, after the complete cycles described in Table 2.*

The sample has then been further analyzed by Scanning Electron Microscope; representative images are reported in Figure 9, together with the fresh particles.

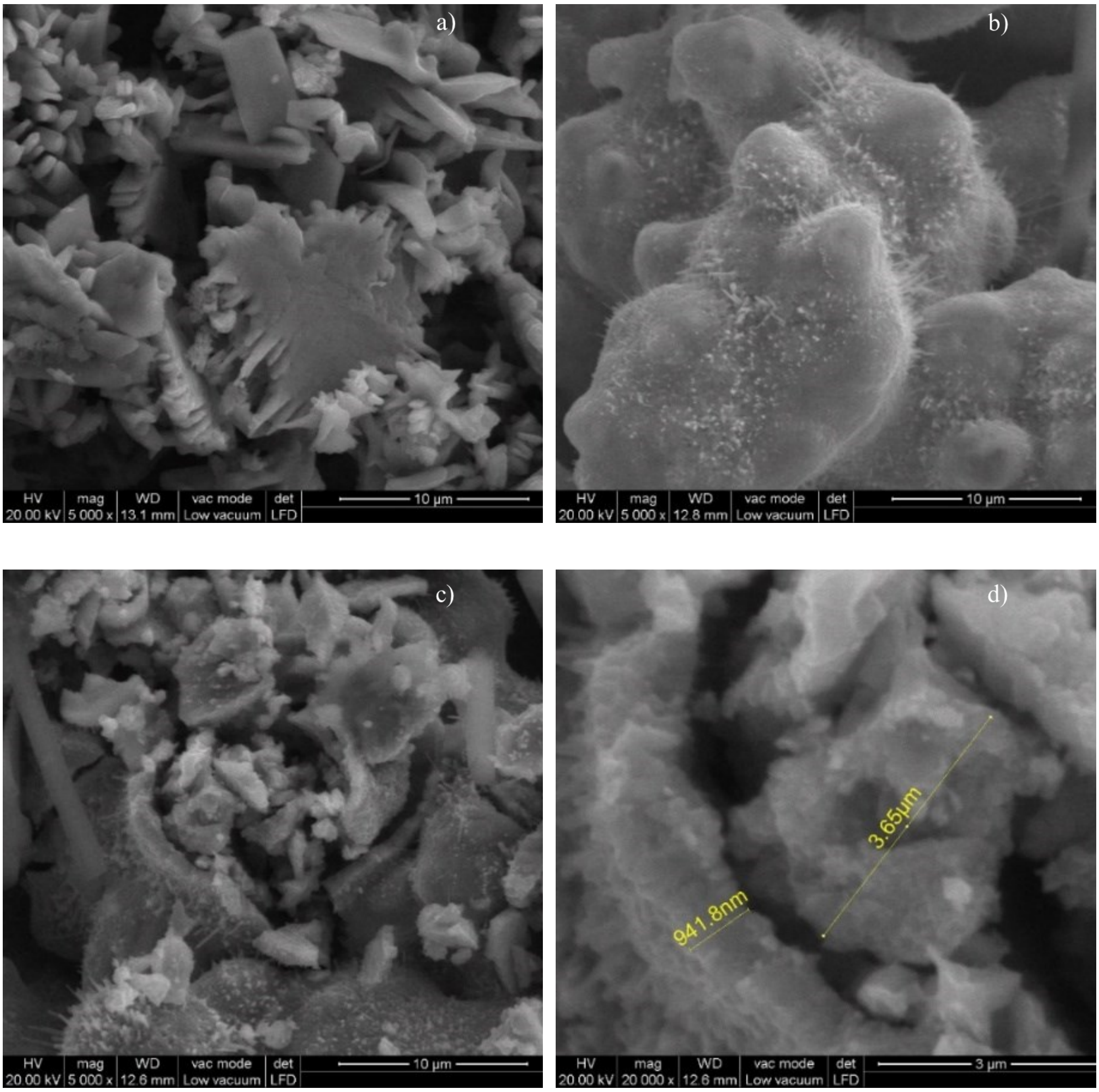

Figure 9*: SEM images of (a) the fresh CuO powder used in the sample, b) the oxidized sample surface after all the cycles, (c) a breakage of the external shell and (d) the internal structure.*

As suggested by the sudden drop of hydraulic resistances of the bed during reduction, Figure 2, the particles have agglomerated and their edges have been rounded, clearly shown by the comparison between Figure 9.a and Figure 9.b. Still, some fibers can be observed on top of the agglomerated surface, clearly shown in Figure 9.b, which may compensate for the surface area decrease caused by the agglomeration process. According to the SEM images, and specifically Figure 9.c, the reduction of the oxide caused a sort of local melting, that created a shell, enveloping other oxide particles, likely shielding them to further exposure to H_2, and then reduction. The breakage of the external layer of the agglomerated sample (Figure 9.c and Figure 9.d), whose thickness was about 1µm, reveals indeed some inner particles, partially reacted; their edges are smoother than the fresh sample ones, and did not completely merge, in the process.

Pre-treatment variation

The conclusion of the previous combined test is that agglomeration takes place during TPR-1. Now the question is whether the former pre-treatment of the sample may contribute to such an evolution during the following TPR. We planned and carried out a test with the purpose of investigating the effect of a pre-treatment consisting only of a thermal cycle under inert flow, on both the agglomeration phenomenon and the peak shape. The same sample amount previously used, discussed in section *Effect of non-reactive flow,* has been used to perform the new test, so that the sample' characteristic and appearance remain consistent with the ones reported in Table 1. The plan for the test is summarized in Table 7; it includes a pre-treatment of the sample under inert conditions, followed by a single TPR-TPO sequence.

Table 7: *Details of the experimental protocol to investigate the effect of an inert pre-treatment. Y_R = reagent (H_2 or O_2) concentration, β = heating rate, T_{fin} = final temperature after the heating ramp, t_s = time at T_{fin}). The total volumetric flowrate, $\dot{V}_{tot}$ is constant in all steps at 100 Ncm^3/min*

	Cycle [-]	**Inert [-]**	**Reagent [-]**	**y_R [%]**	**β [°C/min]**	**T_{fin} [°C]**	**t_s [min]**
Pre-treatment (inert)	1	Ar	-	-	5	200	30
TPR	2	Ar	H_2	10	2.5	500	0
TPO	3	Ar	O_2	10	2.5	500	0

As in previous experiments, the $\Delta P_{line}(\dot{V})$ at ambient temperature and $\Delta P_{line}(T)$ @ 100 Ncm^3/min Ar flowrate were determined, before loading the CuO catalyst into the reactor. Subsequently, $\Delta P_{bed}(\dot{V})$ and the $\Delta P_{bed}(T)$ could be determined, as explained in section *Effect of non-reactive flow*, to finally estimate the bed's initial porosity. The resulting value, ε_{bed}=0.296, indicates that the bed packing was slightly higher than the bed used in section *Effect of non-reactive flow*.

TPR results are reported in Figure 10.a and Figure 11, and TPO in Figure 10.b.

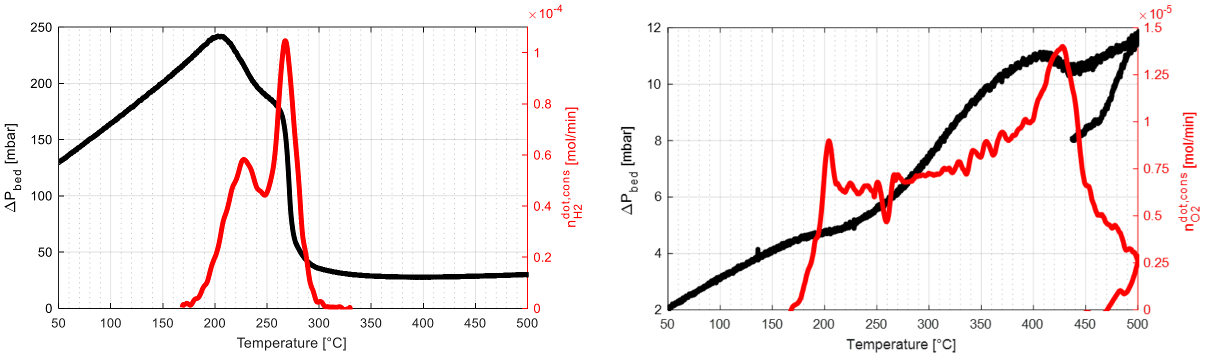

a) b)

Figure 10 *Reagent consumption and pressure drop for CuO a) reduction with H_2 b) reoxidation with O_2 . Conditions as in Table 7*

Table 8*: key parameters for CuO a) reduction with H_2, b) reoxidation with O_2. Conditions as in Table 7.*

a)

T_{act} [°C]	$T_{peak,1}$ [°C]	Secondary peak(s)	T_s [°C]	Peak range [°C]	$\%_{O,CuO}^{cons}$ [%]
175	268	✓	228	125	81.9

b)

T_{act} [°C]	$T_{peak,1}$ [°C]	$T_{peak,2}$ [°C]	T_s [°C]	$\%_{O,CuO}^{reg}$ [%]
160	205	460	425	87.7

As in the TPR-1 of the previous test (section *Effect of non-reactive flow*), the bed has agglomerated. The dramatic drop in the measured $\Delta P_{bed}(T)$ curve confirms that the reduction process is responsible for the agglomeration. Contrary to the previous experiment, though, the hydrogen consumption profile shows two peaks instead of four: this suggests that the formation of the last two peaks in the previous experiment could be due to the different pre-treatment conditions or by random phenomena happening with the rearrangement of the bed, which cannot be consistently reproduced. The double-peak shape could be explained by the same processes by the bed rearrangement that creates several structural phases, exposing different portions of materials and generating uneven reduction process on the surface. The degree of reduction is unexpectedly low if compared to the previous TPR (-5.3% with respect to TPR-1 of section *Effect of non-reactive flow*) which was executed under similar conditions: this could have been caused by experimental errors, as in this particular experiment the TCD signal was quite noisy, or by the absence of the oxidant pre-treatment. However, this last hypothesis seems unlikely, as the high sample purity should have allowed to start with an almost completely oxidized sample, even without an oxidating pre-treatment as in the last test. It is interesting to notice that the axial temperature gradient obtained as described in section *Pressure drop and thermal effects* (i.e., by subtracting the monitored temperature, upstream, from the controlling temperature, downstream) follows the hydrogen consumption profile quite closely, as shown in Figure 11.

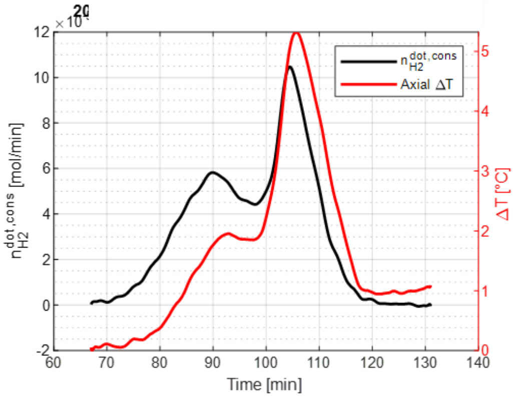

***Figure 11:** Hydrogen consumption and temperature gradient during TPR-1.*
Conditions as in Table 1 and Table 7.

Since thermal peaks are delayed with respect to hydrogen consumption ones, we speculate that the temperature rise in the sample is a consequence of the reaction exothermicity, rather than being the cause of the double-peak profile in the hydrogen consumption curve.

As shown by the data, the TPO-1 carried out on the sample presents two distinct peaks. Although ΔP is much lower, due to the agglomeration that took place in the former TPR, small rearrangements can be observed after each peak, more evident at higher temperature. They indicate additional modifications of the bed, in the direction of a further agglomeration, leaving an easier path for the gas. The degree of oxidation is higher than the preceding TPR's degree of reduction (+5.8%). As it will be mentioned in section *Sequential reduction-oxidation cycles – no bed dilution*, a possible explanation for such a mismatch could be the formation of a small quantity of copper peroxide, but in this case an underestimation of the hydrogen consumed during the previous TPR appears more likely, since the values of $\%_{O,CuO}^{cons}$ agrees with the first TPO quantifications reported in the former test, described in section *Effect of non-reactive flow* (+0.3%). To examine whether the absence of an oxidative pre-treatment could have influenced the bed structure, and to confirm the correlation between the reduction process and the catalyst's agglomeration, the bed pressure drop as a function of flowrate, $\Delta P_{bed}(\dot{V})$, has been calculated by measuring several flowrates and correlating it with Equation 1 before and after the pre-treatment, and after the first TPR. The experimental measurements, along with their fittings, are shown in Figure 12.

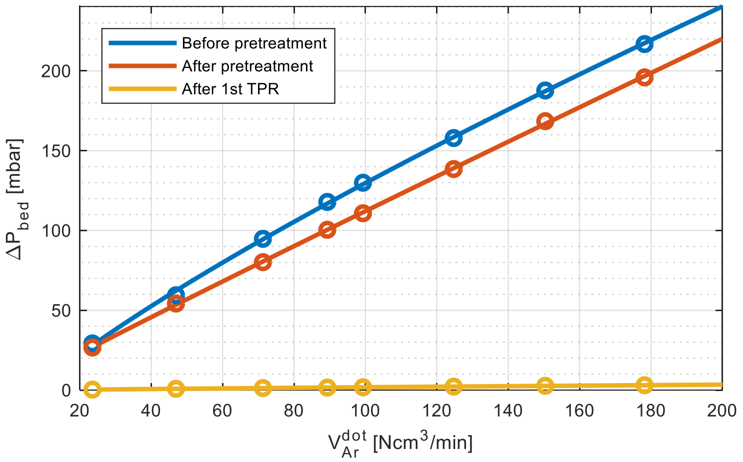

Figure 12: *Pressure drop variation before and after the pre-treatment, and after the TPR-1.*

As the plot shows, the pressure drop generated by the bed is dramatically lower when measured after the reduction process, proving that the agglomeration of the bed happened during the TPR cycle. On the other hand, the inert pre-treatment is also responsible for some bed rearrangement, leading to some shrinkage of the bed, as the corresponding measured pressure drop is lower than the one measured before the pre-treatment. If the values obtained feeding 100 Ncm^3/min Ar are to be taken as a reference, a difference of 20 mbar between the value before and after the pre-treatment is measured. The corresponding value for the previous test was of approximately 1 mbar. If these values are related to the total decrease in the pressure drop before the pre-treatment and after the TPR, in the first case the pre-treatment contributes for 15.5% of the total pressure drop, while in the second case this contribution is only 1.7%.

Considering these results, it is concluded that the pre-treatments marginally affect the bed agglomeration, which remains concentrated in the reduction phase.

As with the previous tests, the sample has been visually inspected at the end of the protocol. The catalyst shrinkage was evident, leading to a final bed height of less than 1 mm; all the individual grains merged and were covered by a layer of black copper oxide (Figure 13).

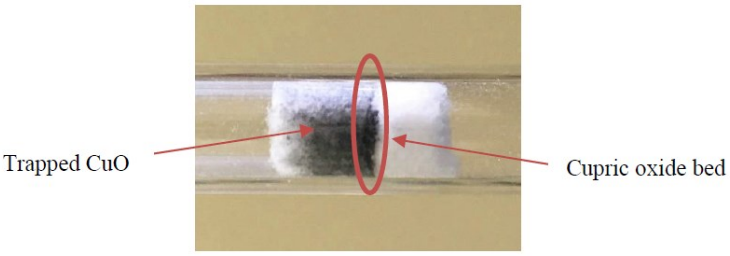

Figure 13: *Bed appearance after all the reaction cycles.*

Furthermore, the sample has been analyzed by SEM; the most significant images are reported in Figure 14. Figure 14.a shows the oxidized sample surface still retained a granular-looking appearance, although the particles have visibly merged, and their external surface has been smoothed.

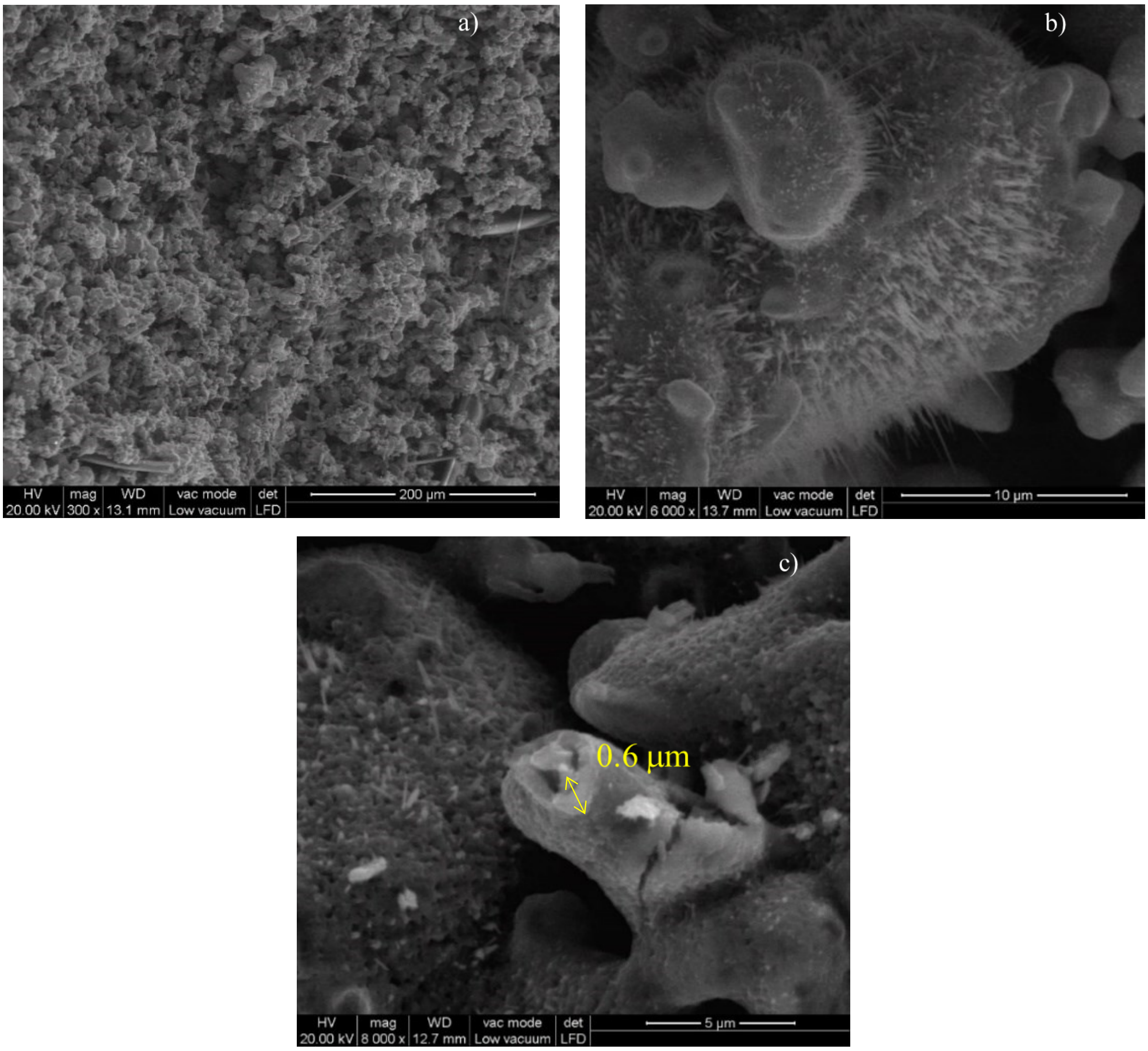

Figure 14: *SEM image of (a) fresh sample surface, (b) magnification of the external surface after all the reaction cycles and c) enlargement on a broken protuberance after the reaction cycles.*

A further magnification allows to identify fibers of approximately 100 nm of diameter on the sample surface, as reported in Figure 14.b. Since they seem to be present in higher number compared to the two other cases (see Figure 9.a and Figure 9.b), it could be concluded that their number and length decrease as more reactive cycles are conducted. A detailed investigation on the formation of superficial nanostructures is reported in Chapter 5. In addition to the fibers, distinct bumps are also found, as the focus of Figure 14.c reports; the breakage of one of them showed that a shell formed even after a single redox cycle. This layer, which is approximately

0.6 μm thick, covered the remaining particles, which still retained a granular aspect. Since Figure 9.d established that the thickness of this layer was of approximately 1 μm after two redox cycles, further hindering the inward diffusion of the reagent.

Conclusions

Heat effects play a relevant, underestimated effect. The addition of an inert, highly heat-conductive bed dilutant (SiC) promoted the CuO reduction to Cu at higher H_2 concentration, i.e. both favouring the kinetics, levelling out temperature gradients in the sample, reducing the diffusive limitations as soon as Cu nuclei are formed on the surface of the unreacted CuO and delaying agglomeration phenomena.

The loss in reactivity cause by physical phenomena, such as agglomeration, was further analysed to clearly identify the responsible process (reduction, oxidation or thermal/non-reactive cycle) or pre-treatment (inert, oxidative) for such decrease. Pressure drop was continuously monitored during all the reaction steps and superimposed to the reaction profiles to find a correlation between them. It was proven that when unsupported CuO is reduced to Cu in a reducing mixture (H_2/Ar) pressure drop falls drastically in correspondence to the highest H_2 consumption (reduction peak) and agglomeration could be attributed to this process, while the contribution of other pre-treatment/reaction step is negligible. SEM analyses of the spent CuO sample show great variations from the initial morphology, as a bulky layer covers the particles and copper oxides nanostructures are created in the surface. The formation of this layer is ascribed to the reduction step as soon as the pressure drop decreases, preventing further H_2 or O_2 diffusion and thus shifting the reduction peak to higher temperatures and/or showing multiple peaks. In most cases, the degree of reduction and oxidation was <100%, suggesting that mass-transfer limitations were influencing the activity as soon as the reaction activates.

Nomenclature

d_p = Particle diameter
ΔP_{bed} = Pressure drop of the bed
ΔP_{line} = Pressure drop of the line
$\Delta P_{line+bed}$ = Pressure drop of the line (tubing) and bed
H_{bed} = Bed height
m_s = Sample mass
T = Temperature
T_{act} = Activation temperature
T_{fin} = Final temperature
T_{peak} = Temperature of the peak
$T_{peak,1}$ = Temperature of the first peak
$T_{peak,2}$ = Temperature of the second peak
T_s = Temperature of the shoulder
t_s = Soak time
V_{bed} = Bed volume
v = Superficial gas velocity
$\dot{V}$ = Volumetric flowrate
$\dot{V}_{tot}$ = Total volumetric flowrate
V_t = Volume tubing
y_R = Reducing gas volumetric percentage
$\%_{O,CuO}^{cons}$ = Degree of reduction
$\%_{O,CuO}^{reg}$ = Degree of oxidation

Greek letters:

β = Heating rate
ε_{bed} = Bed porosity
μ = Dynamic viscosity
ρ = Density

Acronyms:
BSE = Back-Scattered Electron Detector
EDS = Energy Dispersive X-ray Spectrometry
(E)SEM = (Environmental) Scanning electron microscope
PGM = Platinum-Group Metal
TCD = Thermal conductivity detector

TPO = Temperature programmed oxidation
TPR = Temperature programmed reduction

References

[1] Study on the EU's list of Critical Raw Materials (2020) Final Report, (n.d.). https://doi.org/10.2873/904613.

[2] I.E. Wachs, Recent conceptual advances in the catalysis science of mixed metal oxide catalytic materials, in: Catalysis Today, 2005: pp. 79–94. https://doi.org/10.1016/j.cattod.2004.12.019.

[3] J. Adanez, A. Abad, F. Garcia-Labiano, P. Gayan, L.F. de Diego, Progress in chemical-looping combustion and reforming technologies, Progress in Energy and Combustion Science. 38 (2012) 215–282. https://doi.org/10.1016/j.pecs.2011.09.001.

[4] H. Zhao, J. Gui, J. Cao, C. Zheng, Molecular Dynamics Simulation of the Microscopic Sintering Process of CuO Nanograins Inside an Oxygen Carrier Particle, Journal of Physical Chemistry C. 122 (2018) 25595–25605. https://doi.org/10.1021/acs.jpcc.8b04253.

[5] L.F. de Diego, P. Gayán, F. García-Labiano, J. Celaya, A. Abad, J. Adánez, Impregnated CuO/Al2O3 oxygen carriers for chemical-looping combustion: Avoiding fluidized bed agglomeration, Energy and Fuels. 19 (2005) 1850–1856. https://doi.org/10.1021/ef050052f.

[6] P. Gayán, C.R. Forero, A. Abad, L.F. de Diego, F. García-Labiano, J. Adánez, Effect of support on the behavior of Cu-based oxygen carriers during long-term CLC operation at temperatures above 1073 K, Energy and Fuels. 25 (2011) 1316–1326. https://doi.org/10.1021/ef101583w.

[7] J. Adanez, A. Abad, F. Garcia-Labiano, P. Gayan, L.F. de Diego, Progress in chemical-looping combustion and reforming technologies, Progress in Energy and Combustion Science. 38 (2012) 215–282. https://doi.org/10.1016/j.pecs.2011.09.001.

[8] S.J. Gentry, N.W. Hurst, A. Jones, Temperature Programmed Reduction of Copper Ions in Zeolites, Journal of the Chemical Society, Faraday Transactions 1: Physical Chemistry in Condensed Phases. 75 (1978) 1688–1699.

[9] D.W. Green, R.H. Perry, Perry's Chemical Engineers' Handbook, 8th Edition, McGraw-Hill, 2008.

[10] J.A. Rodriguez, J.C. Hanson, A.I. Frenkel, J.Y. Kim, M. Pérez, Experimental and theoretical studies on the reaction of H2 with NiO: Role of O vacancies and mechanism for oxide reduction, Journal of the American Chemical Society. 124 (2002) 346–354. https://doi.org/10.1021/ja0121080.

Chapter 4

Sequential reduction-oxidation cycles on CuO/Cu redox couple

Abstract

Long-term reactivity was investigated with 11 sequential TPR-TPO experiments and a progressive loss in activity was visible from the degree of reduction/oxidation, decreasing from 100% in the 1st cycle to 15% in the 11th cycle. Furthermore, one single step is present after the 5th reaction cycle in the O_2 consumption curve indicating a strong bed restructuration limiting the second step in the oxidation mechanism (from Cu_2O to CuO). SEM analyses and pictures of the fresh and spent samples are a further proof of the different morphological status. The presence of multiple peaks in the reduction profiles (one-step mechanism) is another evidence of a non-uniform reaction progress and a crucial role could be ascribed to an uneven temperature distribution together with physical phenomena. However, axial temperature measurements showed that the additional reduction peaks are not cause by thermal effects in the reactive bed but uniquely to the sample agglomeration, increasing diffusive-type limitations.

Introduction

Metal oxides and the reduction to the corresponding metals have emerged as prominent active compounds in heterogenous catalyzed reactions, covering a large variety of industrial and environmental processes. A crucial feature of metal oxides when exposed to reducing and oxidizing mixtures, e.g. acting as oxygen carrier for chemical-looping processes [26], is the preservation of reactive performance after multiple cycles. During the development of new suitable materials for sequential redox loops, attention must be paid not only to the activity in one reaction cycle but also in long-term response. Specifically, Cu^{2+}/Cu^0 is an appropriate redox couple to be selected as principal component of oxygen donor thanks to its favorable properties (oxygen transport capacity, high reaction rates towards reduction and oxidation, lower cost and environmental issues [26]). However, CuO/Cu has a higher tendency to agglomerate and sinter at high temperatures [27], inevitably decreasing the reactivity, and thus strategies must be identified to avoid or reduce the agglomeration contribution. The identification of suitable supports (α and γ-Al_2O_3, $MgAl_2O_4$, $NiAl_2O_4$) on which specified CuO amount must be efficiently dispersed [28,29] and the synthesis method (mechanical mixing, wet-impregnation, co-precipitation) [26] should be optimized by thoroughly analyzing the correlation between activity and properties and using the information obtained in the process scale-up stage.

In this work, long-term performance of CuO/Cu system was investigated through 11 TPR-TPO cycles and the appearance of multiple peaks was tentatively correlated with an uneven temperature distribution in the reactive bed or agglomeration

Materials and methods

The sequential reduction and oxidation cycles on CuO (Alfa Aesar, 99.995%) were carried using pure gases (H_2, O_2, Ar) connected to mass-flowmeters (Brooks and Bronkhorst High-Tech) through which the desired inlet composition was achieved. Before entering the reactor, the gas feed went through an automatic four-way valve (VICI Valco, Figure 1 in Chapter 1) to optimize the reaction protocol, ensure the total separation between the reducing and oxidizing atmosphere in CuO cyclic experiments. The valve switch between the two positions and mass-flowmeters operation were controlled though purpose-built MATLAB executable programs. The reactive section could be approximated to a plug-flow reactor, in which the sample bed (~ 2 – 5 mm) was inserted into a quartz tube (ID 6 mm) and kept in position by two quartz wool layers. It was then introduced into an electrically heated furnace (Watlow) and two thermocouples (type K) were present in the system to control and monitor the temperature in two different positions (the controlling thermocouple is downstream under the second quartz wool layer and the monitoring thermocouple is upstream, close to the upper surface of the bed) and the temperature-protocols were set on the thermoregulator (Omron) with CX-Thermo software and a purpose-built MATLAB executable program. The temperature used to plot the H_2 or O_2 consumption profiles was the one measured upstream with the monitoring thermocouple, as it better approximate the real bed temperature and it is more sensitive to thermal effects caused by the heat of reaction as it is closer to the bed surface. The monitoring temperature reported in the plots was also corrected for the delay between the thermocouple and the gas-analysis measurements with the following correlation: $T = T_{meas} + \beta(\frac{V_t}{\dot{V}_{tot}})$ in which: T= temperature value corrected from the delay and used in the plots, T_{meas} = temperature measured by the thermocouple [°C], β = heating rate [°C/min], V_t = tubing volume [cm^3] and $\dot{V}_{tot}$= total volumetric flowrate [Ncm^3/min]. A pressure transmitter (MPX coupled with a PicoLog data logger) with a range of 0-500 mbar was also added before the reactor inlet to continuously measure the pressure drop along the reactor, as an indication of macro-agglomeration phenomena during the reaction. Before the analysis section, a silica-gel or zeolite traps (volume < 1 cm^3) were added to remove the water produced during the reducing cycles. The measurement of H_2 and O_2 consumption was performed with a thermal conductivity detector (TCD) and O_2 chemical sensor (Alphasense O2-C2) respectively. The TCD (from Agilent 6890 HP) was optimized to have a high analysis frequency (1 Hz) as the reactor outlet was directly conveyed into the detector without any previous separation with packed columns. Using this strategy, a fast and sensitive identification of transient effects during the reaction was possible and the same measurement frequency was obtained in the oxidation stage with an oxygen sensor. The same experimental protocol was kept for all the tests; it was 1) an inert pre-treatment to desorb water and/or contaminants at 200°C for 30 min with Ar, 2) isothermal oxidative pre-treatment at 250°C achieved at 5°C/min, 5%O_2/Ar with 50 Ncm^3/min), 3) H_2 reduction followed by 4) O_2 oxidation with ramping temperature at fixed heating rate and repeated for 11 cycles. The selection of an inert bed dilutant was based on its thermal conductivity to investigate the thermal effects associated to both reactions and thus silicon carbide (SiC) was chosen. Details of the test conditions, experimental parameter values and thermal properties [7,18,19] are reported in Table 1.

Table 1: *Thermal properties of CuO, Cu_2O, Cu and SiC (cp=specific heat capacity, λ=thermal conductivity, T_m=melting temperature).*

Material	**cp** [J/Kg/K]	**λ** [W/m/K]	**T_m** [°C]
CuO	705	6	1326
Cu_2O	489	4.5	1235
Cu	460	350	1085
SiC	675	490	2730

Results and Discussion

The test carried out so far suggest that reduction and oxidation are not reversible, but the sample redox history determines the future behavior, under oxidizing or reducing atmosphere. To further elaborate on the concept, we carried out a longer series of cycles, alternating reduction and oxidation on the same sample. The investigation is useful both to clarify the limitation of the TPR and TPO as analytical techniques, and to explore the technology of CLC, where the same solids must go through several such cycles.

The experimental protocol for each reduction-oxidation cycle is the same used in the parametric sensitivity (described in section *Materials and methods* and Table 2 and Table 3). Now the initial CuO sample was not removed from the reactor after the first reoxidation as it was tested for 11 reduction-oxidation cycles.

Table 2: *CuO sample features used in redox cyclic experiments.*

Parameter	Symbol	Unit of measure	Values
Mass	m_s	[mg]	50
Particle size range	d_p	[µm]	250-300
Bed height	H_{bed}	[mm]	2
Bed volume	V_{bed}	[cm^3]	0.071

Table 3: *Details of the experimental protocol to investigate the effect of sequential TPR-TPO cycles. (# = number of cycles, y_R = reagent (H_2 or O_2) concentration, β = heating rate, T_{fin} = final temperature after heating ramp, t_s= time at T_{fin}).*
The total volumetric flowrate, $\dot{V}_{tot}$ is constant in all steps at 50 Ncm^3/min,

	#	Inert [-]	Reagent [-]	y_R [%]	β [°C/min]	T_{fin} [°C]	t_s [min]
Pre-treatment (inert)	1	Ar	-	-	5	200	30
Pre-treatment (oxidative)	1	Ar	O_2	5	5	250	60
Reduction	11	Ar	H_2	5	2.5	500	0
Oxidation	11	Ar	O_2	5	2.5	500	0

Results of the 11 reduction-oxidation cycles (TPR-TPO) are displayed as the consumed H_2 or O_2 molar flowrate ($n_{H_2}^{dot,cons}$ or $n_{O_2}^{dot,cons}$), as a function of the monitoring temperature in Figure 1 and Figure 2; a reduction (or oxidation) peak is associated to a higher H_2 (or O_2) consumption. Relevant quantifications data are reported in the corresponding Table 4 and Table 5, as T_{act} (activation temperature, °C), $T_{peak,x}$ (maximum reduction/oxidation temperature in which x is the number of the peak if multiple peaks are present, °C), T_{shift} (difference between T_{peak} in the nth and nth-1 cycle, °C), *Peak width* (range of the reduction peak temperature, °C), *Shoulder* (presence of shoulder in the reduction/oxidation profiles), T_s (if present, shoulder temperature, °C), $\%_{O,CuO}^{cons}$ (percentage of O from CuO consumed with respect to the initial amount and assuming the complete reduction to Cu or $\%_{O,CuO}^{reg}$ (percentage of O regained after the oxidation assuming the complete oxidation to CuO).

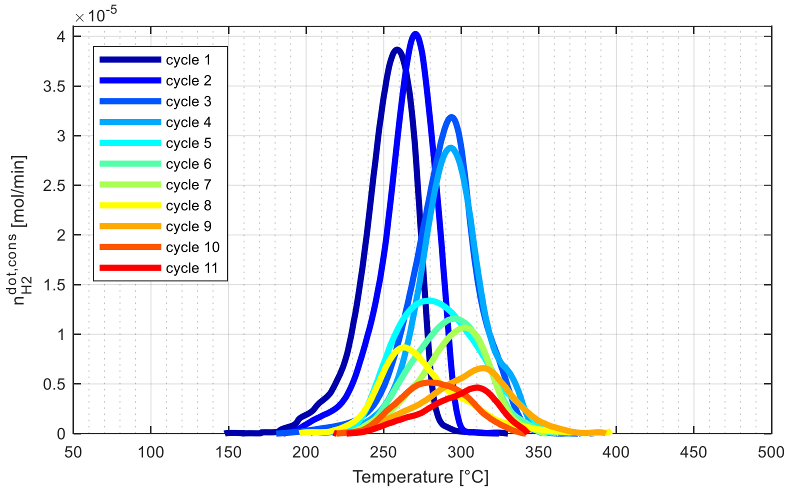

***Figure 1**: Profiles for 11 sequential CuO reductions. Conditions as in Table 3.*

***Table 4:** Relevant calculated parameters for sequential reduction-oxidation cycles (reductions).*

Cycle number	T_{act} [°C]	T_{peak} [°C]	T_{shift} [°C]	Peak width [°C]	Shoulder [-]	T_s [°C]	$\%_{O,CuO}^{cons}$ [%]
1	181	260	-	111	-	-	96.0
2	186	271	+11	106	-	-	97.5
3	190	295	+24	149	-	-	95.4
4	210	295	0	153	✓	330	85.6
5	200	280	-15	130	-	-	58.9
6	222	299	+19	119	-	-	43.0
7	226	305	+6	119	-	-	36.1
8	211	263	-42	161	✓	300	31.2
9	223	315	+52	154	-	-	27.0
10	217	282	-33	112	-	-	19.1
11	225	312	+30	112	-	-	16.0

Figure 1 shows that CuO sample's activity decreases in subsequent cycles, as the degree of reduction (i.e. $\%_{O,CuO}^{cons}$) gradually diminishes. The only exception to this behaviour appears to be the second cycle, for which the calculated hydrogen consumption increases from the value obtained in the preceding TPR, see Table 4. This slight deviation from the established trend could be due to experimental errors, or more likely to some processes occurring during the first

TPR that modified the catalyst's structure, allowing for an increased degree of reduction in the bed.

In the first two cycles the catalyst's performance is satisfactory, as the reaction activates at a low temperature and the reduction process affects close to the totality of the bed (i.e., the degree of reduction approaches 100%), and proceeds rapidly (i.e., the peaks are narrow). As the catalyst undergoes subsequent cycles, however, the reactivity gradually lowers, as indicated by higher activation temperatures and wider peaks, associated with a progressively lower degree of reduction of the bed. From cycle no. 5 onwards, a sharp decrease in reactivity is observed. This is reflected in the calculated reduction efficiency (-26.7% compared to the value for cycle no. 4) and in the peak's shape, in which the value for maximum hydrogen consumption is greatly reduced. The profiles associated with the following cycles show a clear asymmetry, with progressively longer tails at low temperatures, which indicates some sort of resistance in the first stages of the reaction, likely associated with diffusion processes. This trend is inverted in cycle no. 8, whereas cycle no. 10 has once again a symmetrical profile. Moreover, from cycle no. 9 onwards two peaks seem to develop. These observations indicate that in these cycles a different reaction mechanism should be investigated, which involves not only the direct reduction of CuO to elemental Cu, but also its partial reduction to Cu_2O [32], and the associated diffusive limitations. A distinct shoulder is present in cycles no. 4 and 8 could be considered an indication of the release of trapped hydrogen [33], as already mentioned in Chapter 1. Since every TPR has been followed by a TPO, the correct hypothesis for explaining this behavior could be deduced by analyzing the oxygen consumption profiles during the oxidation cycles, shown in Figure 2.

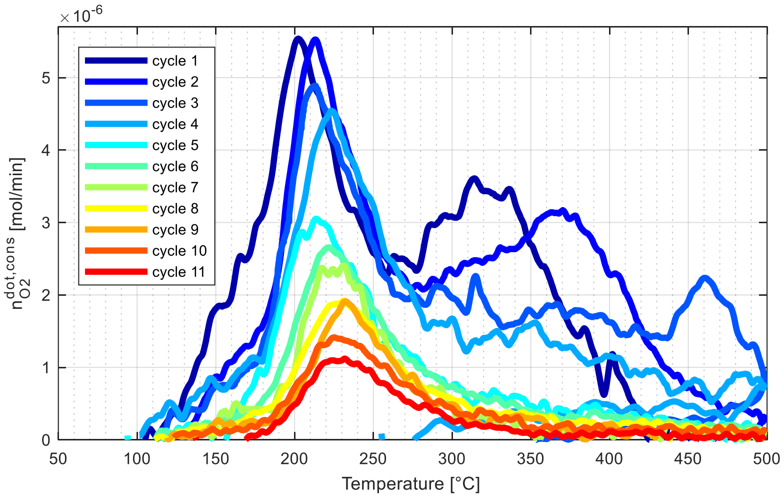

Figure 2*: Profiles for 11 sequential CuO oxidation after reduction. Conditions as in Table 3.*

Table 5: *Relevant calculated parameters for the sequential reduction-oxidation cycles (oxidations).*

Cycle number	**T_{act} [°C]**	**$T_{peak,1}$ [°C]**	**T_{shift} [°C]**	**2^{nd} peak**	**$T_{peak,2}$ [°C]**	**$\%_{O,CuO}^{reg}$ [%]**
1	105	201	-	✓	318	98.2
2	131	215	+14	✓	366	100.4
3	116	211	-4	✓	457	93.8
4	102	223	+12	-	-	80.0
5	115	217	+6	-	-	49.5
6	123	221	+4	-	-	35.4
7	126	224	+3	-	-	26.7
8	120	226	+2	-	-	25.1
9	130	233	+7	-	-	19.7
10	124	227	-6	-	-	18.7
11	137	229	+2	-	-	14.5

O_2 consumption indicates in all the cycles has a first peak, whose maximum temperature ($T_{peak,1}$) always lies between 200°C and 230°C. A second peak appears in the first three cycles alone, and its maximum temperature ($T_{peak,2}$) shifts towards higher values while progressing through the cycles, suggesting an increase of apparent activation energy. Moreover, the degree of oxidation (proportional to the integral of the profile) decreases, from one cycle to the following one, implying a reduced reactivity of the material.

To explain the processes behind these O_2 consumption peaks, the mechanism for CuO oxidation should be considered; the first step involves the creation of a CuO shell on the surface of the reacting solid [49], confirmed by the detection of small quantities of CuO at the reaction onset [34]. Subsequently, the simultaneous migration of copper ions to the inner shell interface and the diffusion of oxygen ions through the CuO shell into the interface allows for the partial oxidation of the core to Cu_2O. Finally, oxygen diffusion completes the core's oxidation to CuO. Since two peaks are evident in the first three oxidation cycles, it can be concluded that they reflect the two reactions occurring in the core:

$2Cu + 1/2O_2 \rightarrow Cu_2O$ Reaction 1

$Cu_2O + 1/2O_2 \rightarrow 2CuO$ Reaction 2

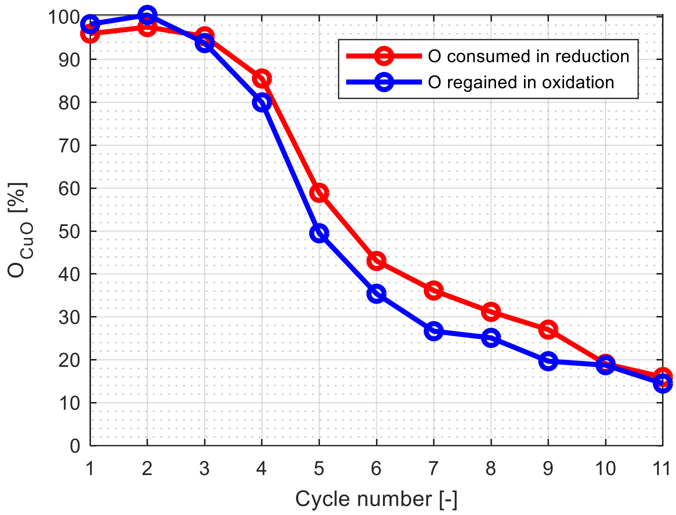

***Figure 3**: Reduction and oxidation efficiencies in 11 redox cycles*. Conditions as in *Table 3.*

An explanation of the whole process consisting of the eleven TPR-TPO cycles could be formulated by considering the efficiencies of the redox cycles, Figure 3. During the first reduction, some of the CuO initially present in the sample is not reduced to copper, since its reduction degree is lower than 100%. Therefore, in this cycle either a small quantity of elemental copper was present before the reduction started, or some copper oxides are still present in the sample at the end of the cycle. During the following TPO, the whole sample is expected to be re-oxidized to its original state, since its degree of oxidation is higher than the preceding TPR degree of reduction. This behavior is then repeated in the second cycle as well. The slightly higher degree of oxidation obtained in these cases could be due to the production of small quantities of copper peroxide (CuO_2), of which however it was not possible to verify the presence. It can also be the positive effect of cycling reduction and oxidation to level off uneven redox states in the original sample.

In the third cycle the trend reverses: the reduction in the TPR is incomplete, as indicated by a degree of reduction of 95.4%, and in the following TPO the sample is not oxidized completely either, because the cycle degree of oxidation (93.8%) is lower than the reduction degree in the preceding step. As in the previous cycles, during the TPR some Cu_2O is expected to form instead of CuO, and some more Cu_2O is expected to form in the following TPO. This pattern of an incomplete bed reduction followed by an incomplete bed oxidation seems to repeat over the cycles for which the degree of reduction is slightly higher than the preceding TPO degree of oxidation. In this case, some of the Cu_2O present in the bed could have reduced again to copper, thus consuming more hydrogen than what could have been predicted by the preceding

TPO degree of oxidation. Since a substantial decrease in the TPR performances is observed in cycle no. 5 (-21.6% with respect to the preceding TPO), while the TPO degree of oxidation in cycles no. 4, 5 and 6 does not decrease significantly compared to the preceding degree of reduction, it is suggested that the sharp decrement in the efficiencies from cycle no. 5 onwards lies in some phenomena happening during the fifth TPR. Therefore, if this test involving cyclical TPR and TPO is to be repeated in the future, a sample characterization before and after the decrease in efficiency is suggested.

Once the eleventh and last TPO cycle had finished, the sample has been removed from the reactor and analyzed. Its appearance is shown in Figure 4. The catalyst's shrinkage was evident, leading to a final bed height of less than 1 mm; all the individual grains merged and were covered by a layer of black copper oxide.

Figure 4: *Spent CuO bed after 11 redox cycles.*

The oxidized sample has been observed with SEM, as shown in Figure 5. The resulting images showed that most of its surface was smooth and covered by short fibers, but scattered across it were granules and bumps, as shown in Figure 5.a. The flattening and smoothing of the surface, which is shown in Figure 5.b, was probably due to the agglomeration of particles combined with the high number of reaction cycles. The breakage of one of the protuberances, shown in Figure 5.c, revealed that the external smooth layer has a thickness of approximately 3 μm; below, an inner porous structure with a pore diameter of 200~800 nm is present. Having also found a similar structure under the external smooth surface, which from Figure 5.d seems to be collapsed in some places (probably during the extraction of the sample from the reactor), suggests that the sample is surrounded by a shell under which a nano-porous structure lies.

An EDS (Energy Dispersive X-ray Spectrometry) analysis reports that under the surface of the sample different compositions of copper oxides prevail, with small quantities of impurities (SiO_2 and CaO, belonging either to the sample or to supporting quartz wool). Furthermore, a quantitative analysis showed the presence of 61.90% Cu and 32.35% atomic oxygen (1.91:1 ratio), which suggests that the sample is composed mainly (approx. 90%) of Cu_2O. Unfortunately, neither the cycle number nor the process (i.e. TPR vs TPO) during which this structure first formed could be known from these analyses, but starting from the moment in which this structure emerged the diffusive resistance associated with the shell should be considered as part of the reactive process.

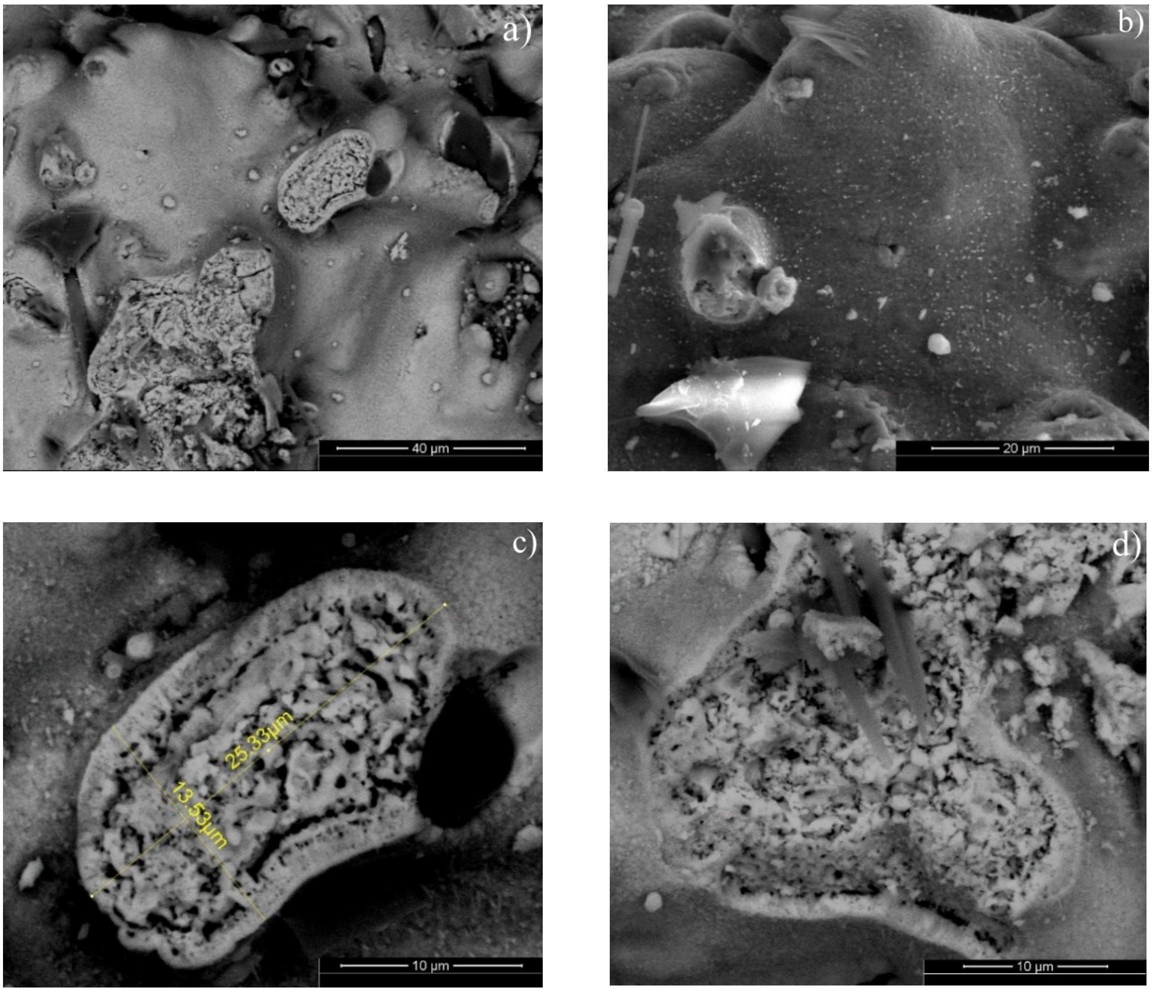

Figure 5: *a) Back-scattered SEM image of the sample surface after 11 TPR/TPO cycles, (b) SEM image of the sample surface, c) magnification of sample surface and d) focus on the structure under its surface.*

Sequential reduction-oxidation cycles with bed dilution

The presence of large temperature gradients in the reactive bed was proved with different measurements and experiments (See Chapter 2). Accordingly, the addition of SiC as an inert material with high thermal conductivity was deemed useful to lower the gradients. The role of SiC is to increase the heat propagation among the particles, thus reduce thermal gradients in the bed; further, it can reduce or even preventing bed agglomeration. The selected dilution ratio was 1:1 w/w, using the same particle size range of the CuO particles, to avoid any influence on the bed fluidynamic. CuO and SiC features are reported in Table 6 and the characteristics of the experimental protocol in Table 7, including an inert and oxidative pre-treatment and 4 sequential TPR-TPO. Pressure drop was monitored during TPR-1 and TPO-1 and $\Delta P_{bed}(\dot{V})$ was measured after each reaction step at room temperature, according to the procedure described in *Chapter 2.*

Table 6: *CuO sample and diluent features used to study sequential reduction-oxidation cycles with bed dilution.*

Parameter	Symbol	Unit of measure	Values
Sample mass	m_s	[mg]	201
Sample particle size range	d_p	[µm]	<45
Diluent type	-	-	SiC
Diluent mass	m_d	[mg]	206
Diluent particle size range	d_p	[µm]	<45
Dilution ratio (SiC:CuO)	SiC dilution	[-]	1:1 w/w
Bed height	H_{bed}	[mm]	6
Bed volume	V_{bed}	[cm^3]	0.302

Table 7: *Characteristics of each experimental step in the investigation of sequential reduction-oxidation cycles with bed dilution ($\dot{V}_{tot}$ = total volumetric flowrate, y_R = reagent concentration, β = heating rate, T_{fin} = final temperature, t_s=isotherm time).*

	Inert [-]	Reagent [-]	$\dot{V}_{tot}$ [Ncm^3/min]	y_R [%]	β [°C/min]	T_{fin} [°C]	t_s [min]
Pre-treatment (inert)	Ar	-	100	-	5	200	30
Pre-treatment (oxidative)	Ar	O_2	100	10	5	250	60
TPR (x4)	Ar	H_2	100	10	2.5	500	0
TPO (x4)	Ar	O_2	100	10	2.5	500	0

The results for the four TPR cycles are presented in Figure 6 and Table 8.

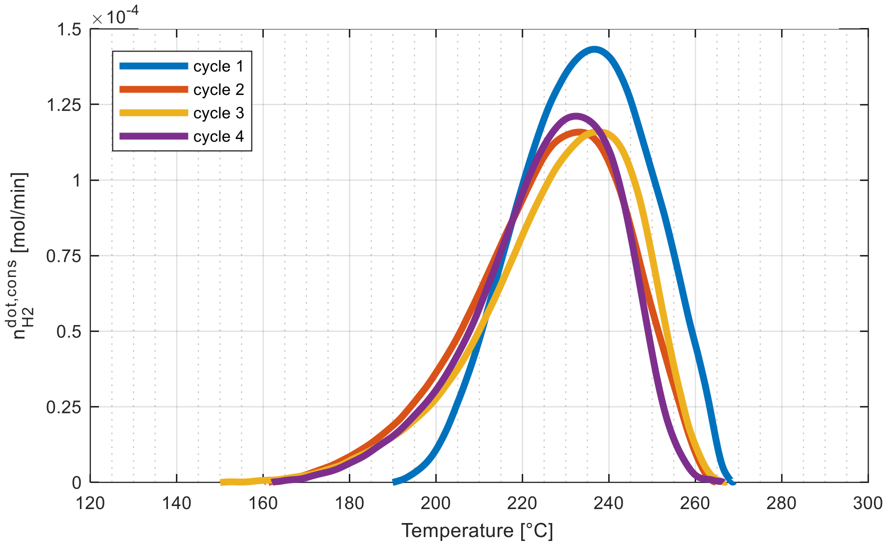

***Figure 6**: H_2 consumption in 4 sequential CuO reductions with SiC dilution (1:1 w/w). Conditions as in Table 6 and Table 7.*

***Table 8**: Relevant calculated parameters for sequential TPR.*

TPR number [-]	T_{act} [°C]	$T_{peak,1}$ [°C]	Secondary peak(s)	T_s [°C]	Peak range [°C]	$\%^{cons}_{O,CuO}$ [%]
1	193	236	-	-	78	89.9
2	155	238	-	-	111	81.3
3	155	240	-	-	111	78.4
4	174	234	-	-	84	76.4

As Figure 6 shows, every reduction produces a single peak, whose temperature remains almost the same during the four cycles (i.e., 237 ± 3 °C). The first peak distinguishes itself from the others for its slightly higher initial reaction temperature, higher reaction rate and increased degree of reduction, the latter of which is higher than all the others obtained in the first TPRs using 200 mg of sample. This effect could be related to the high thermal conductivity of SiC used in these tests, suggesting that heat conduction in the bed plays a significant role in the process, and that the formation of temperature gradients in the bed could be the real cause for the secondary peaks. The following three cycles shows almost superimposable profiles and almost equal degrees of reduction. Moreover, since left-skewed profiles are obtained for cycle 2, 3 and 4, it is suggested that the same phenomena considered in Chapter 2 (*Effect of non-reactive flow)* for the second reduction cycle occur; namely, the generation of structural defects, that decrease the activation temperature, and the decrease of specific surface area, which lowers the reaction rate.

The corresponding four TPO profiles are shown in Figure 7, while the characteristic values for the profiles of each TPO are reported in Table 9.

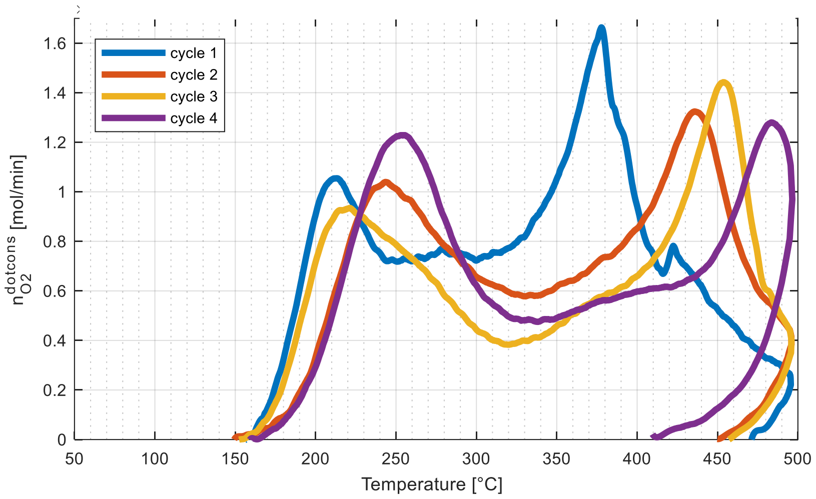

***Figure** 7: O_2 consumption in 4 sequential Cu oxidation, with SiC dilution (1:1 w/w). Conditions as in Table 6 and Table 7.*

***Table 9**: Relevant calculated parameters for sequential TPO.*

TPO number [-]	T_{act} [°C]	$T_{peak,1}$ [°C]	$T_{peak,2}$ [°C]	$\%^{reg}_{O,CuO}$ [%]
1	159	210	377	85.4
2	150	243	436	78.6
3	152	221	455	73.8
4	158	253	483	78.3

All of the TPO curves exhibit a double-peak shape (i.e., a mechanism consisting of two steps), which have a better resolution than the ones obtained in Chapter 3 (*Effect of non-reactive flow* and *Pre-treatment variation)* without dilution, and do not show any additional peak.

The results also indicate that the second peaks always shift towards higher temperatures as the cycle number increases, resembling the results obtained in section *Sequential reduction-oxidation cycles with bed dilution*. Conversely, the first peak does not follow this trend, as in cycle 3 its initial onset at a lower temperature is evident, and its initial reaction rate is higher, indicating that the final SiC and CuO distribution achieved at the end of the reduction step is not reproducible.

Overall, it could be observed that adding SiC to the bed favors the resolution of the oxidation peaks. Considering the high exothermicity of the oxidation process and the good results obtained with SiC addition, it can be concluded that thermal effects developed during the TPOs have a large impact on the test's results. The sequential degrees of reduction and oxidation, finally, suggest that in the first three cycles both the reductions and the oxidations are not complete, since the quantity of consumed reagent is smaller than the one in each previous reaction. This trend is not followed during the fourth cycle, as its degree of reduction is higher than the third degree of oxidation, and it is further surpassed by the fourth oxidation degree. Being these differences small, however, they could be associated with experimental limits in the quantification.

Variation of bed porosity in sequential reduction-oxidation cycles with bed dilution

In the last test, using SiC as bed diluent, the pressure drop variation as a function of pure argon flowrate at ambient temperature has been measured after every thermal cycle; from the measured $\Delta P_{bed}(\dot{V})$ an estimation of the variation of bed porosity has been obtained, following the method described in Chapter 3.

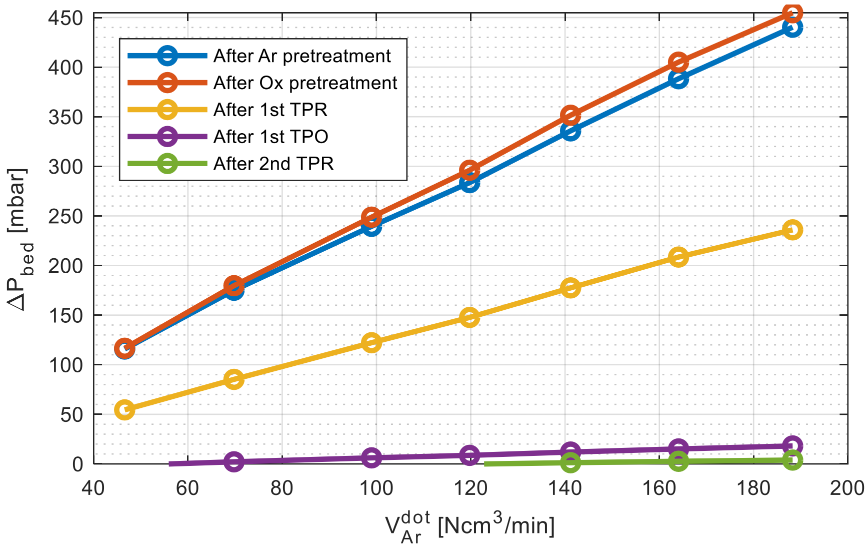

Figure 8: *Pressure drop variation across the diluted bed at room temperature, after each reaction step.*

The results, Figure 8, indicate that the bed agglomerated considerably both during the first TPR and during the first TPO, as two major drops of hydraulic resistance are found when these two cycles are involved.

This effect is also proved by the pressure drop measured during the reactive cycles, Figure 9. during the first TPR, indeed, a pressure drop decrease is detected in correspondence of the peak, and at the end of the first TPO a dramatic fall is registered, notwithstanding an increasing temperature (naturally magnifying the hydraulic resistances). This suggests that the agglomeration continued as the two processes were carried out, and that towards the end of the TPO remarkable by-passes were created in the bed.

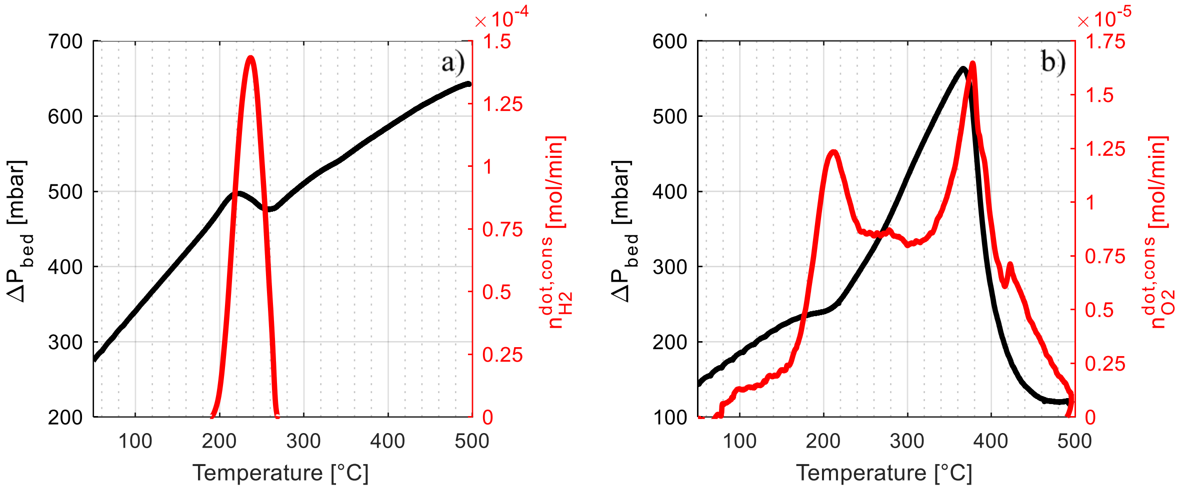

***Figure 9**: Pressure drop variation in the diluted bed compared to the reagent consumption rate during* (a) *TPR-1 and* (b) *TPO-1,*

It is then concluded that the bed dilution with silicon carbide helps to level out temperature gradients inside the bed in the case of TPOs as well but does not prevent the almost complete agglomeration of the catalytic bed, even if this process is delayed to the end of the first TPO. This is further confirmed by the final aspect of the bed, Figure 11, as compared to the initial one, Figure 10. The bed after the 4 cycles became a compact cylinder, Figure 11.a. Its axial shrinkage is smaller than 1 mm but still noticeable, as shown in Figure 11.b. Moreover, the external by-passes created during the oxidation are visible, Figure 11.c, similarly to what happened with the diluted bed samples in the Chapter 2. As the figures show, the agglomeration was quite pronounced, but the decrease in bed volume was not as pronounced as in the test without bed dilution, Figure 4.

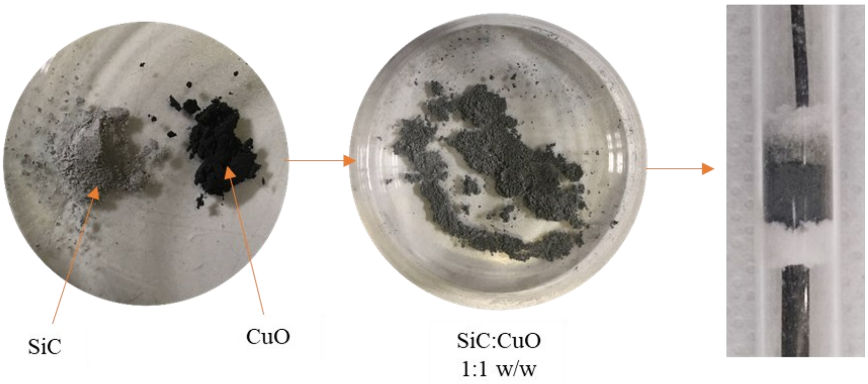

***Figure 10**: Appearance of the components before mixing and after mixing, and in the reactor before the reaction cycles.*

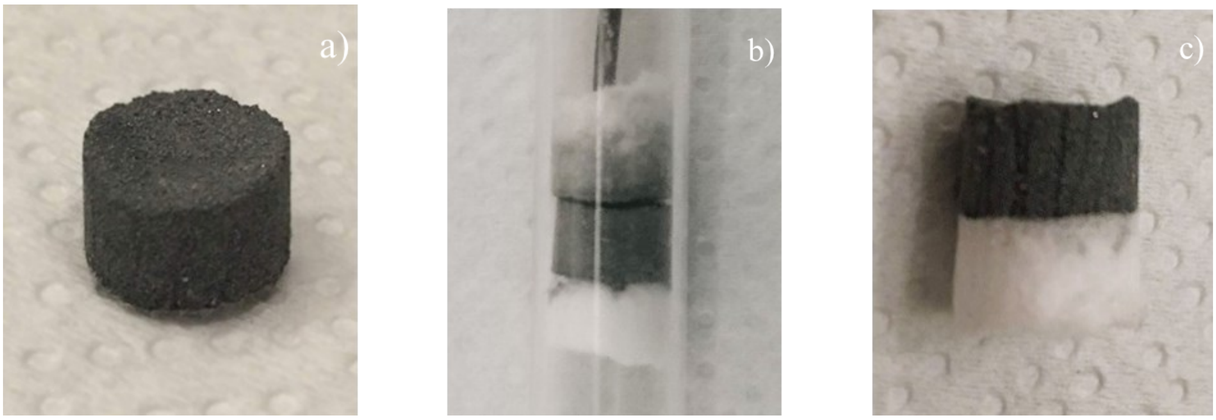

***Figure 11**: Appearance of the diluted bed after the TPO-4:*
(a) *final shape,* (b) *axial shrinkage and* (c) *lateral by-pass channels.*

Conclusions

The long-term reactivity was studied with 11 sequential TPR-TPO experiments and a progressive loss in activity was visible from the degree of reduction/oxidation, decreasing from 100% in the 1st cycle to 15% in the 11th cycle, and peak shape analysis. Particularly, the Cu oxidation mechanism is made of two steps (Cu → Cu_2O → CuO) in standard condition, but as the number of cycles increased, the second peak was shifting to higher temperatures until it disappeared completely in the 5th oxidation cycle. This behavior was attributed to the restructuration of the reactive bed at macro and microscopical level, limiting the complete oxidation to CuO in successive cycles. At the end of the 11 cycles, the sample appeared as a packed cylinder showing visible agglomeration and the formation of a compact surface layer on the underlying particles was showed with SEM analyses. Furthermore, EDS measurements demonstrated that Cu and O atoms had a 1.91:1 ratio in the underneath layers, suggesting Cu_2O to be the prevailing oxide.

Finally, the appearance of multiple peaks was tentatively correlated with an uneven temperature distribution in the reactive bed. Additional sequential TPR-TPO cycles using 1:1 Sic: sample were extremely effective in leveling out temperature gradients inside the bed. Sequential TPRs become much more reproducible, with a single peak. Also, TPO clearly show 2 oxidation steps well reproducible. Still, agglomeration was measured, now mostly concentrate in the second oxidations step, at higher temperature. The role of temperature distribution in the bed emerges as a key factor for reproducible reductio/oxidation cycles, deserving further studies.

Nomenclature

c_p = Specific heat capacity

d_p = Particle diameter

ΔP_{bed} = Pressure drop of the bed

H_{bed} = Bed height

m_s = Sample mass

m_d = Diluent mass

$n_{H2.CuO}^{dot,cons}$ = H_2 molar flowrate consumed

$n_{O2.CuO}^{dot,cons}$ = O_2 molar flowrate consumed

$n_{O,CuO}^{cons}$ = Total sample oxygen consumed

$n_{O.CuO}^{reg}$ = Total oxygen regained by the sample

T Temperature

T_{meas} Temperature measured

T_{act} = Activation temperature

T_{fin} = Final temperature

T_m = Melting temperature

$T_{peak,x}$ = Temperature of the peak number *x*

$T_{peak,1}$ = Temperature of the first peak

$T_{peak,2}$ = Temperature of the second peak

T_s = Temperature of the shoulder

T_{shift} = Temperature difference between T_{peak} in n^{th} and n^{th-1} cycle

t_s = Soak time

V_{bed} = Bed volume

V_t = Volume tubing

$\dot{V}$ = Volumetric flowrate

$\dot{V}_{tot}$ = Total volumetric flowrate

y_R = Reducing gas volumetric percentage

$\%_{O,CuO}^{cons}$ = Degree of reduction

$\%_{O,CuO}^{reg}$ = Degree of oxidation

Greek letters:

β = Heating rate

λ = Thermal conductivity

Acronyms:

EDS = Energy Dispersive X-ray Spectrometry

SEM = Scanning electron microscope

TCD = Thermal conductivity detector
TPO = Temperature programmed oxidation
TPR = Temperature programmed reduction

References

[1] K.C. Taylor, Automobile Catalytic Converters, Springer, Berlin, Heidelberg, 1984.

[2] M.K. Jha, J.C. Lee, M.S. Kim, J. Jeong, B.S. Kim, V. Kumar, Hydrometallurgical recovery/recycling of platinum by the leaching of spent catalysts: A review, Hydrometallurgy. 133 (2013) 23–32. https://doi.org/10.1016/j.hydromet.2012.11.012.

[3] K. Fujiwara, K. Okuyama, S.E. Pratsinis, Metal-support interactions in catalysts for environmental remediation, Environmental Science: Nano. 4 (2017) 2076–2092. https://doi.org/10.1039/c7en00678k.

[4] R.J. (Ruud J.) Wijngaarden, A. Kronberg, K.R. Westerterp, Industrial catalysis : optimizing catalysts and processes, Wiley-VCH, 1998.

[5] K. Fujiwara, S.E. Pratsinis, Single Pd atoms on TiO2 dominate photocatalytic NOx removal, Applied Catalysis B: Environmental. 226 (2018) 127–134. https://doi.org/10.1016/j.apcatb.2017.12.042.

[6] Study on the EU's list of Critical Raw Materials (2020) Final Report, n.d. https://doi.org/10.2873/904613.

[7] D. Bhattacharya, S. Kole, O. Kizilkaya, J. Strzalka, P.P. Angelopoulou, G. Sakellariou, D. Cao, C.G. Arges, Electrolysis on a Chip with Tunable Thin Film Nanostructured PGM Electrocatalysts Generated from Self-Assembled Block Copolymer Templates, Small. 17 (2021). https://doi.org/10.1002/smll.202100437.

[8] L. Du, V. Prabhakaran, X. Xie, S. Park, Y. Wang, Y. Shao, Low-PGM and PGM-Free Catalysts for Proton Exchange Membrane Fuel Cells: Stability Challenges and Material Solutions, Advanced Materials. 33 (2021). https://doi.org/10.1002/adma.201908232.

[9] A.E. Hughes, N. Haque, S.A. Northey, S. Giddey, Platinum group metals: A review of resources, production and usage with a focus on catalysts, Resources. 10 (2021). https://doi.org/10.3390/resources10090093.

[10] Price charts - Johnson Matthey, (2021). http://www.platinum.matthey.com/prices/price-charts#.

[11] K. Everaert, J. Baeyens, Catalytic combustion of volatile organic compounds, Journal of Hazardous Materials. 109 (2004) 113–139. https://doi.org/10.1016/j.jhazmat.2004.03.019.

[12] H. Asakura, M. Kirihara, K. Fujita, S. Hosokawa, S. Kikkawa, K. Teramura, T. Tanaka, Fe-Modified CuNi Alloy Catalyst as a Nonprecious Metal Catalyst for Three-Way Catalysis, Industrial and Engineering Chemistry Research. 59 (2020) 19907–19917. https://doi.org/10.1021/acs.iecr.0c03389.

[13] B. Imelik, J.C. Védrine, Catalyst characterization : physical techniques for solid materials, New York: Plenum Press, 1994.

[14] R. Richards, Z. Ma, F. Zaera, Surface and Nanomolecular Catalysis, Ryan Richards, Taylor an Francis (CRC Press), 2006.

[15] A. Jones, B.D. McNicol, Temperature-programmed reduction for solid materials characterization, M. Dekker, 1986.

[16] J.A. Schwarz, Temperature-Programmed Desorption and Reaction: Applications to Supported Catalysts, Catalysis Reviews. 25 (1983) 141–227. https://doi.org/10.1080/01614948308079666.

[17] C. Pirola, F. Galli, G.S. Patience, Experimental methods in chemical engineering: Temperature programmed reduction—TPR, Canadian Journal of Chemical Engineering. 96 (2018) 2317–2320. https://doi.org/10.1002/cjce.23317.

[18] D.A.M. Monti, A. Baiker, Temperature-Programmed Reduction. Parametric Sensitivity and Estimation of Kinetic Parameters, 1983.

[19] S.J. Gentry, N.W. Hurst, A. Jones, Temperature Programmed Reduction of Copper Ions in Zeolites, Journal of the Chemical Society, Faraday Transactions 1: Physical Chemistry in Condensed Phases. 75 (1978) 1688–1699.

[20] N.W. Hurst, S.J. Gentry, A. Jones, Temperature Programmed Reduction, Catalysis Reviews. 24 (1982) 233–309. https://doi.org/10.1080/03602458208079654.

[21] P. Malet, A. Caballero, The Selection of Experimental Conditions in Temperature-programmed Reduction Experiments, J. Chem. SOC., Faraday Trans. I. 84 (1988) 2369–2375.

[22] G. Fierro, M. lo Jacono, M. Inversi, P. Porta, R. Lavecchia, F. Cioci, A study of Anomalous Temperature-Porgrammed Reduction Profiles of Cu2O, CuO, and CuO-ZnO Catalysts, Journal of Catalysis. 148 (1994) 709–721.

[23] A. Pineau, N. Kanari, I. Gaballah, Kinetics of reduction of iron oxides by H2. Part I: Low temperature reduction of hematite, Thermochimica Acta. 447 (2006) 89–100. https://doi.org/10.1016/j.tca.2005.10.004.

[24] N. Wakao, J.M. Smith, Diffusion in catalyst pellets, Chemical Engineering Science. 17 (1962) 825–834.

[25] L. Zou, J. Li, D. Zakharov, E.A. Stach, G. Zhou, In situ atomic-scale imaging of the metal/oxide interfacial transformation, Nature Communications. 8 (2017). https://doi.org/10.1038/s41467-017-00371-4.

[26] J. Adanez, A. Abad, F. Garcia-Labiano, P. Gayan, L.F. de Diego, Progress in chemical-looping combustion and reforming technologies, Progress in Energy and Combustion Science. 38 (2012) 215–282. https://doi.org/10.1016/j.pecs.2011.09.001.

[27] H. Zhao, J. Gui, J. Cao, C. Zheng, Molecular Dynamics Simulation of the Microscopic Sintering Process of CuO Nanograins Inside an Oxygen Carrier Particle, Journal of Physical Chemistry C. 122 (2018) 25595–25605. https://doi.org/10.1021/acs.jpcc.8b04253.

[28] P. Gayán, C.R. Forero, A. Abad, L.F. de Diego, F. García-Labiano, J. Adánez, Effect of support on the behavior of Cu-based oxygen carriers during long-term CLC operation at temperatures above 1073 K, Energy and Fuels. 25 (2011) 1316–1326. https://doi.org/10.1021/ef101583w.

[29] L.F. de Diego, P. Gayán, F. García-Labiano, J. Celaya, A. Abad, J. Adánez, Impregnated CuO/Al2O3 oxygen carriers for chemical-looping combustion: Avoiding fluidized bed agglomeration, Energy and Fuels. 19 (2005) 1850–1856. https://doi.org/10.1021/ef050052f.

[30] F. Biccari, Intrinsic and Extrinsic Defect Characterization of Copper(I) Oxide Semiconductor", 2008.

[31] D.W. Green, R.H. Perry, Perry's Chemical Engineers' Handbook, 8th Edition, McGraw-Hill, 2008.

[32] J.Y. Kim, J.A. Rodriguez, J.C. Hanson, A.I. Frenkel, P.L. Lee, Reduction of CuO and Cu2O with H2: H embedding and kinetic effects in the formation of suboxides, Journal of the American Chemical Society. 125 (2003) 10684–10692. https://doi.org/10.1021/ja0301673.

[33] J.-Y. Lee, S.M. Lee, Hydrogen trapping phenomena in metals with B.C.C. and F.C.C. crystal structures by the desorption thermal analysis technique, Surface and Coatings Technology. 28 (1986) 301–314.

[34] J.A. Rodriguez, J.C. Hanson, A.I. Frenkel, J.Y. Kim, M. Pérez, Experimental and theoretical studies on the reaction of H2 with NiO: Role of O vacancies and mechanism for oxide reduction, Journal of the American Chemical Society. 124 (2002) 346–354. https://doi.org/10.1021/ja0121080.

[35] G. (Gerhard) Ertl, Handbook of heterogeneous catalysis, Wiley-VCH, 2008.

[36] J.G. Chen, D.A. Fisher, J.H. Hardenbergh, R.B. Hall, A fluorescence-yield near-edge spectroscopy (FYNES) investigation of the reaction kinetics of NiO/Ni(100) with hydrogen, Surface Science. 279 (1992) 13–22.

[37] A. Biasin, J. Fabro, N. Michelon, A. Glisenti, P. Canu, Investigation of thermal effects on heterogeneous exothermic reactions and their impact on kinetics studies, Chemical Engineering Journal. 377 (2019). https://doi.org/10.1016/j.cej.2018.10.116.

[38] H. Bosch, B.J. Kip, J.G. van Ommen, P.J. Gellings, Factors Influencing the Temperature-programmed Reduction Profiles of Vanadium Pentoxide, 1984.

[39] P. Arnoldy, J.C.M. de Jonge, J.A. Moulijn, Temperature-programmed reduction of MoO3 and MoO2, Journal of Physical Chemistry. 89 (1985) 4517–4526. https://doi.org/10.1021/j100267a021.

[40] O.J. Wimmers, P. Arnoldy, J.A. Moulijn, Determination of the Reduction Mechanism by Temperature-Programmed Reduction: Application to Small Fe203 Particles, 1986. https://pubs.acs.org/sharingguidelines.

[41] V. Stuchlý, Parametric sensitivity of complex temperature-programmed desorption, reaction and reduction, Journal of Thermal Analysis. 35 (1989) 837–847.

[42] F. García-Labiano, L.F. de Diego, J. Adánez, A. Abad, P. Gayán, Temperature variations in the oxygen carrier particles during their reduction and oxidation in a chemical-looping combustion system, Chemical Engineering Science. 60 (2005) 851–862. https://doi.org/10.1016/j.ces.2004.09.049.

[43] J.G. Chen, NEXAFS investigations of transition metal oxides, nitrides, carbides, sulfides and other interstitial compounds, Surface Science Reports. 30 (1997) 1–152.

[44] M. Fernández-García, XANES analysis of catalytic systems under reaction conditions, Catalysis Reviews - Science and Engineering. 44 (2002) 59–121. https://doi.org/10.1081/CR-120001459.

[45] A. Pintar, J. Batista, S. Hočevar, TPR, TPO, and TPD examinations of Cu0.15Ce0.85O 2-y mixed oxides prepared by co-precipitation, by the sol-gel peroxide route, and by citric acid-assisted synthesis, Journal of Colloid and Interface Science. 285 (2005) 218–231. https://doi.org/10.1016/j.jcis.2004.11.049.

[46] M.D. Argyle, C.H. Bartholomew, Heterogeneous catalyst deactivation and regeneration: A review, Catalysts. 5 (2015) 145–269. https://doi.org/10.3390/catal5010145.

[47] Q. Imtiaz, A. Armutlulu, F. Donat, M.A. Naeem, C.R. Müller, Preventing Agglomeration of CuO-Based Oxygen Carriers for Chemical Looping Applications, ACS Sustainable Chemistry and Engineering. 9 (2021) 5972–5980. https://doi.org/10.1021/acssuschemeng.1c00560.

[48] C. Moreno-Castilla, A. López-Peinado, J. Rivera_Utrilla, lnmaculada Fernández-Morales, F.J. López-Garzón, The striking behaviour of copper catalysing the gasification reaction of coal chars in dry air, Fuel. 66 (1987).

[49] C. Zheng, J. Cao, Y. Zhang, H. Zhao, Insight into the Oxidation Mechanism of a Cu-Based Oxygen Carrier (Cu → Cu2O → CuO) in Chemical Looping Combustion, Energy and Fuels. 34 (2020) 8718–8725. https://doi.org/10.1021/acs.energyfuels.0c00941.

Chapter 5

Investigation of the axial temperature distribution on CuO reduction with H_2

Abstract

The presence of multiple peaks in the reduction profiles (one-step mechanism) is another evidence of a non-uniform reaction progress and a crucial role could be ascribed to an uneven temperature distribution together with physical phenomena. However, axial temperature measurements showed that the additional reduction peaks are not cause by thermal effects in the reactive bed but uniquely to the sample agglomeration, increasing diffusive-type limitations.

Introduction

The interaction between gas species and active sites on the solid surface is one of the crucial features to characterize and investigate the reactivity towards specific reaction categories, such as reductions and oxidations. Temperature-programmed experiments belongs to the thermo-analytical techniques that provide quantitative information on the redox properties of metal oxides and metals as a function of temperature [1–3], the influence of primary phenomena such as metal-support interaction, pre-treatment impact, role of promoters and influence of more components on the reducibility of a specific phase. Also, calculation of kinetic parameters and reaction rate are performed, indicating the ease of oxygen removal and thus the strength of metal-oxygen bond [1]. The information obtained through these analyses are numerous, but the results can significantly vary depending on the physical and chemical characteristics of the system along with the experimental parameters selected, affecting multiple aspects of reduction profiles [4–8] (Chapter 1). Specifically, reduction profile shape and maximum reduction temperature are both affected by peculiar features of the reactive system (chemical and physical properties, such as mass-transfer limitations and particle agglomeration) and distinctive factors of the experimental technique (fluidynamic and heat distribution).

The focus of this study was to demonstrate the connection between non-uniform temperature distribution in the bed and the presence of multiple peaks in the reduction profile of a one-step mechanism, i.e. one single peak should be displayed.

Materials and methods

Experiments for investigating the thermal effects of CuO (Alfa Aesar, 99.995%) reduction-oxidation cycles along the axial reactor coordinate were carried out in an Inconel tube (ID 12 mm) with a 1/8" multipoint thermocouple with 10 measurement points with a 5 mm gap from each other (Figure 1). Pure gases (H_2, O_2, Ar) connected to mass-flowmeters (Brooks and Bronkhorst High-Tech) were fed with the desired composition. Before entering the reactor, the gas feed went through an automatic four-way valve (VICI Valco) to optimize the reaction protocol, ensure the total separation between the reducing and oxidizing atmosphere in CuO experiments. The valve switch between the two positions and mass-flowmeters operation were controlled though purpose-built MATLAB executable programs. The reactor was then introduced into an electrically heated furnace (Watlow) and the temperature-protocols were set on the thermoregulator (Omron) with CX-Thermo software and a purpose-built MATLAB executable program. The controlling thermocouple was identified as T10. A pressure transmitter (MPX coupled with a PicoLog data logger) with a range of 0-500 mbar was also added before the reactor inlet to continuously measure the pressure drop along the reactor, as an indication of macro-agglomeration phenomena during the reaction. Before the analysis section, a homemade silica-gel and zeolite traps were added to remove the water produced during the reducing cycles. The measurement of H_2 and O_2 consumption was performed with a thermal conductivity detector (TCD) and O_2 chemical sensor (Alphasense O2-C2) respectively. The TCD (from Agilent 6890 HP) was optimized to have a high analysis frequency (1 Hz) as the reactor outlet was directly conveyed into the detector without any previous separation with packed columns. Using this strategy, a fast and sensitive identification of transient effects during the reaction was possible and the same measurement frequency was obtained in the oxidation stage with an oxygen sensor. The same experimental protocol was kept for all the tests (inert pre-treatment to desorb water and/or contaminants at 200°C for 30 min with Ar, isothermal oxidative pre-treatment at 250°C achieved at 5°C/min, 5%O_2/Ar with 50 Ncm^3/min) H_2 reduction and O_2 oxidation with ramping temperature at fixed heating rate) and repeated in the case of long-term performance experiments. The selection of an inert bed dilutant was based on its thermal conductivity to investigate the thermal effects associated to both reactions and thus silicon carbide (SiC) was chosen.

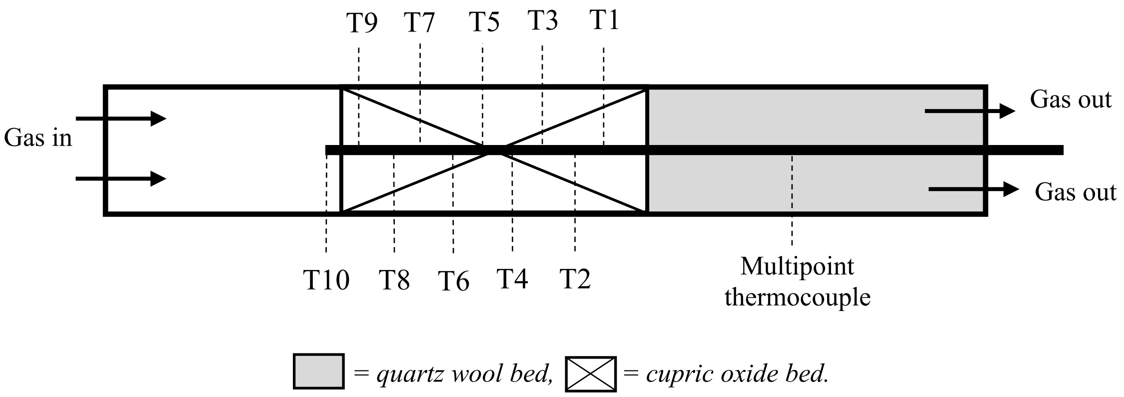

Figure 1: Scheme of the second setup reactor.

Table 1: Thermal properties of CuO, Cu_2O, Cu and SiC (cp=specific heat capacity, λ=thermal conductivity, T_m=melting temperature).

Material	**cp** [J/Kg/K]	**λ** [W/m/K]	**T_m** [°C]
CuO	705	6	1326
Cu_2O	489	4.5	1235
Cu	460	350	1085
SiC	675	490	2730

Results and Discussion

Since previous results (Chapter 3 and 4) indicate a crucial role of temperature distribution in the bed, a larger bed has been considered, and its axial temperature profile during the thermal cycles has been registered, using a multipoint thermocouple. This experiment has been conducted both with a diluted and with a pure CuO one bed.

Bed dilution with SiC

This experiment aims at investigating whether an axial temperature profile arises as TPR and TPO reactions are carried out. The CuO bed has been diluted with a mass of silicon carbide 20 times larger than the CuO one (20:1 w/w), in order to verify whether the particles could still agglomerate in the process even if, theoretically, they were kept isolated from each other through an unreactive inert. The silicon carbide particles have been sieved to a size similar to the CuO ones for a consistent fluid flow in the bed. The CuO bed features are reported in Table 2.

***Table 2:** CuO sample and diluent features used to measure axial temperature gradients with bed dilution.*

Parameter	Symbol	Unit of measure	Values
Sample mass	m_s	[mg]	472
Sample particle size range	d_p	[µm]	100-200
Diluent type	-	-	SiC
Diluent mass	m_d	[mg]	9478
Dilution ratio (SiC:CuO)	SiC dilution	[-]	20:1 w/w
Diluent particle size range	d_p	[µm]	100-200
Bed height	H_{bed}	[mm]	59
Bed volume	V_{bed}	[cm^3]	6.67

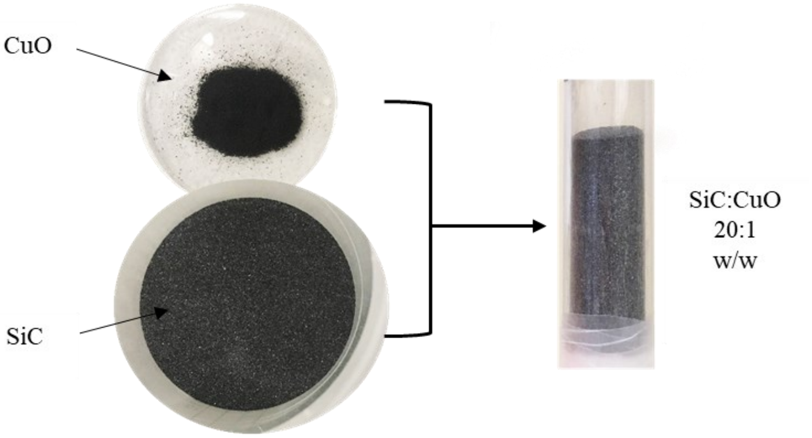

***Figure 2**: Bed components before mixing and after mixing.*

The appearance of the bed after mixing the two components is shown in Figure 2. No visible segregation appears, suggesting an adequate mixing of the two phases. Taking as a reference the reactor scheme of Figure 1, the monitoring thermocouple used in this test was the one denominated T9, while T10 remained outside of the bed, and the bed covered all of the monitored points up to T1. This test included a sample pre-treatment, consisting of one thermal cycle in inert gas and one thermal cycle using an oxidizing mixture, followed by two TPR-TPO cycles, whose parameters are reported in Table 3.

Table 3: *Characteristics of each experimental step in the investigation of axial temperature gradients with SiC bed dilution ($\dot{V}_{tot}$ = total volumetric flowrate, y_R = reagent concentration, β = heating rate, T_{fin} = final temperature, t_s=isotherm time).*

	Cycle [-]	**Inert [-]**	**Reagent [-]**	**$\dot{V}_{tot}$ [Ncm^3/min]**	**y_R [%]**	**β [°C/min]**	**T_{fin} [°C]**	**t_s [min]**
Pre-treatment (inert)	1	Ar	-	250	-	5	200	30
Pre-treatment (oxidative)	2	Ar	O_2	250	10	5	250	60
TPR-1	3	Ar	H_2	250	1	2	500	0
TPO-1	4	Ar	O_2	250	10	2	500	180
TPR-2	5	Ar	H_2	250	10	2	500	0
TPO-2	6	Ar	O_2	250	10	2	500	30

All of the cycles have been carried out using a reagent concentration of 10%, except from the first TPR in which a lower reagent concentration has been used (specifically 1% H_2) to study the effect of a slower reaction on the axial temperature profile.

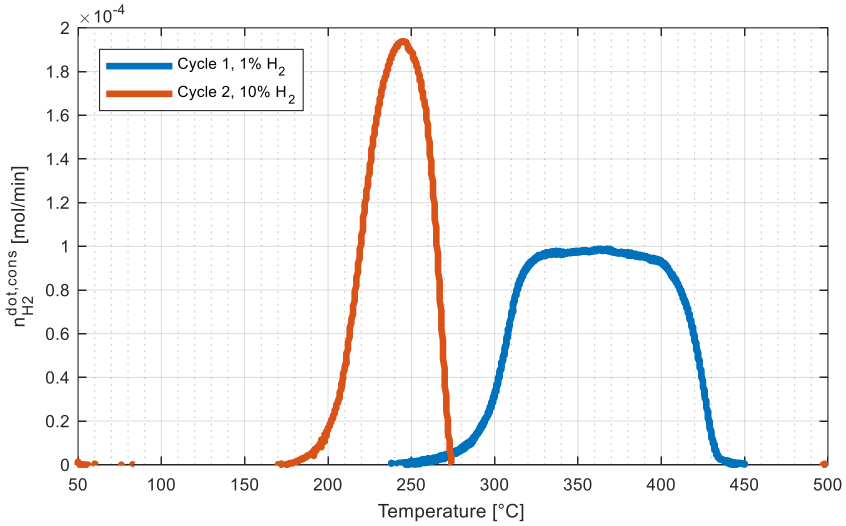

Figure 3*: Hydrogen consumption profiles for TPR-1 and TPR-2, with 20:1 w/w SiC dilution. Conditions as in Table 2 and Table 3*

Table 4*: Relevant calculated parameters for TPR-1 and TPR-2.*

TPR number [-]	**P [K]**	**T_{act} [°C]**	**$T_{peak,1}$ [°C]**	**Secondary peak(s)**	**T_s [°C]**	**Peak range [°C]**	**$\%^{cons}_{O,CuO}$ [%]**
1	115.1	193	361	-	-	210	97.3
2	11.5	177	246	-	-	97	81.4

The results of the two TPR cycles are shown in Figure 3 and Table 4. Even with a high amount of CuO to be reduced, and the P parameter for TPR-1 lying outside of the suggested range (*P*< 20 K [7]) a single peak forms in both cases. As already observed in Chapter 1, with a low hydrogen concentration the peak is broader; this happens because almost all of the reagent being fed is consumed from T = 323°C to T = 400°C; in other words, reduction is starving for H_2. Note that the limitation on the reaction rate due to H_2, in a test at constant heating rate, erroneously reports some activity at a higher temperature (broadening the peak, when temperature is used as an abscissa). Still, the sample have reduced almost completely even (97.3%) with a high bed dilution and with a low reagent concentration, meaning that the reagent was able to reach almost all of the particles and their cores, and no agglomeration took place. On the other hand, TPR-2 run showed a narrower peak centered at a lower temperature and with a significantly lower degree of reduction, 81,4%, indicating a fairly incomplete process.

Thanks to the high dilution with SiC and the low reagent concentration, 1%, the axial temperature profile at peak conditions for TPR-1 run results in quite uniform axial temperature, Figure 4.a, notwithstanding the higher temperature reached. This is reasonable, since the reaction is slow and the reaction heat is evenly distributed thanks to the high thermal conductivity of silicon carbide.

Similar, flat axial temperature profiles are obtained for TPR-2, Figure 4.b, which confirms the capacity of silicon carbide for levelling out temperature gradients inside the sample, even with a faster reaction rate (i.e. a larger rate of heat release from the reaction).

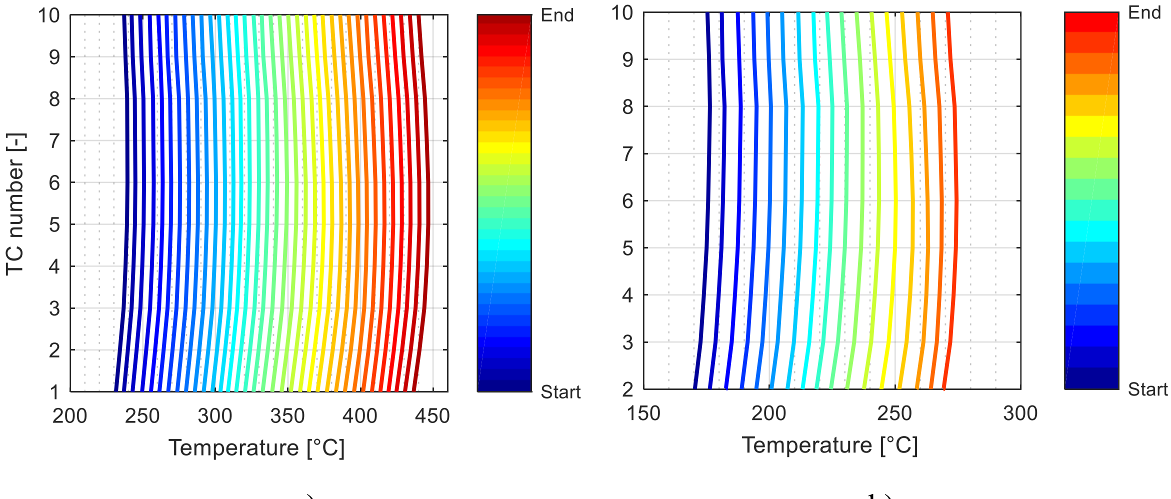

a) b)

Figure 4*: Axial temperature profiles at near peak conditions during the heating ramp (step size: 3 min) with SiC dilution (20:1 w/w)*
(a) TPR-1 (b) TPR-2.

The results of the two TPOs carried out after each TPR are shown in Figure 5 and Table 5.

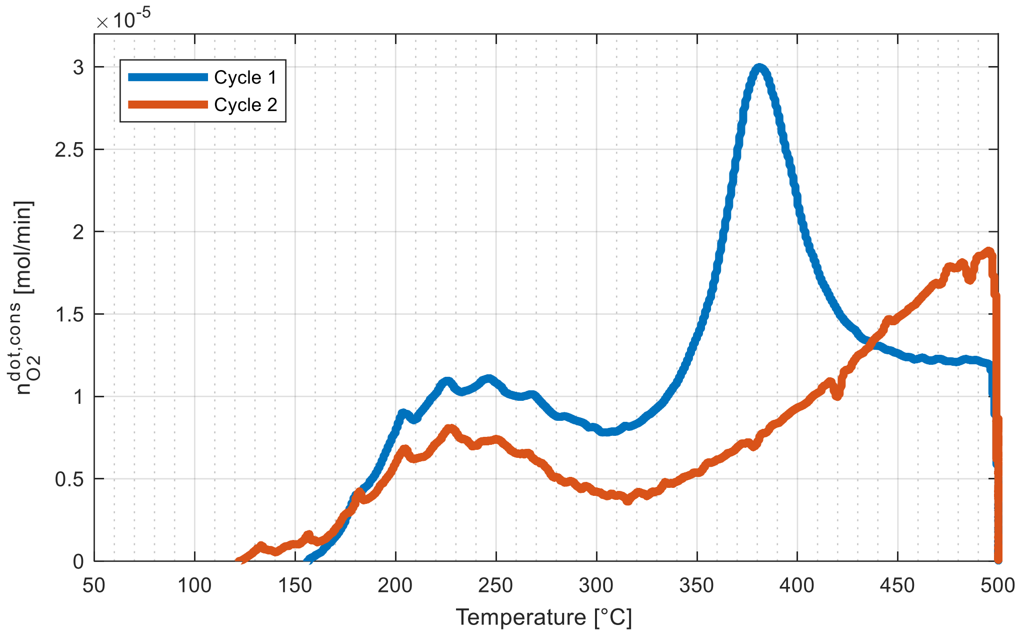

Figure 5: *Oxygen consumption profiles for TPO-1 and TPO-2, with 20:1 w/w SiC dilution. Conditions as in Table 2 and Table 3*

Table 5: *Relevant calculated parameters for TPO-1 and TPO-2.*

TPO number [-]	**T_{act} [°C]**	**$T_{peak,1}$ [°C]**	**$T_{peak,2}$ [°C]**	**$\%_{O,CuO}^{reg}$ [%]**
1	159	230	381	81.2
2	118	232	500	65.0

Both TPOs exhibit two peaks, as already reported in the preceding Chapters. In both cases the first one is distorted and noisy, because of the small temperature oscillations in the furnace, but the temperature of its maximum activity is almost coinciding (230 vs 232°C). The second peak, however, shifts towards higher temperatures in the second cycle, as already observed (Chapter 4). Contrary to the results of Chapter 4, (*Sequential reduction-oxidation cycles with bed dilution)*, it seems like a high bed dilution (i.e., 20:1) with silicon carbide does not prevent the shift of the second peak towards temperatures higher than 500°C in TPO-2. Even though in the first run the sample remained in the oxidant mixture at 500°C for three hours after the heat ramp, advancing the oxidation, the final degree of oxidation is lower than the expected one (i.e., -16.1% with respect to the results of the previous TPR), and the second oxidation's efficiency is further diminished. Both these facts suggest that a high bed dilution hinders the complete oxidation of the sample, possibly because of preferential passages created in the bed, whose height and dilution are high, which may limit the availability of certain portions of the bed to the oxidizing mixture. On the other hand, the complete oxidation of the bed could have also been hindered by the slight agglomeration of the sample which occurred during TPR-1.

As with the previous TPRs, the temperature profiles acquired during the oxidation are compared in Figure 6. Small thermal gradients in the axial direction are detected in either case. At the highest temperature, a difference of less than 1°C is measured between center and edges of the bed, in both cases.

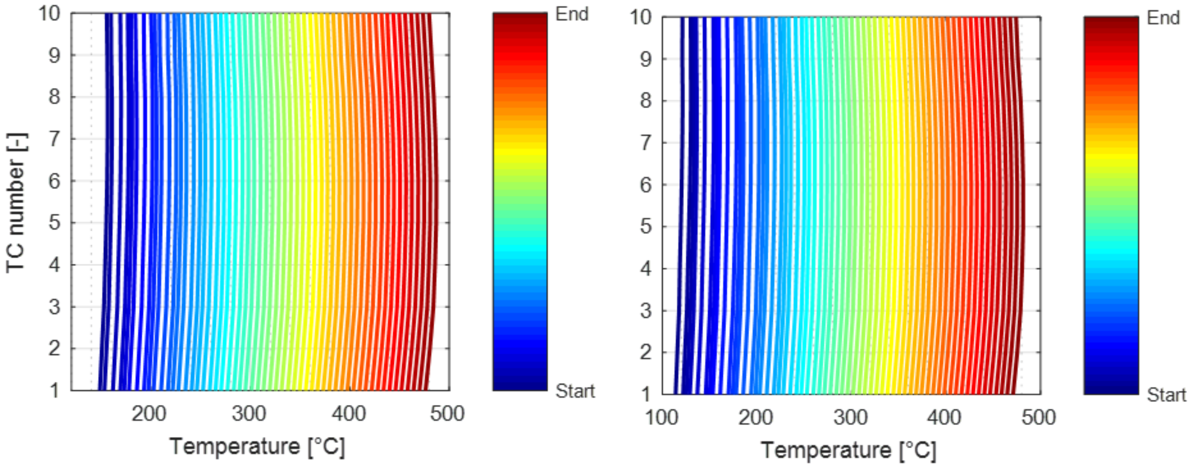

a) b)

Figure 6*: Axial temperature profiles at near peak conditions during heating (step size: 3 min) with SiC dilution (20:1 w/w)*
(a) TPO-1 (b) TPO-2

The four reactive cycles performed on the diluted sample have not caused any visible agglomeration of the bed, which was extracted from the reactor in powdery form, Figure 7. It is therefore concluded that a high bed dilution with thermally conductive inert prevents the agglomeration of the bed, at least on the macroscale, and allows to level out temperature gradient inside the bed.

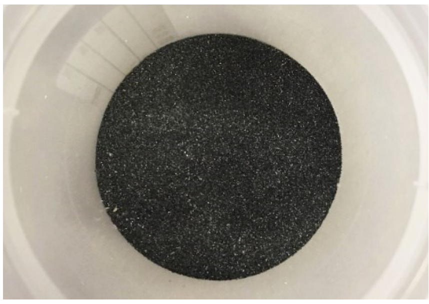

Figure *7: Appearance of the diluted bed after the two TPR-TPO cycles.*

Pure CuO bed

Since a high bed dilution did not identify significant variations of the sample temperature as the peak developed, a bed of pure CuO has been analyzed, using the setup described in *Materials and method*. The investigation aims to prove the sensitivity of the axial measurements to local temperature gradients.

A larger mass of sample has been used, producing a bed approx. 3cm long, to include six of the ten available measuring points of the thermocouple (from T7 to T2); the resulting features of the bed are reported in Table 6. The height of the quartz wool bed has been adjusted to keep the controlling T8 in the gas phase and close to the sample's upper surface. The test protocol is reported in Table 7; the sample underwent a thermal (in inert) and oxidizing pre-treatment, and two TPR-TPO cycles whose parameters are collected in Table 7.

The volumetric percentage of reagent for the TPRs, 7.5%, has been chosen to avoid its total consumption and the simultaneous reduction of multiple layers of the bed.

The same volumetric percentage was also used for O_2 in the two TPOs.

Table 6: *CuO sample used to measure axial temperature gradients with no bed dilution.*

Parameter	Symbol	Unit of measure	Values
Mass	m_s	[mg]	4750
Particle size range	d_p	[μm]	<300
Bed height	H_{bed}	[mm]	29
Bed volume	V_{bed}	[cm^3]	3.27

Table 7: *Characteristics of each experimental step in the investigation of axial temperature gradients with no bed dilution ($\dot{V}_{tot}$ = total volumetric flowrate, y_R = reagent concentration, β = heating rate, T_{fin} = final temperature, t_s=isotherm time).*

	Cycle [-]	Inert [-]	Reagent [-]	$\dot{V}_{tot}$ [Ncm^3/min]	y_R [%]	β [°C/min]	T_{fin} [°C]	t_s [min]
Pre-treatment (inert)	1	Ar	-	250	-	5	200	30
Pre-treatment (oxidative)	2	Ar	O_2	250	10	5	250	60
TPR-1	3	Ar	H_2	250	7.5	2	500	0
TPO-1	4	Ar	O_2	250	7.5	2	500	0
TPR-2	5	Ar	H_2	250	7.5	2	500	0
TPO-2	6	Ar	O_2	250	7.5	2	500	0

The two TPR profiles and their characteristic values are reported in Figure 8 and Table 8.

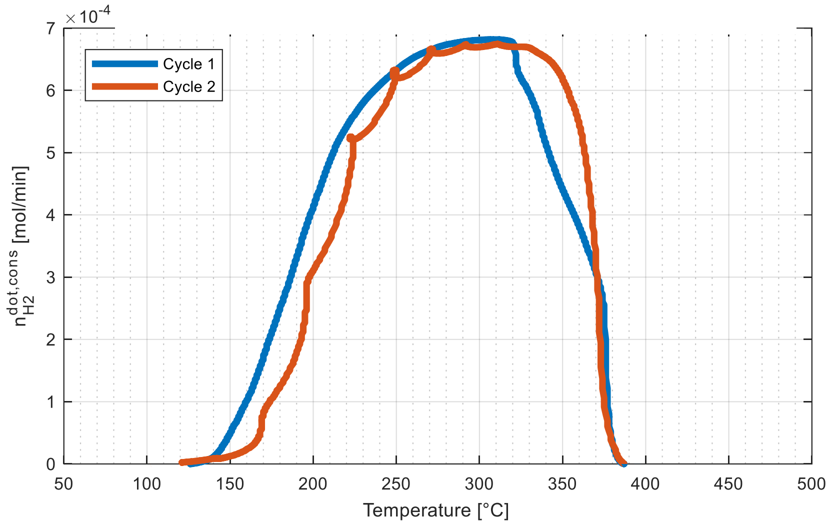

***Figure 8**: Hydrogen consumption profiles for TPR-1 and TPR-2 without SiC dilution. Conditions as in Table 6and Table 7.*

***Table 8**: Relevant calculated parameters for TPR-1 and TPR-2.*

TPR number [-]	P [K]	T_{act} [°C]	$T_{peak,1}$ [°C]	Secondary peak(s)	T_s [°C]	Peak range [°C]	$\%_{O,CuO}^{cons}$ [%]
1	153.17	125	304	-	-	261	93.5
2	153.17	105	304	-	-	281	92.1

One broad peak is obtained in each TPR cycle, even with the operating parameters which bring the *P* parameter outside of the suggested range (*P*<20K [7]) That is a consequence of a relatively small H_2 concentration in the gas. The peaks appear significantly reproducible; in both cases the maximum temperature is the same, and so is the one at which the peak ends, but in the second case the onset of the reaction appears to be at a higher temperature, and proceeds with a lower velocity, because of the combined effect of the creation of structural defects and decrease of the surface area already discussed. The second hydrogen consumption profile seems also to be affected by the slightly oscillating temperature caused by an uneven oven control, which deformed its peak. Both reductions have a high efficiency, and almost all the copper oxide had been reduced.

The axial temperature profiles are shown in Figure 9. We see already in TPR-1, Figure 9.a, a noticeable local temperature increase in the bed as the reduction progresses: the maximum of each profile moves from T7 to T2, i.e. with the gas flow, as the peaks develops without reaching T2, suggesting that the reaction front advances from the top to the bottom of the bed, along with the gas flow. Since the temperature reached by the sample is far away from the melting point of any likely species in the bed (all above 1000°C, see Table 1) throughout the entire thermal cycle, agglomeration cannot be not caused by the exothermicity of the reaction. Similar phenomena happen in TPR-2; in this case the temperature rise caused by the reduction is slightly higher than the previous one, Figure 9.b. This could be caused by the sample agglomeration and the resulting increased spacing of the bed from the control thermocouple, which would not allow the furnace to compensate fast enough for temperature increases given by the reaction. A loss of contact between thermocouples, and especially the one controlling the heating resistance, may explain the onset of oscillation in the oven temperature, that gave rise to the irregular profile of TPR-2 observed in Figure 8. Interestingly, quite remarkable axial gradients developed before the maximum temperature. Overall, the axial temperature gradient is never so large, to suggest that the presence of the double peaks in the reduction profiles could be caused by an inhomogeneous hydrogen consumption in the sample.

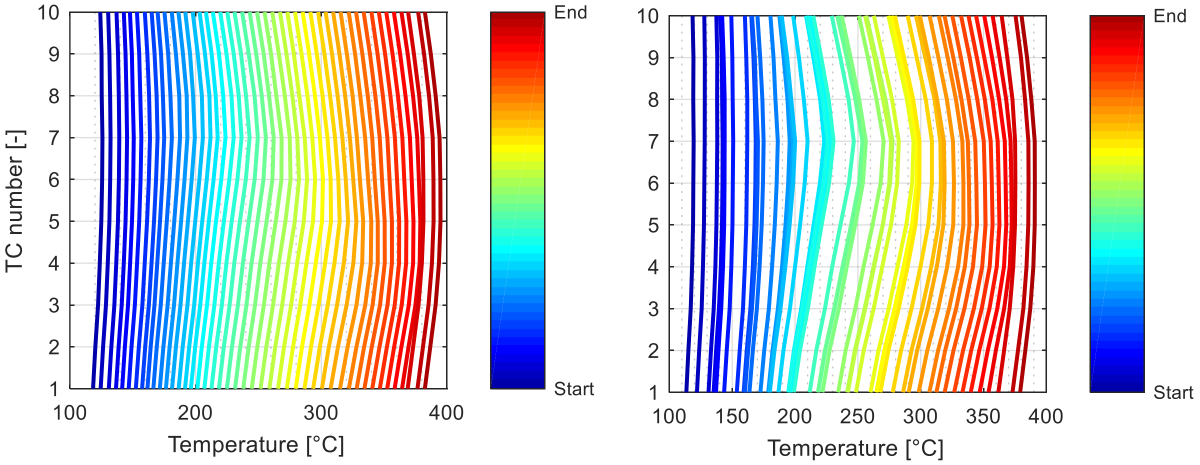

a) b)

***Figure 9**:* (a) *Axial temperature profiles in a pure CuO bed, near peak conditions (step size: 3 min)* (a) *TPR-1 and* (b) *TPR-2.*

Turning to the TPO cycles analysis, the O_2 consumption rates have been now reported as a function of time, together with the controlling temperature, Figure 10.b and Figure 11.b. The unexpected temperature oscillations already suggested above are now clear; they are associated to oscillations in the reaction rate (measured by the O_2 uptake), which is expected to be the origin of the oscillations, not the result.

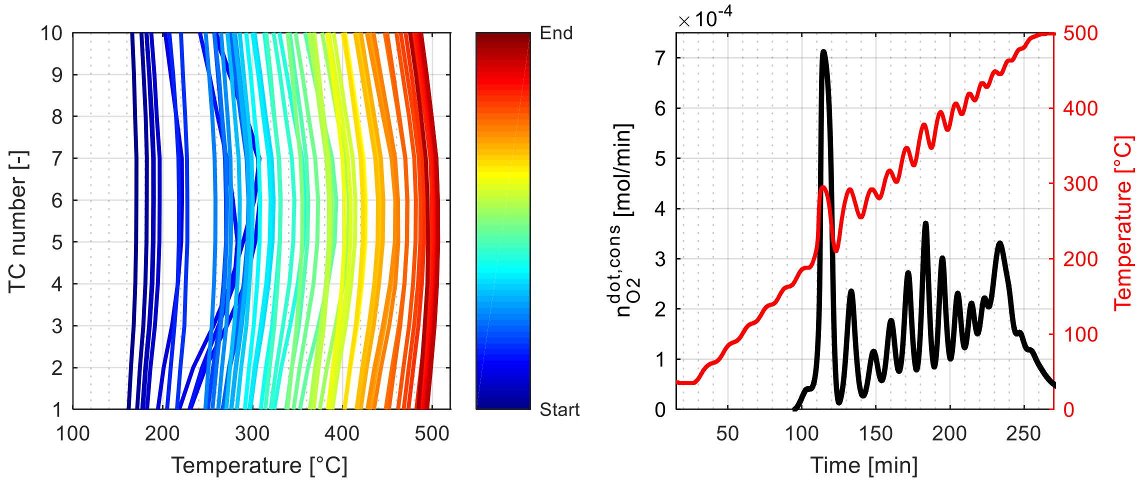

a) b)

***Figure 10**: (a) Axial temperature profile (step size: 3 min) and (b) oxygen consumption and controlling thermocouple values TPO-1.*

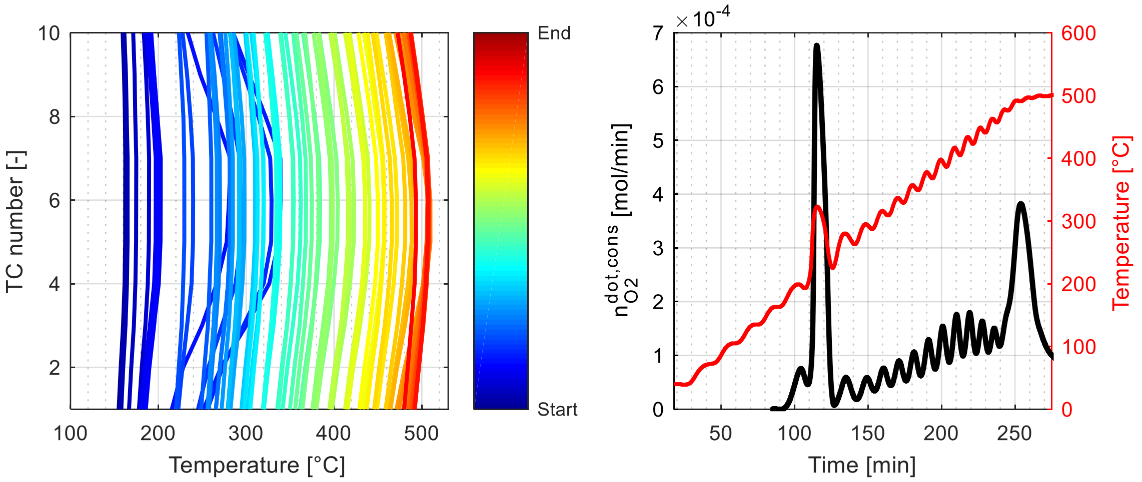

a) b)

***Figure 11**: (a) Axial temperature profile (step size: 3 min) and (b) oxygen consumption and controlling thermocouple values TPO-2.*

***Table 9**: Relevant calculated parameters for TPO-1 and TPO-2.*

TPO number [-]	T_{act} [°C]	$T_{peak,1}$ [°C]	$T_{peak,2}$ [°C]	$\%_{O,CuO}^{reg}$ [%]
1	169	293	461	97.5
2	172	322	494	85.7

The characteristic values for the profiles of the two TPO cycles are presented in Table 9; the temperatures reported correspond to the control thermocouple at the peaks. The bed oxidized almost completely in both TPOs. However, as the first peak developed (i.e., from t = 115 min in both TPOs), the energy released by the reaction was so high that the temperature in the bed increased by almost 100°C. As a consequence, the increase in the kinetic constant made the oxygen consumption accelerate dramatically, further supporting the rate of heat release. From that moment onwards, a distinctly oscillatory behavior established in both temperature and oxygen consumption, because the furnace control tries to compensate for the exothermicity of reaction but was not fast enough to do so. As said above, this was further amplified by the fact that the sample's upper surface moved away from the control point T8 due to bed shrinkage, combined with an inadequate PID controller tuning and thermal delays naturally occurring in a closed furnace. Multiple peaks in the temperature and oxygen consumption are then obtained, which are almost coinciding in time. This indicates that the two variables are correlated, but it is not straightforward to determine whether this behavior is due to the oscillation in the kinetic constant or to the superposition of an additional temperature gradient.

In both cases, especially as the first peak first develops, a heat wave travels fast to the bottom of the sample, since the temperature at the sample's bottom rapidly reaches the upper temperature values, as seen in Figure 10.a and Figure 11.a. Close to the oxidation peak, axial gradients in excess of 100°C can be noticed. This behavior could have been caused by the good thermal conductivity of the sample, which initially consisted of almost pure copper, coupled with the higher reaction enthalpy associated with the oxidation.

In any case, as the temperature of the sample throughout both TPOs never approached the melting temperature of its components, the agglomeration process could not be caused by the oxidation exothermicity either, and its root cause should be investigated in other chemical phenomena.

Confirmation that the bed agglomerated during TPR-1 are given by the monitored pressure loss, that dropped, as shown in Figure 12.

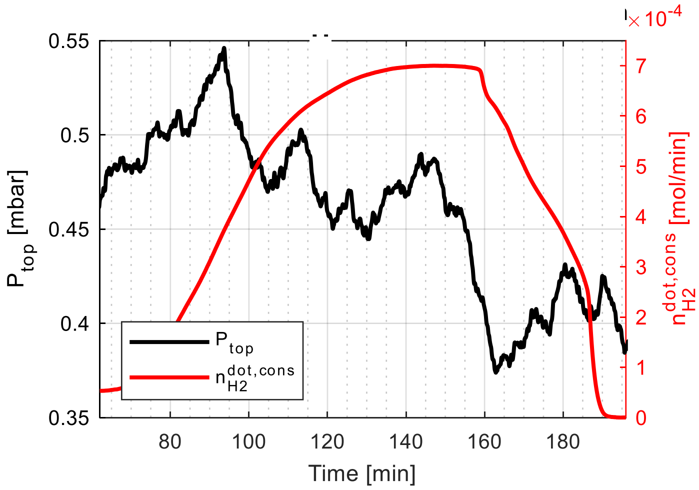

Figure 12: *Pressure at the reactor top and hydrogen consumption in TPR-1.*

This could have been detrimental in the following cycles because the bed may have axially shrunk, thus loosing contact with the controlling point, with its upper surface, and therefore making the temperature control loop less representative of the solid temperature.

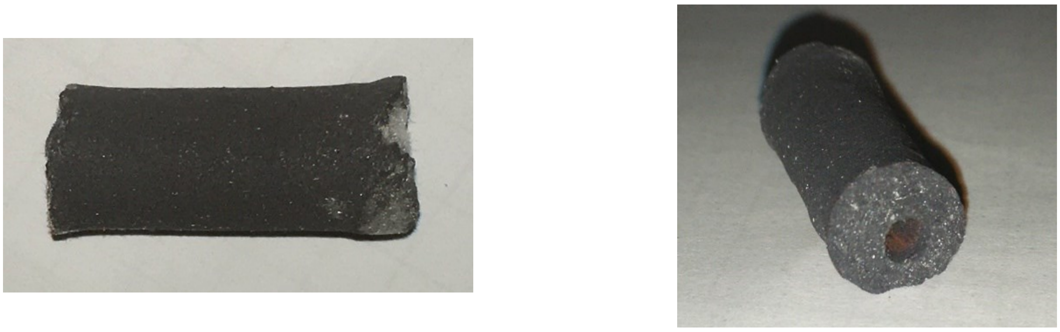
a) b)

***Figure 13**: (a) Axial view of the sample and (b) the sample seen in perspective.*

Indeed, the appearance of the bed at the end of the test, Figure 13, shows that a compact cylinder of copper oxide was produced. The agglomeration most likely happened during TPR-1, as the pressure data of that test indicates. The axial shrinkage of the sample is confirmed; it measured approx. 5 mm. The bed weight was 220 mg less than its initial value (i.e., 4.75 g), or -4.6%, Lilley because of some material lost on the internal surface of the tubular reactor during extraction. The spent oxide composition and structure is unknown, as no further analyses have been carried out, but Figure 13.b. shows evidence of some orange compounds in the hole created by the thermocouple. As copper and Cu_2O are both orangish, it could be hypothesized that in the inner part the sample did not oxidize completely, as also suggested by the last TPO's degree of oxidation.

Conclusions

Axial temperature gradients were measured during TPR and TPO experiments to correlate the appearance of multiple peaks with an uneven temperature distribution in the reactive bed.

Pure CuO and a highly diluted (20:1) beds were tested, using a good thermal conductive material (SiC) as the inert.

During the reduction, a single H_2 consumption peak and low temperature gradients are observed in both cases, suggesting that double peaks are not generated by thermal effects but from physical phenomena (agglomeration and shrinking). On the other hand, the oxidation is much more exothermic than the reduction and the oscillating temperature gradients, reflected on the O_2 consumption profiles, were attributed to the poor furnace control-loop, one the bed shrunk, loosing contact with the controlling thermocouple.

Nomenclature

c_p = Specific heat capacity
d_p = Particle diameter
H_{bed} = Bed height
m_s = Sample mass
m_d = Diluent mass
$n_{H2.CuO}^{dot,cons}$ = H_2 molar flowrate consumed
$n_{O2.CuO}^{dot,cons}$ = O_2 molar flowrate consumed
$n_{O,CuO}^{cons}$ = Total sample oxygen consumed
$n_{O.CuO}^{reg}$ = Total oxygen regained by the sample
P = Malet-Caballero characteristic number [7]
T_{act} = Activation temperature
T_{fin} = Final temperature
T_m = Melting temperature
T_{peak} = Temperature of the peak
$T_{peak,1}$ = Temperature of the first peak
$T_{peak,2}$ = Temperature of the second peak
T_s = Temperature of the shoulder
t_s = Soak time
V_{bed} = Bed volume
$\dot{V}_{tot}$ = Total volumetric flowrate
y_R = Reducing gas volumetric percentage
$\%_{O,CuO}^{cons}$ = Degree of reduction
$\%_{O,CuO}^{reg}$ = Degree of oxidation

Greek letters:

β = Heating rate
λ = Thermal conductivity

Acronyms:

TCD = Thermal conductivity detector
TPO = Temperature programmed oxidation
TPR = Temperature programmed reduction

References

[1] A. Jones, B.D. McNicol, Temperature-programmed reduction for solid materials characterization, M. Dekker, 1986.

[2] J.A. Schwarz, Temperature-Programmed Desorption and Reaction: Applications to Supported Catalysts, Catalysis Reviews. 25 (1983) 141–227. https://doi.org/10.1080/01614948308079666.

[3] C. Pirola, F. Galli, G.S. Patience, Experimental methods in chemical engineering: Temperature programmed reduction—TPR, Canadian Journal of Chemical Engineering. 96 (2018) 2317–2320. https://doi.org/10.1002/cjce.23317.

[4] D.A.M. Monti, A. Baiker, Temperature-Programmed Reduction. Parametric Sensitivity and Estimation of Kinetic Parameters, 1983.

[5] S.J. Gentry, N.W. Hurst, A. Jones, Temperature Programmed Reduction of Copper Ions in Zeolites, Journal of the Chemical Society, Faraday Transactions 1: Physical Chemistry in Condensed Phases. 75 (1978) 1688–1699.

[6] N.W. Hurst, S.J. Gentry, A. Jones, Temperature Programmed Reduction, Catalysis Reviews. 24 (1982) 233–309. https://doi.org/10.1080/03602458208079654.

[7] P. Malet, A. Caballero, The Selection of Experimental Conditions in Temperature-programmed Reduction Experiments, J. Chem. SOC., Faraday Trans. I. 84 (1988) 2369–2375.

[8] G. Fierro, M. lo Jacono, M. Inversi, P. Porta, R. Lavecchia, F. Cioci, A study of Anomalous Temperature-Porgrammed Reduction Profiles of Cu2O, CuO, and CuO-ZnO Catalysts, Journal of Catalysis. 148 (1994) 709–721.

Chapter 6

In-situ growth of CuO 1D nanostructures in cyclic reducing-oxidizing environment

Abstract

The formation of nanostructures on Cu/CuO surfaces (Cu foil and Cu/CuO powder) was investigated for applications in which the oxide acts an oxygen carrier. Specifically, thermal treatment methods with different pretreatments (acid washing, inert, oxidative at different oxygen partial pressures and reducing at different contact times) and multiple reducing-oxidizing cycles were applied to determine the final surface morphology and chemical activity. Cu-foil pre-treated with a nitric acid washing to remove impurities generates higher defects concentration, favoring nanowhiskers growth in the subsequent oxidation. Their density depends on the O_2 partial pressure and annealing temperature. The same outcome could be obtained with lower O_2 partial pressure (e.g. air), and higher temperature or vice versa. Also, applying a reducing (with H_2) pre-treatment to unsupported CuO powder favors nanowhisker formation as the rough and defective morphology is the appropriate substrate to initiate the growth, at increased contact time between the gas and solid surface (0.4s). However, the Cu/CuO reactive system shows strong agglomeration phenomena in consecutive reducing-oxidizing cycles decreasing the surface area and the beneficial effect of higher oxygen content, requiring CuO particles to be well dispersed on adequate supports.

Introduction

The removal of unburnt hydrocarbons, volatile organic compounds and CO emitted from industrial and transportation activities is carried out through catalytic total oxidation which makes the conversion to CO_2 and H_2O feasible at lower temperatures (<600°C) than the energy-intensive homogeneous reaction (>1000°C). Whereas noble metal-based catalysts (Au, Pd, Pt, Rh) have typically been chosen thanks to their well-known high activity toward oxidation reactions, the need of reducing environmental impact and cost has become essential in the development of novel catalytic systems. The widely applied strategy is the replacement of noble metals (classified also as critical raw materials [1]) by transition metals (TM, e.g. Cu, Ni, Fe, Cr, Co, Mn) to catalytically promote oxidations.

TMs and their oxides find applications to take advantage of their capability to reversibly store and release oxygen, in redox reactions. They can support oxidations, such as combustion of carbonaceous fuels [2] and selective oxidations [3–6]. The principle relies on a two-step process: the metal oxide oxidizes the feed while transforming into its reduced state; afterwards, the reduced carrier is oxidized before being returned to the first step to complete the cycle. These Chemical Looping Processes (CLP) have the significant advantage of completely avoiding the use of gaseous oxygen, thus improving the intrinsic safety of the process by minimizing the risk of forming explosive mixtures, removing the necessity of operating in oxygen-lean conditions thereafter increasing single-pass conversion, improving selectivity for partial oxidations and eliminating the purification step for oxygen and products [7]. The oxygen carrier needs to have suitable properties for this purpose and together with the typical high activity and selectivity. The material requires a high oxygen loading and mobility as well as chemical and mechanical stability under repeated redox cycles.

Among transition metals and the corresponding oxides, Cu-based species have proven to be efficient oxidation catalysts for carbon monoxide, methane, ethane, propane together with ethyl acetate, ethanol, toluene, benzene and p-xylene [8,9]. In addition, the CuO-Cu couple is largely studied as oxygen carriers in CLP, thanks to its favorable cost-availability relation and efficient oxygen transport capacity [10]. The practical application has been constrained by some intrinsic limitations, such as the agglomeration and low decomposition temperature [11,12] that decrease the reactivity along with redox cycles. The use of a suitable support (Al_2O_3 [10], SiO_2 [13]) has been studied to increase Cu dispersion and stability, however the presence of agglomerated particles and the formation of Cu/Al_2O_4 complexes together with a lower reactivity of Cu/SiO_2 compared to Ni/SiO_2 remain critical issues [14]. With the purpose of exploiting the advantages of Cu redox proprieties and decreasing the detrimental effect of agglomeration on the oxygen transport capacity, a solution could be to increase the oxygen content by means of total oxygen moles of the material to compensate for the activity loss.

Recently, the formation of shape-controlled CuO nanostructures has gain more attention in gas sensors [15], superconductors [16], li-ion batteries [17], solar energy conversion [18] as well as heterogenous catalysis [19]. The beneficial effect in increased surface area and superficial oxides content is worth the study in catalysis. Covering the surface of copper substrates with copper oxide nanostructures can be achieved with different methods depending on the desired features such as composition, length, diameter and morphology. The wet chemical methods (precursors-based [20], hydrothermal decomposition [21], solvothermal [22], self-catalytic growth [23]) are the most used synthetic route thanks to their good yields in terms of controllability, however they are carried out by mixing different chemicals (inorganic precursors) in aqueous solutions to obtain the desired characteristics and facilitate the synthesis (templates, surfactants and shaping agents). The drawbacks of this procedure are the length of synthesis times, from hours to days, the use of expensive and toxic chemicals that are encapsulated inside the product, hence a purification step of the final product from templates and shaping agents is required and low process reproducibility. On the contrary, thermal oxidation is a direct method to grow CuO nanostructures on copper samples such as thin films, foils or nanoparticles. It is performed by heating the metal sample at high temperature (>400°C) in an oxygen-rich atmosphere (often just air), pure oxygen or oxygen mixture with inert gases [24]. This method is convenient, faster and green since the use of chemicals and consequent purification steps are avoided and nanostructures characteristics are controlled by adjusting the experimental parameters such as oxygen partial pressure, temperature and annealing or contact time. In particular, the density and diameter of the nanostructures are influenced mainly by the oxygen partial pressure and temperature, while the annealing time affects the nanorods diameter [24,25]. The presence of water vapor increases the Cu oxidation rate below 700°C [26,27] and, if present, the effect is higher than the oxygen partial pressure [28].

In this work, CuO nanostructures in whisker-form were synthesized with a thermal method on Cu-foil and Cu/CuO powder, to investigate the possibility of increasing the oxygen content for CLP and surface area for catalytic applications. Specifically, the model system with unsupported CuO powder was chosen as a benchmark to generalize a procedure for producing nanowhiskers on different metal/oxide systems with milder reaction condition (using air as oxidant instead of pure oxygen) and inducing the nanowhiskers formation and growth with the real process mixtures. To do so, different pretreatments (acid washing, inert heating, oxidative at different oxygen partial pressures and reducing at different contact times) and multiple reducing-oxidizing cycles were tested to analyze the final surface morphology, coupled with H_2 and O_2 consumption data.

Materials and Methods

Two forms of copper-based materials were used: Cu foil (Sigma Aldrich, 99.98% purity, 5mm x 5mm) and CuO powder (99.99% purity, Alfa Aesar, particle size < 45 μm). The Cu foil was pre-treated to remove the impurities with deionized H_2O in which, afterwards, 5 ml of HNO_3

(Sigma Aldrich, solution at 70% in water) were added and left for 5 mins. Then, the Cu foil was washed again with deionized H_2O and sonicated in an acetone bath for 5 mins. The Cu powder was used without any pre-treatment.

Surface morphology was examined with an Environmental Scanning Electron Microscope (ESEM, Fei-Quanta 200), equipped with Back-Scattered Electron Detector (BSE). Nanostructure dimensions (length and diameter) were retrieved from ESEM images; the surface elemental analysis was obtained with Energy Dispersive Spectroscopy (EDS, EDAX, Genesis model). The initial and final powder structure was analysed with X-ray Diffraction (XRD, Panalytical X'Pert 3 Powder) with Cu-K_α radiation and 2θ scanning from 3° to 70° with 0.013° step. Results were interpreted with Panalytical High Score Plus 4 with 3 databases (PDF2, Panalytical ICSD, COD).

The thermal treatment on Cu foil was performed in a modified microbalance setup (CI-Precision), with accuracy of 0.1μg to combine thermogravimetric measures with ex-situ characterizations. The foil was placed in a quartz sample-holder, hanging to the balance head with an inert wire, in the middle of a quartz tube to control the atmosphere. The quartz pipe was positioned inside a resistively heated furnace, in which the controlling thermocouple (type J) is in the refractory material surrounding the heating elements, while the monitoring thermocouple (type K) was measured close to the sample. Air (100 Ncm^3/min) was controlled by a mass flowmeter (Brooks) and fed from the top; the balance head is under a small N_2 make-up flow (8 Ncm^3/min) to avoid its elements oxidation; N_2 eventually mixes with air reaching the sample. The temperature was raised to 500°C with a heating rate of 5°C/min and kept constant for 30 mins. The sample was then naturally cooled to RT, keeping the same air flow. A blank experiment with the same amount of an inert material (SiC) was previously performed, to eliminate the interferences on the weight measurement caused by the drag on the wire and sample-holder; the following measurements were adjusted accordingly.

Reduction and oxidation reactions on CuO powders were carried out with a fixed bed, in a quartz tubular reactor (ID=6 mm or 8 mm) in which different amounts of oxide and inert (SiC) were loaded. The tube was inserted into a temperature programmable furnace (Watlow) controlled by a thermocouple (type K) placed right downstream the bed. Temperature was also monitored by a thermocouple (type K) placed upstream, close to the bed upper surface. The temperature protocol was the same for all the samples (from RT to 500°C at 2.5°C/min, no isothermal time and uncontrolled cooling rate); the reducing (or oxidizing) gas mixtures contained 10% H_2 (or 10% O_2) balanced with Ar; they were fed with different flowrates to examine the effect of gas contact time. Before entering the reactor, an automatic four-way valve (VICI Valco) allows to rapidly switch mixture (reducing vs. oxidizing), ensuring the total separation between them. The outlet gases in reductions were analyzed by means of a Thermal Conductivity Detector (TCD, in an Agilent GC-6890 by-passing the separation columns), sampled at 1 Hz, to quantify the H_2 consumption. Similarly, O_2 concentration was measured with an electrochemical O_2 sensor (Alphasense) during oxidations, sampled at 1 Hz. A pressure transducer (MPX5100, Honeywell) was added to the system to evaluate the pressure difference between the reactor inlet and outlet and verify the occurrence of bed agglomeration.

Results and discussion

Results will be presented starting from the Cu-foil, where earlier surface structuring and nanowires formation have been observed. Later, improved pretreatments of the samples, including CuO particles, have been implemented to enhance nanowires formation and density.

Influence of O_2 partial pressure on Cu-foil oxidation morphology

CuO on Cu foils has been generated by oxidation in a flow of air (P_{O_2}= 0.21 bar), increasing its temperature linearly, up to 500°C; the maximum temperature has been kept constant for 30 mins, as the standard procedure reported in [25]. The process has been monitored through the foil weight; its increase was recorded as function of the monitoring temperature and thus the highest value is not 500°C but 510°C (Figure 1). The resulting oxidized sample has been characterized by SEM, Figure 2, and EDS analyses on different areas and spots, Figure 3 and Table 1, to determine the local Cu/O ratio.

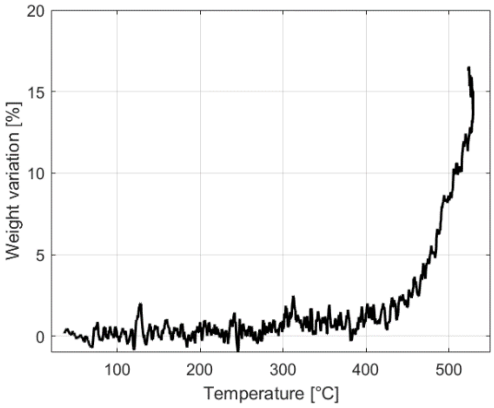

Figure 1: *Weight variation during Cu-foil oxidation with air (P_{O_2}=0.21 bar).*

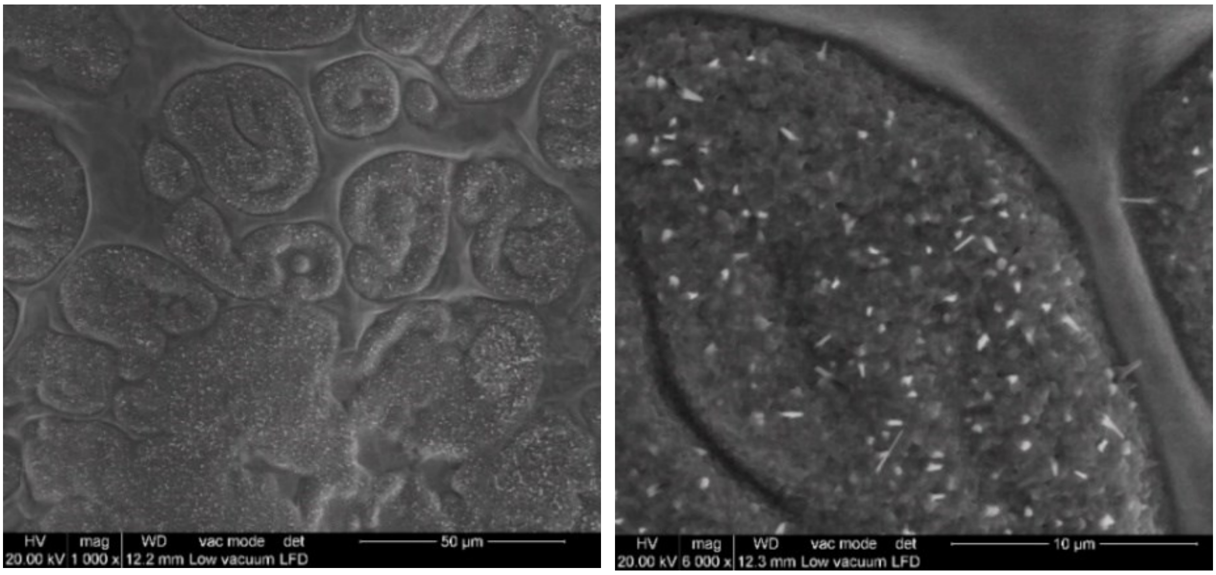

a) b)

***Figure 2**: SEM analyses of Cu-foil sample after oxidation with air: a) x1000, b) x6000.*

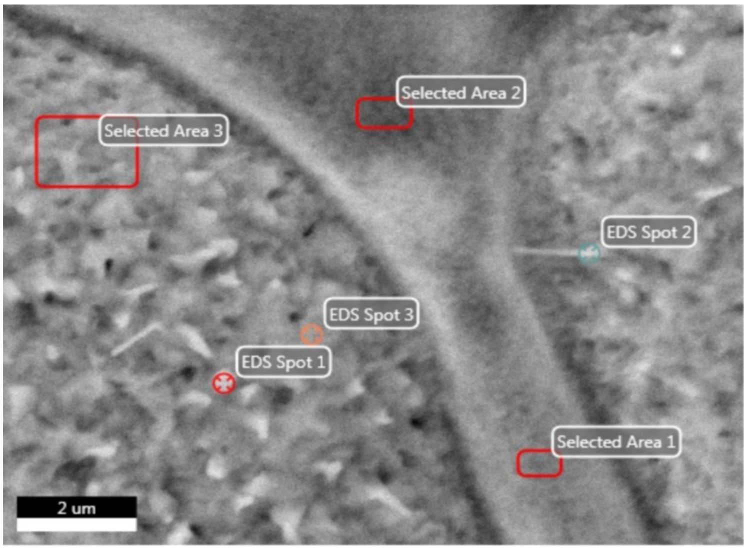

***Figure 3**: areas and spot for EDS analyses of of Cu-foil sample on a representative area after oxidation with air.*

***Table 1**: Cu and O atomic percentage and Cu/O in different areas and spots after Cu-foil oxidation with air (P_{O_2}=0.21 bar) at 500°C for 30 min measured with EDS analyses.*

		Selected Area 1	**Selected Area 2**	**Selected Area 3**	**EDS Spot 1**	**EDS Spot 2**	**EDS Spot 3**
O	Atomic %	45.20	44.27	48.49	46.20	40.05	50.21
Cu	Atomic %	54.80	55.73	51.51	53.80	59.95	49.79
Cu/O		1.21	1.26	1.06	1.16	1.49	0.99

Figure 2.a of Cu foil surface after the oxidative reaction shows different regions with peculiar features. The presence of smooth and rough areas indicates a non-uniform oxidation of the

metal surface, confirmed by EDS analysis. The causes of these peculiar oxide non-uniform oxide distribution can be attributed to the acid pre-treatment to remove impurities and the presence of different superficial oxides, prior to the reaction. The native oxide layer is unevenly etched by the nitric acid reacting on the surface [30], as the reaction is triphasic and the immediate formation of bubbles on the surface causes an uneven contact between the oxides and the acid. The non-uniform liquid-solid reaction generates different surface morphologies that influence the nanostructure yield and formation mechanism. After the oxidation process with lower oxygen partial pressure (P_{O_2}= 0.21 bar), the overall result is a completely oxidized surface, but with different local oxide composition and conformation. This result is confirmed by both thermogravimetric analysis (Figure 1) and EDS analyses (Table 1) on the same sample. The weight ratio between Cu and O in CuO and Cu_2O is 20% and 11.1% respectively; the maximum weight measured, Figure 1, totally attributed to Cu oxidation, was 16.5%$_{wt}$. The oxidation is thus incomplete, and a mixture of CuO-Cu_2O is prevailing over one single oxide. The local distribution of Cu oxides is revealed by EDS analyses (Figure 2 and Table 1). The local Cu/O atomic ratio, frequently above 1, confirms the presence of a CuO-Cu_2O mixture on the surface; the prevalence depends on the region. The average Cu/O ratio in the smooth region (Selected Area 1 and 2 in Figure 3) is significantly > 1 (CuO), suggesting a significant share of Cu_2O, while in the rough region (Selected Area 3) CuO is predominant (Cu/O ≈1). However, punctual EDS analyses in the rough region show the presence of nanostructures dramatically different in Cu/O ratio. The effect of acid pre-treatment and oxidation efficiency can be determined combining the information on surface morphology and composition after the oxidation. The regions in which the acid etches the surface, cleaning from impurities and native oxides, favors the formation of surface defects since the formation of nanowires through defects is promoted [31,32]. The initial stage of these nanostructures is visible in Figure 2.b as the small white filaments growing from the surface in the rough regions. These areas mainly consist of CuO, meaning that the Cu complete oxidation is achieved in the surface layer (Selected Area 3 and EDS Spot 3) on the top of Cu_2O, while the Cu/O ratio increases as the nanowire is formed from the base to the tip (EDS Spot 1 and EDS Spot 2). The areas in which the nitric acid had un uneven contact with the surface are not completely oxidized to CuO. The nanowire composition is represented by EDS Spot 2 in which the Cu/O atomic ratio approaches 1.5, suggesting Cu is still prevalent and a mixed CuO-Cu_2O phase is present.

The heating protocol adopted in Cu foil oxidation is the same as in Literature [24,25], where higher O_2 partial pressures is frequently used (pure O_2, 4.76 times higher than O_2 in air, as we used); that may affect the nanowires morphological features. The sample thermally annealed with a flow of pure O_2 using the same heating protocol, [25] shows a higher nanowire density and length. However, increasing the annealing temperature above 600°C, [25] has the same lower yield of nanowires observed at lower O_2 partial pressure. This effect can be explained by Ehrlich-Schwoebel (ES) barrier concept, that explains surface roughening of metal surfaces [33,34]. Rough regions shown in Figure 3 are constituted by protrusions of the surface with a triangular pyramid shape, and their number is directly proportional to the oxide islands formed during the initial oxidation steps to CuO in the surface portions efficiently etched by the acid pre-treatment [35]. In view of this surface configuration, lower temperatures (< 600°C) favor the formation of small oxide islands while increasing the temperatures (≥ 600°C) the density decreases as their size increases due to a lower ES barrier, i.e. the diffusion resistance to cross a terrace/step is lower as the energy barrier decreases with temperature. This feature justifies the lower nanorods density obtained at higher temperature [24] similar effect could be expected with reduced O_2 partial pressure; in this condition, the driving force for O_2 to diffuse inside and along island edges is lower and thus the growth of existing oxide islands is preferred. Therefore, the oxidant partial pressure affects the nanowires formation and morphological features such that using a pure oxidant (O_2) efficiently increases 12 times nanowires growth rate [25]. Considering the formation mechanism previously disclosed, higher O_2 partial pressures increase nanorods density at lower annealing time and the same uniform distribution can be obtained by decreasing O_2 partial pressure, i.e. using air, but extending the annealing time at the maximum temperature [29]. Furthermore, in high O_2 partial pressure condition, the only morphological feature affect by increased annealing time is nanowires length, and density and diameter and not affected [25].

Nanowhiskers growth on particles with prereduction

Most studies on CuO nanostructures are mainly focused on the identification and optimization of synthesis to generate shape and dimension-controlled structures, with improved morphological features, such as length, diameter, distribution, orientation and number density [24,25,36]. However, the practical implementation of the nanostructured material produced in gas-solid catalytic applications is limited and not widely diffused [19]. The model H_2-reduction and O_2-oxidation heating cycle, from RT to 500°C, at 5°C/min, and 30 min at the maximum temperature, was tested on CuO bulk powder to confirm the possibility that a prereduction step favors oxide nanowires growth during the oxidation step. A comparison between nanowires density was carried out, with and without the reducing step, and at different gas contact time, by means of SEM image analysis and H_2 consumption analyses. Considering that any difference in surface morphology will be attributed to a variable contact and reaction between the reducing gas and the CuO surface, space velocities will be mentioned as low contact time τ_{low}=0.14 s (high space velocity) and τ_{high}= 0.4 s (low space velocity).

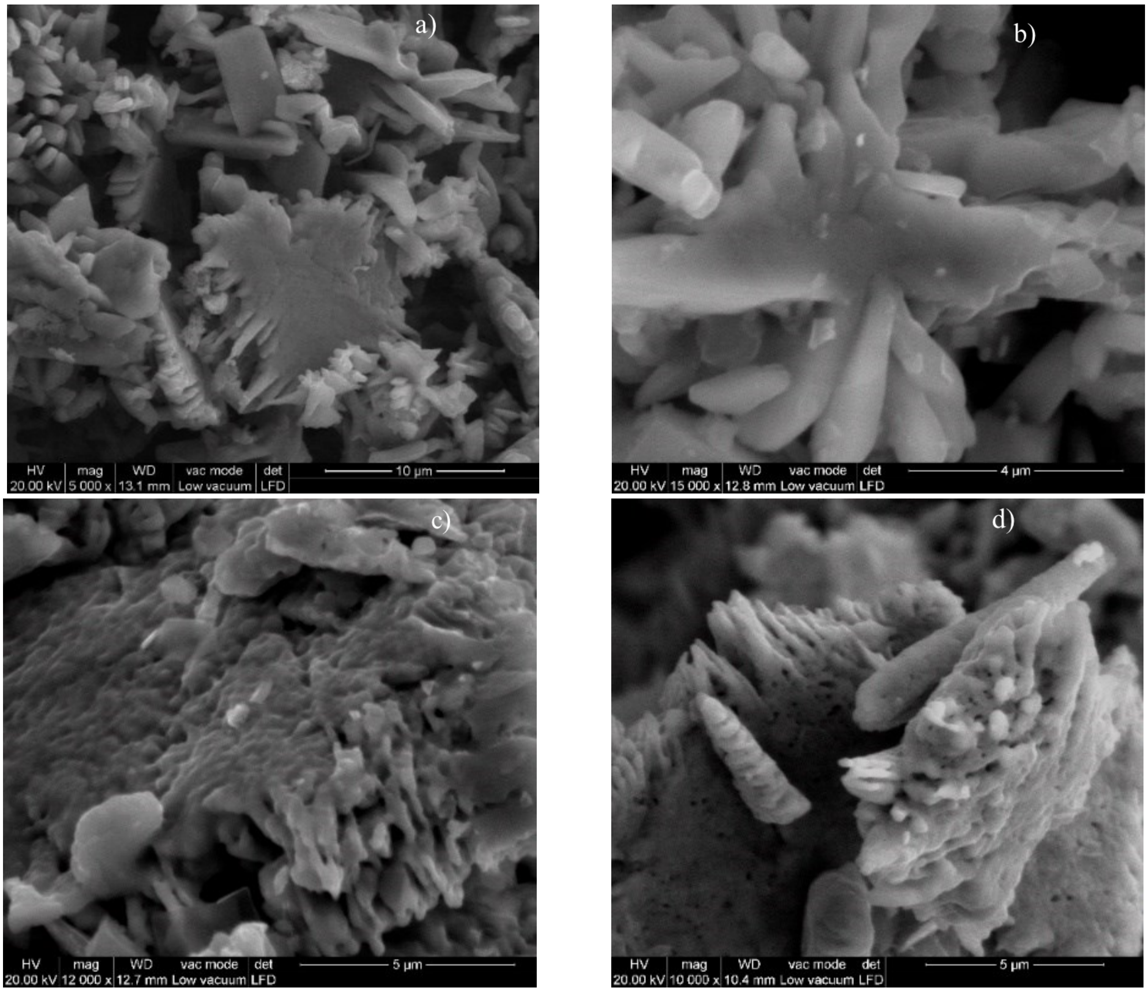

***Figure 4**: SEM figures of unsupported CuO powder: a) fresh, b) after oxidation with 10%O_2, c) after reduction at τ_{high} with 10%H_2,, d) after reduction at τ_{low} with 10%H_2.*

Comparing the fresh sample, Figure 4.a, with the sample after the oxidation without any preliminary reducing step, Figure 4.b, we can observe a similar surface morphology, with negligible particle porosity and surface roughness. The addition of a reducing treatment Figure 4.c and Figure 4.d, modifies the morphology, increasing the roughness, as an effect of particle coalescence achieved by the removal of atomic oxygen with H_2 from the original CuO sample and agglomeration (details are reported in Chapter 3). Comparing the two samples exposed to the H_2 flow, additional discrepancies can be observed, between Figure 4.c and Figure 4.d.

Increasing the contact time (τ_{high}) between the reducing gas and the solid, the surface roughness increases, suggesting a superficial microstructure rearrangement. The lower contact time (τ_{low}) generates superficial cavities, with an average radius of 150 nm that are removed at τ_{high}, indicating a less uniform distribution of copper grains.

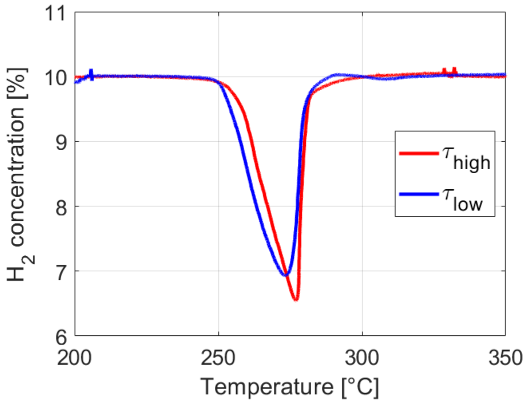

Figure 5: *H_2 consumption profiles for CuO powder at different contact times (τ_{low} = 0.14s, τ_{high} = 0.4s).* m_s = 50 mg, d_p < 45 μm y_{H_2} = 10%, β = 5°C/min.

Table 2: *Relevant calculated parameters from Figure 5, for CuO reduction at different contact times (τ_{low} = 0.14s, τ_{high} = 0.4s). O_{CuO}= total atomic oxygen from CuO consumed, $\%O_{CuO}$ = percentage of atomic oxygen from CuO consumed with respect to the initial amount.*

	τ_{high}	τ_{low}
O_{CuO} consumed	0.932 mmol	0.873 mmol
$\%O_{CuO}$ consumed	74.1%	71.2%
Peak temperature	277°C	273°C

The H_2 consumption curves, Figure 5, and quantifications, Table 2, at different contact time shows an alternative perspective on the results speculated through SEM image analysis. The reduction efficiency ($\%_{O,CuO}^{cons}$, is measured by the ratio between the atomic oxygen consumed (from H_2 consumption) and the atomic oxygen initially available in the CuO sample. The reduction efficiency is comparable for both cases, of short and long gas contact time, since the difference is <3%; however, the O available is not completely consumed. In a previous study (in Chapter 2), we reported that high H_2 inlet flow rates support the flux from the gas phase to the solid surface, and the reduction rate increases. At this stage, CuO is converted into Cu nuclei on the surface and when the relative Cu amount is > 50%, the nuclei start to create a non-porous shell, developing residual oxide. The poorly permeable shell limits the inward H_2 diffusion, and consequently further oxide reduction to metallic Cu. In addition, H_2O outward diffusion, as reaction product, is further limited as the reduction progresses due to the Cu shell lower porosity that enhances the Knudsen diffusion component to the effective diffusion. More precisely, at the maximum reduction rate observed from Figure 5, (T~ 275°C), with 0.1 as theoretical particle porosity and particle dimension of 100 μm, the difference between H_2 and H_2O effective diffusion coefficients is one order of magnitude (1.19E-07 m^2/s and 3.97E-08 m^2/s, respectively). Thus, this mechanism is limiting at increased molecular weight of the species and then it affects H_2O more than H_2. EDS analyses (Table 2) of both samples prove that the surface is almost completely converted to Cu (no O is detected on the τ_{high} sample while 1.59% of O is present on the surface τ_{low}) , while the oxygen consumption data (O_{CuO}) reveals that the reduction is far to be complete in the whole sample volume. Additionally, the maximum reduction temperature for τ_{low} is 4 °C lower compared to τ_{high}. This minor variation can result from the combination of different experimental conditions: τ_{high} test was carried out halving the gas flowrate (50 Ncm^3/min) with the same sample mass (explained in Chapter 2), and a slightly different thermocouple position, after reloading the bed in the reactor. Increasing the flowrate and the presence of a bed dilution shift the reduction peak at lower temperature (Chapter 2) as H_2 concentration gradient between the gas and surface is higher and the heat generated from the reaction together is dispersed with a delayed bed agglomeration, respectively. In these experiments, the combination of higher flowrate and no bed dilution (τ_{low}) has a stronger influence on the reaction rate, i.e. maximum reduction temperature, than combining a lower flowrate with the bed dilution (τ_{high}).

The general conclusion of CuO particles prereduction with H_2, before their oxidation requires combining H_2 consumption with surface analysis: the H_2 treatment on CuO powder using high reductant inlet concentration speeds up the overall conversion to Cu and simultaneously decreases the global reduction efficiency, since the superficial Cu shell is limiting the diffusion of gas species into the oxide particles. The different contact time ($\tau_{high} = 2.85 \cdot \tau_{low}$) is not influencing the global reaction outcome (O_{CuO} consumption) while the surface morphology is strongly affected by this experimental parameter: a less uniform distribution of copper grains generates hollows on the surface at τ_{high} while decreasing the contact time at τ_{low} produces a rougher surface with a uniform grain distribution.

The purpose of H_2 pre-treatment is promoting the surface morphology that is most favorable for nanowhiskers growth. Different mechanisms are proposed for the spontaneous nanowhiskers formation such as vapor-solid (VS) or vapor-liquid-solid (VLS) model [37], short-circuit diffusion [38] and stress-driven mechanism [39]. The VS and VLS models are widely used to describe this process, however few objections can be raised: the oxidation occurs at temperatures much lower than the melting points of Cu and the oxides, thus the equilibrium vapor pressures are so small that these mechanisms appear unlikely to take place. On the other hand, the accumulation and relaxation of compressive stress is considered the representative mechanism for nanowires growth, in which the driving force is the high compressive stress at the oxides interface generated from the difference in molar volume between metal and oxides. First, the mechanism includes the formation of macro-thick oxide layers (Cu_2O and CuO) and the interface between the two oxides generates the compressive strain that promotes the outward diffusion of Cu cations through the grain-boundaries [40] and this is the rate-determining step in intermediate temperatures (<500°C) [41], due to the p-type semiconductive nature of Cu-oxides and Cu. However, the nanowires growth is initiating directly from the CuO surface rather than the grain-boundaries that act as transport preferential pathway for Cu cation diffusion. All things considered, the effect of H_2 pre-treatment should modify the morphological structure to a more advantageous configuration to reduce the effect of the rate-limiting step and, i.e. increase the overall nanowhiskers growth. In view of the reaction mechanism and the controlling phenomena occurring, the higher density of oxide grains leads to an increased number of substrates to initiate and advance the growth mechanism and promote the Cu cation diffusion along the grain-boundaries. Increasing the contact time between the H_2-gas phase and CuO results in a rougher surface with a uniform distribution of grains and without superficial hollows, Figure 4.c, thus the advantageous morphological configuration described beforehand. On the other hand, both at τ_{low} (Figure 4.d) and without any reducing pre-treatment (Figure 4.b) the surface appears smoother, and the initial sites for nanowhiskers formation are reduced.

NW growth in cyclic reduction/oxidation

Given the enhancement in nanowhiskers formation obtained after a prereduction of the samples, here we investigate the further improvements achievable with reiterated reduction/oxidation cycles. A redox cycle is considered as both reduction and the consecutive oxidation. The evolution of nanowires formation in sequential redox cycles is crucial when the application is based on the fluctuation between reducing and oxidizing. Each reduction and oxidation step were carried out in a temperature-transient experiment by constantly increasing the temperature, at 2.5°C/min, slower than above, with a single prereduction step, to better characterize the consumption mechanism and compare the performance of different reaction. Other conditions as specified in Materials and methods, i.e. m_s = 50 mg, d_p < 45 µm, $\dot{V}_{tot}$=100

Ncm^3/min and y_{H_2} or y_{O_2} = 10%. We applied 1 and 2 sequential redox cycles; we also introduced three heating and cooling cycles, in an inert atmosphere, between two redox cycles.

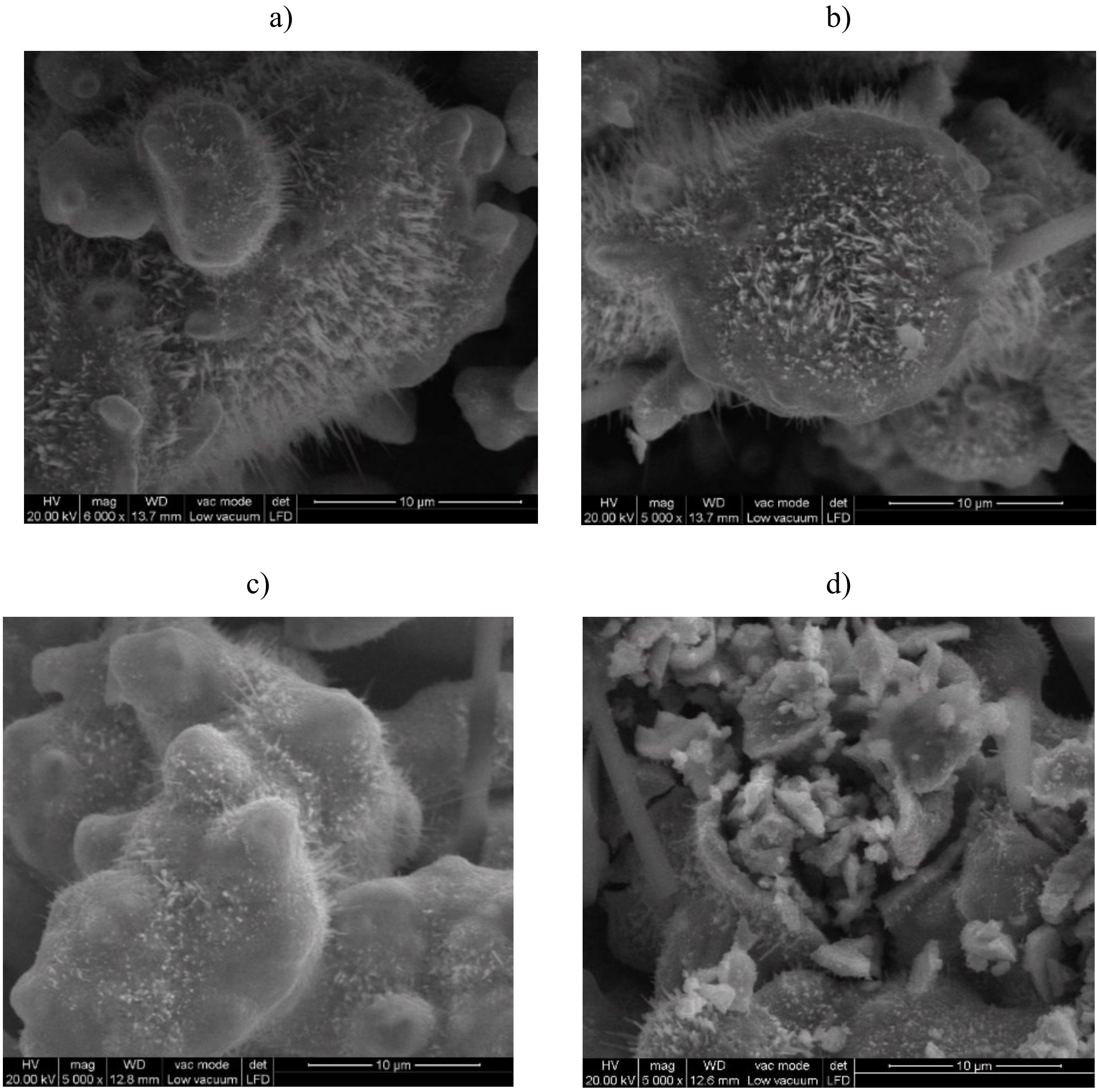

Figure 6: *SEM images of CuO powder after pre-treatment (heating/cooling in inert), and a single reduction and oxidation cycle a) and b), or 2 cycles with intermediate thermal cycles in inert atmosphere c) and d).*

Samples after 1 and 2 redox cycles (with intermediate thermal cycles in inert atmosphere) are compared in Figure 6. It is evident the detrimental impact on nanowires dimensions and density of increasing the cycles number. SEM images after the first reaction cycle (Figure 6.a and Figure 6.b) show the expected outcome of the H_2 pre-reduction, with nanowires ranging from 1 µm to 6 µm in length and high density in the whole oxide surface. Increasing the redox cycles to 2 (Figure 6.c and Figure 6.d), the nanowires average length is shorter than 1 µm and their density is significantly reduced.

The H_2 and O_2 consumption rates are shown in Figure 7. The relevant features (key temperatures and degree of reduction or oxidation) are collected in Table 3.

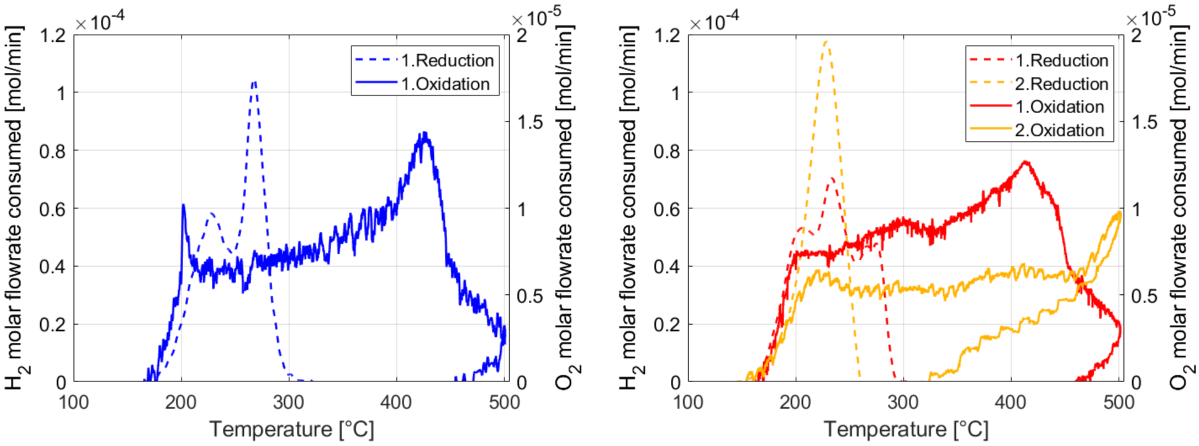

a) b)

***Figure** 7: H_2 (dashed) and O_2 (solid) consumption profiles for a single reduction and oxidation cycle a), or 2 cycles with intermediate thermal cycles in inert atmosphere c), starting from CuO powder.*

***Table 3**: Relevant parameters for CuO reduction and oxidation steps*

	Step	Gas	T_{act} [°C]	$T_{peak,1}$ [°C]	$T_{peak,2}$ [°C]	$\%^{cons}_{O,CuO}$ [%]
1 cycle	**Inert pre-treatment**	Ar				
	1.Reduction	10% H_2	175	268		81.9
	1.Oxidation	10% O_2	160	205	460	87.7
2 cycles	**Inert pre-treatment**	Ar				
	Oxidative pre-treatment	Air				
	1.Reduction	10% H_2	158	233	232, 264, 273	87.2
	1.Oxidation	10% O_2	155	250	415	87.4
	Inert cycle	Ar				
	Inert cycle	Ar				
	Inert cycle	Ar				
	2. Reduction	10% H_2	146	228	-	75.6
	2. Oxidation	10% O_2	155	220	500	72.3

Multiple peaks are observed in the reduction steps. We already reported that particle agglomeration occurs during their reduction with H_2 (Chapter 3). The bed restructuring reflects on the H_2 consumption profiles, Figure 7; the appearance of multiple peaks as proven to indicate the formation of a Cu shell with reduced porosity over the unreacted CuO particles, and not a different chemical reduction mechanism (Chapter 2). The shell causes H_2 diffusion limitations that shift the apparent reduction temperatures to higher values. The difference between the reduction profiles after 1 or 2 redox cycles is ascribed to uneven particle agglomeration, that determine local bed rearrangements unevenly distributed in the bed, and temperature gradients caused by higher sample mass (200 mg). The H_2 consumption rate is higher in the hotspots and the extent increased by the heat of reaction (CuO reduction is exothermic, $\Delta H = -85.763$ kJ/mol CuO) and thus areas at lower temperatures (< T activation) react only when the heat is more uniformly distributed. In the second cycle reduction, after an oxidation and three thermal cycles, only one peak is present at 228°C, Table 3, and the activation is at lower temperature. The appearance of structural defects, i.e. reduction active sites, and surface rearrangements decreases the activation temperature, as the induction time is lower [42], with a simultaneous decrease of reduction rate for temperatures <180°C caused by a decrease in surface area.

The oxidation profiles and quantifications results, also in Figure 7 and Table 3, demonstrate the formation of extra-oxides in the form of nanowires on the Cu-shell obtained after the reduction pre-treatment. The efficiency of reduction and re-oxidation is measured by the $\%O_{CuO}$ and reported in Table 3. The O regained during the oxidation is higher than the $\%O_{CuO}$ consumed by H_2 in the first redox cycle. However, a substantial difference is visible between the two oxygen consumption values: in the 1-redox cycle the difference between $\%O_{CuO, red}$ and $\%O_{CuO, ox}$ is 6.6% while in the 2-redox cycle test is < 1%. The difference is ascribed to the pre-treatment protocol, suggesting that an inert cycle has a higher efficiency than combining an inert and oxidation cycle, due to the different impact on the surface morphology. The application of an oxidative pretreatment uniforms the surface and decrease the superficial defects, identified as the active sites for CuO reduction. In the second redox cycle, Table 3, the amount of oxygen regain is less than the one consumed during the oxidation, meaning that any growth of nanowires or increased density is lost. The nanowhisker density is decreased caused by the partial agglomeration of CuO particles after the first reduction (Chapter 3) creating a non-porous copper oxide layer and subsequently increasing diffusion limitations for further reduction or oxidation processes. Also, the surface appears smooth after the reduction treatment and the growth mechanism of nanowires formation is unfavored due to the disappearance of surface defects. As CuO-based materials have an excellent reactivity towards reducing mixtures by donating the oxygen from the lattice, solutions to prevent agglomeration phenomena must be identified, such as the deposition of Cu/CuO particles on a suitable support to efficiently increase the dispersion. However, the volumetric capacity of the bed to store oxygen will dramatically drop.

The practical implication of these results could be understood by considering a reducing-oxidizing process: the metal oxide acts as an oxygen-donor in which the lattice oxygen is consumed during the reduction step, while the feed (possibly a fuel) is oxidized before the reduced solid is re-oxidized with O_2. Under this perspective, increasing the amount of oxygen available on the metal oxide through nanowires could increase the reduction yield and simultaneously control the product selectivity. The redox process investigated in this study is a model system with H_2, air and CuO as reductant, oxidant and metal oxide respectively, but the same reasoning could be applied to different reducing gas, like fuels, provided that the previously mentioned agglomeration effects are reproduced. If so, the reducing step in the redox loop could serve also as a pre-treatment to generate an improved substrate to facilitate the nanowires growth during the oxidation step. These considerations can be proven with simple experiments: a temperature-programmed reduction (TPR) with the same process reducing mixture to find the maximum reduction temperature (the temperature at which the pre-treatment should be carried out at steady state in consecutive reaction loops), SEM analyses after the first redox cycle and a performance comparison in terms of conversion/selectivity.

Conclusions

The formation of nanostructures on CuO surfaces (Cu foil and Cu/CuO powder) was investigated by applying thermal and chemical treatments, also through multiple cycles.

The non-uniform surface etching during the acid washing of Cu-foil generated areas with different morphologies (apparently rough and smooth) at a different oxide composition (mainly CuO is present in the rough regions while a mixture of Cu_2O-CuO in the smother ones) after an oxidation treatment in air at 500°C for 30 min. This composition depends also on the presence of nanowhiskers confined in the areas with a high concentration of surface defects, caused by the efficient acid etching that favor the initiation of nanowhiskers growth. Nanowhisker dimensions and density can be adjusted by varying the O_2 partial pressure and maximum temperature of the oxidative treatment. Higher O_2 partial pressures increase the NW density at lower maximum temperature, but the same output could be obtained by decreasing O_2 partial pressure at increased temperature.

The application of a complete reduction-oxidation cycle showed that the H_2 treatment prior to the oxidation stage favors the nanowires growth. Specifically, the CuO sample after the oxidation without any reducing step exhibits a surface morphology comparable the fresh one with negligible particle porosity and surface roughness, while the addition of a reducing treatment modifies the morphology, increasing the roughness as an effect of particle agglomeration, after the (exothermic) removal of atomic oxygen by H_2 from the original CuO sample. Also the contact time between the reducing gas phase and oxide influenced the surface morphology: increasing the contact time (0.4s) the surface roughness increases as an effect of the superficial microstructure rearrangement, while a lower contact time (0.14s) generates superficial cavities, indicating a less uniform distribution of copper grains. As we already reported (Chapter 2), the application of different experimental conditions influences the reaction outcome, as the extent of chemical and physical phenomena (mass and heat transfer) varies, reflecting on the morphological configuration of the surface; high H_2 concentration speeds up the overall conversion to Cu and simultaneously decreases the reduction extent, since the superficial Cu shell is limiting the diffusion of gas species into the oxide particles. The different gas contact time is not influencing the global reaction outcome, but the surface morphology. The nanowires formation mechanism includes the generation of macro-thick oxide layers (Cu_2O and CuO) that initiates their growth. Increasing the contact time, leads to a rougher surface with a uniform distribution of grains and without superficial hollows), thus the initial sites for nanowhiskers formation are increased as the rate-limiting step of the process (outward diffusion of Cu cations through grain-boundaries) is favored. However, strong particle agglomeration is occurring in consecutive reduction and oxidation reactions on bulk CuO, thus the importance of disperse the Cu/CuO particles on a suitable support. However, the volumetric capacity of the bed to store oxygen will dramatically drop.

Nomenclature

d_p = Particle diameter

ΔH = Enthalpy of reaction

m_s = Sample mass

P_{O_2} = O_2 partial pressure

T_{act} = Activation temperature

T_{peak} = Temperature of the peak

$T_{peak,1}$ = Temperature of the first peak

$T_{peak,2}$ = Temperature of the second peak

$\dot{V}_{tot}$ = Total volumetric flowrate

y_{H2} = Hydrogen volumetric percentage

y_{O2} = Oxygen volumetric percentage

O_{CuO} = Atomic O from CuO consumed

$\%O_{CuO,\ red}$ = Percentage of atomic oxygen from CuO consumed during reduction

$\%O_{CuO,\ ox}$ = Percentage of atomic oxygen regained by CuO during oxidation

$\%^{cons}_{O,CuO}$ = Degree of reduction

Greek letters:

β = Heating rate

τ_{low} = Low contact time

τ_{high} = High contact time

Acronyms:

BSE = Back-Scattered Electron Detector

CLP = Chemical Looping Combustion

EDS = Energy Dispersive X-ray Spectrometry

(E)SEM = (Environmental) Scanning electron microscope

NW = Nanowires/nanowhiskers

RT = Room temperature

TCD = Thermal conductivity detector

TM = Transition metal

TPO = Temperature programmed oxidation

TPR = Temperature programmed reduction

ES = Ehrlich-Schwoebel

VS = Vapor-liquid

VLS = Vapor-liquid-solid

XRD = X-Ray Diffraction

References

[1] Study on the EU's list of Critical Raw Materials (2020) Final Report, (n.d.). https://doi.org/10.2873/904613.

[2] J. Adánez, A. Abad, T. Mendiara, P. Gayán, L.F. de Diego, F. García-Labiano, Chemical looping combustion of solid fuels, Progress in Energy and Combustion Science. 65 (2018) 6–66. https://doi.org/10.1016/j.pecs.2017.07.005.

[3] P. Pal, S.K. Pahari, A. Sinhamahapatra, M. Jayachandran, G.V.M. Kiruthika, H.C. Bajaj, A.B. Panda, CeO2 nanowires with high aspect ratio and excellent catalytic activity for selective oxidation of styrene by molecular oxygen, RSC Advances. 3 (2013) 10837–10847. https://doi.org/10.1039/c3ra23485a.

[4] M. Dyballa, K. Thorshaug, D.K. Pappas, E. Borfecchia, K. Kvande, S. Bordiga, G. Berlier, A. Lazzarini, U. Olsbye, P. Beato, S. Svelle, B. Arstad, Zeolite Surface Methoxy Groups as Key Intermediates in the Stepwise Conversion of Methane to Methanol, ChemCatChem. 11 (2019) 5022–5026. https://doi.org/10.1002/cctc.201901315.

[5] J.M. Thomas, R. Raja, G. Sankar, R.G. Bell, Molecular-sieve catalysts for the selective oxidation of linear alkanes by molecular oxygen, 1999. www.nature.com.

[6] D. Papageorgiou, A.M. Efstathiou, X.E. Verykios, The selective oxidation of methane to C,-hydrocarbons over lithium-doped TiOz catalysts, Applied Catalysis A: General. 111 (1994) 41–62.

[7] M.S.C. Chan, H.G. Baldovi, J.S. Dennis, Enhancing the capacity of oxygen carriers for selective oxidations through phase cooperation: Bismuth oxide and ceria-zirconia, Catalysis Science and Technology. 8 (2018) 887–897. https://doi.org/10.1039/c7cy01992k.

[8] C.H. Wang, S.S. Lin, C.L. Chen, H.S. Weng, Performance of the supported copper oxide catalysts for the catalytic incineration of aromatic hydrocarbons, Chemosphere. 64 (2006) 503–509. https://doi.org/10.1016/j.chemosphere.2005.11.023.

[9] V. v. Galvita, M. Filez, H. Poelman, V. Bliznuk, G.B. Marin, The role of different types of CuO in CuO-CeO2/Al 2O3 for total oxidation, Catalysis Letters. 144 (2014) 32–43. https://doi.org/10.1007/s10562-013-1144-x.

[10] T. Mattisson, A. Järdnäs, A. Lyngfelt, Reactivity of some metal oxides supported on alumina with alternating methane and oxygen - Application for chemical-looping combustion, Energy and Fuels. 17 (2003) 643–651. https://doi.org/10.1021/ef020151i.

[11] P. Cho, T. Mattisson, A. Lyngfelt, Comparison of iron-, nickel-, copper- and manganese-based oxygen carriers for chemical-looping combustion, Fuel. 83 (2004) 1215–1225. https://doi.org/10.1016/j.fuel.2003.11.013.

[12] E. Jerndal, T. Mattisson, A. Lyngfelt, Thermal analysis of chemical-looping combustion, Chemical Engineering Research and Design. 84 (2006) 795–806. https://doi.org/10.1205/cherd05020.

[13] Q. Zafar, T. Mattisson, B. Gevert, Redox investigation of some oxides of transition-state metals Ni, Cu, Fe, and supported on SiO2 and MgAl2O4, Energy and Fuels. 20 (2006) 34–44. https://doi.org/10.1021/ef0501389.

[14] W. Akram, Sanjay, M.A. Hassan, Chemical looping combustion with nanosize oxygen carrier: a review, International Journal of Environmental Science and Technology. 18 (2021) 787–798. https://doi.org/10.1007/s13762-020-02840-8.

[15] D. Li, J. Hu, R. Wu, J.G. Lu, Conductometric chemical sensor based on individual CuO nanowires, Nanotechnology. 21 (2010). https://doi.org/10.1088/0957-4484/21/48/485502.

[16] W. Gao, S. Yang, S. Yang, L. Lv, Y. Du, Synthesis and magnetic properties of Mn doped CuO nanowires, Physics Letters, Section A: General, Atomic and Solid State Physics. 375 (2010) 180–182. https://doi.org/10.1016/j.physleta.2010.10.065.

[17] L.B. Chen, N. Lu, C.M. Xu, H.C. Yu, T.H. Wang, Electrochemical performance of polycrystalline CuO nanowires as anode material for Li ion batteries, Electrochimica Acta. 54 (2009) 4198–4201. https://doi.org/10.1016/j.electacta.2009.02.065.

[18] S. John, S.C. Roy, CuO/Cu2O nanoflake/nanowire heterostructure photocathode with enhanced surface area for photoelectrochemical solar energy conversion, Applied Surface Science. 509 (2020). https://doi.org/10.1016/j.apsusc.2019.144703.

[19] R.L. Papurello, A.P. Cabello, M.A. Ulla, C.A. Neyertz, J.M. Zamaro, Microreactor with copper oxide nanostructured films for catalytic gas phase oxidations, Surface and Coatings Technology. 328 (2017) 231–239. https://doi.org/10.1016/j.surfcoat.2017.08.066.

[20] C. Xu, Y. Liu, G. Xu, G. Wang, Preparation and characterization of CuO nanorods by thermal decomposition of CuC2O4 precursor, Materials Research Bulletin. 37 (2002) 2365–2372.

[21] T. Jiang, Y. Wang, D. Meng, X. Wu, J. Wang, J. Chen, Controllable fabrication of CuO nanostructure by hydrothermal method and its properties, Applied Surface Science. 311 (2014) 602–608. https://doi.org/10.1016/j.apsusc.2014.05.116.

[22] C. Wu, L. Shen, H. Yu, Y.C. Zhang, Q. Huang, Solvothermal synthesis of Cu-doped ZnO nanowires with visible light-driven photocatalytic activity, Materials Letters. 74 (2012) 236–238. https://doi.org/10.1016/j.matlet.2012.01.125.

[23] C. te Hsieh, J.M. Chen, H.H. Lin, H.C. Shih, Synthesis of well-ordered CuO nanofibers by a self-catalytic growth mechanism, Applied Physics Letters. 82 (2003) 3316–3318. https://doi.org/10.1063/1.1569043.

[24] M. Kaur, K.P. Muthe, S.K. Despande, S. Choudhury, J.B. Singh, N. Verma, S.K. Gupta, J. v. Yakhmi, Growth and branching of CuO nanowires by thermal oxidation of copper, Journal of Crystal Growth. 289 (2006) 670–675. https://doi.org/10.1016/j.jcrysgro.2005.11.111.

[25] A. Kumar, A.K. Srivastava, P. Tiwari, R. v. Nandedkar, The effect of growth parameters on the aspect ratio and number density of CuO nanorods, Journal of Physics Condensed Matter. 16 (2004) 8531–8543. https://doi.org/10.1088/0953-8984/16/47/007.

[26] Z. Feng, C.R. Marks, A. Barkatt, Oxidation-Rate Excursions during the Oxidation of Copper in Gaseous Environments at Moderate Temperatures, Oxidation of Metals. 60 (2003).

[27] R. Haugsrud, The Influence of Water Vapor on the Oxidation of Copper at Intermediate Temperatures, Journal of The Electrochemical Society. 149 (2002) B14. https://doi.org/10.1149/1.1427076.

[28] X. Wang, J.C. Hanson, A.I. Frenkel, J.Y. Kim, J.A. Rodriguez, Time-resolved studies for the mechanism of reduction of copper oxides with carbon monoxide: Complex behavior of lattice oxygen and the formation of suboxides, Journal of Physical Chemistry B. 108 (2004) 13667–13673. https://doi.org/10.1021/jp040366o.

[29] X. Jiang, T. Herricks, Y. Xia, CuO Nanowires Can Be Synthesized by Heating Copper Substrates in Air, Nano Letters. 2 (2002) 1333–1338. https://doi.org/10.1021/nl0257519.

[30] D. Senyildiz, O.T. Ogurtani, G. Cambaz Buke, The effects of acid pretreatment and surface stresses on the evolution of impurity clusters and graphene formation on Cu foil, Applied Surface Science. 425 (2017) 873–878. https://doi.org/10.1016/j.apsusc.2017.07.092.

[31] N. Chopra, B. Hu, B.J. Hinds, Selective growth and kinetic study of copper oxide nanowires from patterned thin-film multilayer structures, Journal of Materials Research. 22 (2007) 2691–2699. https://doi.org/10.1557/jmr.2007.0377.

[32] C.H. Xu, C.H. Woo, S.Q. Shi, Formation of CuO nanowires on Cu foil, Chemical Physics Letters. 399 (2004) 62–66. https://doi.org/10.1016/j.cplett.2004.10.005.

[33] R.L. Schwoebel, E.J. Shipsey, Step motion on crystal surfaces, Journal of Applied Physics. 37 (1966) 3682–3686. https://doi.org/10.1063/1.1707904.

[34] G. Ehrlich, F.G. Hudda, Atomic view of surface self-diffusion: Tungsten on tungsten, The Journal of Chemical Physics. 44 (1966) 1039–1049. https://doi.org/10.1063/1.1726787.

[35] J.C. Yang, B. Kolasa, J.M. Gibson, M. Yeadon, Self-limiting oxidation of copper, Applied Physics Letters. 73 (1998) 2841–2843. https://doi.org/10.1063/1.122608.

[36] A.M.B. Goṇalves, L.C. Campos, A.S. Ferlauto, R.G. Lacerda, On the growth and electrical characterization of CuO nanowires by thermal oxidation, Journal of Applied Physics. 106 (2009). https://doi.org/10.1063/1.3187833.

[37] K.K. Lew, J.M. Redwing, Growth characteristics of silicon nanowires synthesized by vapor-liquid-solid growth in nanoporous alumina templates, Journal of Crystal Growth. 254 (2003) 14–22. https://doi.org/10.1016/S0022-0248(03)01146-1.

[38] C.L. Cheng, Y.R. Ma, M.H. Chou, C.Y. Huang, V. Yeh, S.Y. Wu, Direct observation of short-circuit diffusion during the formation of a single cupric oxide nanowire, Nanotechnology. 18 (2007). https://doi.org/10.1088/0957-4484/18/24/245604.

[39] S.M. Prokes, S. Arnold, Stress-driven formation of Si nanowires, Applied Physics Letters. 86 (2005) 1–3. https://doi.org/10.1063/1.1925756.

[40] L. Yuan, Q. Yin, Y. Wang, G. Zhou, CuO reduction induced formation of CuO/Cu2O hybrid oxides, Chemical Physics Letters. 590 (2013) 92–96. https://doi.org/10.1016/j.cplett.2013.10.040.

[41] L. Yuan, Y. Wang, R. Mema, G. Zhou, Driving force and growth mechanism for spontaneous oxide nanowire formation during the thermal oxidation of metals, Acta Materialia. 59 (2011) 2491–2500. https://doi.org/10.1016/j.actamat.2010.12.052.

[42] J.A. Rodriguez, J.C. Hanson, A.I. Frenkel, J.Y. Kim, M. Pérez, Experimental and theoretical studies on the reaction of H2 with NiO: Role of O vacancies and mechanism for oxide reduction, Journal of the American Chemical Society. 124 (2002) 346–354. https://doi.org/10.1021/ja0121080.

[43] T. Pröll, P. Kolbitsch, J. Bolhàr-Nordenkampf, H. Hofbauer, A novel dual circulating fluidized bed system for chemical looping processes, AIChE Journal. 55 (2009) 3255–3266. https://doi.org/10.1002/aic.11934.

[44] Y. Wei, H. Wang, K. Li, X. Zhu, Y. Du, Preparation and characterization of Ce1-x NixO 2 as oxygen carrier for selective oxidation methane to syngas in absence of gaseous oxygen, Journal of Rare Earths. 28 (2010) 357–361. https://doi.org/10.1016/S1002-0721(10)60358-4.

Chapter 7

Transient experiments to investigate the role of lattice oxygen in the CO oxidation on $LaFeO_3$

Abstract

Perovskites are promising materials to incorporate transition metals in their structure as substitute of the expensive PGMs for TWC applications. Thanks to the mobility of lattice oxygen, perovskites can sustain oxidation reactions even when the oxygen from the gas phase is lower than the stoichiometric. The application of transient experiments (CO-TPR) confirms the mobility of oxygen in $LaFeO_3$ which is slow and governed by a diffusive mechanism for temperatures higher than the activation one, in which also bulk oxygen could reach the surface and take part of superficial reactions.

Introduction

Climate changes are observed on a worldwide scale and these alterations are unprecedented in thousands of years and mostly irreversible. IPCC report from 2021 showed that the emissions of greenhouse gases are mainly caused by human activities and if the current trend continues without prompt actions the global temperature is expected to exceed 1.5°C of warming [1]. In automotive applications, the emission of pollutant gases as NO, CO and unburnt hydrocarbons plays a crucial contribution in the formation of acid rains and air pollution. Catalytic converters are efficient devices to reduce the emission of harmful gases on which Platinum-Group Metals (PGMs) acts as the active centers for the multiple reduction and oxidation reactions [2] thanks to their outstanding performance in terms of low temperature operation, conversion and selectivity. However, PGMs (Pd, Pt, Rh, Ir, Ru) have been recently classified as critical raw materials [3] and the demand is expected to increase in the future due to new promising H_2 technologies for energy applications (electrolyzer [4], fuel-cell [5]), leading to a further increase in their demand [6] and cost, as a forecast of the current 15-year trend [7]. Noble-metal catalysts also undergo to deactivation caused by poisoning with chloride and sulfuric compounds [8] and thus transition metals (Cu, Ni, Cr, Co, Mn, etc.) have become crucial in the development of innovative low-PGM or PGM-free catalytic systems with comparable activity and durability as well as a lower cost. In automotive applications, PGMs promote CO and hydrocarbons combustion together with NO_x reduction and Cu, Fe and Mn in their metallic forms are active towards these reduction and oxidation reactions but their vulnerability with respect to severe oxidative atmosphere [9] prevents their extensive utilization in three-way catalytic reactions (TWC).

Perovskites are promising materials in the general form of ABO_3 in which A and B are cations of different size and the catalytic activity depends on their valence state. The incorporation of inexpensive and available transition metal cations as active sites favors the transition to more sustainable materials [10]. Also, this process tunes the crystallographic configuration of the perovskite, changing the chemical composition and structure, enriching the redox couples and increasing the concentration of structural defects [11]. These features of the perovskitic framework are strictly connected to the mobility of lattice oxygen as the higher number of defects generates oxygen vacancies that increase the amount of active oxygen, contributing to a greater oxidation capability [12]. Most studies on perovskite for TWC applications are dedicated to the oxidation of CO and HC [13] and the CO oxidation with NO [14] and their resistance towards deactivation and poisoning, e.g. coke deposition and SO_2 resistance by tuning the composition of the perovskite. Also, the mobility of lattice oxygen is a crucial feature for the practical application of perovskite as TWC materials, as the real operation conditions are characterized by strong oscillations in oxygen concentration [15]. The discriminating factor to identify the most active catalyst under these transient conditions is its ability to provide oxygen from the lattice when the O_2 from the gas phase is under the stoichiometric value. Therefore, mass-transport and physical phenomena (reagents and oxygen diffusion and adsorption/desorption) should be critically included while developing reaction mechanism and kinetic analysis. Despite the complexity of the exhaust gas mixtures, the reactive system could be studied in a simplified configuration in which both oxidation and reduction reactions are considered, i.e. assisted CO oxidation with NO. Specifically, the participation of lattice oxygen involves the CO oxidation step that initiates the formation of structural vacancies involved in further reaction steps with other species. The connection between oxygen mobility and catalytic activity could be performed by focusing on the CO oxidation. The reaction mechanism on a model perovskite ($LaFeO_3$) is reviewed in the next section.

In this study, the crucial role of oxygen diffusion during CO oxidation was assessed for a model perovskite ($LaFeO_3$). The experimental demonstration of the importance of integrating oxygen diffusion steps in Mars-Van Krevelen mechanism will be performed with transient experiments (switching of the gas) and temperature programmed reduction with CO (CO-TPR) and isothermal experiments at various temperatures without feeding oxygen.

Microkinetic model of CO oxidation

The mechanism of oxidation of CO with lattice oxygen over $LaFeO_3$ is a Mars-Van Krevelen type, [16], in which CO is first absorbed on an active site of Fe $(*)$ (Step 1) and then oxidized by the oxygen present in the catalyst's structure $O_{(l)}$ (Step 2). CO_2 is then formed on the surface of the material ($CO_{2,\,ads}$), and then desorbs from it (Step 3), freeing an active site.

$CO + * \rightarrow CO_{ads}$	$E_{a,\,ads} \sim 0$ eV	*Step 1*
$CO_{ads} + O_{(l)} \rightarrow CO_{2,ads} + V^*$	$E_{a,\,r} = 0.74$ eV	*Step 2*
$CO_{2,ads} \rightarrow CO_2 + *$	$E_{a,\,des}$ = n.a.	*Step 3*

There is therefore an effect both in the gas phase (CO_2 formation) and in the catalyst (formation of vacancies in the structure and restoration of active sites). Besides the surface oxidation step itself (Step 2) there are other two steps whose rate influences the macroscopical result of the reaction, which are adsorption/desorption and O diffusion in the solid.

Adsorption kinetics

Step 1 represents the chemical adsorption of the CO molecule onto the surface, to which it forms a bond stronger than the van der Waals interaction typical of physical adsorption. There is an associated activation energy for adsorption ($E_{a,ads}$) > 0, thereby defining the kinetic constant (k_{ads}) and the rate of adsorption (R_{ads}) in Equation 1 and Equation 2 respectively [17].

$$k_{ads} = \frac{P}{\sqrt{2\pi m k_B T}} \cdot e^{-\frac{E_{a,ads}}{k_B T}} \qquad \text{Equation 1}$$

$$R_{ads} = \frac{d\Theta}{\mathrm{dt}} = k_{ads} \cdot f(\Theta) = k_{ads} \cdot (1 - \Theta) \cdot S(\Theta) \qquad \text{Equation 2}$$

in which P = pressure, m = mass of the adsorbed molecule, k_B = Boltzmann constant, T = temperature and $\Theta = \frac{N_{ads}}{N_{ads,max}}$ = fraction of coverage of active sites on the catalyst's surface. The function $f(\Theta)$=$(1 - \Theta) \cdot S(\Theta)$ is the *sticking function,* which represents the probability with which a molecule adsorbs onto the surface, and $S(\Theta)$ is the *sticking coefficient,* which depends on the absorbate molecule and the nature of the adsorbent. In the present case, the function has been assumed to be of the first order, as a single molecule of adsorbate (CO) occupies a single active site (there is no dissociation). Therefore, the rate of adsorption is defined as the variation of the number of active sites over time, and it depends on temperature, pressure and mass of the adsorbate molecule (Equation 1). An increase in the rate of adsorption is directly proportional to an increase in pressure and inversely proportional to increases in mass and temperature. The effect of temperature is higher compared to pressure and mass influence thanks on the exponential function dependency in Equation 1. The parameter Θ can be obtained through Equation 3:

$$\Theta = \frac{N_{ads}}{A_{sur} \cdot M_{cat} \cdot \rho_{act.site}} \qquad [adim] \qquad \text{Equation 3}$$

In which N_{ads} = moles of adsorbate [mol], A_{sur} = surface area [m^2/g], M_{cat} = catalyst weight [g/mol], $\rho_{act.site}$ = density of superficial active sites. This parameter can assume two extreme values: $\Theta = 0$ when the adsorbing capacity of the surface is at maximum since no active site is currently occupied and $\Theta = 1$ if the surface is saturated and no more active sites remain available. In the interval $0 < \Theta < 1$, Θ is a function of the rates of adsorption and desorption (Equation 4)

$$\Theta = f(R_{ads}, R_{des}) = f(t, T, P) \qquad \text{Equation 4}$$

In this study, the adsorbate is CO and the adsorbent $LaFeO_3$, and the active sites are Fe sites linked to $O_{(l)}$ in the structure, as depicted in Figure 1.

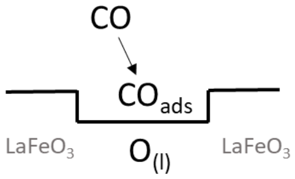

***Figure 1:** Insight of surface adsorption of CO on $LaFeO_3$.*

Assuming the surface is saturated ($\Theta = 1$, so all of the active sites can potentially react with the adsorbate), Equation 3 can be rearranged to calculate the total quantity of $O_{(l)}$ relative to the surface (Equation 5).

$$n_{CO,ads} = A_{sur} \cdot M_{cat} \cdot \rho_{O,sur} \qquad [mol] \qquad \text{Equation 5}$$

This equation could be used both to calculate moles of CO adsorbed on the surface that correspond to the moles of active sites, i.e. superficial oxygen ($n_{O,surf}$) or an approximate value of surface area (A_{sur}). To do so, the Langmuir model of monolayer adsorption must be considered as the surface is assumed at saturation and thus the correlation between A_{sur} and $n_{O,surf}$ still holds. The density of di $O_{(l)}$ active sites is reported in Equation 6, assuming that each Fe site has 4 O(l) around, but periodicity imply that it is still 1:1 Fe:O so that the initial density of Fe and O(l) is equal, at 4.6 10^{18} atoms/cm^2 each.

$$\rho_{O,sur} = 4.6 \cdot 10^{18} \frac{atoms}{m^2} = 7.6 \cdot 10^{-6} \frac{mol}{m^2} \qquad \text{Equation 6}$$

Oxygen diffusion in the lattice

Oxygen is present in the whole structure of the catalyst, from the outer layers to the bulk. The oxidation reaction of CO over $LaFeO_3$ (Step 2) implies the formation of structural vacancies (V*) when $O_{(l)}$ is consumed, inducing a diffusion of oxygen atoms inside the solid (Figure 2).

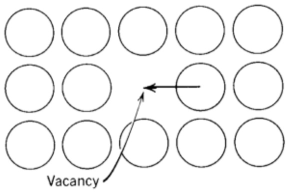

Figure 2: *Insight of vacancy diffusion mechanism.*

The general equation describing 3D unsteady-state isotropic diffusion is reported in Equation 7, assuming that diffusion is favored in preferential pathways

$$\frac{dC_{O,z}}{dt} = D \cdot \left(\frac{\partial^2 C_O}{\partial x^2} + \frac{\partial^2 C_O}{\partial y^2} + \frac{\partial^2 C_O}{\partial z^2} \right) \qquad \text{Equation 7}$$

in which $C_{O,z}$ = oxygen concentration along the axial direction z [mol/cm^3] and D = diffusion coefficient. The behavior of $O_{(l)}$ atoms migration in $LaFeO_3$ can be described with a diffusion of vacancies mechanism [18], in which the diffusion coefficient D can be defined with the general Arrhenius-like relation (Meyer-Neldel rule) reported in Equation 8. It represents an activated diffusion since the jump of an atom to a nearby site (vacancy) requires a certain activation energy to overcome the energy barrier when moving from one equilibrium state to another (Figure 3)

$$D = D_0 \cdot \exp\left(-\frac{E_{a,diff}}{RT} \right) \qquad \text{Equation 8}$$

In which D_0 = pre-exponential factor, $E_{a,diff}$ = activation energy for diffusion, R = gas constant and T= temperature.

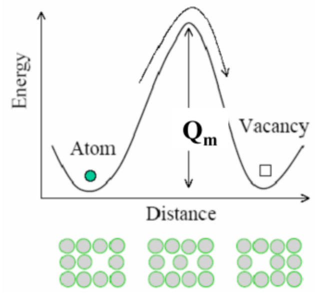

Figure 3: *Energy trend involved in vacancy diffusion mechanism ($Q_m = E_{a,diff}$).*

The pre-exponential factor D_0 (or *frequency factor*) represents the probability of an atom to possess enough energy to jump into the new position and find a vacancy in the vicinity of the site. Equation 9 can then be obtained, which describes the dependence of the diffusion coefficient D on other variables (structure of the material and of the lattice, vibrational motion of atoms).

$$D = D_0 \cdot exp\left(-\frac{E_{a,diff}}{RT}\right) = \upsilon \cdot a^2 \cdot \alpha \cdot exp\left(-\frac{E_{a,diff}}{RT}\right)$$

Equation 9

in which υ = characteristic atomic vibrational frequency, a = lattice constant and α = geometrical factor. With equal microstructure and mechanism, diffusion is favoured by temperature, which becomes the key variable in explaining the results obtained during tests.

A solid's structure can be divided into different zones, and the model for $LaFeO_3$ [19] identifies two of them: surface and bulk. Based on the results obtained during tests without gaseous O_2, this model can be modified (Figure 4) to differentiate between types of $O_{(l)}$: grain boundaries γ and bulk β.

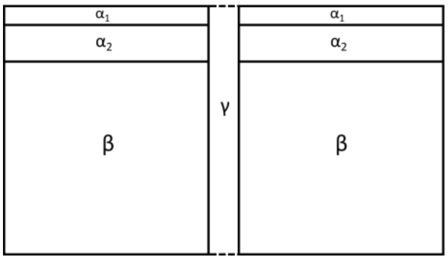

Figure 4: *Schematic representation of two $LaFeO_3$ grains and their structures.*

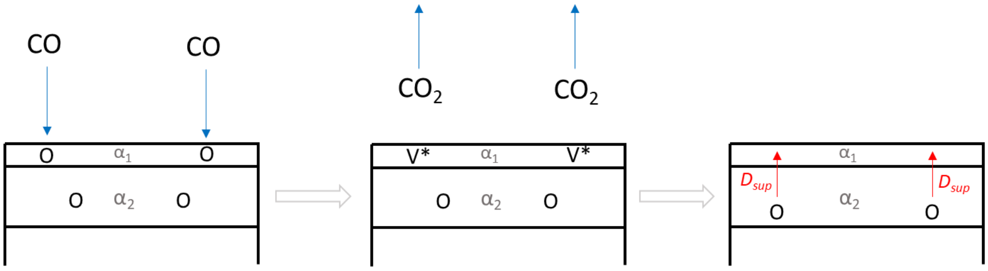

***Figure 5**: Oxygen diffusion in surface* $\boldsymbol{\alpha_1}$ *in LaFeO3.*

The surface α_0 is the physical adsorption layer, of gaseous molecules (O_2, N_2, remaining CO) whose bonds with the surface are weaker than chemical (i.e., van der Waals interactions). Its contribution is negligible since the inert (He) flow during the heating phase physically adsorbed species. The α_1 surface is the real boundary of the solids, with a density of superficial sites and quantity of O represented by Equation 5 and Equation 6. When the surface comes into contact with the CO being fed, Step 1 (CO adsorption) and Step 2 (formation of CO_2 and vacancies) happen (first two images of Figure 5). At the level of the solid the diffusion of vacancies comes into play, which is described by Equation 8 and for which a diffusion coefficient D can be defined as in Equation 9 (assuming D_0 is constant), leading to Equation 10.

$$D = D_0 \cdot \exp\left(-\frac{E_{a,diff\ \alpha_1}}{RT}\right) \qquad \text{Equation 10}$$

In which $E_{a,diff\ \alpha_1}$ is the energy of diffusion through the surface α_1. Grain boundaries γ are the interfaces between grains of $LaFeO_3$, in which there is a faster diffusion of atoms to the surface compared to bulk diffusion [19], with an activation energy of $E_{a,diff\ \gamma}$ (Figure 6).

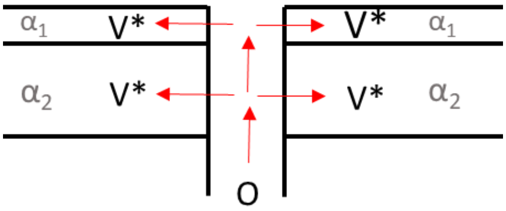

***Figure 6**: Oxygen diffusion in grain boundaries* γ *in LaFeO3.*

The bulk β is the innermost zone of the material, in which there is a slow diffusion with an activation energy $E_{a,diff\ \beta}$.

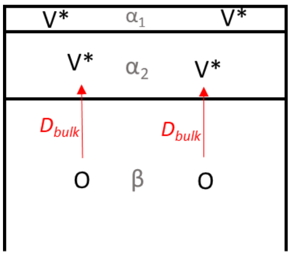

***Figure 7:** Oxygen diffusion in bulk β in LaFeO3.*

Comparing the activation energies of the different zones [19,20], the relation reported in Equation 11 stands:

$$E_{a,diff\ \alpha_1} < E_{a,diff\ \gamma} < E_{a,diff\ \beta} \qquad \text{Equation 11}$$

Therefore, it can be deduced that surface diffusion is activated by lower temperatures compared to the diffusion in grain boundaries or in the bulk.

Materials and methods

$LaFeO_3$ in powder form was synthesized at the Unité de Catalyse et Chimie du Solide, University Lille Nord – 1, France, within a common EU program, with a standard sol-gel method via citrate route [21]. CO-TPO was performed with a fixed bed configuration in a quartz tubular reactor (ID=6 mm) in which 45 mg of $LaFeO_3$ (45 µm – 150 µm) were loaded. The tube was inserted into a temperature programmable furnace (Watlow) controlled by a thermocouple (type K) placed right downstream the bed. Temperature was also monitored upstream by a thermocouple (type K) close to the bed surface. The temperature protocol consisted in a heating ramp (from RT to 500°C at 2°C/min, no isothermal time and uncontrolled cooling rate) with 1% ± 0.4% CO/He. Gases were fed with a total flowrate of 100 Ncm^3/min, obtained with mass-flow controllers (Brooks, Bronkhorst). Before entering the reactor, an automatic four-way valve (VICI Valco) allows to rapidly switch mixture (inert vs. reducing), ensuring the total separation between them. The same logic applies also to isothermal CO oxidation experiments, with the difference that the catalyst mass is higher (102 mg) and the heating ramp up to the desired temperature is carried out in an inert flow (He) at 10°C/min and then a mixture of 0.7% of CO/He is fed by switching the automatic valve. In both cases, the outlet gases (CO, CO_2) were analysed with a by means of FTIR (Shimadzu IRTracer-100), at a frequency of 4 Hz. Prior to the CO-TPR and isothermal CO experiments, the sample was pre-treated in air at 500°C for 2h.

Surface morphology was examined with an Environmental Scanning Electron Microscope (ESEM, Fei-Quanta 200), equipped with Back-Scattered Electron Detector (BSE). Nanostructure dimensions (length and diameter) were retrieved from ESEM images; the surface elemental analysis was obtained with Energy Dispersive Spectroscopy (EDS, EDAX, Genesis model). The initial and final powder structure was analyzed with X-ray Diffraction (XRD, Panalytical X'Pert 3 Powder) with Cu-K_α radiation and 2θ scanning from 3° to 70° with 0.013° step. Results were interpreted with Panalytical High Score Plus 4 with 3 databases (PDF2, Panalytical ICSD, COD).

Quantification of CO_2 produced from isothermal CO experiments and its correlation to the amount of oxygen taken from $LaFeO_3$ are two key parameters in this study. Quantifications are described in detail in the following paragraph and the theoretical elemental analysis of 100 mg sample is reported in Table 1.

Table 1: *Elemental composition and relative weights for $LaFeO_3$*

Element	Molecular weight (g/mol)	Atoms	Weight percentage	Weight of element for 102mg
La	139	1	57.2%	58.3 mg
Fe	56	1	23.0%	23.5 mg
O	16	3	19.8%	20.2 mg

At any time, the quantity of O_2 from the catalyst has been calculated from the CO_2 produced by the reaction. From the volumetric $\%_{CO_2}(t)$ obtained by FT-IR, $\dot{n}_{CO_2}(t)$ (molar flowrate of CO_2) has been calculated with Equation 12.

$$\dot{n}_{CO_2}(t) = \%_{CO_2}(t) \cdot \frac{P \cdot \dot{V}_{tot}}{R \cdot T} \qquad [mol/min] \qquad \text{Equation 12}$$

The total quantity of CO_2 produced, $n_{CO_{2,tot}}$, is the integral of the $\dot{n}_{CO_2}(t)$ profile since the beginning ($\Delta t = t_{fin} - t_{in}$). t_{in} is the time at which the slope of the $\%_{CO_2}$ starts to increase, and t_{fin} the time in which $\%_{CO_2}$ reaches zero (if applicable) (Equation 13).

$$n_{CO_{2,tot}} = \int_{t_{in}}^{t_{fin}} \dot{n}_{CO_2}(t) \cdot dt \qquad [mol] \qquad \text{Equation 13}$$

To standardize the processing of experimental results and eliminate possible differences due to the calibration of the FT-IR with respect to CO_2, the $\%_{CO_2}(t)$ curve has been translated to ensure that $\%_{CO_2}(t_{in}) = 0$. The total quantity of consumed O_2, $n_{O_{2,tot}}$, has been calculated through the stoichiometry of the reaction (0.5mol O_2: 1 molCO_2) as in Equation 14.

$$n_{O_{2,tot}} = 0.5 \cdot n_{CO_{2,tot}} \qquad \text{Equation 14}$$

If a flow of inert is not opened before the test, a correction on the $n_{O_{2,tot}}$ was also performed, considering a small amount of air trapped inside the reactor and piping, before the reaction and it was quantified by calculating the volume of the system and obtaining the corresponding quantity of oxygen ($n_{O_{2,line}}$). The quantity of O_2 from the catalyst that has been consumed, $n_{O_{2,cat}}$, results from the difference between the total quantity consumed, from eq. above, and the due to the oxygen initially in the line (Equation 15).

$$n_{O_{2,cat}} = n_{O_{2,tot}} - n_{O_{2,line}} \qquad [mol] \qquad \text{Equation 15}$$

Depending on the length of the lines, $n_{O_{2,line}}$ varies between $2.214 \cdot 10^{-5}$ mol to $2.937 \cdot 10^{-5}$ mol, corresponding to 0.7 mg and 0.93 mg of O_2 respectively.

The error on the carbon balance was calculated with Equation 16.

$$ErrC = \left(1 - \frac{\dot{n}_C^{out}}{\dot{n}_C^{in}}\right) \cdot 100 \qquad \text{Equation 16}$$

Where $\dot{n}_C^{out}$ = molar flowrate of carbon exiting the reactor [mol/min] as CO or CO_2, and $\dot{n}_C^{in}$= molar flowrate of carbon fed (as CO).

Results and discussion

$LaFeO_3$ characterization

The material used in these tests is $LaFeO_3$ has been characterized by XRD, as in Figure 8. The material has the prevalent structure of an orthorhombic perovskite, and there are traces of iron and lanthanum oxides (Fe_2O_3 and La_2O_3). With a preliminary Rietveld analysis, the relative prevalence of the different compounds has been estimated as 97.3% $LaFeO_3$, 2.4% Fe_2O_3, 0. 2% La_2O_3. From this data and knowing the mass of catalyst used during tests (45 mg) it is possible to estimate the stoichiometric quantity of oxygen, as reported in Table 2.

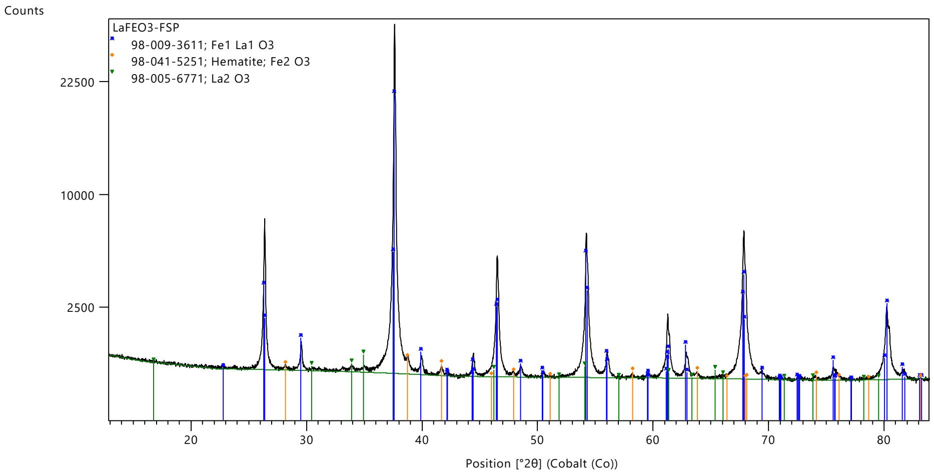

Figure 8: *XRD analysis of the $LaFeO_3$ used in all tests.*

Table 2: *Stoichiometric O content in material used in all tests.*

	Stoichiometric O [%]	**mass of O in 45mg [mg]**
$LaFeO_3$	19.8	8.7
Fe_2O_3	30.1	0.32
La_2O_3	14.7	0.18
Total		9.04

Temperature-programmed CO oxidation with $O_{(l)}$

An overall evaluation of $LaFeO_3$ reactivity towards CO in absence of $O_{2,\ gas}$, i.e. just using the O in the perovskite, was performed with a CO-TPR. From CO consumption and CO_2 formation profiles up to 500°C, variations of the reaction mechanism and oxygen diffusion phenomena could be identified, as well as indications on peculiar temperatures for further isothermal experiments. The resulting CO and CO_2 consumed and produced are overlapped in Figure 9 and the corresponding evolution of the error on the carbon balance is reported in Figure 10.

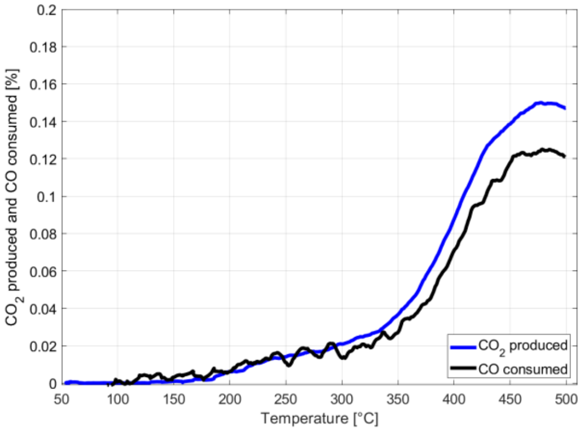

Figure 9: *CO-TPR on $LaFeO_3$ (mass=45 mg, 0.7% CO in He, total flowrate = 100 Ncm^3/min and heating rate = 2°C/min)*

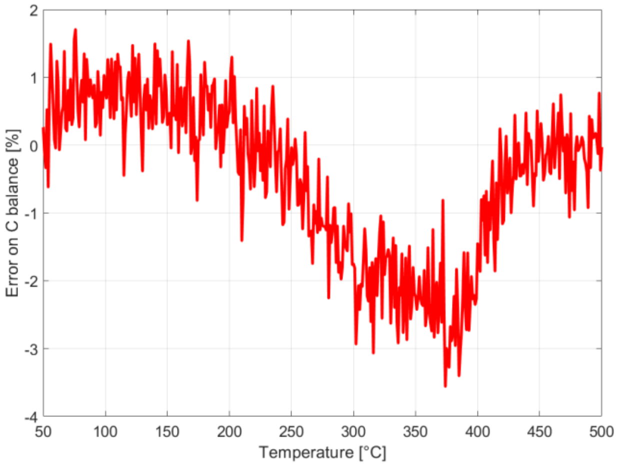

Figure 10: *Error on carbon balance during CO-TPR on LaFeO*$_3$*.*

It can be noticed that the oxidation reaction starts at temperatures lower than 200°C, while from 350°C onwards there is a change in the shape of the profiles, reflected in the carbon balance, Figure 10. Specifically, CO_2 produced departs from the CO consumed and a maximum error of -3% on the C balance (excess of C in the output), reached between 350 and 400°C, demonstrates the over-production of carbon species. This result will be further investigated in the next section.

CO-TPR confirms the conclusions about the mobility of O in $LaFeO_3$, which is slow and governed by a diffusive mechanism for temperatures higher that the activation one. In accordance with what reported in literature, the mobility of O atoms bound to Fe cations is low [22], but unlike what reported by other authors [19] if enough time is given to the O to diffuse into the outer layers of the material, even bulk oxygen takes part in superficial reactions.

Isothermal CO oxidation with $O_{(l)}$

Given the peculiar CO consumption profile obtained through CO-TPR, Figure 9, additional experiments were performed to verify the capacity of the material to oxidize CO even without feeding O_2, just by using the O_2 stored into the material itself and quantify the ratio between the consumed O_2 (obtained by analyzing the curve for the produced CO_2) and the total O_2 in the material, its temperature dependence and the nature of the O_2 (superficial vs bulk). To do so, isothermal experiments at four characteristic temperatures, identified from CO-TPR profile of Figure 9, were carried out. Namely, 350°C was identified as the temperature at which the CO profile changes its slope becoming steeper and thus two temperatures below (250°C, 300°C) and two temperatures above (400°C, 500°) were chosen. CO was fed with a concentration of 0.7% in He and a total volumetric flowrate of 100 Ncm^3/min, as a positive step after an equalization time. Results are reported in Figure 11. As a general comment, we can identify a peak of CO_2 production after the beginning of CO feed, particularly at lower temperature, but the production of CO_2 remains quite significant at the highest temperature. The quantification of the total CO_2 produced ($O_{(l)}$ calculated) for each isothermal experiment and the ratio between the calculated CO_2 produced and the theoretical O amount ($\frac{O_{(l)}\text{ calculated}}{O_{(l)}\text{ stoich}}$) is reported in Table 3. Considering the $LaFeO_3$ mass equal to 102 mg used in the experiments, the theoretical amount of O available is 20.2 mg, see Table 3.

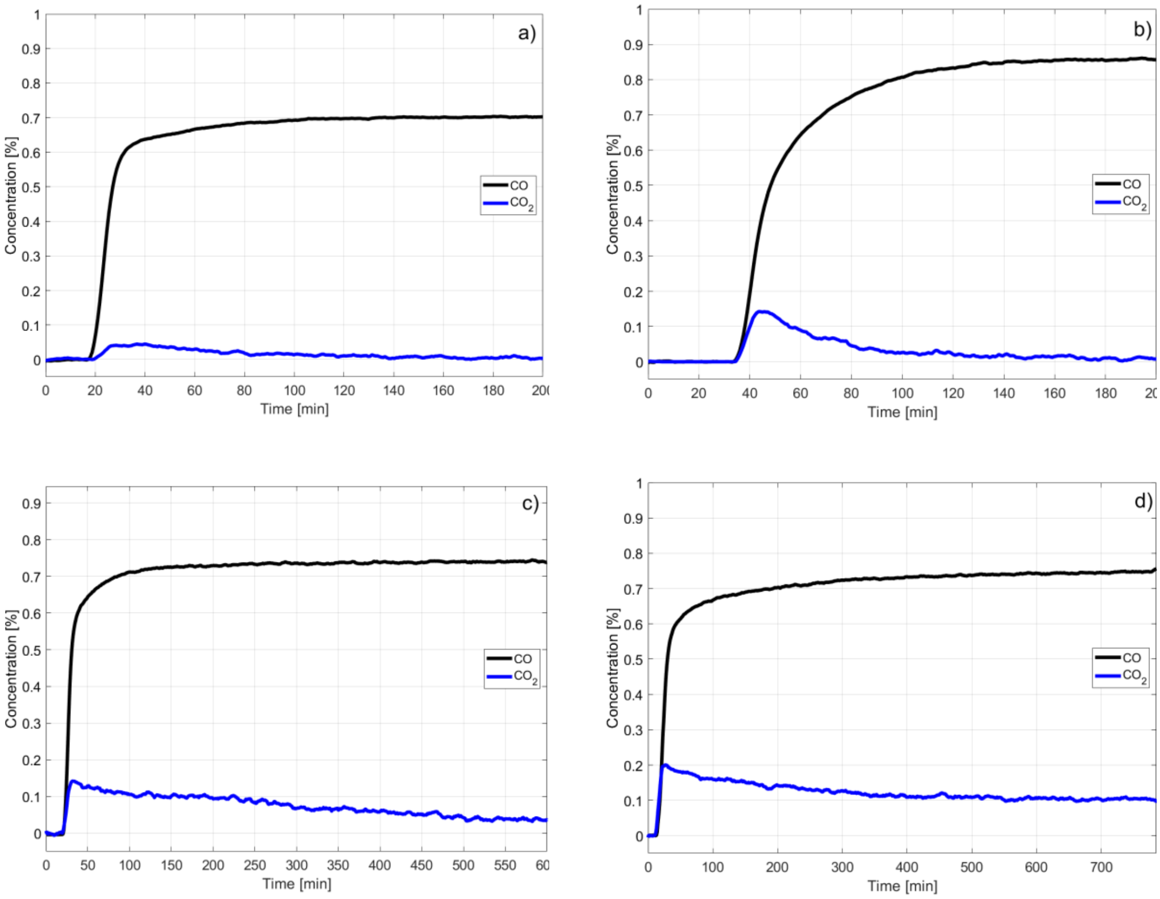

Figure 11: *Isothermal CO oxidation with $O_{(l)}$ on $LaFeO_3$ at a) 250°C, b) 300°C, c) 400°C, d) 500°C mass=102 mg, 0.7% 0.7% CO in He, total flowrate = 100 Ncm^3/min*

Table 3: *Results for CO oxidation at different temperatures on $LaFeO_3$.*

Temperature	$O_{(l)}$ calculated	$\frac{O_{(l)}\text{ calculated}}{O_{(l)}\text{ stoich}}$	Time
250°C	1.0mg	4.9%	3.2h
300°C	3.2mg	15.8%	3.5h
400°C	27.6mg	136.6%	9.6h
500°C	65.5mg	324.2%	12.8h

The quantity of $O_{2,\,cat}$ consumed by the oxidation reaction at 250°C is 1.0 mg, which is 4.9% of the total quantity of $O_{2,\,cat}$ contained in the completely oxidized catalyst, according to the stoichiometry of the material. At the final integration time (t_{fin}) the CO_2 concentration is 0.00016%, assumed negligible. The quantity of consumed $O_{2,\,cat}$ at 300°C is 3.2mg and equal to 15.8% of the stoichiometric quantity inside the material. The CO_2 concentration at the end, t_{fin}, is 0.0018%, once again negligible. Increasing the temperature to 400°C the quantity of consumed $O_{2,\,cat}$ is 27.6mg, which is 136.6% higher than the theoretical one, which should be impossible. The shape of the curve and the $\%_{CO_2}$ at t_{fin} equal to 0.036% suggest that the formation of CO_2 is still ongoing after almost 10 hours of continuously feeding CO. At 500°C, the quantity of consumed O_2 65.5mg, which is 324% of the stoichiometric. It can also be noticed that after 13 hours the volumetric fraction of CO_2 is still equal to 0.1% and appears to have stabile around that value, which again is not possible, given that the co-reactant, $O_{(l)}$, is a finite amount.

This division of the $LaFeO_3$ structure into zones [19], and the relation between their respective activation energies of diffusion (Equation 9) can explain the results obtained in the tests without gaseous O_2 at different temperatures. From the graphical results of Figure 11 it is evident that the material can supply the O_2 needed to oxidize the CO being fed, and this capacity persists for hours. A temperature of 250°C is sufficient to activate the diffusion across the α_1 surface (and is therefore related to $E_{a,diff\,\alpha_1}$), but not the diffusion across grain boundaries or the bulk. This is indicated by the fact that the production of CO_2 stops after 3.2 hrs., which means that all the available $O_{(l)}$ (the one on the surface) has been consumed, and its supply is not being replenished by diffusion from other zones, which is limited by the temperature. It is possible to verify this by applying Equation 6 to the result at 250°C in order to calculate the surface area and evaluate its plausibility. Knowing that M_{cat} = 102 mg, $\rho_{O,sur} = 7.6 \cdot 10^6$mol/m^2 and $n_{O,sur}(250°C) = 3.12 \cdot 10^{-5}$ mol, the calculation results in A_{sur} = 40 m^2/g, which is acceptable for $LaFeO_3$ [23]

At 300°C the curve presents a similar trend to the one at 250°C, stopping the CO_2 production after 3.5 hrs. Because of the higher temperature both the diffusion across the surface α_1 and the diffusion through grain boundaries are activated, increasing the quantity of O_2 consumed (from 1 mg to 3.2 mg). Bulk diffusion is still not active, unlike the case of 400°C. In this latter test, after almost 10 hours of continuously feeding CO the production of CO_2 had yet to cease because the temperature for activating the bulk diffusion has been surpassed, and the time-temperature variables start to have a reciprocal influence: the higher the temperature (above the activation one for bulk diffusion), the less time will be required for the diffusion, and the lower the time to produce CO_2. Also, quantification data in Table 3 indicates that the method of correlating the quantity of CO_2 produced to the O_2 of the material consumed is only applicable when bulk diffusion is not dominant.

CO_2 overestimation

From the results reported in Table 3 the quantity of $O_{(l)}$ consumed by the CO oxidation reaction with no O_2 from the gas, correlated to the quantity of CO_2 produced by the reaction, surpasses the stoichiometric value at 400°C. This means that there is an overproduction of CO_2 which cannot be due to $O_{(l)}$ from the solid. To understand the causes of these anomalous results few hypotheses have been investigated: La-carbonates decomposition, Boudouard reaction and CO oxidation catalyzed by thermocouples.

La-carbonates decomposition

The aim of this experiment was to quantify the CO_2 produced which is not derived from the oxidation of CO through the lattice oxygen, to correct the results of the tests without O_2 from the gas. The $LaFeO_3$ sample was heated up to 800°C in an inert atmosphere and the total amount of CO_2 produced was calculated from the CO_2 concentration in the outlet, Figure 12. A fraction of the CO_2 can in fact be produced by the decomposition of La carbonates that can form on the catalyst's surface through the reaction:

$$La_2(CO_3)_3 \rightarrow La_2O_2CO_3(s) + 2CO_2 \leftrightarrow La_2O_3\ (s) + CO_2 \qquad \textit{Reaction 1}$$

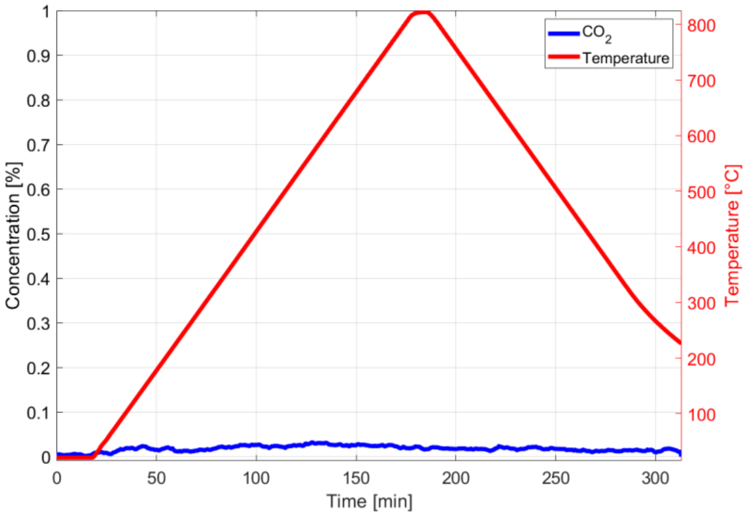

Figure 12: *Inert heating of $LaFeO_3$.*

The first decomposition reaction activates at a temperature of 480°C according to Literature [24], whereas the second one at a 720°C [9]. Accordingly, the $LaFeO_3$ sample has been heated under inert atmosphere up to a temperature of 825°C. Another fraction of the CO_2 surplus may depend not on chemical reaction, but on the instrument used for quantitative analyses. In fact, the quantification of CO_2 via FT-IR is conducted after daily calibrations at known CO_2 concentrations, and with a background whose signal is acquired before the test starts. The latter is influenced by the CO_2 and humidity in atmospheric air, which can vary over time, especially in longer tests like the ones here discussed. Figure 12 shows that CO_2 increases over time but apparently uncorrelated with temperature, as the CO_2 settles at a stable value even during the cooling phase, only to drop after 250 minutes. This result validates the hypothesis of the variation or the background rather than the carbonate decomposition. From the measured CO_2 produced in inert atmosphere, it has been calculated the (fictitious) quantity of O_2 that correspond to this CO_2 (Table 4).

Table 4: *O_2 calculated from CO_2 produced under inert flux.*

Final temperature	**$O_{(l)}$ calculated**
250°C	0.45 mg
300°C	0.53 mg
400°C	0.81 mg
500°C	1.1 mg

The quantity of CO_2 calculated and correlated to the fictitious O_2 in the solid is to be intended as the one produced from ambient temperature up to the final temperature.

Boudouard reaction

Another reaction likely to be involved in this process is the Boudouard reaction, through which CO decomposes into CO_2 and C (solid carbon):

$$2CO_{(g)} \leftrightarrow C_{(s)} + CO_{2(g)} \qquad \textit{Reaction 2}$$

The forward reaction is exothermic (ΔH_r=-172 kJ/mol [3]) meaning that the carbon formation is favored at lower temperature. The maximum C-formation rate is between 500°C and 600°C and the reaction is promoted by the presence of metal particles such as iron and iron oxides [4]. Depending on the synthesis method and quality, LFO can have a pure perovskite structure or it can be a mixture of perovskite crystals and oxides, such as Fe_2O_3 (hematite) and La_2O_3. Furthermore, structural modifications and rearrangements can be induced by reduction-oxidation cycles. For these reasons, the formation of solid carbon on the catalyst surface must be considered as a source of incorrect CO_2 quantification and deactivation of LFO active sites for CO oxidation.

The Boudouard reaction mechanism Is described in steps *IV- VII*

IV) $CO_{(g)} \rightarrow CO_{ads}$
V) $CO_{ads} \rightarrow C_{(s)} + O_{ads}$
VI) $CO_{(g)} + O_{ads} \rightarrow CO_{2\,ads}$
VII) $CO_{2\,ads} \rightarrow CO_{2(g)}$

CO adsorption on Fe-active sites is the common step between the two mechanisms *(I-IV)*, however CO_{ads} competes between the CO_2 formation through lattice (superficial) oxygen $O_{(s)}$ (*II*) and CO dissociation into solid carbon and adsorbed oxygen (*V*). In the last case, CO in the gas phase reacts with the adsorbed oxygen to form CO_2 through an Eley-Rideal mechanism.

Therefore, the total CO_2 monitored at the reactor outlet is produced from two types of oxygen, one of which is continuously replenished by feeding CO. This effect is evident in high temperature experiments (400°C, 500°C), or more generally at temperature higher than 350°C [5], for two reasons: $O_{(l)}$ consumed close or higher than stoichiometric, constant CO_2 concentration-time profile. In the last case, CO_2 concentration settles on an offset value and never goes to zero even after 12h.

A SEM-EDX analysis was carried out to confirm the speculations (Figure 13). The solid carbon formed after the reaction at 500°C (the sample was not re-oxidized before the analysis) is non-negligible, deposited on the surface and thus pyrolytic. Reaction conditions and morphological aspect did not lead to encapsulating or whisker carbon. The hypothesis of an excess CO_2 production from CO by Boudouard reactions appears confirmed by the surface analysis.

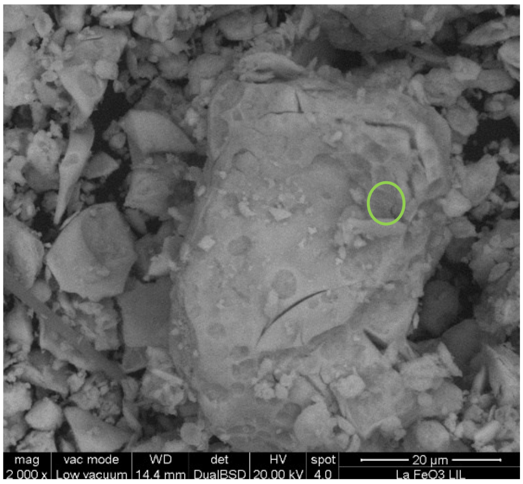

Element	Weight [%]	Atomic [%]
C	7.38	29.9
O	10.21	31.04
La	62.8	21.99
Fe	19.6	17.07

Figure 13: *SEM image and EDX on the green area of $LaFeO_3$ after reduction with CO at 500°C.*

Structural rearrangement

A further aspect which has not been considered yet is the structural rearrangement of $LaFeO_3$ crystals undergoing heating and exposed to reducing/oxidizing atmospheres. It is likely that at low temperatures, when the mobility of bulk $O_{(l)}$ is not activated, these modifications are caused by the exposure to reducing or oxidizing environments, and are limited to the material's surface, which can be interested by the formation of oxides (which are not visible with XRD). At higher temperatures the rearrangement could interest the inner layers as well, due to the mobility of bulk $O_{(l)}$. At high temperatures for longer periods of time (such as in tests at 400°C and 500°C) it is not therefore possible to correlate the results regarding the oxidation of CO, considered as the capacity to supply O_2, to the original material, $LaFeO_3$, since its structure is actually a composite of various microstructures ($LaFeO_3$, oxides, etc.). This means that the reaction mechanism, according to which the oxidation of CO occurs via the formation of vacancies and the following reduction of Fe, is invalid. Surface vacancies, due to the different nature and structure of the surface, would not be present, with the reaction being catalyzed by possible oxides instead. Finally, there will not be reproducibility in the results if the catalyst is tested in a series of reduction/oxidation cycles since the material in the reaction n will be different from the one in the reaction n-1.

Revision of the test protocol

A new test protocol has been designed with two goals 1) to separate the contribution of superficial $O_{(l)}$ from the one of bulk $O_{(l)}$ in the oxidation of CO, and 2) to verify potential structural modifications of the material. In addition, improvements to the set-up (increased optical path of the FT-R cell) are expected to increase the accuracy of the measurements.

To study the behavior of superficial $O_{(l)}$, the test can be divided into the following steps:

1. Heating under inert conditions, to remove from the surface all the residues of H_2O and carbonates that could have been absorbed there, occupying active sites. The material is brought back to reference, initial condition.
2. O_2-TPO, to recover the possibility that in step 1 some of the superficial $O_{(l)}$ is removed by heating, this oxidation aims to restore it, monitoring the variation of O_2 in the output. The maximum temperature at which the sample has to be heated under oxidising conditions needs to be at least the one used in the preceding test, while being lower than the calcination temperature of the material, to bring the material's structure back to its initial state (which means the modifications are still reversible).

3. O_2-TPD. This step consists in heating the sample under an inert flow (as in step 1), monitoring the O_2 loss via a TCD and an oxygen sensor. The expected result is the identification of two peaks, indicating the loss of $O_{(l)}$ from the surface and from the bulk, at increasingly higher temperature. The maximum temperature reached during the analysis would be the one at the end of the first peak, to prevent the activation of the mobility of bulk O(l) and observe only the superficial component (so possible modifications of the structure would only interest the surface), which is quantifiable by the area below the peak.
4. CO oxidation if $O_{(l)}$, through isotherms. Replica of the previous test, that was done with a simplified protocol. The maximum temperature for this test would be lower than needed for the activation of bulk mobility.
5. Replica to steps 1, 2 and 3, to compare the quantity of O_2 that the material reacquires after the reduction test to the one that it can release afterwards. The comparison can also be made based on the temperature at which the O_2 peaks appear, which along with the total quantity of O_2 is an indication of structural modifications in the material (i.e., if this temperature shifts to higher values, there can be a fraction of oxides). Hypothetically, it would be possible to quantify the fraction of each microstructure (oxides, perovskite) inside $LaFeO_3$ from the analysis of TPD peaks.
6. Replica of step 4

The complete sequence is graphically summarized in Figure 14.

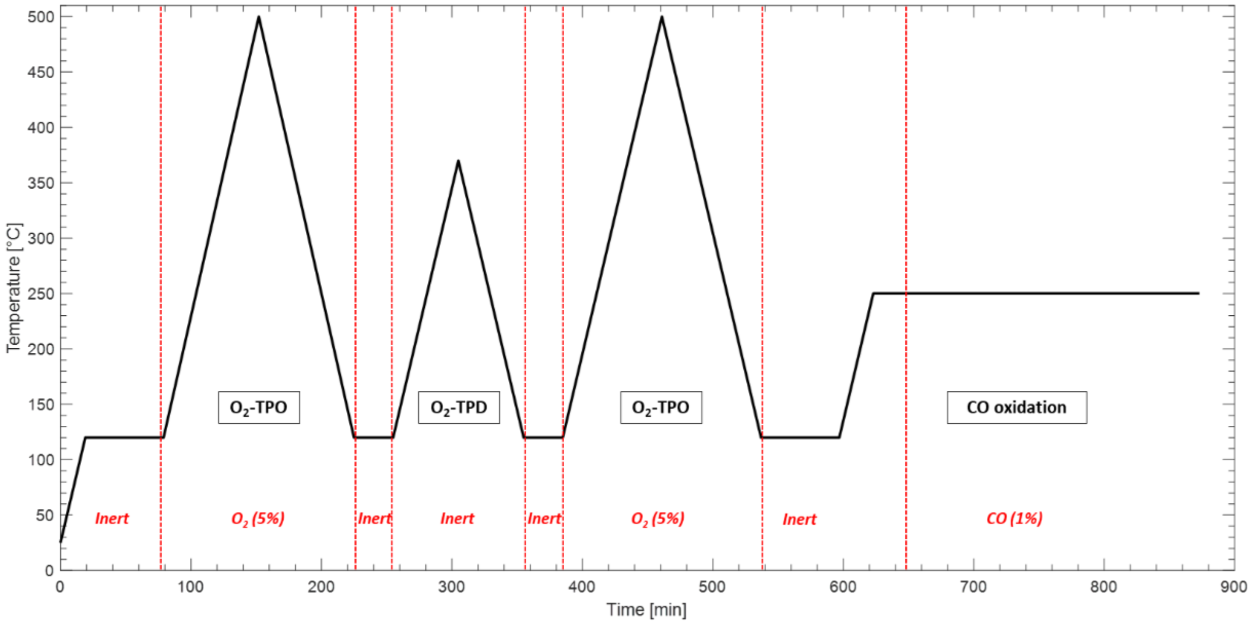

***Figure 14**: Scheme of the revised testing protocol for CO oxidation by lattice O. Heating/cooling rate are constant for all steps and equal to 5°C/min.*

The experimental protocol to isolate the contribution of bulk O(l) would be similar to the previous, simplified one described in the previous section; the only different is that the TPO step (and therefore the oxidation of the surface after heating in inert flow) would not be carried out, to avoid restoring the surface O_2. The temperature for the O_2-TPD phase and for the reduction test would be higher than the ones previously used, in order to activate the bulk mobility and, hypothetically, have the CO oxidation occur using only bulk $O_{(l).}$ The same considerations on quantification, reproducibility and structural modifications can be used in this case as well.

The new protocol aims at more accurately quantifying the oxygen that the material provides to the CO oxidation reaction and check that there is a dynamic variation on the structure of the material when it undergoes reaction and thermal cycles. At each step we evaluate the meaning of the experimental results through the quantitative comparison between $O_{(l)}$ consumed and CO_2 produced according to the reaction $CO + O \rightarrow CO_2$ and the initial quantity of oxygen in the fully oxidized material. An oxygen surplus compared to the stoichiometric value could indicate the occurrence of secondary reactions that produce CO_2 or a variation in the oxide-containing structure formed during oxidation steps. The first aspect has already been thoroughly investigated (see section *CO_2 overestimation*) and the setup has been modified to minimize its contribution. Also, we evaluate the shift of oxidation and desorption peaks during the O_2-TPO and O_2-TPD steps, which indicate the presence of different structures (oxides, perovskite), and the quantification of the peak.

In the first phase of O_2-TPO/O_2-TPD cycles, the 4-way valve is used to feed alternatively a diluted mixture of O_2 at 5% in Ar during the O_2-TPO, or 100% Ar during the O_2-TPD, the initial phase of heating under inert gas up to 120°C (to remove residual humidity from the sample), and between each temperature program (to completely remove O_2 from the line and stabilize the temperature). The mixture exiting the reactor is analyzed in parallel by MS and sensors. The MS is a direct-access mass spectrometer, monitoring mass 28, 32, 40 and 44. Sensors are an O_2 electrochemical sensor and a relative humidity sensor, in series. Ar has been selected as inert because of the O_2 sensor, where diffusion of the mixture plays a role in sensing, and the use of He make the sensor saturate; an inert with a molar mass comparable to N_2 is required.

During the CO oxidation phase, O_2 is substituted with CO in the feed. In this case, the 4-way valve is used to feed Ar during the heating up to the desired temperature, and once this has stabilized to the isothermal value, the valve switches and feeds the reactor with a 1% CO mixture in Ar. In this case the product mixture is monitored in parallel with an FT-IR and a mass spectrometer.

The experimental protocol just described has been followed with temperature specifications reported in Table 5, The sequence follows the scheme of Figure 14.

Table 5: *Temperature specifications for the new protocol.*

	Final temperature [°C]
Inert	120
O_2-TPO	500
O_2-TPD	370
CO oxidation	250

The choice of a final temperature of 500°C for O_2-TPO attempts to completely oxidized the material, below the calcination temperature (600°C). The temperature of 370°C for O_2-TPD is based on the results of previous tests, and from the literature [22], where it has been established that bulk mobility starts at temperatures higher than 400°C. In the tests at low temperature (i.e., < 400°C) the activation of bulk diffusion should be avoided, in order to separate the contribution of the surface from that of the innermost layers of the material.

The results for the O_2-TPO/O_2-TPD cycle are represented in Figure 15.

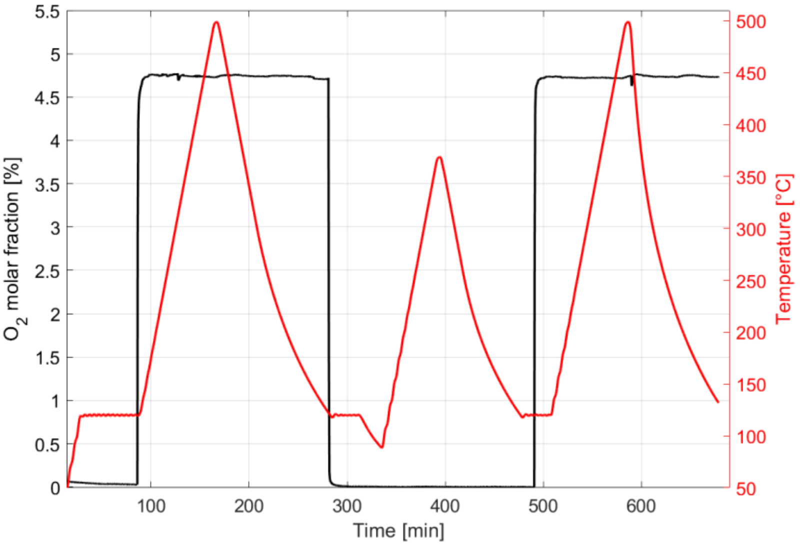

Figure 15: *O_2 concentration in the outlet, during O_2-TPO on $LaFeO_3$ prior to CO oxidation at 250°C.*

In the two TPOs it can be observed that the inlet concentration of O_2 is constant and equal to 4.7%, and significant O_2 consumption are not evident, compared to the sensitivity of the measurements (MS signal eventually was too noisy, thus not reported). Two negative peaks apparently depart from noise, of about 0.1%, at 314°C during TPO-1 and 481°C during TPO-

2, the second one occurs during the cooling ramp may be misplaced in terms of actual bed temperature, due to the thermal inertia of the sample with respect to the measured temperature, below the quartz wool. These peaks have a larger amplitude than the sensor's noise and are not attributable to perturbations in the feed, since the comparison with the signal from the pressure transducer does not show any anomaly in that region (and share the same analog-digital acquisition instrument). A possible physical explanation is the formation of superficial oxides, being more thermally stable do not decompose at the temperatures reached during the O_2-TPD. Unfortunately, the O_2-TPD does not present visible O_2 desorption peaks at temperatures below 370°C. While consistent with some Literature [25], where no variation in the outlet O_2 concentration was reported, it contrasts Others, that reported a desorption of α-O_2 (the superficial one) at temperatures below 400°C [26–29]. O_2 desorption from $LaFeO_3$ is not as intense as in other perovskites based on Mn and Cr [20] because of the low reducibility of Fe^{3+} inside its structure, and TPD is not always used to correlate the catalytic activity data because of the lack of a correspondence between the reducibility and TPD results [19]. Another possible explanation is the low oxygen quantity contained in a 45 mg sample. In general, this type of analysis is carried out on samples heavier than 100 mg (150mg in [15]) that allow to overcome the limit for the instruments' sensibility.

Figure 16 shows the profiles for CO and CO_2, during the CO oxidation test at a 250°C isotherm.

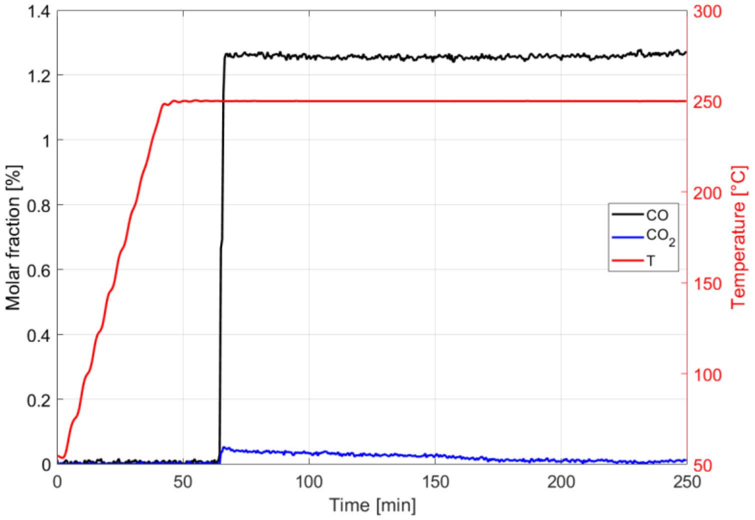

Figure 16: *CO concentration in the outlet, during CO oxidation on $LaFeO_3$ at 300°C, using the new protocol*

The profiles are very similar to those obtained in the corresponding previous test at 250°C, with a clear improvement of the CO profile thanks to the new configuration of the FT-IR cell. This implies that also the CO_2 profile, in particular in the first instants after the CO step, better represents the initial transient. The formation of CO_2, immediately triggered at the outset of CO feed, gradually extinguishes, as expected. The error in the carbon balance is 0.75%. The CO_2 profiles in both tests reach zero concentration after 170 mins (this test, improved protocol) and 200 mins (previous test, simplified protocol). The 30 minutes difference can be caused by a higher CO concentration in this test (1.25% vs. 0.7%), that accelerated the consumption of superficial oxygen.

The total oxygen consumed has been quantified in 2.5 mg, which represents 27% of the stoichiometric oxygen in $LaFeO_3$. Since the temperature is lower than the one needed to activate diffusion, a relatively high fraction of CO_2 production (and therefore O consumption) can be attributed to oxygen not considered in the stoichiometric calculations, e.g. formed in the preceding O_2-TPO step. It is assumed that these oxidated structures have a high thermal stability and are therefore not visible during the O_2-TPD, but a low chemical stability and therefore they produce CO_2 when exposed to a reducing agent.

The protocol has been slightly modified for a replica. The sequence follows the scheme of Figure 14, except for the O_2-TPD that has been removed, since no O_2 desorption was observed. The oxidation of CO with $O_{(l)}$ has been carried out at 300°C, 50°C above the last test. The temperature specifications are reported in Table 6.

Table 6: *Temperature protocol*

	Final temperature [°C]
Inert	120
O_2-TPO	500
CO oxidation	300

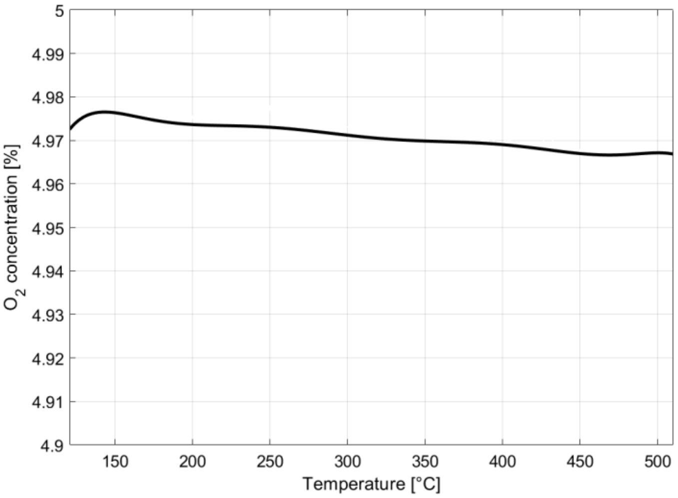

Figure 17: *O_2 concentration in the outlet, during O_2-TPO on $LaFeO_3$ prior to CO oxidation at 300°C.*

The results of O_2-TPO are represented in Figure 17, in terms of O_2 in the outlet, on a largely magnified scale. Apparently, a constant O_2 consumption is taking place, without any oxygen consumption peak, correlated to the oxidation state of the metals inside the structure, suggesting that oxygen transport is extremely slow, controlled by lattice diffusion.

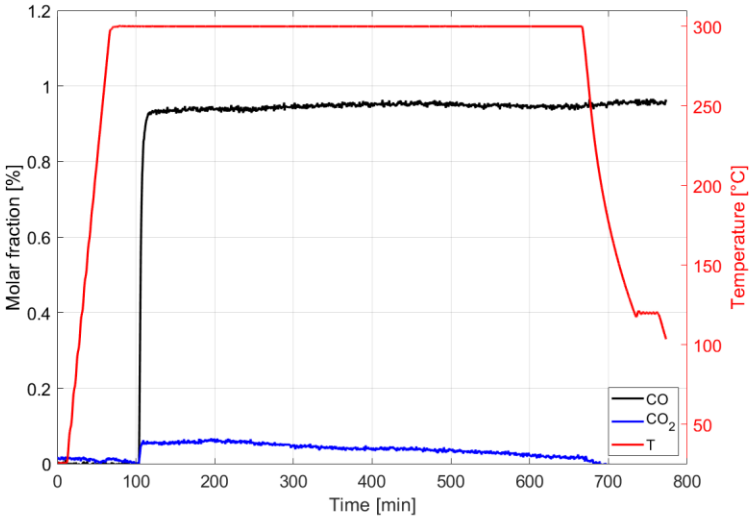

Figure 18: *CO concentration in the outlet, during CO oxidation on* $LaFeO_3$ *at 300°C.*

The results of solids reduction by CO are shown in Figure 18. It can be observed that the CO_2 production slowly decreases over time, until it drops to zero, suggesting that the $O_{(l)}$ available for the reaction at 300°C has been totally consumed.

The same modified protocol has been replicated by significantly (+150°C) increasing the temperature in CO oxidation with $O_{(l)}$ to 450°C. The temperature specifications are reported in Table 7. Note that the O_2-TPO (1% O_2) was also carried out with a slower heating ramp (2°C/min), to beer tack any short-term O_2 consumption.

Table 7: *Modified temperature protocol*

	Final temperature [°C]
Inert	120
O_2-TPO	500 (2°C/min)
CO oxidation	450

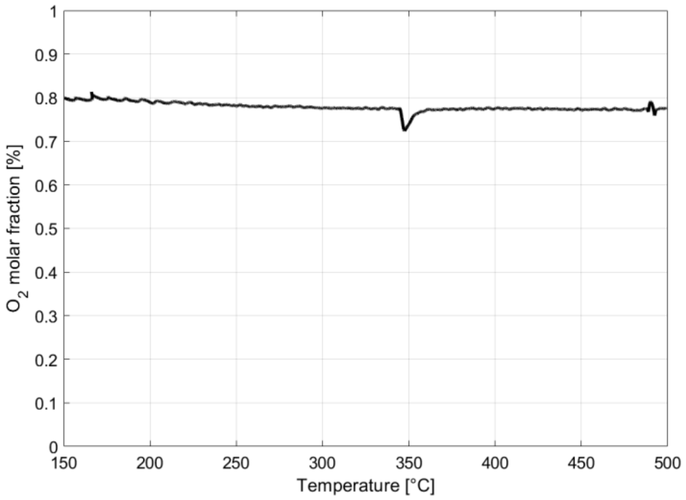

Figure 19: *O_2 concentration in the outlet, during O_2-TPO on $LaFeO_3$ prior to CO oxidation at 450°C.*

The O_2 concentration during the material oxidation (TPO) is shown in Figure 19. Interestingly, a sharp, localized peak of O_2 consumption (lack of O_2 in the outlet) is evident, as already observed (with some skepticism) in a previous TPO, see Figure 15, now detected at 350°C. The same hypothesis previously formulated can be confirmed.

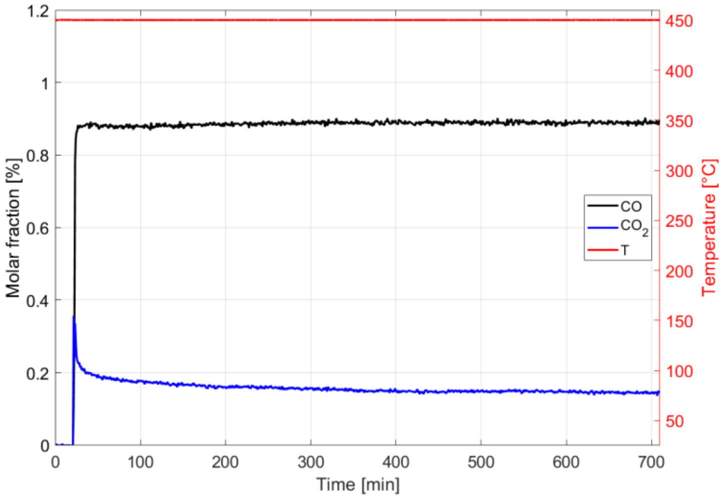

Figure 20: *CO concentration in the outlet, during CO oxidation on $LaFeO_3$ at 450°C.*

During CO oxidation, however, we observe a sustained CO_2 production at this higher temperature, unlike Figure 16 (250°C) and Figure 18 (300°C) where the CO_2 production appeared to complete, even taking a long time. This result confirms that increasing the temperature, the Boudouard reaction sustains the production of CO_2 for temperatures higher than 350-400°C, so that the quantification of consumed oxygen cannot be achieved.

Conclusions

CO oxidation with lattice oxygen under constant heating (CO-TPR) confirms the conclusions about the mobility of O in $LaFeO_3$, which is slow and governed by a diffusive mechanism for temperatures higher that the activation one. In accordance to what reported in literature the mobility of O atoms bound to Fe cations is low [22], but unlike what reported by other authors if enough time is given to the O to diffuse into the outer layers of the material, even bulk oxygen takes part in superficial reactions [19].

CO oxidation with lattice oxygen at constant temperature show sustained production of CO_2 starting from 300°C, because the temperature for activating the bulk diffusion has been surpassed, and the time-temperature variables start to have a reciprocal influence: the higher the temperature (above the activation one for bulk diffusion), the less time will be required for the diffusion, and the lower the time to produce CO_2.

Improvements in the test protocol and experimental set-up were not satisfactory, apparently suggesting that the experiment of accurately detecting the exploitation of O in the solid for reduction requires a more sensible set-up and type of experiment. The sustained CO_2 production at high temperature, likely supported by Boudouard reaction, can be the main confusing effect.

Nomenclature

a = Lattice constant

A_{sur} = surface area

C_O = oxygen concentration

$C_{O,z}$ = oxygen concentration along the axial direction z

ΔH_r = Enthalpy of reaction

D = Diffusion coefficient

D_0 = Pre-exponential factor of frequency factor for the activated diffusion

$E_{a,diff\,\alpha_1}$ = energy of diffusion through the surface α_1

$E_{a,diff\,\beta}$ = energy of diffusion through the surface β

$E_{a,diff\,\gamma}$ = energy of diffusion through the surface γ

$E_{a,ads}$ = activation energy for adsorption

$E_{a,r}$ = activation energy for reaction

$E_{a,des}$ = activation energy for desorption

$E_{a,diff}$ = activation energy for diffusion

$ErrC$ = Error on the carbon balance

k_B = Boltzmann constant

m = mass of the adsorbed molecule

M_{cat} = catalyst weight

N_{ads} = moles of adsorbate

$N_{ads,max}$ = moles of adsorbate at saturation

$n_{CO,ads}$ = Moles of CO adsorbed on the active sites

$n_{O,surf}$ = Superficial oxygen

$\dot{n}_{CO_2}$ = molar flowrate of CO_2

$n_{O_2,tot}$ = Total moles of O_2

$n_{O_2,line}$ = Moles of O_2 in the lines

$n_{O_2,cat}$ = Moles of O_2 in the catalyst

$n_{CO_2,tot}$ = Total moles of CO_2

$\dot{n}_C^{in}$ = molar flowrate of carbon exiting the reactor

$\dot{n}_C^{out}$ = molar flowrate of carbon fed

$O_{2,\,gas}$ = Oxygen in the gas phase

$O_{(l)}$ calculated = Calculated oxygen from the catalyst correlated to CO_2 production

$O_{(l)}$ stoich = Theorical oxygen from the catalyst

$\dot{V}_{tot}$ = Total volumetric flowrate

Greek letters:

α = Surface

β = Bulk
γ = Grain boundary
Θ = fraction of coverage of active sites
$\rho_{act.site}$ = density of superficial active sites
$\rho_{O,sur}$ = density of superficial oxygen

<u>Acronyms:</u>

EDS = Energy Dispersive X-ray Spectrometry
BSE = Back-Scattered Electron Detector
FTIR = Fourier-Transform Infrared Spectrometer
MS = Mass Spectrometer
PGM = Platinum-Group Metal
(E)SEM = (Environmental)Scanning electron microscope
TPR = Temperature programmed reduction
TPO = Temperature programmed oxidation
TPD = Temperature programmed desorption
TWC = Three-Way Catalyst
XRD = X-Ray Diffraction

References

[1] V. Masson-Delmotte, P. Zhai, Y. Chen, L. Goldfarb, M.I. Gomis, J.B.R. Matthews, S. Berger, M. Huang, O. Yelekçi, R. Yu, B. Zhou, E. Lonnoy, T.K. Maycock, T. Waterfield, K. Leitzell, N. Caud, Working Group I-Contribution to the Sixth Assessment Report of the Intergovernmental Panel on Climate Change, 2021. www.ipcc.ch.

[2] K.C. Taylor, Automobile Catalytic Converters, Springer, Berlin, Heidelberg, 1984.

[3] Study on the EU's list of Critical Raw Materials (2020) Final Report, (n.d.). https://doi.org/10.2873/904613.

[4] D. Bhattacharya, S. Kole, O. Kizilkaya, J. Strzalka, P.P. Angelopoulou, G. Sakellariou, D. Cao, C.G. Arges, Electrolysis on a Chip with Tunable Thin Film Nanostructured PGM Electrocatalysts Generated from Self-Assembled Block Copolymer Templates, Small. 17 (2021). https://doi.org/10.1002/smll.202100437.

[5] L. Du, V. Prabhakaran, X. Xie, S. Park, Y. Wang, Y. Shao, Low-PGM and PGM-Free Catalysts for Proton Exchange Membrane Fuel Cells: Stability Challenges and Material Solutions, Advanced Materials. 33 (2021). https://doi.org/10.1002/adma.201908232.

[6] A.E. Hughes, N. Haque, S.A. Northey, S. Giddey, Platinum group metals: A review of resources, production and usage with a focus on catalysts, Resources. 10 (2021). https://doi.org/10.3390/resources10090093.

[7] Price charts - Johnson Matthey, (2021). http://www.platinum.matthey.com/prices/price-charts#.

[8] K. Everaert, J. Baeyens, Catalytic combustion of volatile organic compounds, Journal of Hazardous Materials. 109 (2004) 113–139. https://doi.org/10.1016/j.jhazmat.2004.03.019.

[9] H. Asakura, M. Kirihara, K. Fujita, S. Hosokawa, S. Kikkawa, K. Teramura, T. Tanaka, Fe-Modified CuNi Alloy Catalyst as a Nonprecious Metal Catalyst for Three-Way Catalysis, Industrial and Engineering Chemistry Research. 59 (2020) 19907–19917. https://doi.org/10.1021/acs.iecr.0c03389.

[10] B. Seyfi, M. Baghalha, H. Kazemian, Modified LaCoO3 nano-perovskite catalysts for the environmental application of automotive CO oxidation, Chemical Engineering Journal. 148 (2009) 306–311. https://doi.org/10.1016/j.cej.2008.08.041.

[11] G. Pecchi, M.G. Jiliberto, A. Buljan, E.J. Delgado, Relation between defects and catalytic activity of calcium doped LaFeO 3 perovskite, Solid State Ionics. 187 (2011) 27–32. https://doi.org/10.1016/j.ssi.2011.02.014.

[12] D. Ferri, L. Forni, Methane combustion on some perovskite-like mixed oxides, Applied Catalysis B: Environmental. 16 (1998) 119–126.

[13] A. Glisenti, M. Pacella, M. Guiotto, M.M. Natile, P. Canu, Largely Cu-doped LaCo1-xCuxO3 perovskites for TWC: Toward new PGM-free catalysts, Applied Catalysis B: Environmental. 180 (2016) 94–105. https://doi.org/10.1016/j.apcatb.2015.06.017.

[14] B. Viswanathan, CO Oxidation and NO Reduction on Perovskite Oxides, Catalysis Reviews. 34 (1992) 337–354. https://doi.org/10.1080/01614949208016316.

[15] S. Keav, S.K. Matam, D. Ferri, A. Weidenkaff, Structured perovskite-based catalysts and their application as Three-Way Catalytic converters-a review, Catalysts. 4 (2014) 226–255. https://doi.org/10.3390/catal4030226.

[16] A. Garbujo, M. Pacella, M.M. Natile, M. Guiotto, J. Fabro, P. Canu, A. Glisenti, On A-doping strategy for tuning the TWC catalytic performance of perovskite based catalysts, Applied Catalysis A: General. 544 (2017) 94–107. https://doi.org/10.1016/j.apcata.2017.07.009.

[17] K. Christmann, Technical applications of adsorption, Berlin, 2012.

[18] E.N. Sgourou, Y. Panayiotatos, K. Davazoglou, A.L. Solovjov, R. v. Vovk, A. Chroneos, Self-diffusion in perovskite and perovskite related oxides: Insights from modelling, Applied Sciences (Switzerland). 10 (2020). https://doi.org/10.3390/app10072286.

[19] S. Royer, D. Duprez, S. Kaliaguine, Oxygen mobility in LaCoO3 perovskites, in: Catalysis Today, 2006: pp. 99–102. https://doi.org/10.1016/j.cattod.2005.11.020.

[20] N. Sakai, T. Ho&a, H. Yokokawa, M. Dokiya, T. Kawadab, Oxygen permeation measurement of La1-x CaxCrO3-δ by using an electrochemical method, Solid State Ionics. 86 (1996) 1273–1278.

[21] J. Wu, J.P. Dacquin, C. Cordier, C. Dujardin, P. Granger, Optimization of the Composition of Perovskite Type Materials for Further Elaboration of Four-Way Catalysts for Gasoline Engine, Topics in Catalysis. 62 (2019) 368–375. https://doi.org/10.1007/s11244-018-1083-2.

[22] W. Yang, R. Zhang, B. Chen, N. Bion, D. Duprez, S. Royer, Activity of perovskite-type mixed oxides for the low-temperature CO oxidation: Evidence of oxygen species participation from the solid, Journal of Catalysis. 295 (2012) 45–58. https://doi.org/10.1016/j.jcat.2012.07.022.

[23] P. v. Gosavi, R.B. Biniwale, Pure phase LaFeO3 perovskite with improved surface area synthesized using different routes and its characterization, Materials Chemistry and Physics. 119 (2010) 324–329. https://doi.org/10.1016/j.matchemphys.2009.09.005.

[24] M. Salavati-Niasari, G. Hosseinzadeh, F. Davar, Synthesis of lanthanum carbonate nanoparticles via sonochemical method for preparation of lanthanum hydroxide and lanthanum oxide nanoparticles, Journal of Alloys and Compounds. 509 (2011) 134–140. https://doi.org/10.1016/j.jallcom.2010.09.006.

[25] Y. Yokoi, H. Uchida, Catalytic activity of perovskite-type oxide catalysts for direct decomposition of NO: Correlation between cluster model calculations and temperature-programmed desorption experiments, Catalysis Today. 42 (1998) 167–174.

[26] W. Yang, R. Zhang, B. Chen, D. Duprez, S. Royer, New aspects on the mechanism of C3H6 Selective catalytic reduction of NO in the Presence of O2 over LaFe 1-x(Cu, Pd)xO3-δ perovskites, Environmental Science and Technology. 46 (2012) 11280–11288. https://doi.org/10.1021/es302240m.

[27] T. Nitadori' And, M. Misono, Catalytic Properties of La,-,A:Fe03 (A' = Sr,Ce) and La,-.Ce,Co03, JOURNAL OF CATALYSIS. 93 (1985) 459–466.

[28] P. Xiao, L. Zhong, J. Zhu, J. Hong, J. Li, H. Li, Y. Zhu, CO and soot oxidation over macroporous perovskite LaFeO3, Catalysis Today. 258 (2015) 660–667. https://doi.org/10.1016/j.cattod.2015.01.007.

[29] W. Yang, R. Zhang, B. Chen, N. Bion, D. Duprez, S. Royer, Activity of perovskite-type mixed oxides for the low-temperature CO oxidation: Evidence of oxygen species participation from the solid, Journal of Catalysis. 295 (2012) 45–58. https://doi.org/10.1016/j.jcat.2012.07.022.

Chapter 8

Utilization of CuY zeolites in methane-to-methanol conversion: preliminary investigations on CH_4 activation

Abstract

The direct conversion of CH_4 into CH_3OH on Cu-exchanged zeolites is a potential pathway to efficiently utilize this abundant gas. However, the commercialization of the process is still far from its implementation as the catalytic system (catalyst and reaction conditions) should be designed in such a way that the catalyst exhibits a dominant kinetic preference towards CH_3OH using optimal process parameters. A well-known strategy to overcome selectivity issues is built on the application of a chemical-looping process (MTM) in which O_2 and CH_4 are fed in separate steps. The reaction is then divided into three stages: oxidative activation, CH_4 activation and CH_3OH extraction. In this preliminary study, CH_4 activation step was brought into focus. Specifically, two Y zeolites with different Cu/Al (0.345 and 0.604) and Si/Al (2.9 and 30.8) ratio have been synthesised with a standard liquid ion-exchange procedure and characterized with XRD, ICP-MS, nitrogen adsorption-desorption, SEM, FTIR and Raman technique. CH_4-TPR and CH_4 isothermal adsorption and temperature-programmed desorption in inert flow have been performed to obtain information on the redox properties of the materials and identify a potential (optimal) temperature for the isothermal CH_4 activation in the MTM loop. The choice was based on the trade-off between maximum CH_4 consumption and selectivity (no secondary reactions). Samples performance during CH_4-TPR showed a similar behaviour, but the zeolite characterized with a Cu/Al of 0.604 and Si/Al ratio of 30.8 was the most active material as the total CH_4 consumed was 616 μmol/g zeolite compared to 379 μmol/g zeolite of the second sample. Also, the maximum CH_4 consumption peak was observed at 200°C while secondary reactions (reverse water-gas shift and CH_4 dry reforming) activate at 300°C. The maximum CH_4 uptake capacity was retrieved from CH_4 adsorption, in which a value 90% higher than the CH_4 consumed during the CH_4-TPR was calculated for both zeolites. This result suggests the existence of CH_4 diffusion limitations in the zeolite pore system. These mass-transfer limitations are overcome at higher temperatures (> 400°C) when unreacted CH_4 starts

desorbing from the zeolite framework and simultaneously producing overoxidation products (CO, CO_2).

Introduction

Methane is an abundant component of natural gas and shale gas from which it could be inexpensively extracted. Due to the high cost for transportation, methane streams are usually flared or vented in the atmosphere with negative effects on climate change (GWP for CO_2 is 1 and 28 for methane) [1]. The on-site conversion of methane into high added value commodities, such as methanol or lighter alkanes, represents an environmental-friendly alternative to increase the extraction yield [2]. However, the current technologies (e.g. steam reforming followed by a Fisher-Tropsch to hydrocarbons or methanol) to convert methane into chemicals at large-scale process cannot be economically applied at small scale due to multiple stages (syngas is produced as intermediate) and high temperatures [3]. A low-cost, catalytic and small-scale direct process is then required to replace the indirect route of methane utilization. The direct selective oxidation of methane-to-methanol (MTM) is proposed as a potential and highly effective conversion route [4–6]. Methane is a very chemically stable molecule difficult to activate due to its high symmetry, low polarizability, high ionization energy and strong C-H bond (~440 kJ/mol) [7]. Since the enthalpy of CH_4 partial oxidation to CH_3OH is 1/6 of the total combustion enthalpy and the C-H bond energy in CH_3OH (~47 kJ/mol) is weaker than the CH_4 one, the process is largely limited by a significant trade-off between selectivity and conversion [8]. Therefore, the development of an efficient catalytic system to selectively produce CH_3OH from direct CH_4 oxidation is critical.

Metal-containing zeolites represents a potential alternative to efficiently obtain CH_3OH from the partial oxidation of CH_4 [9–11]. Various factors such as the type of metal active species, the structure/composition of the zeolite and reaction conditions should be considered to produce CH_3OH selectively and overcome overoxidation issues [11,12]. These features and their combination influence the activation barrier energy for breaking the H-CH_3 bond, which is the rate-determining step of the reaction, and the shape selectivity that directs the reaction to specific products. Copper is usually chosen as active species since it has a better reactivity towards CH_4 than other transition metals (Fe, Co, Ni) and related Cu-oxo sites are stabilized in the nanometric and sub-nanometric range inside the zeolite microporous structure. As a matter of fact, the zeolite structural variety (pore size, channel systems, pockets and cages) governs the formation of different Cu-oxo species (mono-, bi- tri-nuclear Cu species) [13–15]. Small-pore zeolites such as MOR, MAZ, MFI and CHA achieve a better CH_4 reactivity and CH_3OH selectivity compared to medium and large-pore ones (FAU, BEA) thanks to the favourable crystallographic location of Cu-oxo sites, Cu-O-Cu orientation angle and lower C-H dissociation energies [16]. Certainly, CH_3OH production is not only influenced by the proprieties of the catalyst, but also the contribution of reaction conditions is significant [12]. The combination of a less performing material with suitable experimental parameters (temperature, reagents concentration, contact time, etc.) can improve the overall activity of the process, as it was observed for Cu-FAU [16,17]. Y zeolites are FAU-type molecular sieves have a pore and supercage dimension of 7.4 Å and 13 Å respectively and a three-dimensional pore structure. Their peculiar property of selective molecules diffusion for specific sizes is largely utilized in petroleum industry for catalytic cracking of petroleum into gasoline range hydrocarbons [18], fluid catalytic cracking [19] and NO_x storage-reduction [20] as the larger intercrystallite void space and pore volume as well as external surface aid sites display a higher activity and stability [21]. Thanks to their large availability and knowledge in petrochemical processes, Y-zeolite represents a potential active and convenient material for CH_4 conversion into CH_3OH.

A well-known strategy to overcome selectivity issues and restrain the total CH_4 oxidation is built on the application of a chemical-looping process in which O_2 and CH_4 feeds are separated [12,16,22,23]. The reaction is then divided into three steps: oxidative activation, CH_4 activation and CH_3OH extraction, in which the first step is required to generate Cu_xO_y precursors of Cu-oxo active species that can activate CH_4 and stabilize the reaction intermediates. Lastly, H_2O is used as a solvent to desorb CH_3OH from the zeolite pores by decreasing the desorption energy [24].

In this preliminary work, two Y zeolite supports with different Si/Al ratios (2.9, 30.8) with two distinct Cu/Al ratios (0.345, 0.608) were Cu-exchanged with a standard liquid ion exchange their activity towards CH_4 activation was assessed as an exploratory investigation for further use in MTM reaction. Specifically, samples were characterized with physicochemical techniques (XRD, ICP-MS, nitrogen adsorption-desorption, SEM, FTIR and Raman) and their redox properties and reactivity towards CH_4 activation was tested with CH_4-TPR (temperature-programmed reduction) and CH_4 adsorption and He-TPD (temperature-programmed desorption) experiments.

Materials and methods

Liquid-ion exchange of copper

The two samples used in this study were prepared with a standard aqueous ion-exchange in copper(II) acetate solution $Cu(CH_3COO)_2$ of commercial Y zeolites in NH_4^+ (CBV 500) and H^+ (CBV 760) form purchased from Zeolyst International. Prior to the Cu ion-exchange procedure, CBV 500 zeolite was calcined at 500°C for 3h to transform the NH_4^+ into the H^+ form. The copper acetate salt (Sigma Aldrich) was diluted in distilled H_2O to obtain 2L of the corresponding solution at 0.015M. Depending on the Cu/Al ratio of each sample, 10 g of the parent zeolites were stirred with the calculated copper acetate volume for 4h. Specifically, 0.345 Cu/Al ratio on CBV 500 sample was obtained with 1.41 L of the prepared solution, while a higher Cu/Al ratio of 0.604 was achieved with 0.16 L as the Al content is lower (1.3% in CBV 760 and 11.6% in CBV 500). An ammonia solution (NH_4OH) was added drop by drop every 2 h to adjust the pH in between 5.2 and 5.7 to avoid Cu precipitation while continuously stirred. The solvent was then removed by filtering the solution in vacuum conditions and washed three times with deionized H_2O to remove the excess of Cu ions. The two samples were then dried overnight at 100C° and then calcined at 550°C for 6h in a static air condition. Samples are identified as *x*CuY*z*, in which *x* is the Cu/Al ratio and *z* corresponds to Si/Al ratio.

Characterizations

Elemental analysis was carried out with an HR-ICP-MS Element 2 instrument from Thermo Scientific, in which the samples were previously dissolved in hydrofluoric acid. X-Ray Diffraction (XRD) patterns were obtained on a Siemens Bruker D5000 with a Bragg-Brentano geometry and $CuK\alpha_1$ with wavelength λ=1.5406 Å to determine the phase purity and crystallinity of the Cu-exchange zeolites. Nitrogen adsorption-desorption isotherms were recorded on BELSORP MINI II system (BEL Japan) at -196°C and prior to the analysis the samples were pre-treated in vacuum atmosphere at 80°C for 1 h and then heated up to 150°C for 2h. Scanning Electron Microscopy (SEM) analyses of the two samples (dispersed on a Si wafer without any coating) were collected on a Hitachi SU8230 SEM with a SE2/ESB detector in high vacuum. Fourier-transform infrared spectroscopy (FTIR) measurements were carried out on a Bruker Vertex 80 with Mercury-Cadmium-Telluride (MCT) detector. Self-supported thin wafers were prepared by using 20 mg of powdered sample previously sieved (<150 μm), pressed (2.5-ton max) and positioned inside a standard FTIR reactor cell with KBr windows by AABSPEC (5 #2000-A multimode). Prior to the analysis, sample were dehydrated at 300°C for 1h in vacuum conditions (1E-03 bar) directly in the IR cell. The measurement was performed at atmospheric pressure, in transmittance mode and with a resolution of 4 cm^{-1} (32 number of scans). Raman spectra were obtained with a Horiba LabRamanHR microscope with a Coherent Sapphire laser (OPSL) emitting at 488 nm. The backscattered Raman signal was scattered over a 2400 lines/mm grating onto a thermoelectrically cooled CCD detector and a 50x objective lens was focusing the excitation beam onto the sample. The catalysts were activated directly inside borosilicate glass capillaries (diameter of 0.3 mm and 0.1 mm of wall thickness) then inserted in fine drilled holes in a metallic copper block and positioned inside a muffle-oven. The activation protocol consisted of heating at 3°C/min in static air to 550°C and kept for 12h and subsequently the open-end capillaries were sealed with a flame to avoid rehydration while residing in the oven at 550°C. Capillaries were then slowly cooled to room temperature to avoid cracks due to thermal shocks.

Activity testing

CH_4-TPR and their prior oxidative activation experiments were performed on the two Cu-exchanged zeolites on a standard catalytic testing rig. 100 mg of the Cu-exchanged samples (0.345CuY2.9 and 0.604CuY30.8) with a particle size range of 250-300 μm were inserted into a stainless-steel U-tube (ID 4 mm) and kept in position with two quartz wool layers, approximating the reactor to a plug-flow configuration. Pure gases (CH_4, O_2, He) bottles were connected to mass-flowmeters (Brooks) and the desired inlet composition was achieved. Before entering the reactor, the gas feed went through a manual four-way valve (Swagelok) to ensure the complete separation between the reducing and oxidizing atmosphere. An electrically heated furnace (Watlow) was used to heat up the catalytic bed and two thermocouples (type K, 1/16”) were used to monitor and control the temperature in different positions: one thermocouple was placed inside the reactor and close to the upper surface of the catalytic bed (monitoring temperature) while the second thermocouple was anchored to the external part of the tube at the same height of the catalytic bed (controlling temperature). Temperature programs were set on the thermoregulator (Omron) with a purpose-built LabView executable software. Profiles of CH_4 and products concentrations were plotted as a function of the monitoring temperature as it is a better approximation of the catalytic bed temperature and it is more sensitive to thermal effects produced by the heat of reaction. Also, the monitoring temperature was corrected for the dead-volume between the thermocouple position and the gas-analysis detector with the following correlation: $T = T_{meas} + \beta(\frac{V_t}{\dot{V}_{tot}})$, in which T_{meas} = temperature measured by the thermocouple [°C], β = heating rate [°C/min], V_t = tubing volume [cm^3] and $\dot{V}_{tot}$= total volumetric flowrate [Ncm^3/min]. To avoid H_2O condensation and remove humidity traces in the system, the lines were heated up to 80°C with heating wires. The outlet gas analysis was performed with an online quadrupole mass-spectrometer (Pfeiffer Omnistar) with SEM detector. Calibrations of the key masses (*m/z* 2, *m/z* 15, *m/z* 16, *m/z* 18, *m/z* 28, *m/z* 31, *m/z* 44) were performed by normalizing the ion currents to the internal standard (*m/z* 4) and linear function with R^2> 0.995 were found in the analysed concentration range.

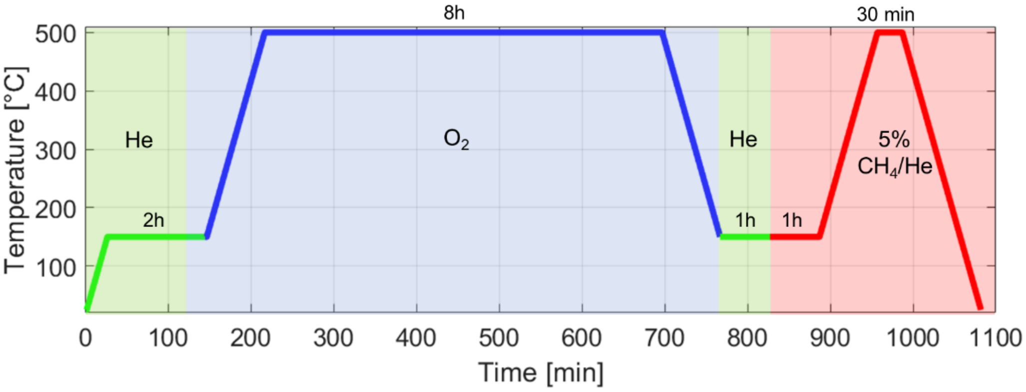

***Figure 1**: Experimental protocol for CH_4-TPR on 0.645CuY2.9 and 0.604CuY30.8 (m_s=250-300μm, $\dot{V}_{tot}$=20 Ncm^3/min, β = 5°C/min).*

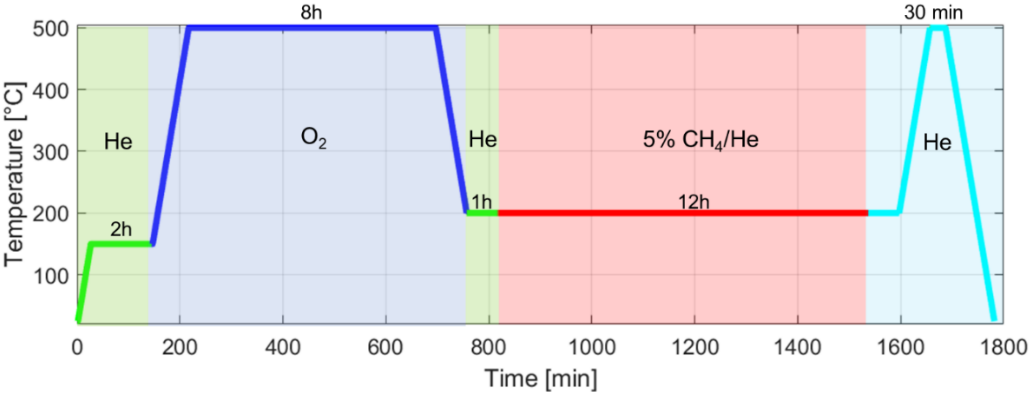

***Figure 2**: Experimental protocol for CH_4 adsorption and desorption on 0.645CuY2.9 and 0.604CuY30.8 (m_s=250-300μm, $\dot{V}_{tot}$=20 Ncm^3/min, β = 5°C/min).*

CH_4-TPR experimental protocol consists of four steps: oxidative pre-treatment in neat O_2 flow (20 Ncm^3/min for 8h at 500°C), inert pre-treatment (He at 150°C for 2h) and CH_4 reaction (20 Ncm^3/min, 5%CH_4/He, 5°C/min up to 500°C for 30 min) and naturally cooling at room temperature. Between each step, the system was flushed for 1h with He (50 Ncm^3/min) and before CH_4-TPR the mixture with desired composition was fed into the MS for 1h bypassing the reactor to obtain the initial baseline. CH_4 adsorption experiments followed the same protocol but the adsorption step was performed isothermally at 200°C and held for 12h with a flowrate of 20 Ncm^3/min of 5%CH_4/He. Subsequently, desorption was carried out in an inert flow (20 Ncm^3/min of neat He) and temperature was raised at 5°C/min up to 500°C. Schematic representations of the experimental protocols are reported in Figure 1 and Figure 2.

Results and discussion

Characterization analyses

0.345CuY2.9 and 0.604CuY30.8 samples were characterized with different techniques to extract the chemical features of the Cu-ion exchanged zeolites after calcination. Specifically, ICP-MS and unit cell values (Table 1), XRD (Figure 3), Nitrogen-adsorption and desorption (Figure 4), SEM (Figure 5), FT-IR (Figure 6) and Raman spectra (Figure 7).

***Table 1**: ICP-MS results and unit cell values for 0.345CuY2.9 and 0.604CuY30.*

	0.345CuY2.9	**0.604CuY30.8**
Al [%]	11.0	1.39
Cu [%]	3.8	0.84
Si [%]	31.5	42.8
Cu/Al [-]	0.345	0.604
Si/Al [-]	2.9	30.8
Unit cell [Å]	24.4585	24.2587

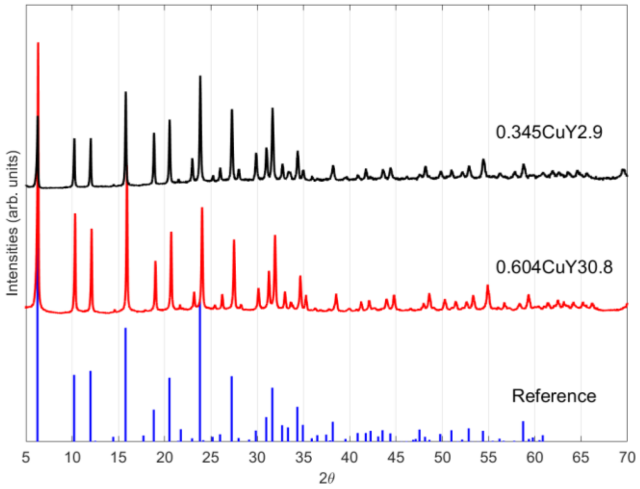

***Figure 3**: XRD patterns of 0.345CuY2.9 (black), 0.604CuY30.8 (red) and reference Y-zeolite (blue) $Cu_{28.1}Na_{4.8}Al_{64}Si_{128}O_{384}$, code 4002504* [25].

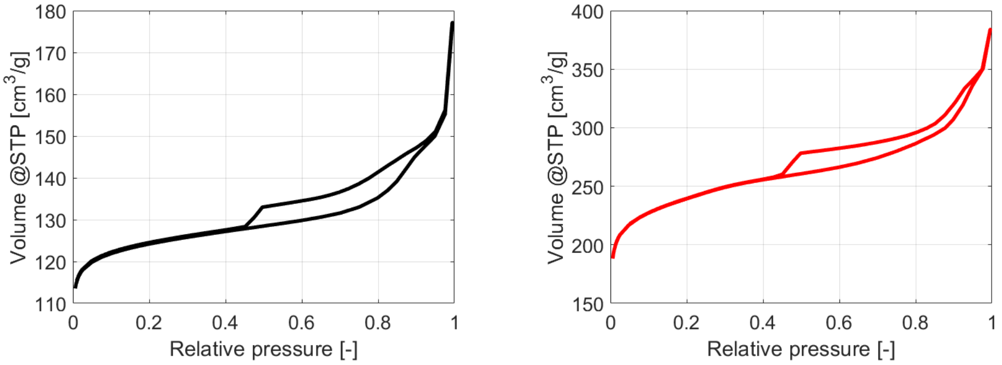

***Figure 4**: Nitrogen adsorption− desorption data plots on 0.345CuY2.9 (black) and 0.604CuY30.8 (red)*

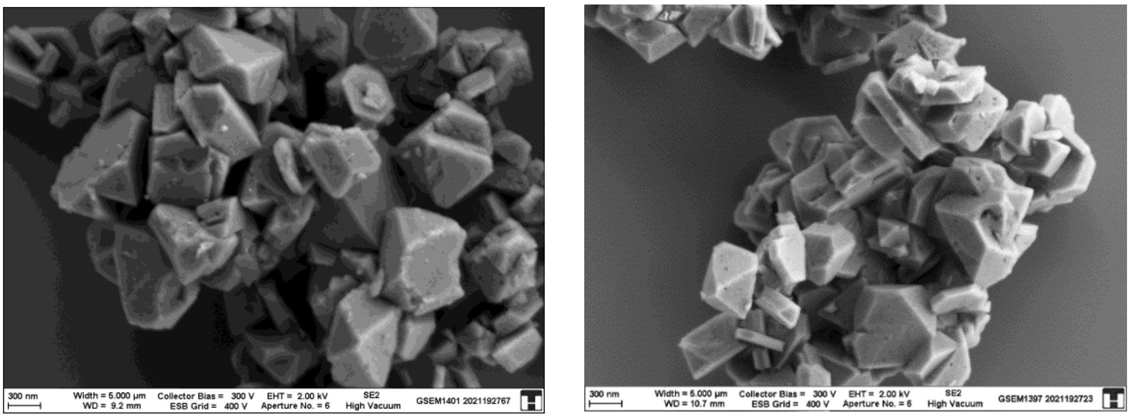

a) b)

***Figure 5**: SEM images of 0.345CuY2.9 (a) and 0.604CuY30.8 (b).*

Table 1 reports the elemental composition of the samples with a largely different Si/Al (2.9 and 30.8) and Cu/Al ratio (0.345 and 0.609), in which the higher amount of Al in 0.604CuY30.8 zeolite is associated to a larger unit cell retrieved from XRD analysis. Specifically, the removal of Al atoms changes the acidity of the catalyst and chemical properties reflecting on variations in reactivity of the acid sites and subsequently to the overall zeolite reactivity [26]. The powder XRD patterns of the Cu-exchanged samples (Figure 3) shows only the characteristic peaks of the Y-zeolite framework and no extra-phases or impurities are detected as the comparison with the reference patterns demonstrates. Nitrogen adsorption-desorption plots (Figure 4) exhibit a Type IV-H4 isotherm typical of mesoporous solids with cut-like pores with internal void of irregular form and broad size distribution [27]. SEM images (Figure 5) show that the ion-exchange procedure was efficient in producing homogenous structures with no Cu agglomerates visible at SEM analysis scale.

FT-IR spectra (Figure 6) were acquired to determine the surface morphology and acidic features of both samples. The region band between 3900 cm^{-1} and 3400 cm^{-1} reveals the nature of hydroxyl groups (OH-) attached to the zeolite lattice and the highlighted wavenumbers are assigned to peculiar OH-groups relevant in the reactivity towards organic molecules, such as OH-groups on- and extra-framework Al species together with their Brønsted and Lewis acidity.

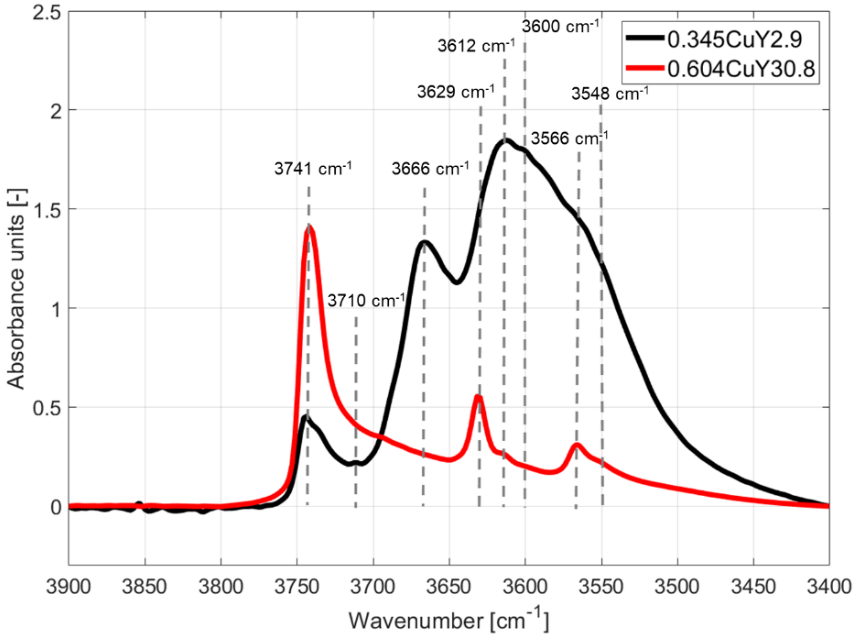

***Figure 6**: FTIR spectra of 0.345CuY2.9 (black) and 0.604CuY30.8 (red), dehydrated and inert conditions, resolution of 4 cm^{-1}.*

Three well-distinct features could be observed in the OH stretching region of 0.604CuY30.8 sample: 3741 cm^{-1}, 3629 cm^{-1} and 3566 cm^{-1}. These wavelengths correspond to the modes of terminal silanols at the external surface, Brønsted acid sites in the supercage (High Frequency (HF) hydroxyls) and low frequency band (LF), assigned to Brønsted acidicH-groups located in the sodalith cage. The small low-frequency shoulders observed for the HF and LF bands in the 0.604CuY30.8 sample are related to the interaction of the corresponding hydroxyl groups with small amounts of remaining EFAL in the samples. This effect is much more pronounced for the 0.345CuY2.9 sample, which contains much more aluminium in the framework and outside the framework (EFAL, due to steaming). The large band at 3666 cm-1 is related to OH-groups from EFAL and the broadness of the bands is related to extensive hydrogen bridging between the various families of hydroxyl-groups. The strong reduction of the terminal silanol band for the 0.345CuY2.9 sample, indicates that some of the EFAL has been deposited at the external surface.

Raman spectra of Cu-exchanged samples (0.345CuY2.9 and 0.604CuY30.8) as well as the parent Y-support (Y2.9 and Y30.8) are reported in Figure 7 to identify the difference ascribed to the Cu-ion exchange process. These results could provide information on the Si/Al ratio in the framework, extra-framework Al sites and the interaction with the framework together with the level of ion-exchanged Cu cations and extra-framework Cu-O clusters from mononuclear to polynuclear size.

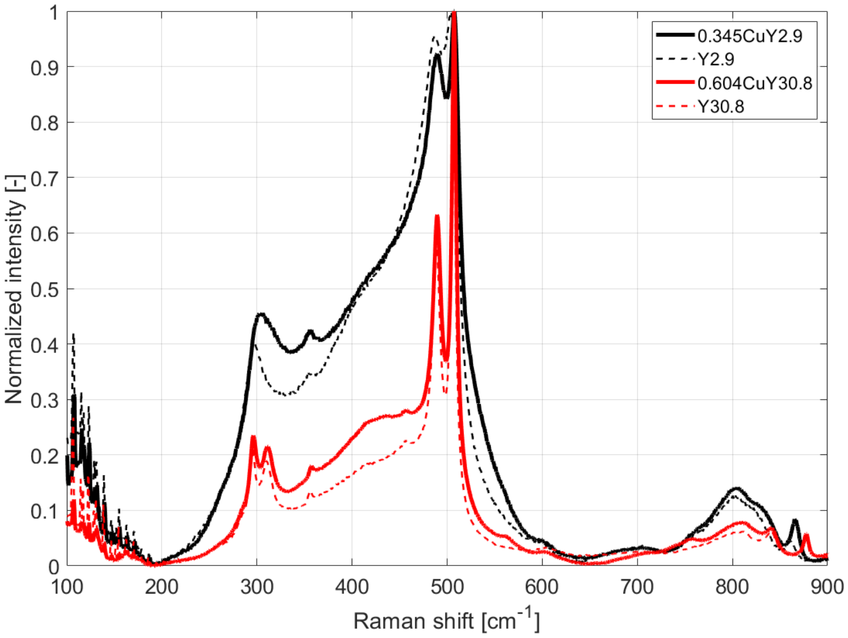

***Figure** 7: Normalized Raman spectra of 0.345CuY2.9 (black, solid line) and 0.604CuY30.8 (red, solid line) samples as well as Y2.9 (dashed line, black) and Y30.8 (dashed line, red) parent zeolites, collected with a blue laser (488 nm).*

The topology characteristic ring vibrations (from 200 cm^{-1} to 600 cm^{-1}) shows the ring opening specific vibrations that cause simultaneous stretching and/or bending of Si-O-(Si,Al) bonds with respect to the main axis ring [28]. The steaming procedure to obtain the Y-parent (zeolite Na-Y) materials splits and narrows the bands related to ring vibrations (489 cm^{-1} and 506 cm^{-1}). The relative intensity of 489 cm^{-1} band changes with Si/Al ratio, decreasing at increased Si/Al ratio as lower amount of Al in the framework produces more well-defined and sharper bands. The Cu ion-exchange and air activation generates peculiar features at increasing Cu content. Specifically, the band at 570 cm^{-1} shifts at higher wavenumbers at increasing Cu/Al ratio as Cu is interacting with Al-sites in the framework. In the analysed samples in Figure 7, a small band increase at 561 cm^{-1} and 755 cm^{-1} is visible for the 0.604CuY30.8 compared to Y30.8 sample without Cu content while in the 0.345CuY2.9 sample is not showing any difference at the same wavenumber with respect to Y2.9. However, no clear evidence of the Cu-activated species on the ion-exchanged samples are noticeable on the Raman spectra and this feature could be associated to Raman fluorescence issues when analysing Cu-containing materials.

CH_4-TPR

The application of CH_4-TPR experiments to 0.345CuY2.9 (Figure 8) and 0.604CuY30.8 (Figure 9) catalysts was performed to gain useful information on their reducing-oxidizing properties as well as the reactivity towards CH_4 in absence of gaseous O_2. Furthermore, it was possible to identify the optimal temperature to maximise CH_4 consumption during the isothermal CH_4 activation in MTM loop, increasing the selectivity by avoiding the production of overoxidation and secondary reaction products. Results are presented as concentration profiles of consumed CH_4 and produced H_2, H_2O, CO, CH_3OH and CO_2 as a function of the monitoring temperature together with quantification data on the total CH_4 consumed. Also, the parent zeolite Y30.8 was tested to verify the negligible contribution in the CH_4 consumption.

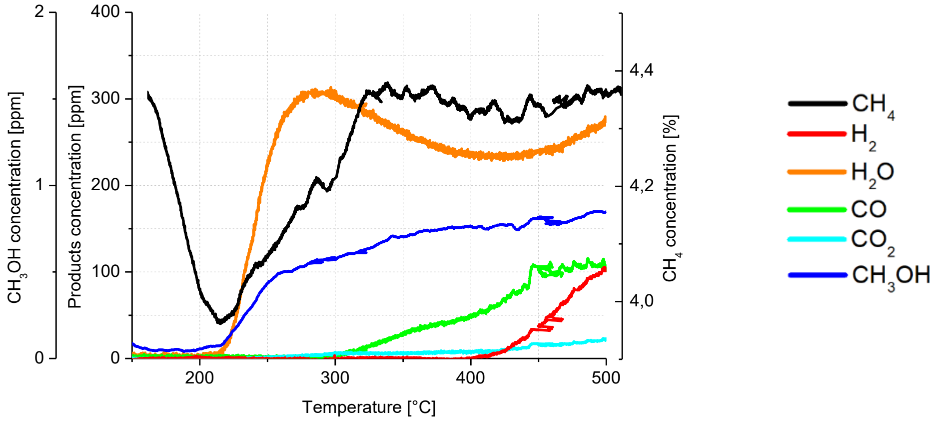

***Figure 8**: CH_4-TPR on 0.345CuY2.9 (mass= 100 mg, particle size= 250 - 300 μm, total volumetric flowrate = 20 Ncm^3/min, CH_4 initial concentration= 5%, heating rate= 5°C/min).*

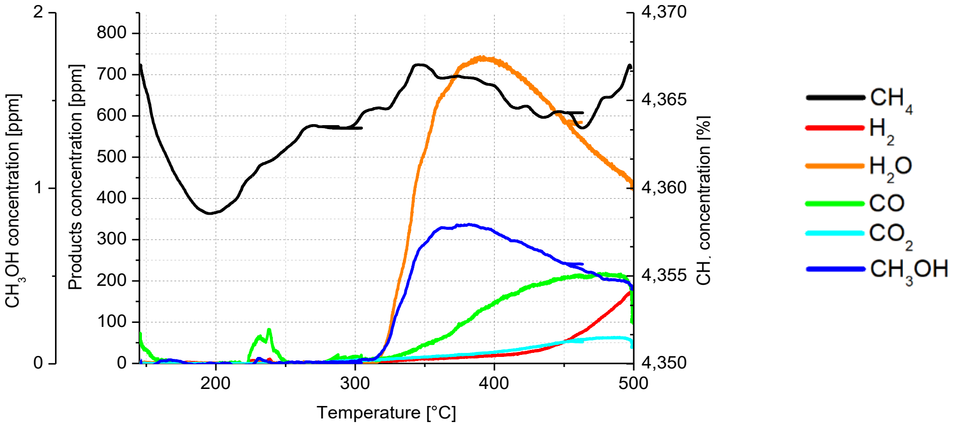

***Figure 9**: CH_4-TPR on 0.604CuY30.8 (mass= 100 mg, particle size= 250 - 300 μm, total volumetric flowrate = 20 Ncm^3/min, CH_4 initial concentration= 5%, heating rate= 5°C/min).*

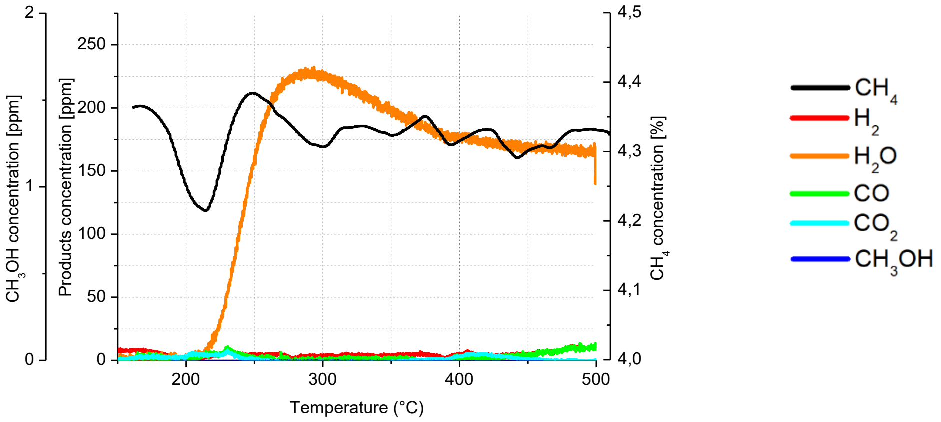

***Figure 10**: CH_4-TPR on Y30.8 (mass= 100 mg, particle size= 250 - 300 µm, total volumetric flowrate = 20 Ncm^3/min, CH_4 initial concentration= 5%, heating rate= 5°C/min).*

The concentration profiles of several gas species (H_2, CH_4, H_2O, CO, CH_3OH and CO_2) were recoreded during CH_4-TPR experiments on 0.345CuY2.9 and 0.604CuY30.8 samples and reported in Figure 8 and Figure 9 respectively. The selection of experimental parameters (catalyst mass, initial CH_4 concentration, total volumetric flowrate and heating rate) relied on the results presented in Chapter 1, in which the combination of these variables strongly affected the results. Even for a model system such as the reduction of unsupported CuO with H_2, mass-transfer limitations played an important role in the overall redox performance of the material. On the contrary, zeolites are characterized by a complex pore distribution and geometry of molecular dimension and the productivity could be constrained by mass-transfer phenomena of reacting molecules to the internal active sites. The two Cu-ion exchanged samples of this study exhibit a mesoporous structure (Figure 4) with irregular shape pores and thus the contribution of mass-transfer becomes even more crucial and it cannot be neglected when performing activity experiments. For these reasons, the total volumetric flowrate for CH_4-TPRs was chosen as a trade-off between the instrumental precision of controlling the flowrate and a low gas-hourly space velocity (GHSV). The value was set to 20 Ncm^3/min with a subsequent GHSV of 9540 h^{-1} for 0.345CuY2.9 and 4340 h^{-1} for 0.604CuY30.8 sample. The strongly reduced GHSV value for the second zeolite was caused by a lower bulk density, calculated through the catalyst mass and volume inside the reactor tube of the corresponding experiment (0.365 g/cm^3 for 0.345CuY2.9 versus 0.802 g/m^3 for 0.604CuY30.8). Also, the initial CH_4 concentration was chosen at 5% to ensure the absence of mass-transfer limitations by increasing the concentration gradient between the gas and solid phase as CH_4 starvation conditions are not likely to happen. A heating rate of 5°C/min was utilized to increase the temperature from 150°C to 500°C and ensure a unform temperature distribution inside the catalytic bed.

CH_4 consumption profiles in Figure 8 and Figure 9 have a similar trend, characterized by a major CH_4 peak around 200C° and a secondary peak at > 400°C. A slightly higher maximum reduction temperature (+7°C) is found for the 0.345CuY2.9 sample, denoting a reproducible reduction behaviour for both zeolites. However, quantification data on CH_4 consumption curves show a clear hierarchy of the activity performance, as that the total amount of consumed CH_4 is higher for the 0.604CuY30.8 zeolite, based on the total CH_4 mol and its value normalized on zeolite mass. Specifically, 3.79E-05 mol CH_4 (379 µmol/g zeolite) and 6.16E-05 mol (616 µmol/g zeolite) were consumed by 0.345CuY2.9 and 0.604CuY30.8 respectively. Negligible CH_4 consumption is visible in the Y30.8 sample (97 µmol/g zeolite) (Figure 10) as the active sites for CH_4 activation are Cu-oxo species in the zeolite framework [12,15,29,30] and the CH_4 consumption could be mainly attributed to physical adsorption at 204°C [31]. Simultaneously with CH_4 consumption, the production of other species is observable in the reaction profiles activated by secondary reactions. The formation of CO_2, H_2O, H_2 and CO are similar for both CuY zeolites in terms of activation temperatures but higher product concentrations are obtained in the 0.604CuY30.8 sample, implying a higher activity for both CH_4 oxidation and secondary reactions. The formation of CO_2 is an indication of CH_4 complete oxidation and its highest concentration is visible at 500°C, thus no production peak is observable for both samples. Also, the CO_2 appearance in the gas stream starts at ~300°C, i.e. 100°C higher than the CH_4 maximum consumption temperature. These features indicate both the formation of partially oxidised intermediates subsequently converting into CO_2 [16] and the high affinity of CuY polar sites towards CO_2 adsorption [32]. The lower CO_2 concentration visible in the outlet stream for 0.345CuY2.9 could be resulting from the lower Si/Al ratio that increases the interactions between the CO_2 quadrupole moment and cations/OH groups in the zeolite framework [32]. The CO_2 profile also indicates the presence of other reactions than CH_4 oxidation. From 300C°C to 400°C, the simultaneous occurrence of reverse-water gas shift (rWGS) (Reaction 1) and CH_4 steam reforming (Reaction 2.) could explain the consumption of CH_4 as well as the low concentration of CO_2 and H_2 in the outlet stream while CO concentration is increasing as product of both reactions. Specifically, H_2 is produced by Reaction 2 and it reacts with CO_2 to from CO and H_2O. H_2O concentration profile is not an accurate indication of the reactions progress as it is strongly influenced by extra-H_2O present in the system, thus any description based on H_2O is neglected.

$$CO_2 + H_2 \rightarrow CO + H_2O \qquad \text{Reaction 1}$$

$$CH_4 + H_2O \rightarrow CO + 3H_2 \qquad \text{Reaction 2}$$

Interestingly, a small amount of CH_3OH (< 1 ppm at 500°C) is produced during the CH_4-TPR and its appearance in the gas stream is associated to H_2O desorption. The use of H_2O to desorb CH_3OH formed on the Cu-oxo active sites on the zeolite is used in the MTM loop after the CH_4 activation step. It is indeed energetically difficult to desorb CH_3OH from the zeolite pores, but it is possible to decrease the adsorption energy using H_2O [6]. H_2O acts as a reactant as it reacts with the methoxy groups to form CH_3OH [33].

Activation temperatures of secondary reaction is a crucial information when selecting the optimal temperature for CH_4 activation in MTM compete loop based on CH_4-TPR data: the temperature of the isothermal operation should be chosen as a trade-off between the maximum CH_4 consumption temperature and the activation of secondary reactions such as CH_4 complete oxidation to increase the overall selectivity towards CH_3OH. Based on the results obtained for the CuY samples, 200C° was chosen as a potential optimal temperature for the CH_4 activation in MTM complete loop and therefore further investigations were performed with this value.

CH4 isothermal adsorption and He-TPD

CH_4 isothermal adsorption and inert temperature-programmed desorption (He-TPD) experiments were carried out on both Cu-exchanged zeolite samples to quantify the total CH_4 uptake at 200°C, compare it with results of CH_4 consumption extracted from CH_4-TPRs and observe the evolution of adsorbed species at increasing temperature. CH_4 isothermal adsorption was carried out at 200°C for 12h by feeding 5%CH_4/He and it was followed by a He-TPD at 5°C/min in He gas flow until 500°C. Desorption profiles of the major species (H_2, H_2O, CH_4, CO, CO_2) are reported in Figure 11 for 0.345CuY2.9 and Figure 12 for 0.604CuY30.8.

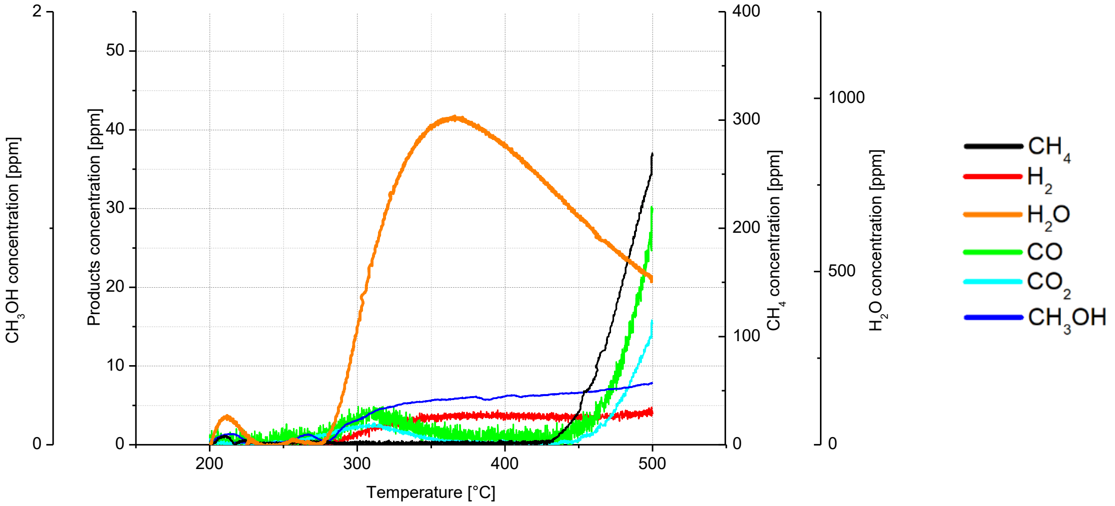

Figure 11: *He-TPD on 0.345CuY2.9 (mass= 100 mg, particle size= 250 - 300 μm, total volumetric flowrate = 20 Ncm^3/min, 100% He, heating rate= 5°C/min).*

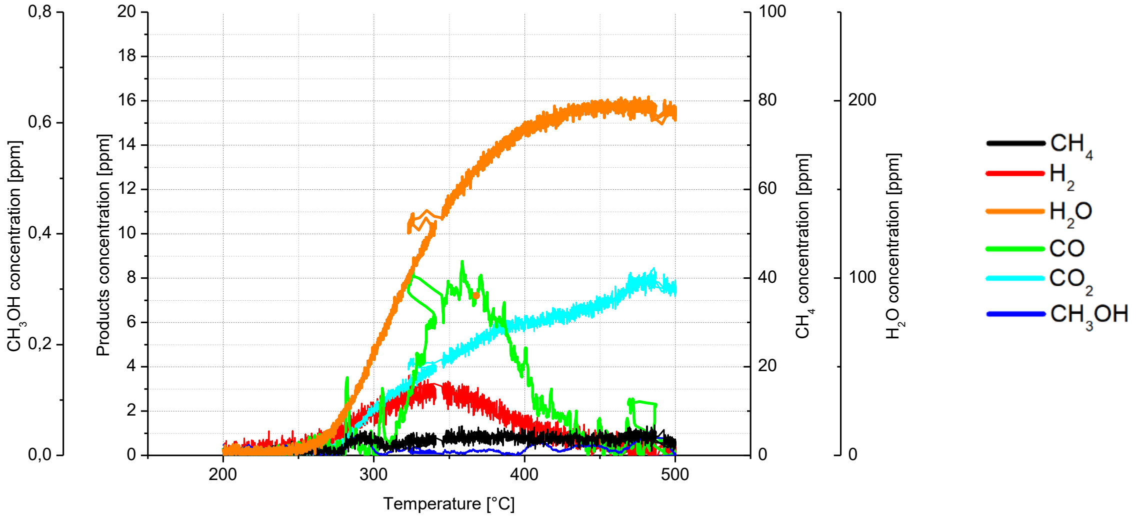

Figure 12: *He-TPD on 0.604CuY30.8 (mass= 100 mg, particle size= 250 - 300 μm, total volumetric flowrate = 20 Ncm^3/min, 100% He, heating rate= 5°C/min).*

The resulting profiles from desorption experiments show a different trend for 0.345CuY2.9 (Figure 11) and 0.604CuY30.8 samples (Figure 12). For the first zeolite, characterized by a lower Cu/Al and Si/Al ratio, a simultaneous CO and CO_2 peak is visible at 310°C suggesting the presence of Cu-oxo active sites specific for the total and partial oxidation of CH_4 (Reaction 3 and Reaction 4).

$CH_4 + 2O_2 \rightarrow CO_2 + 2H_2O$ Reaction 3

$CH_4 + 1/2O_2 \rightarrow CO + 2H_2$ Reaction 4

As the maximum concentration of CO and CO_2 is small (< 5 ppm) in the low temperature range (< 400°C), the density of Cu*x*O*y* nanoparticles promoting these oxidations is supposed to be low [34,35] and the small dimensions are confirmed also by SEM analyses (Figure 5) in which no large Cu particle agglomerates are visible on the surface. In the second sample (Figure 12), larger concentration of CO, CO_2 and H_2 are visible in the desorption profiles suggesting the presence of more active sites for CH_4 partial and total oxidation supported also by a higher Cu/Al ratio. The presence of Brønsted acid sites and divalent cations (Cu^{2+}) favours H_2O dissociation into $CuOH^+$ and H^+ species [36] that recombine to form H_2 and H_2O as visible in Figure 11 and Figure 12. Despite H_2O concentration profile is affected by the extra-H_2O present in the system, the correlation between CH_3OH desorption and H_2O is clear. Minimal amount of CH_3OH (maximum concentration < 0.5 ppm at 500°C for 0.345CuY2.9) starts to desorb at 260°C, i.e. 44°C higher than in the CH_4-TPR experiment (Figure 8). Also, a smaller H_2O peak is present around 205°C, corresponding to the CH_4 consumption peak in CH_4-TPR. The presence of double H_2O formation peaks suggests that only the first peak is associated to CH_4 oxidation while the second peak is connected to the desorption of extra-H_2O from the zeolite framework and, thanks to the higher H_2O concentration, also CH_3OH desorption is visible. A different situation is visible in the 0.604CuY30.8 zeolite, as the H_2O concentration is lower and thus negligible CH_3OH desorption is occurring. For 0.345CuY2.9 zeolite, three species start to desorb (CH_4, CO, CO_2) at higher temperatures (> 400°C) as an effect of the increased CH_4 diffusion from the internal pores [37] and consequent promotion of overoxidation reactions. The trend of these species is different in the desorption profiles of 0.604CuY30.8, in which clear H_2 and CO peaks are visible at low temperature (340-360°C) while the CO_2 formation continues to increase without a relevant peak with a similar behaviour observed in CH_4-TPR (Figure 9).

The total amount of CH_4 uptake during the adsorption experiments is 6120 μmol/g zeolite for 0.345CuY2.9 and 5630 μmol/g zeolite for 0.604CuY30.8. These values are largely higher (+90%) than the CH_4 consumption obtain within the CH_4-TPR experiments, implying that the adsorption process is limited by CH_4 diffusion into the 12-MR framework with a specific CH_4 diffusivity in the order of $10^{-9} – 10^{-8}$ m^2/s [37].

Conclusions

In this preliminary study, the feasibility of Cu-exchanged Y zeolites in MTM loop has been investigated by focusing the attention on the CH_4 activation step. Two Y zeolites with different Cu/Al (0.345 and 0.604) and Si/Al (2.9 and 30.8) ratio have been Cu-exchanged with a standard liquid procedure with copper(II) acetate. The characterizations with XRD, ICP-MS, nitrogen adsorption-desorption, SEM, FTIR and Raman demonstrated the efficient Cu exchanging on the support and no peculiar features were observed. CH_4-TPR and CH_4 isothermal adsorption and He-TPD experiments have been used to identify the optimal temperature conditions for CH_4 activation in MTM loop. CH_4 consumption profiles in both 0.345CuY2.9 and 0.604CuY30.8 samples showed a major peak at around 200°C and the activation of secondary conditions (reverse water-gas shift and dry CH_4 reforming) at > 300°C. However, the sample characterized with a higher Cu/Al and Si/Al ratio showed a higher CH_4 consumption (616 μmol/g zeolite) than the sample with smaller ratios (379 μmol/g zeolite). CH_3OH desorption assisted with H_2O produced during the CH_4 oxidation and extra-H_2O present in the system was visible during CH_4-TPRs in both samples. Sequential CH_4 adsorption and He-TPD was also tested, showing that the maximum CH_4 uptake is 90% higher than CH_4 consumed during TPR experiments, suggesting CH_4 diffusion limitations in the pores. The application of CuY zeolites appears reasonable based on the results obtained for the CH_4 activation step, but further studies are needed to verify their activity in the e compete MTM loop and correlate these measurements with CH_3OH productivity and selectivity.

Nomenclature

T = temperature
T_{meas} = temperature measured by the thermocouple (monitoring)
V_t = tubing volume
$\dot{V}_{tot}$ = total volumetric flowrate

Greek letters:

β = Heating rate

Acronyms:

EFAL		Extra-Framework Aluminum
MTM	=	Methane-to-Methanol
FAU		Faujasite
FTIR		Fourier-Transform Infrared Spectrometer
GHSV		Gas-Hourly Space Velocity
GWP		Global Warming Potential
MCT		Mercury-Cadmium-Telluride detector
MOR		Mordenite
HF		High frequency
ICP-MS		Inductively coupled plasma mass spectrometry
LF		Low frequency
SEM		Scanning Electron Microscopy
XRD		X-Ray Diffraction
TPR		Temperature programmed reduction
TPD		Temperature programmed desorption
WGS		Water Gas Shift

References

[1] R. Mansoor, M. Tahir, Recent Developments in Natural Gas Flaring Reduction and Reformation to Energy-Efficient Fuels: A Review, Energy and Fuels. 35 (2021) 3675–3714. https://doi.org/10.1021/acs.energyfuels.0c04269.

[2] R. Franz, E.A. Uslamin, E.A. Pidko, Challenges for the utilization of methane as a chemical feedstock, Mendeleev Communications. 31 (2021) 584–592. https://doi.org/10.1016/j.mencom.2021.09.002.

[3] K. Jawaharraj, N. Shrestha, G. Chilkoor, S.S. Dhiman, J. Islam, V. Gadhamshetty, Valorization of methane from environmental engineering applications: A critical review, Water Research. 187 (2020). https://doi.org/10.1016/j.watres.2020.116400.

[4] N.R. Foster, Direct catalytic oxidation of methane to methanol - a review, Applied Catalysis. 19 (1985) 1–11.

[5] B. Han, Y. Yang, Y. Xu, U.J. Etim, K. Qiao, B. Xu, Z. Yan, A review of the direct oxidation of methane to methanol, Cuihua Xuebao/Chinese Journal of Catalysis. 37 (2016) 1206–1215. https://doi.org/10.1016/S1872-2067(15)61097-X.

[6] M. Ravi, M. Ranocchiari, J.A. van Bokhoven, The direct catalytic oxidation of methane to methanol- a critical assessment, Angewandte Chemie. 129 (2017) 16684–16704. https://doi.org/10.1002/ange.201702550.

[7] I. Suelves, M.J. Lázaro, R. Moliner, B.M. Corbella, J.M. Palacios, Hydrogen production by thermo catalytic decomposition of methane on Ni-based catalysts: Influence of operating conditions on catalyst deactivation and carbon characteristics, International Journal of Hydrogen Energy. 30 (2005) 1555–1567. https://doi.org/10.1016/j.ijhydene.2004.10.006.

[8] A. Holmen, Direct conversion of methane to fuels and chemicals, Catalysis Today. 142 (2009) 2–8. https://doi.org/10.1016/j.cattod.2009.01.004.

[9] M.B. Park, S.H. Ahn, A. Mansouri, M. Ranocchiari, J.A. van Bokhoven, Comparative Study of Diverse Copper Zeolites for the Conversion of Methane into Methanol, ChemCatChem. 9 (2017) 3705–3713. https://doi.org/10.1002/cctc.201700768.

[10] E. Borfecchia, P. Beato, S. Svelle, U. Olsbye, C. Lamberti, S. Bordiga, Cu-CHA-a model system for applied selective redox catalysis, Chemical Society Reviews. 47 (2018) 8097–8133. https://doi.org/10.1039/c8cs00373d.

[11] M. Dyballa, D.K. Pappas, K. Kvande, E. Borfecchia, B. Arstad, P. Beato, U. Olsbye, S. Svelle, On How Copper Mordenite Properties Govern the Framework Stability and Activity in the Methane-to-Methanol Conversion, ACS Catalysis. 9 (2019) 365–375. https://doi.org/10.1021/acscatal.8b04437.

[12] D.K. Pappas, E. Borfecchia, M. Dyballa, I.A. Pankin, K.A. Lomachenko, A. Martini, M. Signorile, S. Teketel, B. Arstad, G. Berlier, C. Lamberti, S. Bordiga, U. Olsbye, K.P. Lillerud, S. Svelle, P. Beato, Methane to Methanol: Structure-Activity Relationships for Cu-CHA, Journal of the American Chemical Society. 139 (2017) 14961–14975. https://doi.org/10.1021/jacs.7b06472.

[13] E.M.C. Alayon, M. Nachtegaal, A. Bodi, J.A. van Bokhoven, Reaction conditions of methane-to-methanol conversion affect the structure of active copper sites, ACS Catalysis. 4 (2014) 16–22. https://doi.org/10.1021/cs400713c.

[14] E.M.C. Alayon, M. Nachtegaal, A. Bodi, M. Ranocchiari, J.A. van Bokhoven, Bis(μ-oxo) versus mono(μ-oxo)dicopper cores in a zeolite for converting methane to methanol: An in situ XAS and DFT investigation, Physical Chemistry Chemical Physics. 17 (2015) 7681–7693. https://doi.org/10.1039/c4cp03226h.

[15] D.K. Pappas, A. Martini, M. Dyballa, K. Kvande, S. Teketel, K.A. Lomachenko, R. Baran, P. Glatzel, B. Arstad, G. Berlier, C. Lamberti, S. Bordiga, U. Olsbye, S. Svelle, P. Beato, E. Borfecchia, The Nuclearity of the Active Site for Methane to Methanol Conversion in Cu-Mordenite: A Quantitative Assessment, Journal of the American Chemical Society. 140 (2018) 15270–15278. https://doi.org/10.1021/jacs.8b08071.

[16] V.L. Sushkevich, J.A. van Bokhoven, Methane-to-Methanol: Activity Descriptors in Copper-Exchanged Zeolites for the Rational Design of Materials, ACS Catalysis. 9 (2019) 6293–6304. https://doi.org/10.1021/acscatal.9b01534.

[17] D.K. Pappas, E. Borfecchia, M. Dyballa, K.A. Lomachenko, A. Martini, G. Berlier, B. Arstad, C. Lamberti, S. Bordiga, U. Olsbye, S. Svelle, P. Beato, Understanding and Optimizing the Performance of Cu-FER for The Direct CH4 to CH3OH Conversion, ChemCatChem. 11 (2019) 621–627. https://doi.org/10.1002/cctc.201801542.

[18] R.J. Madon, Role of ZSM-5 and Ultrastable Y Zeolites for Increasing Gasoline Octane Number, Journal of Catalysis. 129 (1991) 275–287.

[19] J. Scherzer, Designing FCC catalysts with high-silica Y zeolites, Applied Catalysis. 75 (1991) 1–32.

[20] T. Kanazawa, Development of hydrocarbon adsorbents, oxygen storage materials for three-way catalysts and NOx storage-reduction catalyst, in: Catalysis Today, 2004: pp. 171–177. https://doi.org/10.1016/j.cattod.2004.06.119.

[21] N. Taufiqurrahmi, A.R. Mohamed, S. Bhatia, Nanocrystalline zeolite Y: Synthesis and characterization, in: IOP Conference Series: Materials Science and Engineering, 2011. https://doi.org/10.1088/1757-899X/17/1/012030.

[22] K.A. Lomachenko, A. Martini, D.K. Pappas, C. Negri, M. Dyballa, G. Berlier, S. Bordiga, C. Lamberti, U. Olsbye, S. Svelle, P. Beato, E. Borfecchia, The impact of reaction conditions and material composition on the stepwise methane to methanol conversion over Cu-MOR: An operando XAS study, Catalysis Today. 336 (2019) 99–108. https://doi.org/10.1016/j.cattod.2019.01.040.

[23] J.P. Lange, V.L. Sushkevich, A.J. Knorpp, J.A. van Bokhoven, Methane-to-Methanol via Chemical Looping: Economic Potential and Guidance for Future Research, Industrial and Engineering Chemistry Research. 58 (2019) 8674–8680. https://doi.org/10.1021/acs.iecr.9b01407.

[24] G. Turnes Palomino, P. Fisicaro, S. Bordiga, A. Zecchina, E. Giamello, C. Lamberti, Oxidation States of Copper Ions in ZSM-5 Zeolites. A Multitechnique Investigation, Journal of Physical Chemistry B. 104 (2000) 4064–4073. https://doi.org/10.1021/jp993893u.

[25] D. Chateigner, X. Chen, M. Ciriotti, R.T. Downs, S. Gražulis, W. Kaminsky, A. le Bail, L. Lutterotti, Crystallography Open Database Open-access collection of crystal structures of organic, inorganic, metal-organics compounds and minerals, excluding biopolymers., (n.d.). http://www.crystallography.net/cod/.

[26] R. Beaumont, D. Barthomeuf, X, Y, Aluminum-Deficient and Ultrastable Faujasite-Type Zeolites II. Acid Strength and Aluminum Site Reactivity, Journal of Catalysis. 27 (1972) 45–51.

[27] K.S.W. Sing, D.H. Everett, R.A.W. Haul, L. Moscou, R.A. Pierotti, J. Rouquerol, T. Siemieniewska, Reporting physisorption data for gas/solid systems with Special Reference to the Determination of Surface Area and Porosity Reporting physisorption data for gas/solid systems-with special reference to the determination of surface area and porosity, Pure & Applied Chemistry. 57 (1985) 603–619.

[28] P. Bornhauser, G. Calzaferri, Ring-Opening Vibrations of Spherosiloxanes, Journal of Physical Chemistry. 100 (1996) 2035–2044. https://pubs.acs.org/sharingguidelines.

[29] S. Grundner, M.A.C. Markovits, G. Li, M. Tromp, E.A. Pidko, E.J.M. Hensen, A. Jentys, M. Sanchez-Sanchez, J.A. Lercher, Single-site trinuclear copper oxygen clusters in mordenite for selective conversion of methane to methanol, Nature Communications. 6 (2015). https://doi.org/10.1038/ncomms8546.

[30] M.A. Newton, A.J. Knorpp, A.B. Pinar, V.L. Sushkevich, D. Palagin, J.A. van Bokhoven, On the Mechanism Underlying the Direct Conversion of Methane to Methanol by Copper Hosted in Zeolites; Braiding Cu K-Edge XANES and Reactivity Studies, Journal of the American Chemical Society. 140 (2018) 10090–10093. https://doi.org/10.1021/jacs.8b05139.

[31] A.A. Gabrienko, S.A. Yashnik, A.A. Kolganov, A.M. Sheveleva, S.S. Arzumanov, M. v. Fedin, F. Tuna, A.G. Stepanov, Methane Activation on H-ZSM-5 Zeolite with Low Copper Loading. The Nature of Active Sites and Intermediates Identified with the Combination of Spectroscopic Methods, Inorganic Chemistry. 59 (2020) 2037–2050. https://doi.org/10.1021/acs.inorgchem.9b03462.

[32] J. Pires, M. Brotas De Carvalho, F.R. Ribeiro, E.G. Derouane ’, Carbon dioxide in Y and ZSM-20 zeolites: adsorption and infrared studies, Journal of Molecular Catalysis. 85 (1993) 295–303.

[33] A.R. Kulkarni, Z.J. Zhao, S. Siahrostami, J.K. Nørskov, F. Studt, Cation-exchanged zeolites for the selective oxidation of methane to methanol, Catalysis Science and Technology. 8 (2018) 114–123. https://doi.org/10.1039/c7cy01229b.

[34] X. Wang, N.M. Martin, J. Nilsson, S. Carlson, J. Gustafson, M. Skoglundh, P.A. Carlsson, Copper-modified zeolites and silica for conversion of methane to methanol, Catalysts. 8 (2018). https://doi.org/10.3390/catal8110545.

[35] K.T. Dinh, M.M. Sullivan, K. Narsimhan, P. Serna, R.J. Meyer, M. Dincă, Y. Román-Leshkov, Continuous Partial Oxidation of Methane to Methanol Catalyzed by Diffusion-Paired Copper Dimers in Copper-Exchanged Zeolites, Journal of the American Chemical Society. 141 (2019) 11641–11650. https://doi.org/10.1021/jacs.9b04906.

[36] G.J. Kim, D.-S. Cho, K.-H. Kim, J.-H. Kim, The reaction of CO2 with CH4 to synthesize H2 and CO over nickel-loaded Y-zeolites, Catalysis Letters. 28 (1994) 41–52.

[37] H. Maghsoudi, V. Nozari, S.R. Zamzami, Diffusion of methane in high-silica CHA zeolite, Heat and Mass Transfer/Waerme- Und Stoffuebertragung. 55 (2019) 1619–1625. https://doi.org/10.1007/s00231-018-02547-0.

Conclusions

The central idea of the research activities reported in the PhD thesis is that catalysts are dynamic materials: the structure changes together with the local reaction conditions and it is strictly connected to the reactivity. The application of different reaction conditions induces structural rearrangements at atomic level reflecting at surface scale with structural modifications, such as sintering and agglomeration. The knowledge of these relevant processes between catalyst bulk and surface and their connection to reactivity parameters (conversion, yield and selectivity) gives important information on catalyst and reactor design, to improve the overall performance, predict deactivation behaviours and actions to increase catalyst efficiency.

In the perspective of investigating the interaction between reaction conditions, physical/chemical phenomena occurring on the catalyst and hence on reactivity, temperature was chosen as transient variable and the combination of conversion, product formation and surface characterization (SEM) results were assembled to draw a conclusion on each process investigated.

The application of temperature-programmed experiments (reduction and oxidation) to a model reactive system (unsupported CuO reduction with H_2 and reoxidation with O_2) was thoroughly investigated under different aspects. The influence of experimental conditions (sample mass, particle size, gas reactant concentration, total volumetric flowrate, heating rate) was studied to correlate the reduction (or oxidation) profiles to macroscopic performance (degree of reduction/oxidation) and chemical/physical phenomena (reaction mechanism, mass- and heat-transfer limitations). The profiles (peak shape and key temperatures) were significantly affected by the experimental conditions and their combinations, identifying a primary role for the sample mass, gas reactant flow rate (i.e. higher concentration or total flow rate) and heating rate, while a negligible contribution was given by the particle size, for both CuO reduction and Cu oxidation. The common explanation key is the limitation due to external mass transfer, in a heterogenous reaction without significant internal mass transfer limitations.

Heat effects play a relevant, underestimated effect. The addition of an inert, highly heat-conductive bed dilutant (SiC) promoted the CuO reduction to Cu at higher H_2 concentration, i.e. both favoring the kinetics, levelling out temperature gradients in the sample, reducing the diffusive limitations, as soon as Cu nuclei are formed on the surface of the unreacted CuO and delaying agglomeration phenomena.

The final morphological configuration was severely affected by the sequential reduction and oxidation processes, implying that the selection of the experimental variables for TPR/TPO protocols could not be solely performed through a characteristic number, disregarding mass-transfer limitations. Specifically, it was demonstrated that the selection of different set of variables to fit *P* characteristic number in its optimal range produces divergent results in terms of peak shape, characteristic temperatures and reduction degree, and thus it should be used with caution as a TPR design criteria.

The loss in reactivity caused by physical phenomena, such as agglomeration, was further analysed to clearly identify the process (reduction, oxidation or just thermal, non-reactive cycle) or pre-treatment (inert, oxidative) responsible for such a decrease. It was proven that when unsupported CuO is reduced to Cu in a reducing mixture (H_2/Ar), pressure drop falls drastically in correspondence to the highest H_2 consumption (reduction peak) and agglomeration was attributed to this process, while the contribution other pre-treatment/reaction steps is negligible. SEM analyses of the spent CuO sample show dramatic variations from the initial morphology, as a bulky layer covers the particles and copper oxides nanostructures are created in the surface. In most cases, the degree of reduction and oxidation was <100%, suggesting that mass-transfer limitations induced by the formed layer were influencing the activity, as soon as the reaction activates.

The long-term reactivity was studied with 11 sequential TPR-TPO experiments and a progressive loss in activity was visible from the degree of reduction/oxidation, decreasing from 100% in the 1st cycle to 15% in the 11th cycle, and peak shape analysis. Particularly, the Cu oxidation mechanism is made of two steps (Cu $\rightarrow$ Cu_2O $\rightarrow$ CuO) in standard condition, but as the number of cycles increased, the second peak was shifting to higher temperatures until it disappeared completely in the 5th oxidation cycle. This behavior was attributed to the restructuration of the reactive bed at macro and microscopical level, limiting the complete oxidation to CuO in successive cycles.

Axial temperature gradients were measured during TPR and TPO experiments to correlate the appearance of multiple peaks with an uneven temperature distribution in the reactive bed. During the reduction, a single H_2 consumption peak and low temperature gradients are observed in both cases, suggesting that double peaks are not generated by thermal effects but from physical phenomena (agglomeration and shrinking). On the other hand, the oxidation is much more exothermic than the reduction and the oscillating temperature gradients, reflected on the

O_2 consumption profiles, were attributed to the poor furnace control-loop, once the bed shrunk, loosing contact with the controlling thermocouple.

The formation of nanostructures on CuO surfaces (Cu foil and Cu/CuO powder) was specifically investigated, by applying thermal and chemical treatments, also through multiple cycles. Nanowhiskers are observed, whose dimensions and density can be adjusted by varying the O_2 partial pressure and maximum temperature of the oxidative treatment. Higher O_2 partial pressures increase the nanowhiskers density at lower maximum temperature, but the same output could be obtained by decreasing O_2 partial pressure at increased temperature. The application of a complete reduction-oxidation cycle showed that the H_2 treatment prior to the oxidation stage favors the nanowires growth. Also, the contact time between the reducing gas phase and oxide influenced the surface morphology: increasing the contact time, the surface roughness increases as an effect of the superficial microstructure rearrangement, while a lower contact time generates superficial cavities, indicating a less uniform distribution of copper grains.

CO oxidation with lattice oxygen under constant heating (CO-TPR) confirms the conclusions about the mobility of O in $LaFeO_3$, which is slow and governed by a lattice diffusive mechanism; for temperatures higher that the activation one, CO oxidation with lattice oxygen at constant temperature show sustained production of CO_2 starting from 300°C, because the temperature for activating the bulk diffusion has been surpassed, and the time-temperature variables starts a reciprocal influence: the higher the temperature (above the activation for bulk diffusion), the less time will be required for the diffusion, and the lower the time to produce CO_2.

The feasibility of Cu-exchanged Y zeolites in MTM loop has been investigated by focusing the attention on the CH_4 activation step. Two Y zeolites with different Cu/Al (0.345 and 0.604) and Si/Al (2.9 and 30.8) ratio have been Cu-exchanged with a standard liquid procedure with copper(II) acetate. CH_4-TPR and CH_4 isothermal adsorption and He-TPD experiments have been used to identify the optimal temperature conditions for CH_4 activation in MTM loop. CH_4 consumption profiles in both 0.345CuY2.9 and 0.604CuY30.8 samples showed a major peak at around 200°C and the activation of secondary conditions (reverse water-gas shift and dry CH_4 reforming) at > 300°C. However, the sample characterized with a higher Cu/Al and Si/Al ratio showed a higher CH_4 consumption (616 μmol/g zeolite) than the sample with smaller ratios (379 μmol/g zeolite). CH_3OH desorption assisted with H_2O produced during the CH_4 oxidation and extra-H_2O present in the system was visible during CH_4-TPRs in both samples.

Sequential CH_4 adsorption and He-TPD was also tested, showing that the maximum CH_4 uptake is 90% higher than CH_4 consumed during TPR experiments, suggesting CH_4 diffusion limitations in the pores. The application of CuY zeolites appears reasonable based on the results obtained for the CH_4 activation step, but further studies are needed to verify their activity in the e compete MTM loop and correlate these measurements with CH_3OH productivity and selectivity.

A general conclusion of these studies is that common materials used as catalysts change dramatically structure and reactivity at different scales, during exposure to reducing or oxidizing environment. The accurate description of such changes, and the reproducibly of them, requires further efforts, increasing the accuracy of the characterization, and hopefully observing in-situ the transformations, while they develop with operando techniques.